ANNUAL REPORTS ON NMR SPECTROSCOPY

Volume 35

- Proton tunnelling effects in metal hydride NMR
- Structural studies of hydrogen-bonded peptides and polypeptides by solid-state NMR
- NMR imaging
- NMR studies of interfacial phenomena

ACADEMIC PRESS

ANNUAL REPORTS ON

NMR SPECTROSCOPY

This Page Intentionally Left Blank

ANNUAL REPORTS ON

NMR SPECTROSCOPY

Edited by

G. A. WEBB

Department of Chemistry, University of Surrey, Guildford, Surrey, England

VOLUME 35

ACADEMIC PRESS

San Diego ● London ● Boston
New York ● Sydney ● Tokyo ● Toronto

This book is printed on acid-free paper.

Copyright © 1998 by ACADEMIC PRESS

All Rights Reserved

No part of this publication may be reproduced or transmitted in any form or by any means electronic or mechanical, including photocopy, recording, or any information storage and retrieval system, without permission in writing from the publisher.

Academic Press
525 B Street, Suite 1900, San Diego, California 92101-4495, USA
http://www.apnet.com

Academic Press Limited
24–28 Oval Road, London NW1 7DX, UK
http://www.hbuk.co.uk/ap/

ISBN 0-12-505335-5

A catalogue record for this book is available from the British Library

Typeset by Keyset Composition, Colchester, Essex
Printed in Great Britain by MPG Books Ltd, Bodmin, Cornwall

98 99 00 01 02 03 MP 9 8 7 6 5 4 3 2 1

List of Contributors

I. Ando, *Department of Polymer Chemistry, Tokyo Institute of Technology, Ookyama, Meguro-ku, Tokyo, Japan*

S. Ando, *Department of Polymer Chemistry, Tokyo Institute of Technology, Ookyama, Meguro-ku, Tokyo, Japan*

N. Asakawa, *Department of Polymer Chemistry, Tokyo Institute of Technology, Ookyama, Meguro-ku, Tokyo, Japan*

J. Grandjean, *University of Liège, Institute of Chemistry B6a, Sart-Tilman, B-4000 Liège, Belgium*

T. Kameda, *Department of Polymer Chemistry, Tokyo Institute of Technology, Ookyama, Meguro-ku, Tokyo, Japan*

S. Kuroki, *Department of Polymer Chemistry, Tokyo Institute of Technology, Ookyama, Meguro-ku, Tokyo, Japan*

H. Kurosu, *Department of Polymer Chemistry, Tokyo Institute of Technology, Ookyama, Meguro-ku, Tokyo, Japan*

William S. Price, *Water Research Institute, Sengen 2-1-6, Tsukuba, Ibaraki 305, Japan*

A. Shoji, *Department of Biological Sciences, Gunma University, Tenjin-cho, Kiryu, Gunma, Japan*

Sławomir Szymański, *Institute of Organic Chemistry, Polish Academy of Sciences, Kasprzaka 44, 01-224 Warszawa, Poland*

This Page Intentionally Left Blank

Preface

Volume 35 of Annual Reports on NMR Spectroscopy contains items representing the application of NMR in four different scientific areas.

The very interesting area of Proton Tunnelling Effects in Metal Hydride NMR is discussed by S. Szymański, Structural Studies of Hydrogen-Bonded Peptides and Polypeptides by Solid State NMR are covered by N. Asakawa, T. Kameda, S. Kuroki, H. Kurosu, S. Ando, I. Ando and A. Shoji, W. Price deals with recent developments in NMR Imaging, and NMR Studies of Interfacial Phenomena are reported by J. Grandjean.

It is a great pleasure for me to offer my thanks to all of these authors for their very successful endeavours in producing very valuable accounts of their chosen areas of scientific activity. My sincere thanks also go to the production staff at Academic Press (London) for their help and cooperation in the production of this volume.

University of Surrey
Guildford, Surrey
England

G. A. WEBB
April 1997

This Page Intentionally Left Blank

Contents

NMR Studies of Interfacial Phenomena
J. GRANDJEAN

Colour plates are located between pp. 182–3.

Proton Tunnelling Effects in Metal Hydride NMR

SŁAWOMIR SZYMAŃSKI

Institute of Organic Chemistry, Polish Academy of Sciences, Kasprzaka 44, 01-224 Warszawa, Poland

The discovery, at the end of the 1980s, of coherent proton tunnelling in transition metal polyhydrides seems to be one of the most interesting findings ever made in NMR spectroscopy. This subtle quantum phenomenon, observed in liquids at ambient temperatures in the form of anomalously large proton–proton couplings, shows up an unprecedented thermal stability. No less intriguing is the fact that the tunnelling frequency or the coupling magnitude apparently increases with increasing temperature. Under impact of temperature there also evolves an incoherent process that eventually prevails, causing a collapse of the hydride spectrum into a singlet with no fine structure discernible. In the present contribution a detailed account is given of the relevant experimental studies. Moreover, theoretical models involving both the microscopic origin of the phenomenon and its responses to temperature are reviewed. Emphasis is laid on the most recent approaches providing a consistent quantum-mechanical picture of both the coherent tunnelling and the associated incoherent process.

ANNUAL REPORTS ON NMR SPECTROSCOPY
VOLUME 35 ISBN 0-12-505335-5

Copyright © 1998 Academic Press Limited
All rights of reproduction in any form reserved

1. INTRODUCTION

In NMR spectroscopy, the magnetic nuclei are generally thought of as semiclassical objects. Quantum mechanics is applied only to their spins; their spatial degrees of freedom are described classically. There are only rare instances where the latter also call for a quantum-mechanical treatment. About 30 years ago it was anticipated that tunnelling motion of a methyl group in a solid might produce extra splittings of the proton resonance signal.[1] A few years later such splittings were identified experimentally in a powder sample of ethyl iodide.[2] The experimental material accumulated since then, including recent high-resolution data obtained for single molecular crystals,[3–6] involves hindered quantum rotors such as CH_3 and NH_n^+ groups and their per-deuterated counterparts. In any such case, one deals with a specific quantum motion which only permutes identical particles among their equilibrium positions. In systems composed of like particles, the symmetrization postulate of quantum mechanics correlates the orbital degrees of freedom of the particles with their spin coordinates. This is the ultimate reason why quantum tunnelling in such systems can lead to splittings in NMR spectra. In solid-state NMR, the observations of tunnelling splittings have so far been restricted to cryogenic temperatures.

In liquid-phase NMR one necessarily works far above the cryogenic range. Until the late 1980s it was hardly imaginable that the usual semiclassical approach could fail in this regime. The semiclassical stereotype had at last to be revised under the pressure of a growing number of reports on strange proton–proton *J*-couplings that could not be explained in terms of the usual electron-mediated interactions. The couplings were observed between hydride protons in complexes of some transition metal hydrides dissolved in organic solvents.[7–12] These couplings show very strong dependence on temperature and reach unusually large magnitudes at high temperatures. Further variations with temperature are obscured by gradually evolving incoherent processes leading to coalescence and ultimate collapse of the offending multiplets. In 1989, tentative explanations of these unusual couplings were proposed in two simultaneous, preliminary reports by Zilm *et al.*[13] and by Weitekamp *et al.*,[14] followed by more detailed accounts.[15–18] The unusual phenomena were explained in terms of a concerted pairwise tunnelling of the hydrides through the vibrational potential. For pairs of spin-$\frac{1}{2}$ particles the original formulation of Heisenberg's quantum-mechanical exchange coupling[19,20] is applicable. This virtual coupling between the particles' spins is formally identical with the familiar NMR *J*-coupling. Hence the NMR multiplets of the hydride unit can have the usual appearance and only the meaning of the relevant coupling constants needs to be modified. In place of the ordinary (magnetic) coupling constant, J^{mag}, one observes an apparent coupling constant

$$J^{\mathrm{app}} = J^{\mathrm{mag}} - \nu_{\mathrm{t}}, \tag{1}$$

where ν_t is the tunnelling splitting or, more precisely, a thermal average of such splittings over a ladder of vibrational levels. For subsequent vibrational levels the magnitudes of tunnelling splittings increase steeply. The dependence of J^{app} on temperature is generally related to the fact that the contributions to ν_t from different vibrational levels vary with temperature.[13–18]

The idea that these anomalous couplings are due to quantum-mechanical exchange is based on a strong experimental evidence from isotopic studies. When one of the tunnelling protons is replaced by a different hydrogen nuclide, the symmetrization postulate underlying Heisenberg coupling is no longer applicable and, accordingly, only the usual, magnetic component of the coupling can be observed.[13,15,16] The quantum-mechanical origin of these anomalous phenomena has therefore generally been accepted in the literature. However, one faces a variety of approaches when it comes to details. In regard to the experimental data gathered prior to 1992, at least four substantially differing models, each invoking two or three free parameters only, afforded good fits to the observed dependences on temperature of the exchange couplings.[16,18,21,22] Further variants are able to reproduce these crucial dependences qualitatively. Presently, there seems to be emerging a clearer picture that is due to a series of recently published studies, including refined quantum-chemical calculations of the relevant vibrational potential[23–25] and NMR measurements on isotopically labelled hydrides over a broad temperature range.[26] Two of the most recent approaches[27,28] are aimed at a consistent explanation of both kinds of thermal effects observed in NMR spectra: the coherent tunnelling that produces resolved, temperature-dependent splittings of the resonance signals, and the gradually evolving incoherent processes that ultimately prevail.

So far as is possible the arrangement of the present review follows the history of both experimental and theoretical studies on this fascinating subject.

2. A SURVEY OF EXPERIMENTAL DATA

In 1984, conclusive proof was reported that H_2 molecules can be coordinated to the metal centres of some transition metal complexes, retaining many of the properties of molecular hydrogen.[29] In particular, the proton–proton distance in the coordinated molecule is similar to that in the free molecule. Such a dihydrogen structure can be identified when the compound is prepared from HD: large values of J_{HD}—up to 35 Hz, which is not far from the value of ~43 Hz in a free HD molecule—are observed for the dihydrogen ligand (see, e.g., a review by Heinekey and Oldham[30]). The unusual H–H couplings were first supposed to be magnetic couplings within hypothetical dihydrogen ligands coordinated to the metal centre.[11,12] In view of the already mentioned findings from isotopic studies, the explanation in terms of magnetic couplings could not be sustained.

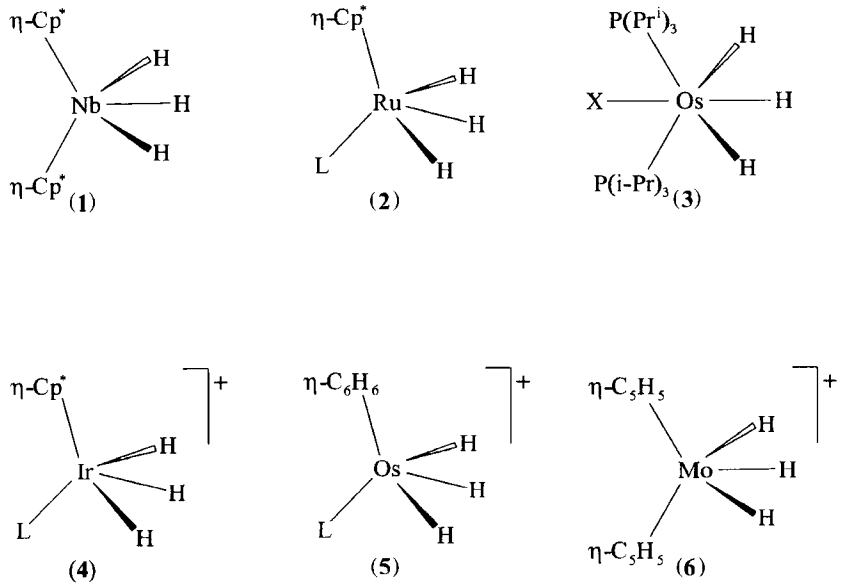

Fig. 1

The list of compounds exhibiting the unusual effects is dominated by derivatives for which there is no conclusive evidence of a possible contribution of dihydrogen structures. The compounds that are structurally characterized as trihydrides include neutral complexes of niobium*,[7,12,31,32] ((**1**) in Fig. 1), ruthenium,[9,10,33–35] (**2**), and osmium,[36] (**3**) trihydrides. Further examples include cationic complexes of iridium,[11,13,15,26] (**4**), osmium,[37] (**5**), and molybdenum,[31] (**6**) trihydrides. Except for (**3**) and (**5**), the ligands include one or two variously substituted cyclopentadienyl anions; tertiary phosphines or phosphites are coligands in all the compounds but (**1**) and (**6**).

Neutron diffraction studies on (**4a**) (Cp* = C_5H_5, L = PMe_3) reveal that the hydride protons are located at the vertices of a slightly distorted equilateral triangle with edges of 1.67, 1.70, and 2.66 Å; the Ir–H distances are in the range 1.583–1.591 Å.[15] In the ^1H NMR spectra of (**1**)–(**6**) (^{31}P-decoupled for (**2**)–(**5**)) the singlet of the hydride protons that is observed at high temperature decoalesces into an A_2B pattern upon cooling the sample. In solution the compounds (**1**)–(**6**) have an effective symmetry plane crossing the metal atom,

*Already in 1982 J. A. Labinger in his chapter on niobium and tantalum hydrides (*Comprehensive Organometallic Chemistry*, Vol. 3 (ed. G. Wilkinson, F. G. A. Stone and E. W. Abel), p. 707, Pergamon Press, Oxford, 1982) quoted an unpublished observation by F. N. Tebbe of a coupling of about 100 Hz between hydride protons in a substituted niobocene trihydride.

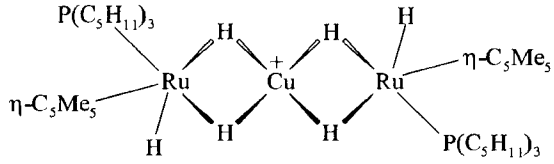

(7)

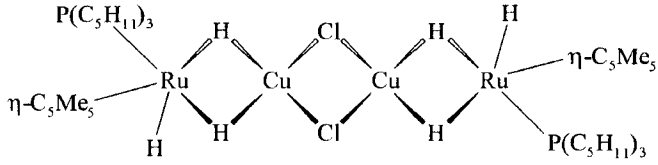

(8)

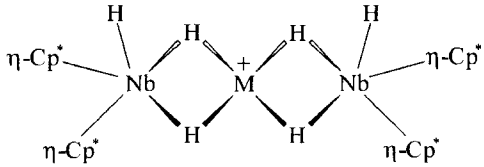

(9)

Fig. 2

one of the hydrides, and the centres of the coligands. The unusual couplings occur between each of the terminal hydride protons and the proton in the symmetry plane. Generally, along with increase of temperature, the coupling magnitude also increases. For (**4b**) (Cp* = C_5H_5, L = 1-methyl-4-phospha-3,6,8-trioxabicyco[2.2.2]octane) J^{app} varies from 972 Hz at 176 K to 1565 Hz at 196 K.[15] The latter is probably the largest indisputable value of J^{app} reported so far. It is nearly an order of magnitude larger than the proton–proton coupling in molecular hydrogen, about 280 Hz, which is believed to be the largest magnetic proton–proton coupling. Use of a chiral phosphine ligand afforded an assessment of the *J*-coupling between the otherwise magnetically equivalent terminal hydride protons: the value of 3.4 Hz found for (**4c**) (Cp* = C_5H_5, L = P(H)(Ph)(*n*-decyl)) is independent of temperature and typical for magnetic coupling mechanism.[15]

Quantum exchange couplings are also observed for cationic[33,38] ((**7**) in

Fig. 2) and neutral[33,38] (**8**) adducts of a ruthenium trihydride complex with Lewis acids containing Cu(I), and for a series of cationic adducts of niobocene trihydride (**1a**) and its derivatives (**1b**) ($Cp^* = C_5H_4(SiMe_3)$) and (**1c**) ($Cp^* = C_5H_3(SiMe_3)_2$) with Lewis acids of Cu(I), Ag, and Au[32,39,40] (**9**). The structures of (**7**)–(**9**) were determined from X-ray studies.[38,39,40] In these compounds the high-temperature singlet of the hydride protons decoalesces into a broadened A_2B multiplet which, on further cooling, either sharpens with a retention of the A_2B form or transforms into an ABC pattern. The latter behaviour, observed for (**9**) where M = Cu(I)[32,40] and Au,[39,40] and also for (**7**)[38] is consistent with the X-ray data revealing different Ru–H (for (**7**)) and Nb–H (for Au derivatives of (**9**)) distances for the two bridging hydrogen atoms.[38,40] In the low-temperature spectra of (**7**) and (**9**) the anomalous coupling occurs between the hydride proton not involved in the bridge and one of the bridging protons. For the derivatives of (**9**), transformation of the low-temperature ABC multiplet into an A_2B one at intermediate temperatures was explained in terms of isomerization of the complex with two bridging hydrides in each moiety of the molecule into a hydride/dihydrogen form with only one hydride involved in the bridge. The latter may be either a stable species or a sort of intermediate on the reaction path.[40]

First observations of quantum exchange couplings in non-trihydride systems involved cationic complexes of tantalum dihydrides[41] ((**10**) in Fig. 3). In (**10a**) (L = $P(OMe)_3$) the proton–proton distance of 1.67 Å, i.e. similar to that in trihydride (**4a**) ($Cp^* = C_5H_5$, L = PMe_3) was estimated[42] from longitudinal relaxation data following the procedure described in Refs 43. The ^{31}P-

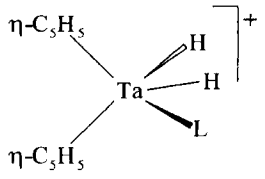

(**10**)

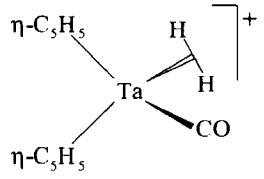

(**11**)

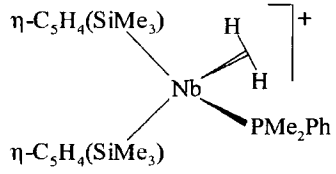

(**12**)

Fig. 3

decoupled spectra of the hydride protons of (**10**) show an AB pattern at low temperatures. The temperature behaviour of the spectra is similar to that of (**1**)–(**9**).

A related tantalum derivative (**11**) has been reported[42] that was formerly believed to be a typical dihydrogen complex.[44] The more recent studies[42] on the isotopomer (**11**)-*d* prepared from HD gave a value of J_{HD} of 27.5 Hz, which was in a fair agreement with the previous guess as to the structure. The NMR behaviour of (**11**)-*d* at low temperatures was, however, incompatible with that of a typical dihydrogen complex where the dihydrogen ligand should undergo rapid reorientation on the NMR timescale.[30] In ^{1}H spectra of (**11**)-*d*, below 208 K the high-temperature triplet at $\delta = -5.17$ ppm decoalesced into two tripets, at $\delta = -5.14$ and $\delta = -5.78$, both with $J_{HD} = 27.5$ Hz. Similar decoalescence was observed in ^{2}H spectra. The two low-temperature signals were ascribed to the protons (deuterons) occupying the *exo* and *endo* positions. The activation energy of 40 kJ/mol (9.6 kcal/mol) for the assumed stochastic exchange between *exo* and *endo* positions was calculated from lineshape analysis. However, no decoalescence was observed for both the perprotio and perdeuterio ((**11**)-d_2) derivatives. This can hardly be rationalized in terms of reduced activation energy of the stochastic exchange since for the d_2 derivative the activation energy should actually increase owing to the isotopic H/D effect. The authors conclude that (**11**) represents a new class of dihydrogen complexes, with a nonrotating dihydrogen ligand. The failure to observe decoalescence in the perprotio and perdeuterio derivatives is attributed to very strong exchange couplings in these compounds, exceeding by many times the chemical shift differences between *exo* and *endo* positions. In the case of two interacting nuclei, such a strong interaction would cause an apparent collapse of the multiplet to a singlet. Similar features were observed for a niobium derivative (**12**).[45] The H–H distances for (**11**) and (**12**), calculated from T_1 data under the assumption of slow reorientation of the dihydrogen ligand, are 1.06 Å[42] and 1.17 Å,[45] respectively. The difference in the proton–proton distance is clearly reflected in the magnitudes of J_{HD} for the corresponding isotopomers (27.5 Hz for (**11**)-*d* and ~15 Hz for (**12**)-*d*).

Wherever it will not lead to ambiguity, in the following all of the derivatives of (**1**)–(**12**) exhibiting exchange couplings will generally be referred to as metal hydrides. In view of the findings described in the preceding paragraph, clear distinction between genuine hydrides and complexes containing a stretched dihydrogen ligand does not always seem possible.

2.1. Dependence of the spectra on temperature

Apart from their unusual magnitudes, the most striking feature of the couplings in question is their unprecedented sensitivity to temperature. With a remarkable exception involving niobocene trihydride (**1a**), where J^{app} first

decreases to zero and then, along with further increase of temperature, reappears again,[31] the (absolute) magnitude of the coupling always increases monotonically with increasing temperature. Studies on the limiting low-temperature behaviour are obviously restricted by solubility problems. At high temperatures the natural limit is set by the onset of coalescence phenomena: the chemical shifts of the hydride protons ultimately undergo averaging and further observation of the couplings is not possible. It is interesting that, generally, the chemical shifts show only a mild dependence on temperature. The changes of the appearance of the spectra due to incoherent exchange processes are extremely well described by the standard Alexander–Binsch[46,47] lineshape equation.[39,42,48]

Recently, the variation of J^{app} with temperature was studied systematically over a wide temperature range of 125–201 K for a series of derivatives of (**4**).[26] Representative examples of the observed trends are shown in Fig. 4 together with similar data reported previously for derivatives of (**1**) and (**2**).

It is remarkable that at a fixed temperature the magnitudes of J^{app} for a series of derivatives of (**4**) differing only in the ligand L correlate inversely with the basicity of the ligand (the higher the basicity, the smaller the coupling).[15,26] Similar trends were found for neutral ruthenium complexes (**2**).[35]

The magnitudes of J^{app} show a rough inverse correlation with activation enthalpies of the incoherent processes occurring at elevated temperatures.[26] For the above-mentioned series of derivatives of (**4**), the activation enthalpies fall in the range of 38–50 kJ/mol (9–12 kcal/mol), while the corresponding activation entropies are below 1 e.u.[26]

2.2. Isotopic effects

As already mentioned, studies on the metal hydrides with hydrogen selectively substituted by deuterium or tritium yielded definite evidence of the quantum exchange origin of the unusual coupling. For magnetic spin–spin couplings, substitution of one (two) of the interacting nuclei with a different isotope results mainly in a rescaling of J by the ratio (the squared ratio) of the corresponding gyromagnetic coefficients. The discrepancies arising from

Fig. 4. Dependence of J^{app} on temperature for selected transition metal trihydride complexes. Data for compounds (**1b**) ($Cp^* = C_5H_4(SiMe_3)$), (**1c**) ($Cp^* = C_5H_3(SiMe_3)_2$), (**2a**) ($Cp^* = C_5Me_5$, L = P-P^{i}r$_3$), and (**2b**) ($Cp^* = C_5Me_5$, $L = P(C_6H_{11})_3$) were taken from Ref. 12. Data for compound (**4b**) ($Cp^* = C_5H_5$, L = 1-methyl-4-phospha-3,6,8-trioxabicyco[2.2.2]octane) were taken from Ref. 16. Data for compounds (**4a**) ($Cp^* = C_5H_5$, $L = PMe_3$), (**4d**) ($Cp^* = C_5H_5$, $L = PPh_3$), (**4e**) ($Cp^* = C_5H_5$, $L = AsPh_3$), (**4f**) ($Cp^* = C_5H_5$, L = P-P^{i}r$_3$), (**4i**) ($Cp^* = C_5H_5$, $L = P(C_6H_{11})_3$), (**4j**) ($Cp^* = (C_5Me_5$, $L = PPh_3$), and (**4k**) (C_5Me_5, $L = PMe_3$) were taken from Ref. 26.

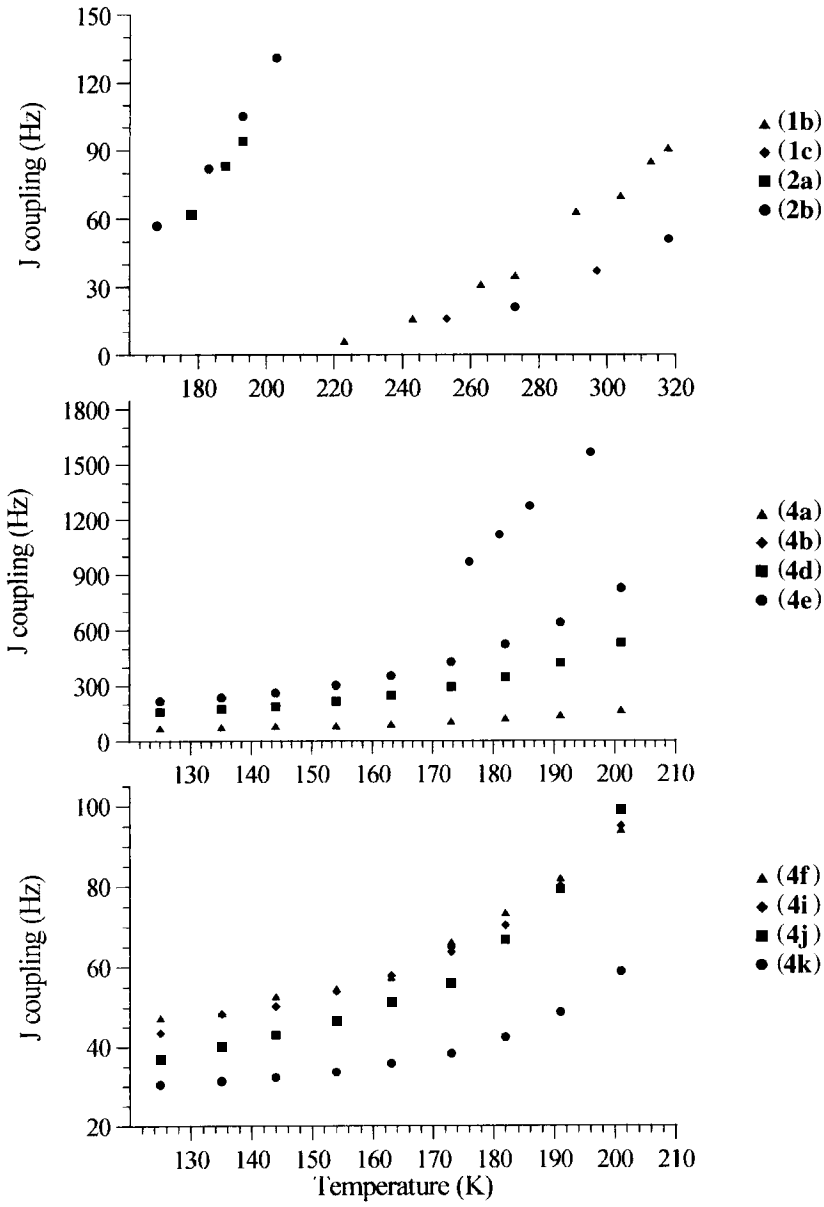
J coupling (Hz)
150
120
90
60
30
0
180 200 220 240 260 280 300 320
▲ (1b)
◆ (1c)
■ (2a)
● (2b)
J coupling (Hz)
1800
1500
1200
900
600
300
0
130 140 150 160 170 180 190 200 210
▲ (4a)
◆ (4b)
■ (4d)
● (4e)
J coupling (Hz)
100
80
60
40
20
130 140 150 160 170 180 190 200 210
Temperature (K)
▲ (4f)
◆ (4i)
■ (4j)
● (4k)

changes in the system's vibrational degrees of freedom do not usually exceed a few per cent of the coupling magnitude.

Extensive studies on isotopically labelled iridium trihydride complexes were carried out by Heinekey *et al.*[15,16,26] In (**4d**) (Cp* = C_5H_5, L = PPh_3), for which the limiting low-temperature value of J^{app} is 260 Hz, substitution of the hydride proton in the symmetry plane with a deuteron results in a collapse of the signal of the terminal protons to a broadened singlet ($\Delta\nu_{1/2} \simeq 12$ Hz).[15] Such a picture is repeated over a range of temperatures for a number of iridium hydrides. Longitudinal relaxation of the introduced deuteron is too slow to be responsible for the absence of a visible splitting if the coupling in the parent perprotio species is of purely magnetic origin. Substitution of a deuteron in one of the two equivalent terminal positions leaves the coupling between the remaining terminal and the central proton still slightly enhanced, by 3–6%.[15,16,26] The latter observation, combined with the findings for (**4c**) mentioned at the beginning of Section 2, provided the first evidence for the two-particle nature of the phenomenon and quelled speculation on the possibility of a straight analogy between the trihydrides and tunnelling methyl groups. A pairwise mechanism has received independent confirmation from the more recent observations of exchange couplings in the dihydrides (**10**).

Proper identification of individual resonances in ^1H spectra of partially deuterated trihydrides was facilitated by large upfield isotope effects on the proton chemical shifts.[15]

Decisive proof of the quantum exchange origin of the unusual couplings stems from ^3H NMR studies on partially tritiated iridium hydrides.[13,15,16,26] In the monotritiated derivatives of (**4e**) (Cp* = C_5H_5, L = $AsPh_3$) the H–T coupling constants in the $H_AT_BH_A$ and $H_AH_BT_A$ isotopomers were found to be 24 and 29 Hz, respectively[13,15] (accounting for a non-first-order character of the triton multiplet in the latter isotopomer would probably reduce the discrepancy between these two values). At the same temperature (185 K) the value of J^{app} in the perprotio species is 500 Hz. It is the observed reduction by a factor of 20, instead of an increase to ~530 Hz, of the coupling magnitude upon tritium substitution that enabled the authors to rule out magnetic interactions as the coupling mechanism.

Heinekey *et al.* reported values of H–T couplings for a series of nine tritiated derivatives of (**4**), where Cp* = C_5Me_5.[26] These values are in the range 19.1–29.4 Hz and do not vary with temperature. They were used to determine the magnetic components in the observed J^{app} values. For five compounds of the series T–T couplings were also measured. The latter lie in the range 19.3–31.1 Hz and are temperature independent. The evident absence of quantum exchange between the tritons and its simultaneous occurrence in the respective perprotio species is rationalized in terms of mass effect causing a substantial reduction of the tunnel splittings.[16,26] As already mentioned, a possible example of exchange coupling between isotopes of hydrogen other than protons may be (**11**)-d_2.[42]

Heinekey *et al.*[26] investigated isotopic effects on the thermally activated rearrangements. As in the case of tantalum dihydride (**10a**) (L = $P(OMe)_3$) studied by Chaudret *et al.*,[42] the rearrangement rates observed for iridium trihydrides (**4**) are insensitive to successive deuteration of the hydride sites. The same is true for H/T substitution in the latter compounds.[26]

2.3. Dependence of the spectra on pressure

The effects of pressure increase on the spectra of (**1b**) (Cp* = $C_5H_3(SiMe_3)_2$) were investigated by Ernst *et al.*[49] Depending on the temperature, the coupling constant J^{app} is reduced by 5–8 Hz upon increasing the pressure up to 5 kbar. At low temperatures the decrement can reach 20% of the value at ambient pressure. At constant temperatures, the dependences of J^{app} on pressure are nonlinear and resemble pressure dependences of the specific volume, $V_{sp}(p, T)$, of the solvent which was methylcyclohexane-d_{14}. A good fit for the experimental values of $J^{app}(p, T)$ was obtained using a linear relationship

$$J^{app}(p, T) = a(T) + bV_{sp}(p, T) \tag{2}$$

with a temperature-independent slope parameter b and an offset parameter $a(T)$ dependent on temperature.

In (**1b**), the rate constant of the thermally activated rearrangement is dependent on pressure and attains a minimum at an intermediate pressure.

3. BASIC PRINCIPLES OF EXCHANGE COUPLING

The phenomenon that is the subject of this review has in many respects been a challenge to common intuitions involving the properties of molecules in solution at ambient temperatures. Tunnelling effects involving a molecular fragment, an atomic core in the simplest case, commuting back and forth in space are not as challenging as the phenomenon considered here, where the nuclei are only permuted at their binding sites. In condensed matter at high temperatures the former are generally incoherent processes,[50,51] while the latter is ostensibly coherent over a wide temperature range. In the metal hydrides an incoherent process starts to dominate only at high temperatures. At a phenomenological level, this incoherent effect can be explained in terms of the familiar stochastic permutations of the hydride protons among their binding sites. In favour of such in interpretation are the already mentioned excellent lineshape fits obtained in the framework of the standard Alexander–Binsch lineshape theory.[39,42,48,49] The mutual status of both the incoherent and coherent processes simultaneously affecting the same nuclei has been clarified only recently. This was achieved in the framework of a consistent quantum-mechanical model invoking vibrational relaxation as the ultimate mechanism

of thermal effects observed in the hydride spectra.[27] Consistent treatments of coherent and incoherent processes are reviewed in Section 6. The present section focuses on the concept of the effective spin Hamiltonian, which affords a convenient description of the coherent effect. Although the latter concept has a long history,[19,20] its previous applications were to a large extent confined to electronic systems in solids (see, e.g., Ref. 52). Some logical difficulties concerning its application to nuclear systems in the context of NMR spectroscopy have been resolved only recently.[53]

The simplest model of the system of interest, retaining all the relevant features, includes two neighbouring hydrides occupying geometrically non-equivalent sites A and B. Assuming perfect separability of the overall molecular rotations from internal motions, quantum-mechanical description of the relevant orbital degrees of freedom of the system can be done in terms of a Hamiltonian referred to a molecule-fixed frame. In the presence of an external magnetic field the Hamiltonian is to be augmented by terms describing both indirect spin–spin and Zeeman interactions. The spin operators entering Zeeman terms are referred to a laboratory frame. This is not inconsistent with the convention regarding the spatial variables (see below). The Hamiltonian, expressed in angular frequency units, is

$$H = -\omega(r_1) I_{Z_1} - \omega(r_2) I_{Z_2} + 2\pi J(r_1, r_2) \mathbf{I}_1 \mathbf{I}_2 + \hbar^{-1}[T(r_1, r_2) + U(r_1, r_2)] \quad (3)$$

where it is assumed that the laboratory Z axis is parallel to the direction of the external field. In this rigorous quantum-mechanical description, the spatial particles' coordinates entering the Zeeman and spin–spin interaction terms are dynamic variables. Obviously, the terms describing the kinetic (T) and potential energies (U) that govern the spatial, and in particular, vibrational motions do not contain the spin degrees of freedom. The through-space dipole–dipole interactions are neglected in Eq. (3) because one can anticipate that they will average out to zero owing to molecular tumbling. For the same reason one can neglect the spatially anisotropic parts of the chemical shift and J-coupling tensors; in Eq. (3) $\omega(r)$ is a scalar quantity which describes the distribution of effective proton Larmor frequency within the molecular volume around the hydride sites. Because H is a proper quantum-mechanical Hamiltonian, it is invariant under simultaneous permutation of spatial and spin coordinates of the (like) particles, represented by the product of the spatial, P^R, and spin, P^S, permutation operators.

The sequential vibrational states of the model system will in general be separated by energy quanta that are large in comparison with Zeeman energies ($1\ \mathrm{cm}^{-1} = 30\,000$ MHz!). The most natural approach to the eigenproblem of Eq. (3) is thus to solve first the purely spatial or vibrational problem, with the Hamiltonian $H^{\mathrm{vib}} = T(r_1, r_2) + U(r_1, r_2)$, and only then include the spin-space part. The former is invariant under permutation of the purely spatial particles' coordinates. This means in particular that the two potential minima of $U(r_1, r_2)$

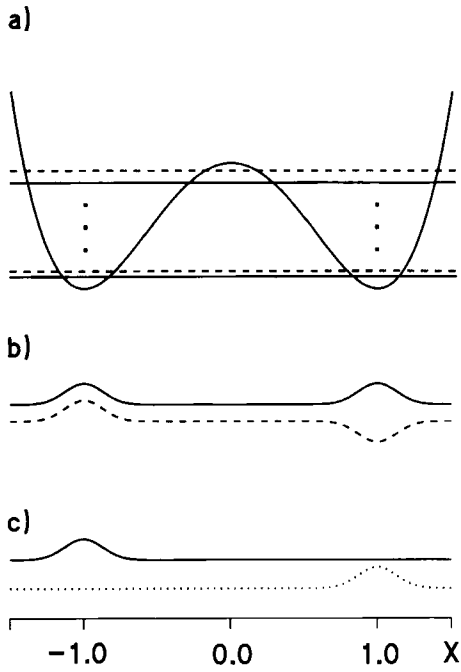

Fig. 5. Schematic representation of the two-well potential (a), of the symmetric and antisymmetric eigenfunctions of two lowest-energy states (b), and of the corresponding home-based functions (c), for the tunnelling hydride pair. The two equivalent potential minima at the values −1 and 1 of the tunnelling coordinate, X, correspond to the two permutations of the hydrides at the binding sites. In absence of magnetic fields, the permutation symmetry of the system cannot be broken by any interactions with an environment.

in configuration space, corresponding to the arrangements where proton 1 is at site A and proton 2 at B and vice versa, are perfectly equivalent (see Fig. 5). They remain so even when the spatial system's degrees of freedom are subject to stochastic (nonmagnetic) perturbations from the condensed environment. Accordingly, the eigenstates of H^{vib} are either symmetric (+) or antisymmetric (−) under P^R. Exact solution of the vibrational eigenproblem can be found numerically provided that both $U(r_1, r_2)$ and the kinetic energy tensor[54] entering $T(r_1, r_2)$ are known (such calculations would generally involve the use of curvilinear coordinates, in which case the form of T could be quite complicated). However, some important properties of the eigenstates of H^{vib} below the potential barrier separating the potential minima in configuration space (the hindered states) can be anticipated on general physical grounds.

The repulsive part of U tries to keep the protons apart so that even for excited (but still hindered) states the amplitude of double occupancy of one

binding site should be small and so should the amplitude of a vacancy at a site. Similarly, there should be small amplitude for finding any of the nuclei in the barrier region. Hence, even in its vibrationally excited, hindered states the molecule retains a definite structure. The importance of the notion of molecular structure for a proper consideration of the present problem was emphasized by Inati and Zilm.[53]

For an infinite energy barrier separating the two potential minima in configuration space, the eigenstates of the combined system would exist in two-component, degenerate bands. The two-dimensional manifold of each such band would be generated by two nonoverlapping one-particle functions concentrated around the respective sites A and B. An orthogonal basis of the manifold is spanned by the two product states describing the two arrangements of the particles at the sites. These product states account only for the on-site delocalization of each of the particles. The genuine eigenstates must conform to the formal symmetry requirements: the situation where particle 1 is at site A and particle 2 at B must be treated on equal footing with that where particle 2 is at site A and particle 1 at B. This is obeyed by the appropriate Heitler–London functions, i.e. the sum and the difference of the two product states. These two combinations are transformed under the particle permutation with the signs (+) and (−), respectively, and are thus the proper (orthogonal) eigenstates. Beyond the on-site delocalization already accounted for in the product functions, the latter also show a long-distance delocalization that results from the formal nondistinguishability of the particles. In configuration space, each of the corresponding probability distribution functions therefore has two equivalent peaks around the two equivalent potential minima and vanishes in the barrier region.

For a finite energy barrier separating these two minima the perfect degeneracy will be lifted. The resulting intraband splittings, $\nu_t^{(j)}$, are customarily defined as differences between even and odd energy levels,

$$\nu_t^{(j)} = (E_j^+ - E_j^-)/h \tag{4}$$

The corresponding exact eigenfunctions $\phi_{\pm j}(r_1, r_2)$ are by definition adapted to the formal symmetry requirements. As long as the actual potential resembles its extreme, infinite-barrier form, the eigenfunctions must also resemble their infinite-barrier counterparts, exhibiting similar on-site and long-distance delocalizations. The appropriate linear combinations of these eigenfunctions, sometimes called home-based[55] or homebase functions,

$$\psi_{\mathrm{AB}j}(r_1, r_2) = 2^{-1/2}[\phi_{+j}(r_1, r_2) + \phi_{-j}(r_1, r_2)] \tag{5a}$$

$$\psi_{\mathrm{BA}j}(r_1, r_2) = 2^{-1/2}[\phi_{+j}(r_1, r_2) - \phi_{-j}(r_1, r_2)] \tag{5b}$$

resemble in turn the (only on-site delocalized) product functions mentioned above. Unlike the product functions, the home-based functions can in principle

retain some residual long-distance delocalization: beyond the main peak located around one of the potential minima, the corresponding probability distribution can have a small secondary peak around the other minimum.

It follows directly from Eqs (5a) and (5b) that, like their infinite-barrier counterparts, the home-based functions are transformable into each other by P^R, the operator that permutes the spatial particle coordinates. The home-based functions form a complete orthonormal basis set which is an alternative to one comprising the genuine eigenfunctions. For the lowest band one approaches the infinite-barrier limit and the corresponding home-based functions can to a good approximation be factorized into appropriate one-particle functions, usually Gaussian functions, located at the sites A and B,

$$\psi_{AB1}(r_1, r_2) \approx \chi_A(r_1)\chi_B(r_2) \tag{6}$$

The accuracy of such an approximation can be improved by multiplying the right-hand side of Eq. (6) by a type of two-particle step function, $g(|r_1 - r_2|)$, which nullifies (in the hard-core approximation of the interproton repulsion) the already small amplitude of the product function in the region where the interparticle distance drops below some critical value (e.g. below ~1 Å for hard-core protons[13,16]).

It must be stressed that the long-distance delocalization, imposed by the postulate of nondistinguishability, is in a sense trivial and by no means invalidates the notion of molecular structure underlying the above reasoning: It is not important which of the nondistinguishable nuclei resides at a given moment in a given site; the only important thing is that the probability of finding one at that site be close to certainty.

In systems composed of n like particles, excited levels can come in clusters comprising more than the $n!$ elements necessary to form a set of home-based functions. As long as the molecular structure is retained, such clusters must be separable into "localizable" bands of which each can deliver a set of home-based functions that is closed with respect to all possible permutations of (spatial) particles coordinates.

We now turn to the complete Hamiltonian of Eq. (3). As already mentioned, the spin-dependent elements of H that couple different vibrational levels are strongly nonsecular and can be neglected. The matrix representation of H is thus decomposed into independent blocks for individual (hindered) bands. In calculating the matrix elements one has to take into account the symmetrization postulate, which correlates the spin and spatial states according to Fermi statistics. There are four correlated states for each band, all transforming with the minus sign upon permutation of the spin and spatial proton coordinates; one denoted below by σ represents the singlet state, and three, designated by θ, represent the $M_Z = -1$, 0, and 1 triplet states:

$$\sigma_j = \phi_{+j}(r_1, r_2)[\alpha(1)\beta(2) - \beta(1)\alpha(2)]2^{-1/2} \tag{7a}$$

$$\theta_{1j} = \phi_{-j}(r_1, r_2)\alpha(1)\alpha(2) \tag{7b}$$

$$\theta_{0j} = \phi_{-j}(r_1, r_2)[\alpha(1)\beta(2) + \beta(1)\alpha(2)]2^{-1/2} \tag{7c}$$

$$\theta_{-1j} = \phi_{-j}(r_1, r_2)\beta(1)\beta(2) \tag{7d}$$

In the present context it is convenient to use a unitary transformed basis set. The new basis functions for band j, all behaving properly upon permutation of spatial and spin particle coordinates, are Slater determinants of the specific spin orbitals whose orbital parts are the appropriate home-based function*:

$$\zeta_{1j} = \theta_{1j} = 2^{-1/2}[\psi_{ABj}(r_1, r_2) - \psi_{BAj}(r_1, r_2)]\alpha(1)\alpha(2) \tag{8a}$$

$$\zeta_{2j} = 2^{-1/2}(\theta_{0j} + \sigma_j) = 2^{-1/2}[\psi_{ABj}(r_1, r_2)\alpha(1)\beta(2) - \psi_{BAj}(r_1, r_2)\beta(1)\alpha(2)] \tag{8b}$$

$$\zeta_{3j} = 2^{-1/2}(\theta_{0j} - \sigma_j) = 2^{-1/2}[\psi_{ABj}(r_1, r_2)\beta(1)\alpha(2) - \psi_{BAj}(r_1, r_2)\alpha(1)\beta(2)] \tag{8c}$$

$$\zeta_{4j} = \theta_{-1j} = 2^{-1/2}[\psi_{ABj}(r_1, r_2) - \psi_{BAj}(r_1, r_2)]\beta(1)\beta(2)] \tag{8d}$$

If the residual long-range delocalization of the home-based functions, commented upon after Eq. (5b), is neglected, then these Slater basis functions acquire straightforward physical interpretation. Each of them describes a definite spatial arrangement of the nuclear spins. For example, ζ_{2j} represents situation where site A is occupied by a particle in the spin state α and site B by a particle in the state β. Function ζ_{3j} describes the permuted arrangement of these spin states at the sites A and B. Neither of these two functions is an eigenfunction of H^{vib}. They can serve to clarify the term "tunnelling", which may be somewhat ambiguous in the present context since no net transport of mass is involved here. If interactions engaging the nuclear spins were absent, the system prepared initially in the state ζ_2 (we drop the band index) would under the action of H^{vib} continuously oscillate between the states ζ_2 and ζ_3, with the frequency of $\nu_t/2$. This process could be described in terms of the oscillating probabilities of the two spatial spin configurations, α at site A with β at site B, $p[\alpha(\text{A})\beta(\text{B}); t]$, and β at A with α at B, $p[\beta(\text{A})\alpha(\text{B}); t]$,

$$p[\alpha(\text{A})\beta(\text{B}); t] = \cos^2(\pi\nu_t t) \tag{9a}$$

$$p[\beta(\text{A})\alpha(\text{B}); t] = \sin^2(\pi\nu_t t) \tag{9b}$$

*The standard Slater determinant involves products of one-particle spatial functions, while home-based functions are only approximately factorizable into one-particle functions. Home-based functions and product functions behave in the same way under permutation(s) of the spatial particle coordinates, which is the crucial property underlying the very concept of Slater determinant.

The tunnelling thus involves an oscillatory exchange of spins between the nuclear sites, and this is why the process has been termed quantum-mechanical spin exchange.

The matrix elements of H in the Slater basis defined in Eqs (8a–d) can be calculated easily. The nonvanishing elements are listed below; the origin of the energy scale is set at the average band energy, calculated taking account of spin statistics, $(E_j^+ + 3E_j^-)/4$.

$$H_{11}^{(j)} = \tfrac{1}{2}[-\omega_A^{(j)} - \omega_B^{(j)} + \pi(J^{\mathrm{mag}(j)} - \nu_t^{(j)})] \tag{10a}$$

$$H_{22}^{(j)} = \tfrac{1}{2}[-\omega_A^{(j)} + \omega_B^{(j)} - \pi(J^{\mathrm{mag}(j)} - \nu_t^{(j)})] \tag{10b}$$

$$H_{23}^{(j)} = H_{32}^{(j)} = \pi(J^{\mathrm{mag}(j)} - \nu_t^{(j)}) \tag{10c}$$

$$H_{33}^{(j)} = \tfrac{1}{2}[\omega_A^{(j)} - \omega_B^{(j)} - \pi(J^{\mathrm{mag}(j)} - \nu_t^{(j)})] \tag{10d}$$

$$H_{44}^{(j)} = \tfrac{1}{2}[\omega_A^{(j)} + \omega_B^{(j)} + \pi(J^{\mathrm{mag}(j)} - \nu_t^{(j)})] \tag{10e}$$

where

$$\omega_A^{(j)} = \int_V \int_V \mathrm{d}r_1\, \mathrm{d}r_2\, \psi_{ABj}^*(r_1, r_2)\, \omega(r_1)\, \psi_{ABj}(r_1, r_2) \tag{11}$$

and

$$J^{\mathrm{mag}(j)} = \int_V \int_V \mathrm{d}r_1\, \mathrm{d}r_2\, \psi_{ABj}^*(r_1, r_2) J(r_1, r_2)\, \psi_{ABj}(r_1, r_2) \tag{12}$$

and $\omega_B^{(j)}$ is defined by analogy with Eq. (11), with $\omega(r_2)$ replacing $\omega(r_1)$. In Eqs (10a–e) terms involving matrix elements of $\omega(r)$ and $J(r_1, r_2)$ between two different home-based functions are neglected since such terms practically vanish. The above formalism can be generalized over systems of n like nuclei of arbitrary spin number, occupying n sites.

Inspection of Eqs (10a–e) reveals that matrix representation of the single-band Hamiltonian in the Slater basis is the same as that of the standard NMR spin Hamiltonian in the ordinary spin product basis. In the latter Hamiltonian, instead of the magnetic coupling constant, one has to insert an apparent J-coupling defined according to Eq. (1). It is the above identity of matrix representations that is implicitly referred to in virtually all of the existing explanations of the phenomenon. It must be stressed again that without restrictions of the symmetrization postulate the single-band manifold would comprise all eight possible combinations of spatial and spin basis functions and this crucial coincidence of the Hamiltonian matrices could not take place.

In setting the standard NMR Hamiltonian, formal symmetry of like particles

is abandoned and, accordingly, no reference is made to the symmetrization postulate. Why then, in spite of such an apparent violation of the very foundations of quantum mechanics, can this standard approach work at all? Such a question would hardly arise if one did not face the phenomena that are the subject of the present review. According to Inati and Zilm,[53] the answer is that the quantum postulates are in fact implicit in the standard NMR theory. Instead of the proper spin basis referred to the particle labels (as used in Eqs (7a)–(8d), in the standard approach one actually uses a spin basis that is fixed at the nuclear sites. Such site-fixed basis is in a natural one-to-one correspondence with the genuine quantum-mechanical basis formed from Slater determinants (for like fermions) or from Slater permanents (for like bosons). In the two-particle case considered presently, the correspondence between site-fixed spin functions and the Slater spin-space functions of Eqs (8a–d) has already been pointed out in the discussion following Eq. (8d). If the site-fixed spin functions of the standard NMR theory were multiplied by purely spatial Slater determinants (or permanents) formed from exact or approximate home-based functions, the fundamental quantum postulates would be satisfied.[53] However, for ordinary spin systems there is no need to perform such a procedure explicitly.

Except for the simplest systems of spin-$\frac{1}{2}$ nuclei, the rigorous quantum-mechanical procedure leading to Eqs (10a–e) (and employed here for didactic purposes) would be rather inconvenient to handle a general case of quantum exchange. Spin operators affording a compact formulation of an effective Hamiltonian could only with difficulty be reconstructed from the individual matrix elements calculated in this way. A solution addressing a general case of n like particles tunnelling among n nuclear sites in $n! - 1$ possible ways is proposed by Inati and Zilm,[53] who make an explicit use of site-fixed spin basis from the start. They thereby obtain the effective spin Hamiltonian whose matrix representation (in the product spin basis) is identical with that of the corresponding quantum-mechanical Hamiltonian in the Slater basis. These results have been reproduced by Szymański[56] in a different way, involving an explicit transformation from the particle-fixed to site-fixed spin basis. The required effective Hamiltonian, supposed to be a thermal average over vibrational bands (the band index has been dropped), has the form

$$H^{\text{eff}} = -\sum_k \omega_k I_{Zk} + 2\pi \sum_{k<l} J_{kl}^{\text{mag}} \mathbf{I}_k \mathbf{I}_l + \pi \sum_{q=1}^{n!-1} \gamma_q \nu_{\text{t}q} P_q^S \tag{13}$$

where the summations over k and over kl are over the sites and pairs of sites, respectively, and the index q enumerates the $n! - 1$ spin operators P_q^S that permute the n nuclei among the n sites; for even permutations γ_q is equal to 1, and for odd permutations it is equal to 1 for bosons and to -1 for fermions. One can easily verify that for a pair of spin-$\frac{1}{2}$ nuclei the quantum exchange term $\pi\gamma_{(kl)}\nu_{\text{t}(kl)}P_{(kl)}^S$ can be transformed into the corresponding Heisenberg term

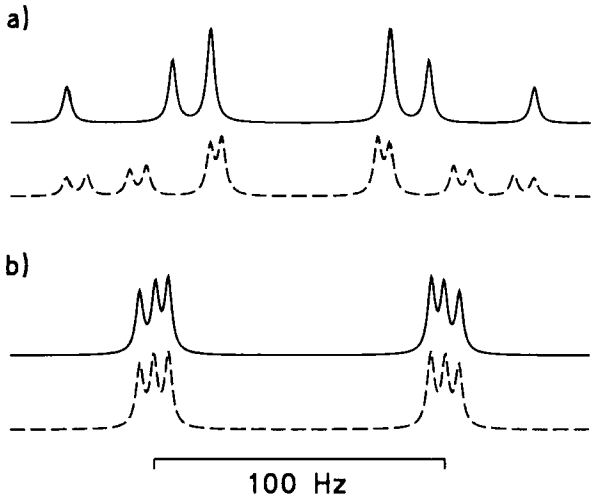

Fig. 6. Comparison of theoretical NMR spectra for a pair of like particles of spin 1, coupled by the usual J-interaction ($\nu_t = 0$, dashed lines) and by quantum exchange ($J^{mag} = 0$, solid lines). The spectra were calculated assuming chemical shift difference, Δ, of 100 Hz, and natural linewidth, $1/\pi T_2$, of 3 Hz. Case (a): $J^{mag} = 25.0$ Hz and $\nu_t = 12.5$ Hz. Case (b): $J^{mag} = 5.0$ Hz and $\nu_t = 2.5$ Hz. Compared are spectra for which $J^{mag} = 2\nu_t$, since for such relationship the corresponding spectral patterns become similar in the weak-coupling limit (see (b)).

$-2\pi\nu_{t(kl)}\mathbf{I}_k\mathbf{I}_l$. This stems from the well-known relationship $P^S_{(kl)} = 2\mathbf{I}_k\mathbf{I}_l + E/2$, where E is unit operator, which is valid for spin-$\frac{1}{2}$ particles.[20] The same relationship can be used to show that a sum of two mutually inverse cyclic permutations of three spin-$\frac{1}{2}$ particles can be transformed into a sum of three corresponding Heisenberg terms (see, e.g., Ref. 55). Quantum exchange coupling between two spin-1 particles, e.g. two deuterons (whose occurrence in a tantalum dihydride or dihydrogen complex (**11**)-d_2 can be suspected), would produce different spectral patterns from the ordinary J-coupling. This is illustrated in Fig. 6 (see also Section 4.4).

When the number of tunnelling particles, n, exceeds 2, the exchange parameters ν_{tq} in Eq. (13) are no longer equal to tunnelling splittings within a band. Closed-form relationships between the former and the latter can be derived easily when the number of feasible tunnelling motions is limited by energetic constraints. For example, for methyl-like rotors one can in general consider only the torsional coordinate. The torsional bands are split into three components of which two form a perfectly degenerate pair. The corresponding exchange parameter equals one-third of the energy difference between the nondegenerate and the doubly degenerate sublevels (see, e.g., Ref. 53). In general, the exchange parameters can be expressed in terms of the level

splittings by making use of a unitary matrix transforming the eigenbasis of the spatial Hamiltonian into a complete set of home-based states. Explicit derivation of such a matrix for a general n-particle system may be a difficult problem.

The Hamiltonian in Eq. (13) can be considered as a thermal average of the single-band Hamiltonians for a ladder of vibrational levels because rapid thermal transitions responsible for such an averaging can effectively occur only between levels of the same permutation symmetry. Transitions violating these selection rules are concerned with conversion of spins and as such are extremely slow in liquids. It is this fact that was invoked to explain the, at first glance, puzzling thermal stability of the quantum exchange couplings.[14,15]

4. MODELS OF TEMPERATURE EFFECTS ON EXCHANGE COUPLING

In this section models aimed at a quantitative description of temperature dependence of ν_t in terms of a few adjustable parameters are reviewed. As has already been mentioned, with increasing temperature incoherent exchange processes are gradually activated. The same vibrational potential that governs both the magnitude and dependence on temperature of the coherent effect is also relevant for the dynamics of the incoherent process. In the approaches to be reviewed presently, no explicit account is made of this natural connection. The very recent models describing both effects consistently will be described under separate heading.

4.1. The Landesman–Zilm model

This model, proposed by Zilm *et al.*[13,15–17] is the first attempt at a quantitative explanation of the microscopic origin and temperature behaviour of exchange coupling between the hydride protons. It is based on the Landesman theory of pairwise quantum exchange of ^{3}He in solid helium.[57] As in the case of two neighbouring ^{3}He sites in a crystal lattice, the relevant properties of the tunnelling hydride pair are modelled by two three-dimensional, isotropic harmonic oscillators located at two neighbouring hydride sites; double occupancy is prevented by hard-core repulsion. The same force constant is assumed for both sites. Two lowest eigenstates of the two-proton system are described in terms of Heitler–London functions formed from the corresponding Gaussians that are the ground-state eigenfunctions of the two harmonic oscillators; these Heitler–London functions are modulated by appropriate two-particle correlation function accounting for the hard-core repulsion (see

comment on Eq. (6)),

$$g(|r_1 - r_2|) = \begin{cases} 0 & \text{if } |r_1 - r_2| < \lambda \\ 1 & \text{otherwise} \end{cases} \tag{14}$$

Under such assumptions the Landesman theory gives the following estimate of the tunnel splitting of the fundamental band:

$$\nu_t^{(1)} = \frac{-3ha}{8\pi^2 m\delta^3}\sqrt{\frac{3}{\pi}}\exp\left(-\frac{3}{4}\frac{a^2+\lambda^2}{\delta^2}\right) \tag{15}$$

where a is the equilibrium interproton distance, m is the proton mass, and λ is the distance of the closest approach allowed by the hard-core repulsion (see Eq. (14)); δ is the zero-point motion amplitude of a three-dimensional isotropic harmonic oscillator. Equation (15) is valid when this characteristic oscillator length is much smaller than the hard-core diameter, which condition is easily fulfilled for the metal hydrides. As is evident from the above equation, the ground-state tunnelling splitting is critically dependent on the on-site delocalization parameter, δ, of the individual particles. This observation led Zilm *et al.* to assume that dependence on temperature of the average splitting can be obtained by replacing δ^2 in Eq. (15) by the corresponding temperature-dependent delocalization parameter of a harmonic oscillator, calculated by Dunitz *et al.*,[58]

$$\delta^2(T) = \frac{3h}{8\pi^2 mc\bar{\nu}}\coth\left(\frac{hc\bar{\nu}}{2k_B T}\right) \tag{16}$$

where $\bar{\nu}$ is the harmonic oscillator fundamental frequency. In this way the expression for thermally averaged tunnelling splitting,

$$\nu_t(T) = \frac{-3ha}{8\pi^2 m\delta^3(T)}\sqrt{\frac{3}{\pi}}\exp\left(-\frac{3}{4}\frac{a^2+\lambda^2}{\delta^2(T)}\right) \tag{17}$$

relates it to the familiar thermal ellipsoid parameters which can be obtained from neutron diffraction or X-ray studies. It is to be noted that by virtue of Eq. (16) ν_t is a sensitive function of the fundamental oscillator frequency and of the particles' masses: the effect would be quenched for large mass and/or large oscillator frequency.

In the derivation of Eq. (17), Zilm *et al.*[16] invoke the familiar expression defining $\nu_t(T)$ as the Boltzmann average of tunnelling splittings for a ladder of vibrational levels,

$$\nu_t(T) = \sum_j p_j(T)\,\nu_t^{(j)} \tag{18}$$

where $p_j(T)$ is Boltzmann population of band j. This expression was introduced as a phenomenological postulate involving methyl-like quantum rotors.[59] Its validity in the latter context has been impressively demonstrated for a tunnelling CD_3 group in a molecular crystal.[4] Connecting Eq. (18) with Eq. (17), Zilm *et al.*[15,16] introduce a series of approximations. These include in particular the assumption that tunnelling splittings for the relevant excited bands can be calculated in the same way as for the fundamental band of a pair of harmonic oscillators. However, even in the latter case the pertinent formalism, involving integration over the hypersurface separating the potential minima in configuration space,[60–63] may be reliable only when the corresponding home-based function is known with accuracy near the hypersurface.[55] The approximate home-based functions, constructed from eigenfunctions of excited states of the individual harmonic oscillators,[16] can hardly fulfil this condition. In view of these approximations, Eq. (17) may be regarded as more a counterpart than a consequence of Eq. (18). It therefore has an independent phenomenological status as the Landesman equation for two Gaussian states with temperature-dependent widths.[16] A heuristic picture underlying Eq. (17) is that thermally induced on-site delocalization of the individual hydrides enhances the propensity of the latter to tunnel through the vibrational potential, which is reflected in the growing magnitude of $\nu_t(T)$ with increasing temperature. It is to be noted that the predicted sign of the average splitting is inherently negative. It is therefore an instance of *antiferromagnetic* exchange coupling, since the model predicts that the bands where the (nonmagnetic) singlet state has lower energy than the triplet state prevail on the average.

Equation (17) afforded good least-squares fits of the experimental J^{app} vs T trends for a series of derivatives of (**1**), (**2**) and (**4**).[16] The fitted parameters were the interproton equilibrium distance, a, and the fundamental oscillator frequency, $\bar{\nu}$; the closest-approach distance, λ, was kept fixed at 1 Å. The unknown magnetic contribution to J^{app} was approximated by a constant of magnitude ranging from -25 to $+25$ Hz, depending on the compound. In all cases values of a around 1.6 Å and values of $\bar{\nu}$ around 500 cm^{-1} were obtained. The value of δ calculated for (**4a**) (Cp* = C_5H_5, L = trimethylphosphine) was in a fair agreement with the largest thermal vibration amplitude obtained from neutron diffraction data. It must be added that the experimental thermal ellipsoids for the hydride protons in (**4a**) are significantly anisotropic since the largest diameter is about twice the smallest.[16]

The assumption that the three-dimensional potentials are isotropic may thus bias the Landesman–Zilm model. An improvement proposed by Heinekey *et al.*[26] relies upon eliminating the dimension that most offends the above assumption. This is the dimension corresponding to stretching motions, which are governed by a much stiffer potential than the motions perpendicular to bond stretches. In the improved version of the Landesman–Zilm model the relevant on-site vibrations are described by two isotropic, two-dimensional

harmonic oscillators modelling the bending/wagging modes of the hydride pair. The dependence of ν_t on temperature is now given by[26,64]

$$\nu_t(T) = \frac{-ha}{\pi^3 m\lambda\delta'^2(T)} \exp\left(-\frac{a^2+\lambda^2}{2\delta'^2(T)}\right) \tag{19}$$

where

$$\delta'^2(T) = \frac{h}{4\pi^2 mc\bar{\nu}} \coth\left(\frac{hc\bar{\nu}}{2k_B T}\right) \tag{20}$$

In comparison with its original version, the Landesman–Zilm model reduced to two dimensions afforded better fits of the experimental $J^{app}(T)$ data over a wider temperature range.[26] In addition to a and $\bar{\nu}$, use of the improved model also made it possible to determine the hard-core diameter, λ, for a series of derivatives of (**4**). The latter parameter was found to vary in the narrow range 0.9–1.1 Å. In the above studies the magnitudes of the magnetic contributions to $J^{app}(T)$ were known, up to the sign, from NMR spectra of partially tritiated compounds. The (absolute) magnitudes of the magnetic proton–proton coupling constants are in the range 17.9–26.9 Hz. The "plus" sign was assigned to these magnetic coupling constants because for "minus" sign no fit could be obtained. If the Landesman–Zilm model (and its two-dimensional variant) correctly predicts the sign of ν_t as inherently negative then, in view of earlier observations by Heinekey,[31] the reverse applies, that is the "minus" sign is to be ascribed to the magnetic coupling in niobocene trihydride (**1a**) (see Section 2.1).

The very foundations of the three-dimensional Landesman–Zilm model were examined by Hiller and Harris.[65] These authors argue that the Landesman theory is biased by nonorthogonality of the approximate home-based functions. As a further drawback they see the lack of an explicit account of the specific metal–proton potential, which is the dominating factor that holds the hydrides apart. Moreover, the two-dimensional basis assumed in theoretical calculations of exchange splittings is too small since, for reasonable potential parameters, it would lead to an unphysical ground state possessing a node. Hiller and Harris[65] develop their own theory of exchange splitting for the fundamental band that is free of these drawbacks. One of the improvements involves expansion of the basis set to four states. The two additional basis functions represent virtual double-occupancy states, i.e. states where both protons reside in the same binding site. Short-ranged proton–proton correlations are described more accurately than in the Landesman model by use of a correlation function that is more general than the step function of Eq. (14) and can be optimized.

The magnitudes of exchange couplings in the ground state predicted by Hiller and Harris[65] are two to four orders of magnitude larger than the

corresponding values obtained with the Landesman–Zilm model. It is to be noted that for the realistic value of 1.7 Å for the separation between the proton sites the magnitudes of exchange couplings delivered by the model of Hiller and Harris could approach the experimental low-temperature values only with the assumption of relatively high oscillator frequency, exceeding 750 cm^{-1}. In the Landesman–Zilm model, the corresponding estimates, obtained from least-squares fits, are grouped around 500 cm^{-1}.

The three-dimensional version of the Landesman–Zilm model was applied by Ernst *et al.*[49] to their variable-pressure data obtained for (**1b**) (Cp* = $C_5H_3(SiMe_3)_2$). For a series of J^{app} vs T experimental data sets obtained for different pressures, least-square fits were performed, with a and $\bar{\nu}$ as free parameters and with fixed values of 1 Å for λ and of −10 Hz for J^{mag}. No separate functional dependences of a and $\bar{\nu}$ on pressure could be determined since the responses of these two quantities to varying pressure were highly correlated. Statistical error analysis of the results obtained from the least-squares fits led the authors to question the validity of the model. It must be stressed, however, that the Landesman–Zilm model and especially its two-dimensional variant[26] are able to reproduce the available experimental data with the relative errors, $|J_{theor}(T) - J_{exp}(T)|/|J_{exp}(T)|$, seldom exceeding 2%; the values determined for the model parameters a and $\bar{\nu}$ also seem reasonable. The model is qualitatively correct when dependence of ν_t on the masses of the tunnelling particles is concerned. In the trihydrides, no exchange coupling was detected for the corresponding perdeutero and pertritio derivatives.[16,26] Calculations based on Eq. (19) confirm that for deuterons the magnitude of ν_t should be reduced by at least three orders of magnitude as compared to protons.[16]

4.2. Effective translational tunnelling

The model described below is considered extremely approximate by its proponents, Bowers *et al.*[18] It nevertheless gives a fair reproduction of experimental J^{app} vs T trends for a number of trihydrides. The concerted tunnelling motion of a pair of protons between the pertinent binding sites is compressed into a single Cartesian coordinate x that measures the instantaneous distance between the particles. The symmetric two-well potential along the tunnelling coordinate is modelled by a superposition of a harmonic potential, $k'x^2/2$ and a Gaussian barrier, $d\exp(-x^2/2\sigma^2)$. The kinetic energy tensor is assumed constant, equal to the inverse reduced mass of a pair of protons. The resulting spatial Hamiltonian is therefore identical to that in the case of a single particle of mass equal to half the proton mass undergoing translational tunnelling in the assumed two-well potential. The system's eigenenergies were calculated numerically. The tunnel splittings at the hindered levels, all inherently negative, were then averaged according to Eq. (18)

and these Boltzmann averages were compared with experimental values. The procedure was repeated, according to a simplex minimization procedure, for different potential parameters until the best fit was obtained. For all compounds studied, the same value of −25 Hz was assumed for the magnetic parts of the apparent coupling constants. One of the compounds, (**4a**) (Cp* = C_5H_5, L = PMe_3) was reinvestigated by Heinekey *et al.*[26] In the latter study, where use was made of the improved Landesman–Zilm model, the best fit was obtained for a similar absolute value of J^{mag} (calculated from measured $|J_{HT}|$ value of 27.3 Hz) but taken with "plus" sign. Thus, despite the fact that in both cases good fits could be obtained for (**4a**), there is a discrepancy of about 50 Hz (or about 30% of the maximum observed value of J^{app}) in the values of ν_t evaluated within the respective models.

4.3. A model invoking dihydrogen structures

Limbach *et al.*[21] have proposed a quantum exchange model in which it is assumed that in solution the trihydrides, T, are in a rapid dynamic equilibrium with metastable hydride/dihydrogen isomers, D (Fig. 7).

It is further assumed that in the D form a facile rotation of the dihydrogen ligand can take place around an axis perpendicular to the H–H bond and pointing to the metal atom. Accordingly, even the lowest torsional level of the dihydrogen ligand in isomer D can suffer a large tunnelling splitting. The splitting actually observed is a population-weighted average of both the tunnelling splittings and magnetic J-couplings in the interconverting forms D and T. For form T average tunnelling splitting can be neglected over the whole temperature range. Presupposing low equilibrium molar fraction of the D form, one gets an Arrhenius-type equation describing the temperature dependence of ν_t,

$$\nu_t(T) = -\nu_{tD}(T)\exp[(T\Delta S - \Delta H)/RT] \tag{21}$$

where ΔS and ΔH are the standard entropy and enthalpy differences for T and D isomers, and $\nu_{tD}(T)$ is thermal average, defined according to Eq. (18), of tunnelling splittings at sequential torsional levels of D. The latter quantity should follow a similar pattern of dependence on temperature to the corresponding quantity for a methyl-like quantum rotor. Namely, it should remain nearly constant, equal to the splitting of the lowest level, over some temperature range and then decay steeply (being negative all the time) to zero as the temperature is further increased. Such behaviour is typical for rigid quantum rotors for which the signs of the splittings at sequential torsional levels alternate (see, e.g., Ref. 4). In the temperature range where $\nu_{tD}(T)$ is nearly constant, the absolute magnitude of J^{app} should increase exponentially with temperature. Along with further temperature increase, the growth

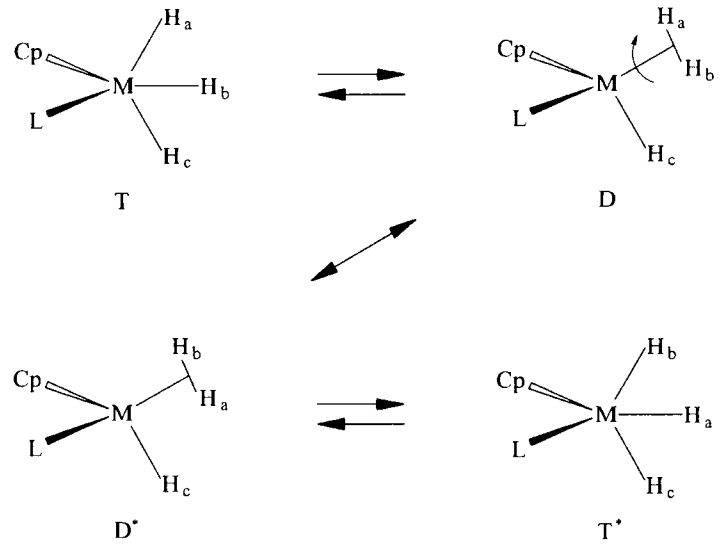

Fig. 7

of the splitting should be slowed until a maximum is reached. At still higher temperatures the behaviour of ν_t would be dominated by a rapid decay of ν_{tD} with temperature. Equation (21), with temperature-independent $\nu_{tD}\exp(\Delta S/R)$ and ΔH treated as free parameters and with an assumed constant value of J^{mag}, afforded good fits of the experimental J^{app} vs T data for 13 trihydrides of iridium, ruthenium, and niobium, including the adduct (**7**). For the majority of the compounds the estimated reaction enthalpies were below 8 kJ/mol (2 kcal/mol) or, for (**4d**) (Cp* = C_5H_5, L = PPh_3), (**4e**) (Cp* = C_5H_5, L = $AsPh_3$) and (**4f**) (Cp* = C_5H_5, L = P-Pr^i_3), even below 4 kJ/mol (1 kcal/mol). This would suggest that for the latter compounds even at temperatures below 200 K the dihydrogen forms could occur in amounts exceeding 10%. For these three compounds the calculations should be repeated using the normalized version of Eq. (21), obtained by dividing its r.h.s. by $1 + 2\exp[(T\Delta S - \Delta H)/RT]$). A version of Eq. (21) where $\exp[(T\Delta S - \Delta H)/RT]$ was simplified into $\exp(-\Delta E/RT)$ was used to fit experimental data for (**9a**) (Cp* = $C_5H_3(SiMe_3)_2$, M = Au) encompassing a broad temperature range of 187–279 K.[40] The calculated values of ΔE were in the range 10.0–12.0 kJ/mol (2.4–2.8 kcal/mol), depending on the solvent. In the latter paper the definition of the D form was changed: it may be either a stable species corresponding to a minimum on the energy surface or a sort of reaction intermediate concerned with a minimum on the tunnelling path.

Such a high abundance of the D forms as that estimated for (**4d–f**)[21] should

be reflected in the magnitudes of H–T coupling constants in the monotritiated derivatives. Relatively large values of J_{HT}, in the range 23–30 Hz, were reported recently for monotritiated derivatives of (**4d–f**).[26] This might speak in favour of the model of Limbach *et al.* On the other hand, the magnitudes of J_{HT} in these compounds should vary with temperature along with varying equilibrium populations of the dihydride isomers. If the isomerization enthalpies reported above are realistic, these variations should span a few hertz, which could easily be detected experimentally. However, the J_{HT} values in the monotritiated derivatives of (**4d–f**) and in the remaining iridium trihydrides investigated are reported as temperature-independent.[26] This observation cannot be reconciled easily with the T/D equilibrium model. Moreover, Arrhenius plots of the data obtained for a wide temperature range[26] significantly depart from linearity, and in a manner indicating an increase of the growth rate of J^{app} with increasing temperature (see Fig. 8). This behaviour conflicts with the predictions of the model. On the other hand, this model was found to be most plausible for explaining the results of high-pressure studies[49] (Section 2.3). Similarly, the recent findings concerning nonrotating dihydrogen (and specifically, HD) ligands in tantalum and niobium complexes[42,45] seem to provide new

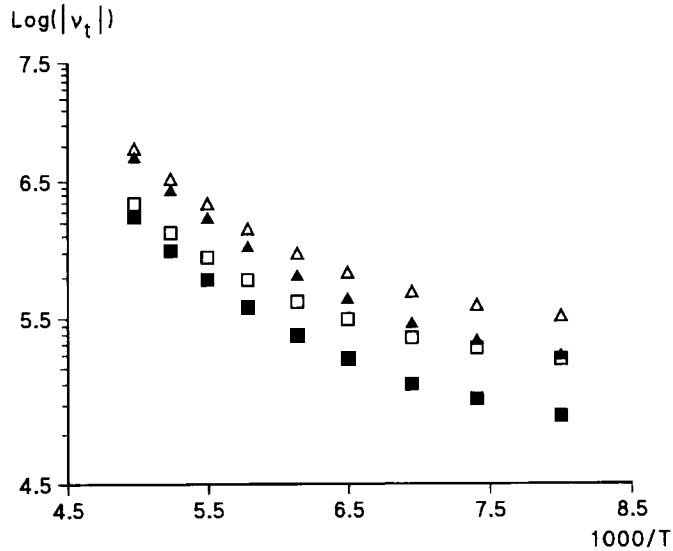

Fig. 8. Arrhenius plots of trial curves of dependence of ν_t on temperature for (**4d**) (Cp* = C_5H_5, L = PPh_3) (squares) and (**4f**) (Cp* = C_5H_5, L = P-Pr$^i_3$) (triangles). Open and solid symbols represent values of $|J^{app}| + |J^{mag}|$ and $|J^{app}| - |J^{mag}|$, respectively. The values of $J^{app}(T)$ and J^{mag} (27.6 Hz for (**4d**) and 26.9 Hz for (**4f**)) were taken from ref. 26. Note significant nonlinearity of the curves for any combination of relative signs of J^{app} and J^{mag}.

arguments in favour of the idea of the approach of Limbach *et al.* These findings allow removal of the difficulties of the original formulation concerned with the fact that typical dihydrogen ligands are known to undergo rapid stochastic reorientation which would make the possible exchange coupling unobservable in NMR spectra.

4.4. Tight-binding models

In the theoretical approaches reviewed above, a pairwise exchange is assumed from the start. Such a simplification seems well motivated by the experimental findings reported in Section 2. This nevertheless disregards the fact that the majority of experimental data were obtained for trihydrides, where three-particle processes cannot be excluded *a priori*. The only attempt at tackling the problem in its full complexity is due to Hiller and Harris.[22] These authors apply a second-quantized, tight-binding description of the hydride system. Tight-binding models have commonly been used for years to study electronic properties in solids,[66] including the prominent phenomena of high-temperature superconductivity.[67] There have also been a few applications of such models to heavy particles adsorbed on metal surfaces.[68–70] The tight-binding approach of Hiller and Harris[22] that is reported briefly below addresses a series of questions involving the microscopic origin of exchange couplings in the trihydrides and the unusual temperature behaviour of these couplings. In the first place, however, this second-quantized approach provides an independent derivation of the effective Hamiltonian in which the exchange couplings are represented in terms of spin angular momentum operators rather than permutation operators.

In the model considered, the motions of the three hydrides in a trihydride molecule are confined to the plane through the three equilibrium positions. Serious problems may arise when a theory developed to tackle many-body problems in solids is applied to a group of a few atoms arranged into a molecule. Here too there arises the difficult question of how to separate out a suitable single-particle part from the essentially nonseparable Born–Oppenheimer potential. In the approach considered, it is assumed that the pertinent single-particle potential can be modelled by a periodic angular function with three nonequivalent minima separated by three maxima. Explicit calculations are carried out for an idealized case of threefold rotational symmetry of the one-body potential. In view of the existing structural data, this seems to be an over-idealization, in spite of the authors' arguments to the contrary. The results derived for the idealized case may nevertheless be interesting in a general context.

In the limiting case of threefold symmetry, the eigenstates of the one-body Hamiltonian are the familar solutions of the corresponding Mathieu equation. As in the case of methyl-like quantum rotors, the one-particle eigenstates

below the barrier, the hindered states, cluster into three-component bands. (It should not lead to confusion that in this subsection the term "band" refers to a cluster of one-particle eigenstates rather than, as in the remaining parts of the present chapter, to a cluster of states of the complete system.) In each band, two states form a perfectly degenerate pair separated from the third state by a tunnelling energy quantum. For each hindered band the eigenstates, delocalized over the three potential minima or the three sites, are unitarily transformed into home-based, i.e. orthogonal, localized states. The latter form basis states or Wannier states for setting the complete, second-quantized Hamiltonian, which also includes two-body interactions. It is turned into a tight-binding Hamiltonian[66] by neglecting proton–proton interactions between home-based states located around different equilibrium sites. The two-body interactions that are retained in the Hamiltonian include both repulsion and Hartree–Fock exchange interactions between protons located at the same site (the latter interactions can occur only between different bands). In this second-quantized approach the symmetrization postulate is accounted for automatically via appropriate commutation properties of the creation and annihilation operators.

One of the advantages of the tight-binding approach is that the Hamiltonian can be decomposed into independent blocks concerned with different sets of band occupation numbers. For three particles there are only three different occupation schemes: (i) all three particles in the same band; (ii) two particles in the same band and the third one in a different band; and (iii) each particle in a different band. The structures of the Hamiltonian matrices for a given occupation scheme are analogous and differ only in the values of the parameters involved. In addition to the average energies of the individual one-particle bands and tunnelling splittings, t_s, of such bands (these splittings, characterizing the fictitious one-body system, should not be confused with the splittings for the complete system that are to be evaluated), the parameters that define a given multiple-band Hamiltonian include two-body terms, U_{st} and U_{st}^{H}, describing direct repulsion and Hartree–Fock interaction, respectively, between bands s and t. Of course, the Hartree–Fock terms can occur only for $s \neq t$, that is, for occupation schemes (ii) and (iii). We remember that in the tight-binding approximation both U_{st} and U_{st}^{H} comprise only on-site interactions. In setting the Hamiltonian matrices for the relevant multiple-band Hamiltonians, the dimensions concerned with double occupancies of individual sites are eliminated, although the effects of these double occupancies on the single-occupancy states are approximately accounted for using Van Vleck's perturbation theory.[71] Such a reduction of the sizes of the Hamiltonian matrices is based on an implicit assumption that for all relevant vibrationally excited states the structure of the pertinent molecular fragment is retained. In this way the above quantitative approach parallels the qualitative reasoning presented in Section 3 to justify the validity of the effective Hamiltonian, Eq. (13), derived in a more traditional fashion.

In the low-temperature limit, the only relevant term is the single-band Hamiltonian describing the situation in which all three particles occupy the fundamental band. The Hamiltonian can be expressed in terms of only two parameters, t_1 and U_{11}. Upon neglecting the symmetrization postulate, this second-quantized Hamiltonian can be transformed into an effective Hamiltonian. Up to an irrelevant shift in the energy origin, the effective Hamiltonian derived along this line proves equivalent to its counterpart in Eq. (13). However, in the second-quantized approach spin permutation operators are no longer the natural representatives of quantum exchange interactions. Such interactions are now described directly in terms of spin angular momentum operators. For example, in a system with threefold rotational symmetry (of the one-body potential), effective spin–spin interactions between three identical spin-1 nuclei (e.g. deuterons) are described as follows:[22]

$$H^{\text{eff}}_{\text{spin}-1} = -\Omega[\mathbf{I}_1 \cdot (\mathbf{I}_2 \times \mathbf{I}_3)]^2 - \tfrac{1}{2}\chi \sum_{k \neq l} [\mathbf{I}_k \mathbf{I}_l + (\mathbf{I}_k \mathbf{I}_l)^2] \tag{22}$$

where

$$\Omega = \hbar^{-1} \frac{6t_1^3}{U_{11}^2} \tag{23}$$

and

$$\chi = \hbar^{-1} \frac{-2t_1^2}{U_{11}} \left(1 - \frac{3t_1}{U_{11}}\right) \tag{24}$$

Equation (22) provides a direct confirmation of the fact already commented upon that for particles of spin greater than $\frac{1}{2}$ the Heisenberg Hamiltonian no longer applies. As can easily be verified, for spin-1 particles (and only for such particles) the operators $\mathbf{I}_k \mathbf{I}_l + (\mathbf{I}_k \mathbf{I}_l)^2$ and $[\mathbf{I}_1 \cdot (\mathbf{I}_2 \times \mathbf{I}_3)]^2$ can be expressed in terms of spin permutation operators, $E + P^S_{(kl)}$ and $2E - P^S_{(123)} - P^{S-1}_{(123)}$ respectively, where the symbol χ designates a cross product of spin vectors, E is identity permutation, and index (123) denotes cyclic permutation of three objects. The correspondence with Eq. (13) is therefore evident.

The quantities Ω and χ describe three-particle rotation and pairwise exchange, respectively, in a three-particle system. In a system lacking perfect threefold symmetry there will be three different quantities χ but still one Ω. The authors cited[22] point to the fact that within the tight-binding approximation rotation would necessarily be dominated by pairwise exchange. Spectroscopically, these two processes could not be distinguished for spin-$\frac{1}{2}$ particles; in such a system the rotation term in the counterpart of Eq. (22) is decomposed into three Heisenberg terms which would merge with the Heisenberg terms

describing pairwise exchanges. With broken threefold symmetry, the effective spin–spin interactions in the three-proton system in a trihydride could be described as follows:[22]

$$H^{\text{eff}}_{\text{spin}-1/2} = -\sum_{k \neq l} \tfrac{1}{2}(\Omega - \chi_{kl})\mathbf{I}_k \mathbf{I}_l \tag{25}$$

In the case of protons, that is fermions, in the model presented, the low-temperature exchange coupling would be antiferromagnetic. We recall that experimental study on (**4c**) did not detect exchange coupling between terminal hydride protons.[15] The second-quantized approach by Hiller and Harris[22] is actually referred to a hypothetical three-proton system in which quantum exchange can occur between each pair of binding sites. In their approach, the microscopic exchange mechanism in the low-temperature limit can be explained in terms of interplay between delocalization, measured by the parameter t, and correlation. As is seen from Eqs (23) and (24), quantum exchange would be suppressed by an enhanced correlation owing to a substantial on-site repulsion, U. As remarked by the authors themselves, because of an inherent domination of pairwise exchange over three-body rotation, the tight-binding approach would not be appropriate to describe tunnelling in methyl-like systems; extreme correlation renders such systems tractable within a rigid-rotor model.

By considering the appropriate multiple-band Hamiltonians, Hiller and Harris derive explicit expressions for the relevant level-splittings at excited vibrational levels. For band occupation schemes of types (ii) and (iii) above, in addition to the parameters t and U the splittings depend also on Hartree–Fock on-site interactions, U^{H}, which in the case of fermions favour states with high spin. Accordingly, exchange couplings in the vibrationally excited states would predominantly be ferromagnetic. The splittings for the ground and vibrationally excited states were estimated numerically assuming that the on-site parameters U and U^{H} could be calculated in a three-dimensional isotropic-harmonic oscillator approximation to the home-based or Wannier states; in these calculations the two-body potential was approximated by Coulombic repulsion. The t parameters were derived from the one-particle Mathieu equation (see above) with the pertinent one-particle potential described by a cosine function with period of $2\pi/3$ and the barrier V. For V of the order of 200 meV (~4.5 kcal/mol) the estimates gave a value of about −10 Hz for the fundamental band and about 0.1 MHz for the lowest excited bands.

To explain the dependence of the observed couplings on temperature, the authors[22] consider the spatial system's degrees of freedom in interaction with a quantum-mechanical thermal bath. The impact of the bath is described in terms of Mori–Zwanzig theory,[72,73] with an account of the specific selection rules that forbid thermal transitions concerned with conversion of spins. The

theoretical apparatus employed in the discussion of thermal interactions is rather sophisticated. Fortunately, the general picture arrived at within the approach of Hiller and Harris can be translated into the familiar model of classical multisite spin exchange. Namely, tunnel splittings at different vibrationally excited levels are analogous to the Larmor site-frequencies, and Boltzmann populations of individual vibrational levels correspond to the equilibrium site populations; accordingly, the magnetization vectors at individual sites become counterparts of the coherences engaging tunnelling-split sublevels, which oscillate with the corresponding tunnelling frequencies. From here on such coherences will be referred to as tunnelling coherences. The off-diagonal vibrational relaxation rate constants that couple tunnelling coherences of the fundamental band with those of the excited bands are supposed to be smaller than the differences between the respective tunnelling frequencies (about 0.1 MHz, see above). In the multisite-exchange picture, the analogous situation involves the case where rate constants of nuclear jumps from the most populated site, one representing the fundamental band, to the remaining sites are smaller than the corresponding Larmor frequency differences. The analogy with the tunnelling system of Hiller and Harris requires that Larmor frequencies of these remaining sites all be shifted in the same direction relative to the frequency of the most populated site. For the assumed magnitudes of the relevant quantities, in the case of multisite exchange one would actually observe only one NMR signal whose position, changing with temperature, would nevertheless remain close to the resonance frequency of the most populated site. Owing to the very short lifetimes of the remaining sites, their resonance signals would be too broad to be detected. With an increase in temperature, the only observable signal would suffer a gradual shift towards the resonances of these remaining sites or, more precisely, towards a population-weighted average of the site frequencies. In thermal averaging of the quantum exchange splittings the behaviour would be similar: the antiferromagnetic coupling of the lowest band would gradually be dominated by the growing ferromagnetic contributions from the excited bands, which gain population with increase in temperature. The authors assume that the whole process of thermal changes takes place in the regime that in the classical multisite-exchange model is sometimes termed "initial broadening" and which precedes the stage of signal coalescence. The latter assumption seems to be the weakest point of the approach discussed. It is nevertheless worthwhile to consider this approach in some detail, including a comparison of the theoretical predictions with experimental data. It is probably the first attempt at a detailed treatment of thermal effects in NMR spectra of these metal hydrides.

In the initial broadening regime, temperature-dependent positions of individual (broadened) resonances can be evaluated using the familiar second-order perturbation formalism for eigenvalues of the pertinent Hahn–Maxwell–McConnel (HMM) matrix.[74] In the present context, only the dominating signal would be of interest. In the calculations of temperature-

dependent tunnelling frequency, Hiller and Harris use a sophisticated variant of Green's function theory which is applied to the evolution of the system's density matrix in the presence of a driving radiofrequency field and vibrational relaxation. For the system considered, the above approach corresponds to the standard second-order perturbation calculations, which fact allows us to carry on the analogy with multisite exchange. In particular, we can immediately see that in the case of the HMM matrix the corrected eigenvalues delivered by consistent perturbation calculations will still be far from the population-weighted average eigenvalue (such an average can only be obtained in the calculus suitable to the motional narrowing regime). It is therefore hardly surprising that the average exchange splitting arrived at within the model of Hiller and Harris differs significantly from the Boltzmann average of Eq. (18). This is one of the most remarkable features of the model, distinguishing it from the remaining quantitative approaches reviewed in the present section.

Despite this essential difference, Hiller and Harris managed to reproduce theoretically the experimental J^{app} vs T curves for (**4d**),[16] ($Cp^* = C_5H_5$, $L = PPh_3$) and for niobocene trihydride (**1a**) dissolved in methylcyclohexane-d_{14} and in $CDFCl_2$,[31] achieving similar accuracy to the cited authors. In the approach reviewed presently, the model parameters U, U^H and the mean radius of one-particle rotation in the Mathieu equation were fixed. Fits were obtained by varying two parameters only: the one-particle potential barrier, V, and an effective, temperature- and frequency-independent thermal coupling constant C_0. The latter is determined by both the system–bath coupling Hamiltonian and the spectral density of bath fluctuations at the typical vibrational frequency of the system. In all three cases the calculated optimum values of V were in the range 205–215 meV. The best-fit values of C_0 were more diversified: for (**4d**) two similar values, about 17 000 Hz and about 13 000 Hz, were determined, depending on whether the raw experimental data were corrected for a possible magnetic contribution or not. For (**1a**), a value for C_0 of about 900 Hz was calculated for $CDFCl_2$ solution and of about 1700 Hz for methylcyclohexane solution. In the latter case, when the temperature is increased from the lowest attainable value, first a decay and then a reappearance of J^{app} are observed.[31] Hiller and Harris interpret this behaviour as a change in the character of exchange coupling, from antiferromagnetic at low temperature to ferromagnetic at elevated temperature. This is at variance with the interpretation by Heinekey,[31] who attributes this effect to mutual cancellation of the magnetic and exchange terms in J^{app}, where the exchange term has the same minus sign over the whole temperature range. For (**4d**) Hiller and Harris obtain ferromagnetic exchange coupling over the whole temperature range studied. The same data were fitted by the Landesman–Zilm model,[16] according to which the coupling should remain antiferromagnetic at any temperature.

The relevant vibrational relaxation rate constants should be of the same order of magnitude as C_0. Even for the largest reported value of C_0 (17 kHz), the estimated rate constants do not leave the microsecond range, which is

about four orders of magnitude longer than vibrational relaxation times commonly observed in liquids.[75] It thus seems that the assumption that the initial broadening regime is suitable for describing the thermal averaging cannot be maintained.

In a more recent paper Hiller and Harris[76] reduce their tight-binding model to two sites, in agreement with experimental inferences, and assume that thermal averaging of exchange splittings takes place in the motional narrowing regime. Such an assumption suggests itself as the most natural if physically reasonable magnitudes of the relevant vibrational rate constants are considered. Consequently, in conformity with other authors,[13–18] thermally averaged exchange coupling is supposed to be the Boltzmann average, Eq. (18). No attempt was made, however, to compare the predictions of the modified model with experimental data.

Hiller and Harris[76] find their modified model flexible enough to yield a close analogue of the Landesman–Zilm model, the validity of which they earlier questioned.[65] In this more recent paper[76] they also propose their own explanation of the disappearance of signal splittings from spectra at high temperatures. Simple rationalization invokes the random exchange process that leads to magnetic equivalence and thereby makes the coupling unobservable regardless of its magnitude. Hiller and Harris consider also the possibility of a direct impact of the bath on the individual level splittings that may reduce the magnitude of the average coupling. It is estimated that the latter process develops in such a narrow temperature interval that one can speak of a quenching temperature for quantum exchange.[76] No experimental observations of such quenching have so far been reported: an increase of J^{app} with increasing temperature is generally observed as long as some residual fine structure remains discernible in the gradually broadened spectrum.

5. *AB INITIO* CALCULATIONS

The unusual NMR behaviour of the metal hydrides may originate from specific features of the Born–Oppenheimer potential governing the spatial motions of the hydride atoms. First attempt at explaining this behaviour by quantum-chemical *ab initio* calculations is due to Daudey *et al.*[77] These authors performed comparative study on isostructural and isoelectronic tantalum and niobium trihydrides. This was done for model compounds in which cyclopentadienyl ligands were replaced by Cl^- ions to achieve feasibility of the calculations. Of the two groups being compared, only niobium derivatives present anomalous couplings. It was found that for the chlorine analogue of the latter a hydride/dihydrogen isomer is more stable than trihydride form, while the reverse is true for the tantalum model compound. The above inference for niobium compound is not confirmed by experiment. It can nevertheless suggest

that contribution of a metastable dihydrogen form is more probable for niobium trihydrides than for tantalum trihydrides. Accordingly, in the former the trihydride moiety may be more flexible than in the latter.

In a series of papers, Lluch *et al.*[23–25] reported on systematic *ab initio* studies on iridium trihydrides, using (**4g**) ($Cp^* = C_5H_5$, $L = PH_3$) and (**4h**) ($Cp^* = C_5H_5$, $L = CO$) as model compounds,[23,24] and on cationic molybdenocene and tungstenocene, and neutral tantalocene and niobocene trihydrides.[25] For all these compounds similar features of the relevant Born–Oppenheimer potential were identified. Scissor vibration of a pair of neighbouring hydride ligands modifies both interproton distance, r, and the distance between midpoint of the interproton vector and the metal atom, x. The instantaneous arrangements with r substantially shorter and x markedly longer than the corresponding equilibrium distances are energetically favoured due to formation of a virtual dihydrogen structure. Despite the fact that there is no local minimum corresponding to such a structure, the region of configuration space where one deals with the virtual dihydrogen ligand is thermally accessible. This is critical for a facile tunnelling between the equivalent potential minima. Upon reaching that region, the two-hydrogen system enters an easy route to librate around the axis connecting the midpoint between the hydrogens and the transition metal. The relevant motions can be fairly represented on a three-dimensional surface defined by r, x, and the dihedral angle, θ, between the instantaneous plane containing both hydrogens and the metal atom, and the "equilibrium" plane crossing the respective equilibrium positions. The saddle point between the equivalent equilibrium configurations corresponds to $\theta = \pi/2$, $r = r_c < r_{equil.}$, and $x = x_c > x_{equil.}$. Selected geometric parameters calculated for the relevant structures for a series of trihydrides are given in the legend to Fig. 9. The picture revealed by the above *ab initio* studies seems to be close to reality, as has recently been demonstrated by Ernst *et al.*[28] Except for the fact that no genuine dihydrogen isomer was found in the calculations (even as a metastable form), it proves fairly close to the intuitive model previously proposed by Limbach *et al.*[21] (see Section 4.3).

In order to perform a preliminary numerical evaluation of tunnel splittings, Lluch *et al.*[24,25] make a series of simplifications which seem to bury much of the beauty of the above picture. The relevant motions are simplified to a three-stage process to be further projected onto a single, aperiodic tunnelling coordinate. First, the nuclei execute a scissor motion in the equilibrium plane (see Fig. 9a). It ends up with the parameters r and x reaching their critical magnitudes, r_c and x_c, which indicates formation of a virtual dihydrogen (Fig. 9b). Then comes the phase of rigid rotation of the virtual dihydrogen, measured by the values of θ increasing from zero to π (Figs 9b and 9c). At the end of this second phase the virtual dihydrogen is back in the equilibrium plane, but with permuted nuclear labels (Fig. 9d). The final phase, which is the reverse of the first one, comprises opening the scissors. The length of the

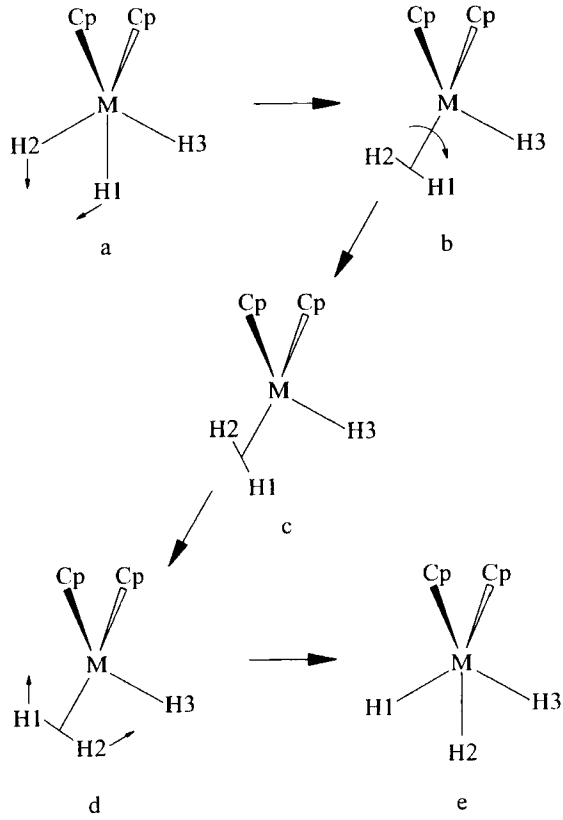

Fig. 9. Mechanism of hydride pair tunnelling in metallocene trihydride complexes proposed by Lluch *et al.*[25] on the basis of their quantum-chemical calculations. Along the optimized exchange path the H1–H2 distance decreases from its equilibrium value of 1.64–1.82 Å, depending on the metal atom, to about 0.76–0.78 Å for the intermediate structures b–d. Simultaneously, the distances M–H1 and M–H2 increase from their equilibrium values of 1.67–1.75 Å by about 0.10–0.13 Å on transforming into structure b and by another 0.10–0.15 Å upon reaching the saddle point, c. A similar mechanism was identified for iridium trihydride complexes.[24]

tunnelling coordinate describing the above motion is calibrated under a simplifying assumption that in the first and third phases the nuclei move along appropriate straight lines. The part representing rotation is approximated by twice the length of the circumference whose diameter is r_c; the factor of 2 stems from the fact that there are two nuclei moving.

The one-dimensional, double-well model reported above is essentially equivalent to the simple model of Weitekamp *et al.*[18] reviewed in Section 4.2. In the presently described calculations of tunnelling splittings for vibrationally excited levels, the main improvement is that potential energy values along the

reaction coordinate are much more reliable, being obtained from advanced *ab initio* calculations. In both cases the calculations yield a constant "minus" sign for splittings at sequential levels. This may be an artefact originating in the fact that an intrinsic periodicity of one of the coordinates is lost upon compressing the motion into a single aperiodic coordinate.

In a quantum-chemical *ab initio* study by Eisenstein *et al.*[78] devoted to neutral osmium trihydrides (**3**), no evidence was found for a metastable or virtual dihydrogen form participating in tunnelling. The compounds investigated experimentally, (**3a**) (L = P-Pr$^i_3$, X = Cl) and (**3b**) (L = P-Pr$^i_3$, X = I),[36] were modelled by the respective derivatives, (**3c**) and (**3d**), in which the P-Pr$^i_3$ ligand was replaced by PH_3. For both model structures the calculated equilibrium geometries are in good agreement with the experimental data for the parent compounds.[36] Equilibrium geometry of each such trihydride comprises a coplanar arrangement of the three hydrides, the halogen, and the metal atom, with the phosphine ligands roughly orthogonal to the plane. The H–Os–H angle between the terminal and central hydrogen is about 57°. The calculated frequency of the in-plane scissor motion is about 900 cm^{-1} as compared to 450 cm^{-1} for the out-of-plane twist vibration of the hydride pair. The latter vibration was therefore assumed to be the leading component of the tunnelling mechanism. It was found that along with gradual twist of the hydride pair from the equilibrium plane, the optimized H–H distance, r, decreased from the equilibrium value of ~1.51 Å to the minimum values of 1.38 Å (for (**3c**)) and of 1.35 Å (for (**3d**)) attained for the twist angle, θ, of $\pi/2$. The calculated energy barriers are 53.9 kJ/mol (12.9 kcal/mol) for (**3c**) and 61.0 kJ/mol (14.6 kcal/mol) for (**3d**).

Guided by these inferences, Eisenstein *et al.* assume a two-dimensional model of tunnel motion, with r and θ as the tunnelling coordinates. They use a rovibrational Hamiltonian in which the kinetic energy term involving r is formulated according to the concept of reaction path Hamiltonian,[79] and the term describing rotation has the usual appearance except that the associated moment of inertia varies with varying r. In calculating the tunnelling splittings for the ladder of rovibrational levels, an explicit use is made of the formal system's symmetry; the eigenenergies and eigenfunctions of the even and odd levels are calculated separately. The assumed model with explicitly periodic coordinate yields tunnelling splittings whose signs alternate for successive levels. The values of splittings for individual levels are not reported. The authors present only the corresponding Boltzmann averages for (**3c**) and (**3d**), calculated according to Eq. (18) in the temperature range 100–350 K. The high-energy levels where the tunnelling splittings exceed 10 cm^{-1} are not included in the averages. This cutoff value was suggested by the commonly assumed averaging mechanism invoking rapid thermal transitions between vibrational levels: since vibrational relaxation processes occur generally in the picosecond range (i.e., the corresponding rate constants are of the order of a few cm^{-1}) thermal transitions would be ineffective in coupling tunnelling

coherence of such a high frequency with the coherences at lower vibrational levels, oscillating with lower frequencies. Introducing such a sharp cutoff in the averaging is certainly a crude approximation, especially in the high-temperature region. In the approaches already reviewed, where similar explicit Boltzmann averaging was employed, the problem of how many levels are to be included in the average was not commented upon.

At a qualitative level, the model discussed presently[78] remains in agreement with experimental observations for (**3a**) and (**3b**).[36] In particular, it predicts that in the relevant temperature range the compound with Cl ligand should show up much larger exchange splitting than its iodo-substituted analogue. It is noteworthy that, at variance with the majority of the remaining approaches, the present one yields ferromagnetic exchange coupling (i.e. $\nu_t > 0$) in the temperature range where the average coupling differs significantly from zero.

6. CONSISTENT TREATMENT OF COHERENT AND INCOHERENT EFFECTS

In the present section two very recent approaches are reviewed in which both the coherent tunnelling and the incoherent nuclear exchange appear as associated processes.[27,28] The main idea of these approaches is to consider the dynamics of the tunnelling system with an explicit account of the perturbations exerted by a quantum-mechanical thermal bath on its spatial degrees of freedom. Coupling to a thermal bath was previously considered by Hiller and Harris[22,76] in their attempts at explaining only one aspect of the thermal phenomena, the impact of temperature on the magnitude of exchange coupling (Section 4.4). The dependence of ν_t on temperature is poorly structured (see Fig. 4). This is probably the main reason why such different approaches as those reviewed in Section 4 were all able to reproduce the experimental data on $\nu_t(T)$ with a similar, fairly good accuracy. The models to be reviewed presently are subject to more stringent constraints because within each of them a natural connection between the temperature behaviours of both ν_t and the rate constant of the incoherent process is obtained. In view of this, success can be claimed only upon achieving a consistent parametrization of both these quantities varying with temperature.

6.1. Tunnelling coherence as damped oscillation

Like in the works of Hiller and Harris,[22,76] in the papers reviewed presently[27,28] it is assumed that the perturbations exerted by the bath are weak enough to be treated within a second-order approach. Despite some differences in details, in both these papers the same general result is arrived at. The main points of

the theory developed in Ref. 27 are reported below.

In the latter paper, the vibrational relaxation processes are described in terms of the quantum-mechanical version[80–82] of Wangsness–Bloch–Redfield (WBR)[83–85] theory. In absence of an external magnetic field, the system dynamics can be described by the WBR equation of motion for the reduced density matrix, ρ^R, comprising the sole spatial degrees of freedom. By common practice, dynamic frequency shifts are neglected. In the superoperator/supervector notation (see, e.g., Ref. 82), the equation assumes the form

$$\frac{\mathrm{d}|\rho^R\rangle\rangle}{\mathrm{d}t} = (-\mathrm{i}\mathbf{L}^R + \mathbf{R})|\rho^R\rangle\rangle \tag{26}$$

where the double ket symbol is used to distinguish Liouville representation of an operator (i.e., a supervector) from vectors in state space. In Eq. (26) $\mathbf{L}^R$ is the spatial superHamiltonian, generated by the spatial, spin-independent part of the Hamiltonian in Eq. (3), and $\mathbf{R}$ is the relaxation matrix. It can safely be assumed that the relaxation processes described in Eq. (26) will not be affected by an external magnetic field.

A distinctive feature of Eq. (26) is that, owing to an invariance of all of the underlying interactions, including the system–bath interactions, under permutation of the spatial coordinates of the particles, the $\mathbf{L}^R$ and $\mathbf{R}$ superoperators undergo partitioning into independent blocks. For the two-particle system considered here, there are four such blocks or symmetry partitions, $(++)$, $(--)$, $(+-)$, and $(-+)$, which are spanned by supervectors $|mn++\rangle\rangle \equiv |m+\rangle\langle n+|$, ..., $|mn--\rangle\rangle \equiv |m-\rangle\langle n-|$, ..., $|mn+-\rangle\rangle \equiv |m+\rangle\langle n-|$, ..., and $|mn-+\rangle\rangle \equiv |m-\rangle\langle n+|$, ..., respectively, where the vectors $|m\pm\rangle$ represent eigenfunctions $\phi_{\pm m}$ of the spatial Hamiltonian in Eq. (3). The individual symmetry partitions of $\mathbf{R}$ are blocked out further. The $(++)$ and $(--)$ blocks of $\mathbf{R}$ have the usual appearance resulting from the so-called secular approximation:[81] the only relevant off-diagonal elements, $R^{\pm\pm}_{mm,nn}$, occur within the subblocks describing the dynamics of level populations. The quantum-mechanical WBR relaxation matrix has the property of conservation of mass,[81] which is expressed in terms of the following relationship between the diagonal and off-diagonal elements of $\mathbf{R}$:

$$R^{\pm\pm}_{mm,mm} = -\sum_{n\neq m} R^{\pm\pm}_{nn,mm} \tag{27}$$

Within the framework of quantum-mechanical WBR theory it is warranted that the elements $R^{\pm\mp}_{nn,mm}$ and $R^{\pm\mp}_{mm,nn}$ obey the principle of detailed balancing.[80–82] Hence the stationary solutions of Eq. (26),

$$(-\mathrm{i}\mathbf{L}^R + \mathbf{R})|\rho_0^R \pm \pm\rangle\rangle = 0 \tag{28}$$

represent Boltzmann distributions of equilibrium populations within each of the two manifolds of energy levels:

$$|\rho_0^R \pm \pm\rangle\rangle \propto \sum_n \exp(-E_n^{\pm}/k_B T)\,|nn \pm \pm\rangle\rangle \tag{29}$$

Any deviation from the equilibrium distribution would be suppressed in the course of picoseconds, which is the characteristic time scale of the vibrational relaxation processes.

As far as the partitions $(+-)$ and $(-+)$ are concerned, by examining detailed expressions for the pertinent off-diagonal elements of $\mathbf{R}$ one arrives at a relationship which connects these elements to the rate constants of population transfer, namely[27]

$$R^{+-}_{mm,nn} = R^{-+}_{mm,nn} \approx \tfrac{1}{2}(R^{++}_{mm,nn} + R^{--}_{mm,nn}) \tag{30}$$

Equation (30) is valid only for the hindered bands for which, owing to the near degeneracy of the pairs of levels of different symmetry, $R^{++}_{mm,nn} \approx R^{--}_{mm,nn}$. In the absence of dynamic frequency shifts, the diagonal elements of the $(+-)$ and $(-+)$ blocks of $\mathbf{R}$ are given by an exact formula:[27]

$$R^{+-}_{mm,mm} = R^{-+}_{mm,mm} = \tfrac{1}{2}(R^{++}_{mm,mm} + R^{--}_{mm,mm}) \tag{31}$$

The relationships described in Eqs (30) and (31) are crucial for the whole reasoning presented in Ref. 27. They immediately imply that the dynamics of the coherences involving pairs of states within individual tunnelling-split bands must closely resemble the dynamics of level populations. (This is the point that must have been overlooked in the approach by Hiller and Harris[22] reviewed in Section 4.4.) However, instead of the stationary solutions describing Boltzmann population distributions within the $(+)$ and $(-)$ energy level manifolds, for the $(\pm\mp)$ partitions one has to deal with quasi-stationary solutions represented by two appropriate eigensuperkets, $|\eta \pm \mp\rangle\rangle$, of $-i\mathbf{L}^R + \mathbf{R}$ such that

$$(-i\mathbf{L}^R + \mathbf{R})\,|\eta^R \pm \mp\rangle\rangle = (\mp i\nu_t - K)\,|\eta^R \pm \mp\rangle\rangle \tag{32}$$

In the present discussion it is again helpful to keep in mind the analogy between the dynamics of individual tunnel coherences and the classical multisite nuclear exchange. The coherences described in Eq. (32) are combinations of tunnelling coherences at individual vibrational levels. They thus correspond to exchange-averaged magnetization in the multisite exchange model considered in the limit of motional narrowing (as we shall see later on, this is a limited analogy). They evolve as damped oscillations with the frequencies of $\pm\nu_t$ and the same damping-rate constant K. The latter is generally several orders of magnitude smaller than vibrational relaxation constants and this is why the supervectors in Eq. (32) can be referred to

as quasi-stationary solutions of the relaxation equation. For the sake of brevity, these long-lasting coherences will further be called average tunnelling coherences. By virtue of the above-mentioned similarity with the behaviour of level populations, for each of the partitions $(+-)$ and $(-+)$ any instantaneous combination of coherences different from the respective (unique!) average tunnelling coherence will be dissipated away in the course of picoseconds. However, at variance with the population distribution, the average tunnelling coherence arrived at in this rapid process will not persist forever but will eventually decay, though in a much longer time period. For NMR experiments on tunnelling systems of the sort discussed presently, only these long-lived coherences are relevant. The discussion of such an experiment will be preceded by a closer description of the average tunnelling coherences.

In this point the approaches of Refs 27 and 28 differ slightly, owing mainly to the fact that in the former these coherences are described by approximate closed-form expressions while in the latter the formalism is developed for the purposes of a direct computer implementation. The closed-form description of Ref. 27 will be reported first.

It is valid in the case, believed to be the case of the metal hydrides, where tunnelling splitting at some hindered level near the top of the potential barrier, say level N, *achieves magnitude comparable with the matrix elements* $R^{\pm\mp}_{N-1\,N-1,NN}$, that is, with the vibrational relaxation rate constants $W^{\pm}_{NN-1} \equiv R^{\pm\pm}_{N-1\,N-1,NN}$. In view of the fact that the (absolute) magnitudes of tunnelling splittings at sequential levels grow steeply, the splitting at the level immediately preceding, i.e. level N, will generally be much smaller than $W^{\pm}_{NN-1}$. The approximate form of the average tunnelling coherence was obtained in Ref. 27(a) under the assumption that population transfer between levels separated by two or more vibrational quanta is much less effective than between neighbouring levels. The required description was obtained using perturbation calculus, up to second order, for eigenvectors and eigenvalues of a complex, non-Hermitian matrix. Below we report the pertinent expressions from Ref. 27(a) reformulated according to the prescription given in Ref. 27(b) (see below). In these expressions, the elements $R^{\pm\mp}_{mm,nn}$ are approximated by $\frac{1}{2}(W^{+}_{nm} + W^{-}_{nm}) \equiv W_{nm}$. Thus,

$$\nu_t \approx \frac{1}{Z}\left(\sum_{n=1}^{N-1} \exp(-E_n/k_B T)\,\nu_t^{(n)} + \frac{\nu_t^{(N)} W^2_{NN-1} \exp(-E_N/k_B T)}{(2\pi\nu_t^{(N)})^2 + W'^2}\right) \tag{33}$$

$$K \approx \frac{W_{NN-1}}{Z}\left(1 - \frac{W_{NN-1} W'}{(2\pi\nu_t^{(N)})^2 W'^2}\right)\exp(-E_N/k_B T) \tag{34}$$

where $E_n = (E_n^{+} + E_n^{-})/2$ is the average energy of the (hindered) band n, Z is half the spatial partition function, and

$$W' = W_{NN-1} + \tfrac{1}{2}(W^{+}_{N+1N}\exp[-(E^{+}_{N+1} - E_N)/k_B T] + W^{-}_{N+1N}\exp[-(E^{-}_{N+1} - E_N)/k_B T]) \quad (35)$$

In Eq. (35) there occur levels $(N+1)^+$ and $(N+1)^-$ which immediately follow the respective levels N^+ and N^- forming a hindered band. If the former also form a hindered band (one with tunnelling splitting exceeding W_{mn}, perhaps substantially, since by definition the splitting at level N is already comparable to W_{mn}), one can put $E^{+}_{N+1} = E^{-}_{N+1} \equiv E_{N+1}$ and $W^{+}_{N+1N} = W^{-}_{N+1N} \equiv W_{N+1N}$. The corresponding (unnormalized) eigensupervectors are practically equal to Boltzmann averages of tunnel coherences at levels $1, 2, \ldots, N-1$:

$$|\eta^{R}\pm\mp\rangle\rangle \approx \sum_{n=1}^{N-1} \exp(-E_n/k_B T)\,|nn\pm\mp\rangle\rangle + O^{\pm\mp}(p_N) \quad (36)$$

where $O^{\pm\mp}(p_N)$ denotes a small contribution from band $N+1$, of the order of the Boltzmann population of level N. The corresponding weighting factor is generally a complex quantity. The results reported above provide a formal justification to the phenomenological postulate defining the observed tunnelling splitting as the Boltzmann average of Eq. (18); the Boltzmann average appears now as a first-order approximation to ν_t.

As can be deduced from Eq. (34), the damping rate constant describing decay of the average tunnelling coherence should show up Arrhenius-type dependence on temperature, provided that certain conditions to be mentioned below are satisfied. The expression for K reported above is formulated in terms of vibrational rate constants describing transfer of population *down* the ladder of vibrational levels. This is at variance with the original presentation in Ref. 27(a) where the same quantity was expressed in terms of geometric averages of the respective constants *down* and *up*. Transformation to the form in Eq. (34) was effected by invoking detailed balancing. A consideration of the latter property clearly suggests that rate constants describing transport down the energy scale should exhibit milder dependence on temperature than the corresponding rate constants describing the reverse processes.[27b] The former are thus better suited to the Arrhenius pre-exponential factors than the geometric averages employed in Ref. 27(a); these averages are biased by the necessarily high sensitivity of the rate constants *up* to temperature. Actually, a significant departure from an Arrhenius-type behaviour might only result from the intrinsic dependence on temperature of the population ratios entering the expression for W' in Eq. (35). The dependence of W' on temperature induced by the varying population ratios would to a large extent be suppressed when the energy gaps separating band N from the levels $(N+1)^{\pm}$ were large and/or transfer of population from these levels to the levels $N^{\pm}$ was less effective than from the latter to still lower levels. When, moreover, the energy gap separating two lowest hindered bands is much greater than $k_B T$, variations

with temperature of the partition function can be neglected. Under such circumstances, which seem quite likely to be encountered in practice, the temperature behaviour of K should follow Arrhenius law rather closely. In this point there is a breakdown of the analogy between dynamics of tunnelling coherences and that of site magnetizations in the multisite exchange. In the former case, along with increasing the temperature, the damping rate of the average tunnelling coherence increases steeply. On the other hand, the dephasing rate of exchange-averaged site magnetization decreases with increasing temperature (motional narrowing). The difference is due to the fact that multisite exchange must exactly obey conservation of the overall site population while the set of tunnelling coherences, by definition comprising only hindered levels, does not form such a closed system. Temporary escape of population from the hindered manifold to highly excited levels, which is enhanced by temperature, implies an effective loss of coherence that will not be regained on return.

In the parallel approach,[28] the eigenvectors $|\eta\pm\mp\rangle\rangle$ and eigenvalues $\pm i\nu_t - K$ are calculated numerically. The elements of the complex matrix $-i\mathbf{L}^R + \mathbf{R}$ are derived from appropriate model assumptions to be reported in Section 6.3.

The spirit of the theory reported in the present section is similar to that of earlier treatments of the related problem for hindered, methyl-like quantum rotors, where only a pair of tunnelling-split torsional bands was taken into account.[86,87] Coherent dynamics of a hindered quantum rotor perturbed by stochastic classical forces was considered by Hennel.[88] He discussed the impact of such forces on the oscillating probabilities of finding the rotor in each of its two equilibrium orientations. For these probabilities he also obtained damped oscillation behaviour, which result is essentially in agreement with the quantum-mechanical picture presented above.

6.2. Tunnelling coherence dynamics in NMR spectrum

One of the main results of the theory developed in Ref. 27 relies upon a clarification of the relationship between damped oscillation behaviour of the average tunnelling coherences and the phenomena observed in NMR spectra of the metal hydrides. This is achieved by looking at the NMR experiment from a somewhat nonstandard perspective. In the following account of the above theory, magnetic spin–spin interactions between the tunnelling protons are neglected; this is done merely for sake of clarity.

When the two-hydride system, placed in an external magnetic field, is driven by a radiofrequency pulse, the pre-existing Zeeman order is initially converted into coherences between Zeeman sublevels. Such coherences involve pairs of states that differ only in the spin part of the state functions. In the absence of Larmor frequency differences between the hydride sites, further evolution of

the system would follow the well-known pattern of oscillating magnetization in the plane perpendicular to the field direction. The entire evolution would be confined to the spatial symmetry partition $(--)$ (the partition $(++)$ corresponds to nonmagnetic singlet state). The spatial degrees of freedom would remain dormant. When the sites are magnetically nonequivalent, which is the case in the metal hydrides, the anisochronous part (of the order of a kilohertz) of the Zeeman interactions introduces a sort of spin–orbit coupling. The latter is of course invariant under simultaneous permutations of spin and spatial coordinates of the protons involved but is no longer so with respect to separate spatial and spin permutations. It can therefore mediate in transferring the Zeeman coherences to the remaining partitions and, in particular, to those $(+-)$ and $(-+)$ which include tunnelling coherences. Since the magnitude of the spin–orbit coupling is comparable with that of the average tunnelling splitting, ν_t, the average tunnel coherences (of the frequencies $\pm\nu_t$) can be created effectively. The evolution involves thus an interplay between the Zeeman and the average tunnel coherences. Because the latter undergo damping (with rate constant K), the overall coherence that gives rise to the observable oscillating magnetization is gradually lost.

The above process can be described in a rigorous quantum-mechanical language, using the appropriate WBR equation for density superket comprising both spatial and spin degrees of freedom, $|\rho^{RS}(t)\rangle\rangle$. The spatial part of the density superket includes only the equilibrium modes, $|\rho_0^R \pm \pm\rangle\rangle$, and the long-lived tunnel coherences $|\eta^R \pm \mp\rangle\rangle$, because any other spatial order, even if it existed, would be dissipated away in the course of picoseconds. By virtue of the symmetrization postulate, each of these relevant spatial components is correlated with a unique instantaneous spin supervector of appropriate symmetry,

$$\begin{aligned}|\rho^{RS}(t)\rangle\rangle = {} & |\rho^S(t)--\rangle\rangle|\rho_0^R++\rangle\rangle + |\rho^S(t)++\rangle\rangle|\rho_0^R--\rangle\rangle \\ & + |\rho^S(t)+-\rangle\rangle|\eta^R-+\rangle\rangle + |\rho^S(t)-+\rangle\rangle|\eta^R+-\rangle\rangle \end{aligned} \tag{37}$$

where ρ^{RS} has unit trace and the spatial supervectors are normalized such that all have the same lengths of unity. Because there is only one spatial vector for each symmetry partition, the spin and space quantities in Eq. (37) can be summed up separately and then recorrelated without any loss of information. This can be effected using the superantisymmetrizer (or, for bosons, supersymmetrizer),

$$\begin{aligned}\mathbf{A}^{RS} = {} & \tfrac{1}{4}[(E^S \times E^{S*})E^R \times E^{R*}) - (P^S \times E^{S*})(P^R \times E^{R*}) \\ & - (E^S \times P^{S*})(E^R \times P^{R*}) + (P^S \times P^{S*})(P^R \times P^{R*})] \end{aligned} \tag{38}$$

where E^S and E^R denote unit operators in the corresponding state spaces. In this way, the evolving density superket comprising spin and spatial variables

assumes the form:

$$|\rho^{RS}(t)\rangle\rangle = 2\mathbf{A}|\rho^{S}(t)\rangle\rangle|\rho^{R}_{0AB}\rangle\rangle \tag{39}$$

where

$$\begin{aligned}|\rho^{S}(t)\rangle\rangle = {} & |\rho^{S}(t)--\rangle\rangle + |\rho^{S}(t)++\rangle\rangle \\ & + |\rho^{S}(t)+-\rangle\rangle + |\rho^{S}(t)-+\rangle\rangle\end{aligned} \tag{40}$$

and

$$\begin{aligned}|\rho^{R}_{0AB}\rangle\rangle = {} & \tfrac{1}{2}(|\rho^{R}_{0}++\rangle\rangle + |\rho^{R}_{0}--\rangle\rangle \\ & + |\eta^{R}-+\rangle\rangle + |\eta^{R}+-\rangle\rangle)\end{aligned} \tag{41}$$

The subscript AB is used in the description of the spatial supervector in the l.h.s. in Eq. (41) because, as can be seen from Eqs. (5a), (29) and (36), the leading term in that supervector comprises the Boltzmann average of "localized" shift superkets $|ABn\rangle\rangle \equiv |\psi_{ABn}\rangle\langle\psi_{ABn}|$ constructed from appropriate home-based functions that are concentrated around only one of the two equivalent potential minima. The specific form of the spin-space density superket, as displayed in the r.h.s. of Eq. (39), can be given a clear physical interpretation in the spirit of the work by Inati and Zilm.[53] Namely, the spin part, defined according to Eq. (37), is implicitly referred to the space-fixed spin basis which is natural for the above set of home-based functions.

Evolution of the density supervector $|\rho^{SR}\rangle\rangle \equiv 2\mathbf{A}|\rho^{S}(t)\rangle\rangle|\rho^{R}_{0AB}\rangle\rangle$ is governed by the Liouville superoperator in the r.h.s. of Eq. (26) augmented by the Zeeman superHamiltonian, $\mathbf{L}^{RS}_{Z}$. The latter is a quantum-mechanical superHamiltonian generated by the Zeeman term in the Hamiltonian in Eq. (3) and as such it is invariant under simultaneous permutation of spin and spatial particle coordinates. The complete WBR equation describing NMR experiments is therefore a proper quantum-mechanical equation obeying the requirements of the symmetrization postulate. Upon an appropriate elimination of the redundant spatial part, $|\rho^{R}_{0AB}\rangle\rangle$, from the complete density supervector, it is turned into an effective equation of motion for the spin-density supervector of Eq. (40).[27] This effective equation is analogous to the Alexander–Binsch equation, but instead of the usual magnetic spin–spin interaction term there appears now quantum exchange term. Upon rewriting to the more familiar Hilbert space form, it reads

$$\frac{\mathrm{d}\rho^{S}}{\mathrm{d}t} = -\mathrm{i}[-\omega_{A}I_{z1} - \omega_{B}I_{z2} - \pi\nu_{t}P^{S}, \rho^{S}] - \frac{K}{2}[\rho^{S} - P^{S}\rho^{S}P^{S\dagger}] \tag{42}$$

Obviously, the quantum exchange term will for this system (two particles of

spin $\frac{1}{2}$) be transformed into the Heisenberg term, $-2\pi\nu_t \mathbf{I}_1 \mathbf{I}_2$. For a pair of tunnelling bosons, the quantum exchange term would come with the "plus" sign. Magnetic spin–spin coupling, neglected here for clarity, would appear in Eq. (42) in its usual form.

The formal reasoning reported above reveals that damping of the average tunnelling coherence is seen in the NMR experiment as an apparent classical exchange of localized particles. The rate constant of the apparent exchange, k, equals half the rate constant of the damping process,

$$k = \tfrac{1}{2}K \tag{43}$$

We emphasize that the spin permutation operator entering Eq. (42) derives from the superantisymmetrizer of Eq. (38). It is interesting to note that it describes not only the coherent exchange but the stochastic exchange as well. It may seem surprising that there is a connection between the latter, seemingly classical process and the symmetrization postulate, the more so as the theory leading to Eq. (42) can without change be applied to any system of two like nuclei undergoing typical "classical" exchange. In such a system, tunnelling coherences will also be created (unless the nuclei are equivalent, but then there is no exchange) by a radiofrequency pulse, only the corresponding oscillation frequencies will be much lower than the damping rate constants. Dissipation of such coherences is caused by perturbations exerted on the spatial variables while it is observed by monitoring the spin degrees of freedom. No wonder then that the symmetrization postulate correlating the former and the latter is again active, now in transferring the spatial disorder to the spin part.

6.3. A comparison with experiment

As compared to the approaches described in Sections 4.1–4.4, the theory reported in the two preceding subsections imposes more stringent restrictions on the models aimed at explaining the tunnelling phenomena in the metal hydrides. Any such model should be capable of reproducing at least qualitatively the most striking feature of the systems in question, which is the dominance, maintained over a broad temperature range, of coherent tunnelling over the incoherent exchange,

$$|2\pi\nu_t(T)| > \frac{K(T)}{2} \tag{44}$$

At a qualitative level, this goal was achieved in Ref. 27, where a one-dimensional tunnelling path was considered and thermal effects were parametrized by two vibrational rate constants describing population transfers between levels N and $N+1$, and between $N+1$ and $N+2$ (see comment

preceding Eq. (33)). The assumed tunnelling coordinate represents correlated rotation of the hydride pair in the plane perpendicular to the bisector of the H–M–H angle. The proton–proton distance is allowed to decrease to some critical value of about 1 Å along with the interproton vector being twisted by the angle $\pi/2$ relative to the equilibrium orientation. The assumed model of tunnelling motion can be regarded as a simplified version of the two-dimensional model by Eisenstein *et al.*[78] (Section 5). The hindered eigenstates of such a quantum rotor with variable moment of inertia were determined numerically following the procedure by Pyka *et al.*[89] Because the tunnelling coordinate is periodic, the signs of the calculated tunnelling splittings at sequential levels alternate. The thermally averaged quantities $\nu_t(T)$ and $K(T)$ were calculated according to Eqs (33) and (34), respectively. A sharp increase of both with increasing temperature was obtained. In the whole temperature range considered, the inequality of Eq. (44) was fulfilled. The results reported in Ref. 27(a) are biased by the questionable assumption concerning the use of geometric averages of population transfer rate constants up and down the vibrational ladder (see discussion following Eq. (36)). Repeated calculations with the more appropriate choice of temperature-independent parameters did not bring about any essential modifications to the above conclusions since the recalculated values of $\nu_t(T)$ and $K(T)$ are close, to within 5%, to those obtained previously.[27b] In the model assumed in Ref. 27, the sign of ν_t proves critically dependent on whether the number of relevant hindered bands, $N + 1$, obtained for the assumed torsional potential, is even or odd. For the values of potential parameters adopted in Ref. 27, positive values of $\nu_t(T)$ (that is, ferromagnetic exchange coupling) were obtained in the whole temperature range considered.

The parametrized model proposed by Ernst *et al.*[28] succeeds in a quantitative fit of both $\nu_t(T)$ and $K(T)$ over a broad temperature range of 125–210 K, using three adjustable parameters to describe the isolated system and one such parameter to represent coupling to thermal bath. The experimental data for the compound studied, which was (**4d**) (Cp* = C_5H_5, L = PPh_3), were taken from the work by Heinekey *et al.*[26] The assumed model for hydrogen pair exchange is inspired by quantum-chemical results by Lluch *et al.*[24] (see Section 5 and Fig. 9). The relevant motions of the hydride pair are parametrized by two variables, θ measuring rotation about the bisector of the H–M–H angle and β describing an instantaneous value of the latter angle, or, in other words, the stage of the scissor vibration of the two hydrogens. When β decreases to certain critical value corresponding to formation of a virtual dihydrogen ligand, the scissor vibration merges into a lift-off motion, resulting in a substantial increase of the distance between metal atom and the centre of mass of the hydrogen pair. At this lift-off stage, the barrier to rotation is reduced considerably compared to its values at the early stages of the scissor vibration where the H–H distance is still large. These motions were represented in terms of a motion surface. The potential energy over the motion surface was described

by a function of β and θ defined by two constants and three free parameters. The latter include bending (scissoring) force constant, f, the barrier to rotation at the equilibrium distance, B_e, and the parameter α that measures the decay of the barrier to rotation along with increasing distance between M and the centre of mass of the hydride pair. The energy levels, the tunnelling splittings and the wavefunctions for the above vibrational problem were obtained by solving numerically the corresponding Schrödinger equation, with the use of the flexible model method.[90]

Interactions between thermal bath represented by a large set of harmonic oscillators and the hydride system were described in a three-dimensional, molecule-fixed Cartesian coordinate system. They were taken to be linear in both the bath coordinates and the Cartesian displacements of the hydride pair from its equilibrium position. The perturbations exerted by the bath were supposed to be isotropic and uncorrelated for different (Cartesian) coordinates. The displacements of the system particles were expressed in terms of parameters defining the motion surface, which allowed calculation of the relevant matrix elements of the system–bath Hamiltonian using the system's wavefunctions obtained numerically. Further assumptions regarding the system–bath interactions involve the supposition that coupling constants between the system and bath displacements depend only on the frequencies of the bath modes rather than on the modes themselves (see, e.g., Refs 22, 51, 86, 87). Assuming finally that the above dependence is so mild in the relevant frequency range that it can be approximated by a constant, the authors quoted[28] were able to calculate all the relevant vibrational relaxation constants W_{mn} (Section 6.1), introducing only one free parameter, S, independent of temperature, to describe the strength of the system–bath coupling. The quantities ν_t and K were determined numerically by handling the relevant block of the WBR superoperator in Eq. (32). The whole procedure described above was repeated with varying potential parameters f, B_e, and α, and the thermal parameter S until the best fit of both $\nu_t(T)$ and $K(T)$ to the corresponding experimental data was achieved. The contribution of magnetic terms to the experimental splittings was accounted for using the data for the pertinent tritium derivative.[26] The quality of the fit so obtained is really impressive (see Fig. 10). As compared to the previous quantitative studies (Section 4), the real breakthrough of the approach of Ref. 28 involves the fact that a consistent parametrization employing so few free variables is now extended to the incoherent process as well.

Among the fitted model parameters, the barrier to rotation at equilibrium distance, B_e, has the most immediate physical interpretation. The relatively large value of $8003 \pm 78\ \mathrm{cm}^{-1}$ (about 96 kJ/mol) obtained for B_e indicates that in absence of the "lift-off" motion no facile rotation path would exist for the hydride pair. Under increased pressure the freedom of this lift-off motion would be limited. The earlier observation[49] that increased pressure leads to a decrease of tunnelling splitting provides independent confirmation of the

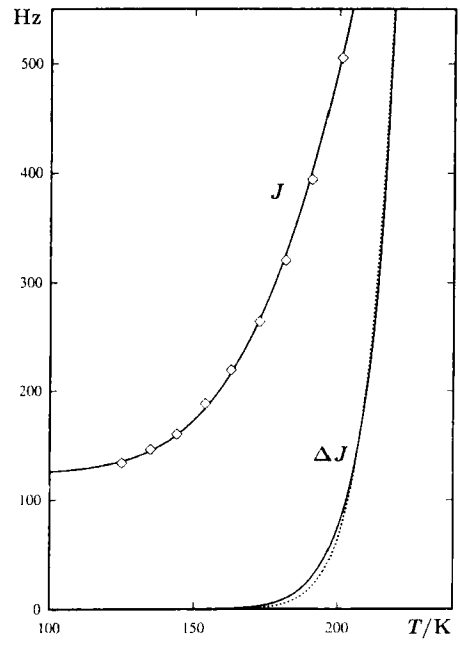

Fig. 10. The temperature-dependent hydrogen pair exchange in (**4d**) (Cp* = C_5H_5, L = PPh_3). The full lines show the tunnel frequency $J = -\nu_t$ and the damping rate constant $\Delta J = K/2\pi$ fitted to the experimental data from Ref. 26 using the two-dimensional, four-parameter model by Ernst *et al.*[28] described in Section 6.3. The dotted line shows the experimental curve $k(T)/\pi$ calculated from the experimental activation enthalpy and entropy parameters of the incoherent exchange, reported in Ref. 26. (Reproduced with permission from Ref. 28. Copyright 1997 American Institute of Physics.)

tunnelling mechanism proposed by Ernst *et al.*[28] The authors quoted find the calculated fundamental frequencies of the torsional vibration, 649.6 cm^{-1}, and the bending (scissoring) vibration, 725.6 cm^{-1}, in fair agreement with the pertinent experimental values for related metal hydrides. No regular behaviour was observed in the signs of tunnelling splittings at sequential excited levels. These levels can be classified as concerned with torsional, bending, or combined vibrations. The signs at sequential torsional levels alternate, while they remain negative at bending levels. The splitting of the fundamental band is negative, and so is the average splitting in the whole temperature range considered (caution: the sign convention adopted in Ref. 28 is the reverse of that of the present review). The calculated magnitude of the fundamental band splitting is −124.5 Hz.

The "best fit" curve $J(T) \equiv -\nu_t(T)$ shown in Fig. 10 departs only slightly from the respective Boltzmann average, calculated for 25 pairs of tunnelling-

split levels, with the highest level having an energy of about 3500 cm^{-1} relative to the ground level. The "best fit" curve $K(T)$ can to a good approximation be described by the Eyring formula, with the values of activation enthalpy of 33.0 kJ/mol (7.9 kcal/mol) and activation entropy of $-33.4\ J\ mol^{-1}\ K^{-1}$ (-8.0 cal $mol^{-1}\ K^{-1}$).

The fitted thermal coupling parameter, S, delivers values of population transfer rate constants. Those describing transport *down* the ladder of energy levels prove almost independent of temperature; the calculated rate constants for the transitions from the first excited torsional and bending levels to the fundamental level, 2.7×10^{11} and $9.3 \times 10^{10}\ s^{-1}$, are typical for vibrational relaxation processes in liquids.

7. CONCLUDING REMARKS

The discovery of quantum exchange couplings in metal hydrides seems to be one of the most intriguing findings ever made in the general area of liquid-phase NMR. Despite being restricted to a specific class of compounds, it provided an inspiration to reconsider the very principles of NMR theory in a wider context, including the question of the status of the symmetrization postulate and its possible relevance for the lineshape theory of "classically" exchanging systems.

The often contradictory results produced within the models parametrizing exchange couplings should not be wondered at. In this regard the situation in the metal hydrides does not differ greatly from that which existed until late 1970s in the studies on quantum exchange in solid helium[55] where again even the sign of the coupling could for a long time not be agreed upon. Compared to typical vibrational energies, tunnelling quanta are extremely small so that correspondingly subtle theoretical tools are needed, especially when vibrationally excited states are concerned.

Quantum-chemical studies described in Section 5 suggest that, regardless of formal structure of the valence shell, a similar tunnelling mechanism is operative in trihydrides of various transition metals. A common feature of these compounds is relative stability of a dihydrogen-like transition state. The results illustrated in Fig. 10 may indicate that tunnelling phenomena in these trihydrides are now to a large extent understood. It is noteworthy that in this most successful approach an extreme correlation was assumed between the individual hydrides; the spatial motions were considered in regard to the hydride pair as a whole. This is in contrast with the approaches derived from theories dealing with related phenomena in quantum crystals. In the latter context the interesting correlated behaviour is evaluated by considering short-ranged, two-body corrections to the basically one-body description of the system's particles. Specific chemical forces acting within the hydride system are apparently better approximated by the assumption of extreme correlation

than by an effective potential artificially separated into one-body and two-body parts. Further studies are necessary to check whether the same tunnelling mechanism, involving a dihydrogen-like structure, is valid also for the adducts of ruthenium and niobium hydrides with Lewis acids. Metal dihydrides containing stretched dihydrogen ligands may constitute a separate problem. The quantum-chemical results obtained for osmium trihydrides, where no merging of wagging vibrations into a "lift-off" motion was found, may be regarded as a warning against premature generalizations.

In the present review, considerable attention was paid to the tight-binding approach despite the fact that, for the reasons mentioned in the preceding paragraph, it does not seem very useful when exchange coupling is to be described quantitatively. However, in view of the well-documented versatility of tight-binding models, an attempt at employing such a model in one more field could not be neglected.

An important element of the successful approach described in section 6 is the damped oscillation description of the tunnelling coherence dynamics, translated consistently into a quantum-mechanical analogue of the Alexander–Binsch equation. The quantum-mechanical theory was developed in the context where it was clear from the start that the Alexander–Binsch equation, employed on a phenomenological basis, properly describes the spectra of the unusual hydrides. In the latter field, the main contribution of the quantum theory of NMR lineshape relies upon a novel interpretation of the parameters entering that equation. For systems comprising more than two nuclei the situation is more complicated. For methyl-like quantum rotors an analogue of the Alexander-Binsch equation is the phenomenological Clough equation[91] in which both the coherent tunnelling and the stochastic nuclear exchange are described in terms of the appropriate cyclic permutation operators. The stochastic term represents classical random jumps of the rotor between its three (equivalent) equilibrium orientations. The Clough equation was recently arrived at independently, by a simple extension of the NMR lineshape theory developed for metal hydrides.[6] However, detailed derivation to be reported soon yields a generalized equation containing an additional stochastic term that has no classical interpretation. Numerical simulations of single-crystal NMR spectra of methyl-like quantum rotors reveal that for appropriate model systems such nonclassical stochastic behaviour could be detected experimentally. Verification of this theoretical inference may be a challenging task for future experimental studies on quantum tunnelling in systems of several like nuclei.

ACKNOWLEDGEMENTS

Financial support of the Polish Committee for the Advancement of Research (KBN) under grant no. 3 T09A 062 12 is gratefully acknowledged.

REFERENCES

1. F. Apaydin and S. Clough, *J. Phys. C, Ser. 2*, 1968, **1**, 932.
2. C. Mottley, T. B. Cobb and C. S. Johnson, *J. Chem. Phys.*, 1971, **55**, 5823.
3. T. Bernhard and U. Haeberlen, *Chem. Phys. Lett.*, 1991, **186**, 307.
4. A. Detken, P. Focke, H. Zimmermann, U. Haeberlen, Z. Olejniczak and Z. T. Lalowicz, *Z. Naturforsch.*, 1995, **50A**, 95.
5. Z. Olejniczak, A. Detken, B. Manz and U. Haeberlen, *J. Magn. Reson.*, 1996, **A118**, 55.
6. S. Szymański, Z. Olejniczak and U. Haeberlen, *Physica B*, 1996, **226**, 161.
7. M. D. Curtis, L. G. Bell and W. M. Butler, *Organometallics*, 1985, **4**, 701.
8. R. G. Bergman and T. M. Gilbert, *J. Am. Chem. Soc.*, 1985, **107**, 3502.
9. (a) R. A. Paciello and J. E. Bercaw, *Abstract of Papers*, The 191st National Meeting of the American Chemical Society, New York, American Chemical Society, Washington, DC, 1986; INOR 82. (b) R. A. Paciello, Ph.D. thesis, California Institute of Technology, Pasadena, CA, 1987.
10. T. Arliguie, B. Chaudret, J. Devillers and R. Poilblanc, *C.R. Seances Acad. Sci., Ser. 2*, 1987, **305**, 1523.
11. D. M. Heinekey, N. G. Payne and G. K. Schulte, *J. Am. Chem. Soc.*, 1988, **110**, 2303.
12. A. Antiñolo, B. Chaudret, G. Commenges, M. Fajardo, F. Jalon, R. H. Morris, A. Otero and C. T. Schweltzer, *J. Chem. Soc., Chem. Commun.*, **1988**, 1210.
13. K. W. Zilm, D. M. Heinekey, D. M. Millar, N. G. Payne and P. Demou, *J. Am. Chem. Soc.*, 1989, **111**, 3089.
14. D. H. Jones, J. A. Labinger and D. P. Weitekamp, *J. Am. Chem. Soc.*, 1989, **111**, 3087.
15. D. M. Heinekey, J. M. Millar, T. F. Koetzle, N. G. Payne and K. W. Zilm, *J. Am. Chem. Soc.*, 1990, **112**, 909.
16. K. W. Zilm, D. M. Heinekey, J. M. Millar, N. G. Payne, S. P. Neshyba, J. C. Duchamp and J. Szczyrba, *J. Am. Chem. Soc.*, 1990, **112**, 920.
17. K. W. Zilm and J. M. Millar, in *Advances in Magnetic Optical Resonance*, Vol. 15 (ed. W. S. Warren), p. 163, Academic Press, New York, 1990.
18. C. R. Bowers, D. H. Jones, N. D. Kurur, J. A. Labinger, M. G. Pravica and D. P. Weitekamp, in *Advances in Magnetic Resonance*, Vol. 14 (ed. W. S. Warren,), p. 269, Academic Press, New York, 1990.
19. W. Heisenberg, *Z. Phys.*, 1926, **38**, 411; *ibid.*, 1926, **39**, 499; *ibid.*, 1927, **41**, 239.
20. P. A. M. Dirac, *The Principles of Quantum Mechanics*, Ch. 9, Clarendon Press, Oxford, 1956.
21. H. H. Limbach, G. Scherer, M. Maurer and B. Chaudret, *Angew. Chemie Int. Ed.*, 1992, **31**, 1369.
22. E. M. Hiller and R. A. Harris, *J. Chem. Phys.*, 1993, **98**, 2077.
23. A. Jarid, M. Moreno, A. Lledós, J. M. Lluch and J. Bertran, *J. Am. Chem. Soc.*, 1993, **115**, 5861.
24. A. Jarid, M. Moreno, A. Lledós, J. M. Lluch and J. Bertran, *J. Am. Chem. Soc.*, 1995, **117**, 1069.
25. S. Camanyes, F. Maseras, M. Moreno, A. Lledós, J. M. Lluch and J. Bertrán, *J. Am. Chem. Soc.*, 1996, **118**, 4617.
26. D. M. Heinekey, A. S. Hinkle and J. D. Close, *J. Am. Chem. Soc.*, 1996, **118**, 5353.
27. (a) S. Szymański, *J. Chem. Phys.*, 1996, **104**, 8216; (b) *ibid.*, 1997, **106**, 3430.
28. C. Scheurer, R. Wiedenbruch, R. Meyer, R. R. Ernst and D. M. Heinekey, *J. Chem. Phys.*, 1997, **106**, 1.
29. G. J. Kubas, R. R. Ryan, B. I. Swanson, P. J. Vergamini and H. J. Wasserman, *J. Am. Chem. Soc.*, 1984, **106**, 451.

30. D. M. Heinekey and W. J. Oldham, *Chem. Rev.*, 1993, **93**, 913.
31. D. M. Heinekey, *J. Am. Chem. Soc.*, 1991, **113**, 6074.
32. A. Antiñolo, F. Carillo, J. Fernández-Baeza, A. Otero and B. Chaudret, *Inorg. Chem.*, 1992, **31**, 5156.
33. B. Chaudret, G. Commenges, F. Jalon and A. Otero, *J. Chem. Soc., Chem. Commun.*, **1989**, 210.
34. T. Arliguie, C. Border, B. Chaudret, J. Devillers and R. Poilblanc, *Organometallics*, 1989, **8**, 1308.
35. D. M. Heinekey, N. G. Payne and C. D. Sofield, *Organometallics*, 1990, **9**, 2643.
36. D. G. Gusev, R. Kuhlman, G. Sini, O. Eisenstein and K. G. Caulton, *J. Am. Chem. Soc.*, 1994, **116**, 2685.
37. D. M. Heinekey and T. G. P. Harper, *Organometallics*, 1991, **10**, 2891.
38. T. Arliguie, B. Chaudret, F. A. Jalon, A. Otero, J. A. Lopez and F. J. Lahoz, *Organometallics*, 1991, **10**, 1888.
39. A. Antiñolo, F. Carillo, B. Chaudret, J. Fernández-Baeza, M. Lafranchi, H. H. Limbach, M. Maurer, A. Otero and M. A. Pellinghelli, *Inorg. Chem.*, 1994, **33**, 5163.
40. A. Antiñolo, F. Carillo-Hermosilla, B. Chaudret, M. Fajardo, J. Fernández-Baeza, M. Lafranchi, H. H. Limbach, M. Maurer, A. Otera and M. A. Pellinghelli, *Inorg. Chem.*, 1996, **35**, 7873.
41. B. Chaudret, H. H. Limbach and C. Moise, *C.R.C. Acad. Sci., Ser. 2*, 1992, **315**, 533.
42. S. Sabo-Etienne, B. Chaudret, H. Abou el Makarim, J. C. Barthelat, J. P. Daudey, S. Ulrich, H. H. Limbach and C. Moise, *J. Am. Chem. Soc.*, 1995, **117**, 11602.
43. K. A. Earl, G. Jia, P. A. Maltby and R. H. Morris, *J. Am. Chem. Soc.*, 1991, **113**, 3027. M. T. Bautista, E. P. Capellani, S. D. Drouin, R. H. Morris, C. T. Schweitzer, A. Stella and J. P. Zubkowski, *J. Am. Chem. Soc.*, 1991, **113**, 4876.
44. S. Sabo-Etienne, B. Chaudret, H. Abou el Makarim, J. C. Barthelat, J. P. Daudey, C. Moise and J. C. Leblanc, *J. Am. Chem. Soc.*, 1994, **116**, 9335.
45. F. A. Jalón, A. Otero, B. R. Manzano, E. Villaseñor and B. Chaudret, *J. Am. Chem. Soc.*, 1995, **117**, 10123.
46. S. Alexander, *J. Chem. Phys.*, 1962, **37**, 974.
47. G. Binsch, *J. Am. Chem. Soc.*, 1969, **91**, 1304. D. A. Kleier and G. Binsch, *J. Magn. Reson.*, 1970, **3**, 146.
48. H. H. Limbach, G. Scherer, L. Meschede, F. Aguilar-Parilla, B. Wehrle, J. Braun, C. Hoelger, H. Benedict, G. Buntkowsky, W. P. Fehlhammer, J. Elguero, J. A. S. Smith and B. Chaudret, in *Ultrafast Reaction Dynamics and Solvent Effects, Experimental and Theoretical Aspects*, AIP Conf. Proc., Vol. 298 (ed. Y. Gauduel and P. J. Rossky), p. 225, American Institute of Physics, 1994.
49. R. Wiedenbruch, M. Schick, A. Pampel, B. H. Meier, R. Meier, R. R. Ernst, S. Chaloupka and L. M. Venanzi, *J. Phys. Chem.*, 1995, **99**, 13088.
50. P. E. Parris and R. Silbey, *J. Chem. Phys.*, 1985, **83**, 5619.
51. R. Meyer and R. R. Ernst, *J. Chem. Phys.*, 1990, **93**, 5518.
52. C. Herring, in *Magnetism*, Vol. IIB (ed. G. T. Rado and H. Suhl), p. 2, Academic Press, New York and London, 1966.
53. S. J. Inati and K. W. Zilm, *Phys. Rev. Lett.*, 1992, **68**, 3273.
54. C. Eckart, *Phys. Rev.*, 1935, **47**, 552.
55. M. Roger, J. H. Hetherington and J. M. Delrieu, *Rev. Mod. Phys.*, 1983, **55**, 1.
56. S. Szymański, *J. Mol. Struct.*, 1994, **321**, 115.
57. A. Landesman, *Ann. Phys. (Paris)*, 1973–1974, **8**, 53.
58. J. D. Dunitz, V. Schomaker and K. N. Trueblood, *J. Phys. Chem.*, 1988, **92**, 856.
59. C. S. Johnson and C. Mottley, *Chem. Phys. Lett.*, 1973, **22**, 430.
60. C. Herring, *Rev. Mod. Phys.*, 1962, **34**, 631.
61. T. Holstein, *J. Phys. Chem.*, 1952, **56**, 832.

62. R. A. Guyer and L. I. Zane, *Phys. Rev.*, 1969, **188**, 445.
63. A. K. McMahan, *J. Low Temp. Phys.*, 1972, **8**, 115; *ibid.*, 1972, **8**, 159.
64. J. D. Close, *J. Chem. Phys.*, 1996, **105**, 2317.
65. E. M. Hiller and R. A. Harris, *J. Chem. Phys.*, 1993, **99**, 7652.
66. W. A. Harrison, *Electronic Structure and the Properties of Solids: The Physics of the Chemical Bond*, Dover Publications, New York, 1989.
67. H. B. Pang, T. Xiang, Z. B. Su and L. Yu, *Phys. Rev. B*, 1990, **41**, 7209.
68. P. Reilly, R. A. Harris and K. B. Whaley, *J. Chem. Phys.*, 1991, **95**, 8599.
69. Q. Zhang and K. B. Whaley, *J. Chem. Phys.*, 1991, **95**, 1417.
70. K. B. Whaley and L. M. Falicov, *J. Chem. Phys.*, 1987, **87**, 7160.
71. J. H. Van Vleck, *Phys. Rev.*, 1929, **33**, 467. C. P. Slichter, *Principles of Magnetic Resonance*, p. 364, Springer, Berlin, 1978.
72. H. Mori, *Prog. Theor. Phys. Kyoto*, 1956, **33**, 423.
73. R. Zwanzig, *Lect. Theor. Phys.*, 1960, **3**, 106.
74. (a) E. L. Hahn and D. E. Maxwell, *Phys. Rev.*, 1952, **88**, 1070. (b) H. M. McConnel, *J. Chem. Phys.*, 1958, **28**, 430.
75. M. J. Pilling, *Reaction Kinetics*, Oxford Chemistry Series, No. 22, Oxford University Press, 1975.
76. E. M. Hiller and R. A. Harris, *J. Chem. Phys.*, 1994, **100**, 2522.
77. J. C. Barthelat, B. Chaudret, J. P. Daudey, P. De Loth and R. Poilblanc, *J. Am. Chem. Soc.*, 1991, **113**, 9896.
78. E. Clot, C. Leforestier, O. Eisenstein and M. Péllisier, *J. Am. Chem. Soc.*, 1995, **117**, 1797.
79. W. H. Miller, *J. Chem. Phys.*, 1980, **72**, 99.
80. A. Abragam, *The Principles of Nuclear Magnetism*, Ch. 11, Oxford University Press, London, 1961.
81. K. Blum, *Density Matrix. Theory and Applications*, Ch. 7, Plenum Press, New York, 1981.
82. S. Szymański, A. M. Gryff-Keller and G. Binsch. *J. Magn. Reson.*, 1986, **68**, 399.
83. R. K. Wangsness and F. Bloch, *Phys. Rev.*, 1953, **89**, 728.
84. F. Bloch, *Phys. Rev.*, 1956, **102**, 104; *ibid.*, 1957, **105**, 1206.
85. A. G. Redfield, *IBM J. Res. Dev.*, 1957, **1**, 19; *Adv. Magn. Reson.*, 1965, **1**, 1.
86. A. Heuer, *Z. Phys. B—Condensed Matter*, 1992, **88**, 39.
87. D. Braun and U. Weiss, *Physica B*, 1994, **202**, 264.
88. J. W. Hennel, *Rev. Roum. Phys.*, 1988, **33**, 653.
89. J. Pyka, I. Foltynowicz and J. Makarewicz, *J. Mol. Spectrosc.*, 1990, **143**, 137.
90. R. Meyer, *J. Mol. Spectrosc.*, 1979, **76**, 266.
91. S. Clough, in *NMR. Basic Principles and Progress*, Vol. 13 (ed. P. Diehl, E. Fluck and R. Kosfeld), p. 113, Springer, Berlin, 1976.

Structural Studies of Hydrogen-bonded Peptides and Polypeptides by Solid-state NMR

N. ASAKAWA,[1,2†] T. KAMEDA,[1] S. KUROKI,[1,3†]
H. KUROSU,[1] S. ANDO,[1] I. ANDO[1] and A. SHOJI[4]

[1]*Department of Polymer Chemistry, Tokyo Institute of Technology, Ookyama, Meguro-ku, Tokyo, Japan*

[2]*Department of Biomolecular Engineering, Tokyo Institute of Technology, Nagatsuta, Midori-ku, Yokohama, Kanagawa, Japan*

[3]*Advanced Polymer Lab., Japan High Polymer Center, Sengen, Tsukuba, Ibaraki, Japan*

[4]*Department of Biological Sciences, Gunma University, Tenjin-cho, Kiryu, Gunma, Japan*

ANNUAL REPORTS ON NMR SPECTROSCOPY
VOLUME 35 ISBN 0-12-505335-5

Copyright © 1998 Academic Press Limited
All rights of reproduction in any form reserved

The nature of hydrogen bond has received much attention in various scientific fields. It is well known that hydrogen-bonding plays crucial roles in forming higher-order structure in peptides, polypeptides and proteins.

Systematic studies of the hydrogen-bonding effects on ^{13}C, ^{15}N and ^{17}O NMR chemical shifts for amide carbonyl-carbon, amide nitrogen, and carbonyl-oxygen atoms in solid peptides and polypeptides containing various amino acid residues have been made.

This review describes the recent studies on hydrogen-bonded structures in the solid state through the observation of NMR chemical shifts and also through theoretical calculations of nuclear shieldings in order to gain further insight into the nature and effects of hydrogen-bonding.

1. INTRODUCTION

It is well known that the hydrogen bond plays an important role in forming higher-order structures of peptides and polypeptides including proteins. Accordingly, the nature of the hydrogen bond has been widely studied by various spectroscopic methods. High-resolution NMR spectroscopy has also been used as one of the most powerful means for obtaining useful information on the details of the hydrogen bond.

NMR chemical shifts are one of the most important parameters for providing information about molecular structure. Since the electronic structure around the amide carbonyl-carbon and nitrogen atoms in peptides and polypeptides is greatly affected by the nature of hydrogen bond, the NMR chemical shifts for these atoms are sensitive to the special arrangement of the nuclei comprising the hydrogen bond.

It is difficult, however, to estimate exactly the hydrogen-bonding effect on the chemical shift because the observed chemical shifts of peptides are often averaged values for all of the rotational isomers owing to interconversion by rapid rotation about the bonds in solution. On the other hand, chemical shifts in the solid state provide direct information about the hydrogen bond present in peptides and polypeptides with a fixed conformation. From such a viewpoint, systematic studies on the hydrogen-bonding effects on the ^{13}C, ^{15}N and ^{17}O chemical shifts of amide carbonyl-carbon, amide nitrogen, and carbonyl-oxygen atoms of peptides and polypeptides containing various amino acid residues of the solid state have been made.

In this review article, we introduce recent studies on the hydrogen-bonded structures of peptides and polypeptides in the solid state through the observation of NMR chemical shifts and through theoretical calculations of nuclear shieldings (chemical shifts) with a view to finding a deeper understanding of the nature and influence of hydrogen bonds.

2. THEORY AND EXPERIMENT

2.1. Theory of NMR spectra

Several physical parameters affect NMR spectra.[1] These are indirect scalar coupling (J-coupling), direct dipolar coupling, quadrupolar coupling, and chemical shift. J-coupling emerges from the interaction mediated by electrons between nuclei. J-coupling, particularly ^1H–^1H coupling, has played a crucial role in liquid-state, or solution-state, NMR spectroscopy; scalar ^3J-coupling data give the dihedral angle in a molecule through the Karplus equation. A large number of studies of protein structure have exploited this scheme. Direct dipolar coupling does not influence the solution NMR spectrum, since the direct dipolar coupling is represented by a traceless second-rank tensor and rapid molecular motions unavoidably average this traceless tensor. Moreover, in solid-state NMR, direct dipolar coupling exhibited severe line width problems before magic-angle spinning (MAS)[2] and dipolar decoupling experiments (DD)[3] were performed. More recently, some groups have tried to develop methods for detecting the direct dipolar coupling of spin-$\frac{1}{2}$ pairs in rotating solids; thereby one can determine internuclear distances of spin pairs by detection of the dipolar coupling.

Chemical shifts have been exploited for the identification of molecules because the different electronic environments around a nucleus, i.e. the electron density and three-dimensional spread of electron wavefunctions, give different chemical shift values. Although the quantum-mechanical description of nuclear shielding, i.e. chemical shift, was given in 1950, highly accurate nuclear shielding calculations for large molecules could not be carried out because the available computational facilities were not adequate. However, the development of computers has enabled us to carry out shielding calculations with medium-size basis sets for large molecules.

2.2. Chemical shift tensor for ^{13}C and ^{15}N nuclei

Let us consider a nucleus in a molecule with a particular magnetic shielding environment. The effect of the environment is described by the Hamiltonian ($\mathcal{H}$)

$$\mathcal{H} = \gamma \mathbf{I} \cdot \sigma \cdot \mathbf{B} \tag{1}$$

where γ is the gyromagnetic ratio of the nucleus, $\mathbf{I}$ is the spin operator, σ is the shielding tensor and $\mathbf{B}$ is the magnetic field. The NMR experiment measures σ_{zz} in the frame with the z axis along the magnetic field B. If we take the Z component of the external magnetic field to be B_0, we obtain

$$\mathcal{H} = \gamma I_z \sigma_{zz} B_0 \tag{2}$$

for the shielding Hamiltonian. Note that the chemical shift (δ) is defined as the difference between any given shielding and shielding for a given nucleus in a reference molecule. For powder samples, the NMR spectrum appears as the superposition of signals with the nuclear shieldings (σ_{zz}) for several different orientations of the principal axis system (PAS) of the sample with respect to the magnetic field. The observed resonance frequency (ω) associated with this orientation of the shielding tensor is given by

$$\omega = -\gamma B_0(\sigma_{xx}\cos^2\alpha\sin^2\beta + \sigma_{yy}\sin^2\alpha\sin^2\beta + \sigma_{zz}\cos^2\beta) \tag{3}$$

where α and β are two of the three Euler angles that specify the orientation of the PAS in the frame of the spinning system, and σ_{xx}, σ_{yy} and σ_{zz} are the principal values of the shielding tensor. When integrated over all values of the angles (α, β), which are defined as the orientation of a PAS with respect to the magnetic field, this lineshape represents the absorption spectrum of a powder sample, in which all orientations of the principal axes with respect to the magnetic field are present with equal probability. Bloembergen and Rowland[4] derived the lineshape function $I(\omega)$ for a powder spectrum. The intensity is directly proportional to the number of molecules with shielding tensor orientation (α, β), as

$$\int_{\Omega} P(\alpha,\beta)\,\mathrm{d}\alpha\sin\beta\,\mathrm{d}\beta = \int_{-\infty}^{\infty} I(\omega)\,\mathrm{d}\omega = \int_{-\infty}^{\infty} F(\sigma)\,\mathrm{d}\sigma \tag{4}$$

where $P(\alpha, \beta)$ is the probability that the principal shielding axes of a molecule have the orientation specified by α and β.

Herzfeld–Berger analysis

The powder spectrum offers information about the exact principal values (δ_{11}, δ_{22} and δ_{33}) of a chemical shift tensor only when there is no severe overlap between the powder spectra. In most cases of NMR of organic molecules, this situation might not be encountered; powder spectra would be composed of some signals that are derived from several chemically and electronically inequivalent environments.

Herzfeld and Berger[5] developed a method for determining the principal values of chemical shift tensors from the accurate measurement of the spinning sideband intensities under the condition of MAS with a low spinning rate. While this method, called the Herzfeld–Berger analysis, maintains the high-resolution NMR spectrum, one can obtain principal values of several chemical shift tensors at once.

From the viewpoint of computation, the original Herzfeld–Berger analysis was not necessarily suitable for writing the simulation program. Fenzke *et al.*

developed a novel method for determining the principal values of a chemical shift tensor from MAS sideband intensities, in which one calculates the mean square deviation of the calculated sideband intensities from the experimental results and minimizes the deviation.[6]

2.3 Chemical shift tensor and quadrupolar coupling for the ^{17}O nucleus

The ^{17}O nucleus has spin 5/2 and so has a quadrupole moment. Solid-state ^{17}O spectra contain quadrupolar interactions, and for this the central transition signal $(-1/2, 1/2)$ becomes broad by a second-order perturbation. Therefore, a static ^{17}O NMR signal contains eight kinds of NMR parameters such as the nuclear quadrupolar coupling constant (e^2qQ/h) (which comes from the electrostatic interaction between the nuclear quadrupolar moment (eQ) and the electric field gradient tensor elements (V_{11}, V_{22} and V_{33})); the asymmetry parameter (η_Q); and the principal values of the shielding tensor (σ_{11}, σ_{22} and σ_{33}). To determine these parameters, computer simulation is carried out to superimpose the theoretical lineshape on to the observed spectrum.

In the presence of a quadrupolar interaction the quadrupolar Hamiltonian ($\mathcal{H}_{Q\pm1/2}$) at the resonance frequency ω_0 can be expressed by[43]

$$\mathcal{H}_{Q\pm1/2} = -\frac{R}{6\omega_0}[A(\phi)\cos^4\theta + B(\phi)\cos^2\theta + C(\phi)] \tag{5}$$

where

$$R = \omega_Q^2[I(I+1) - \tfrac{3}{4}]$$

$$w_Q = \frac{3e^2qQ}{2I(2I-1)h}$$

$$A(\phi) = -\frac{27}{8} - \frac{9}{4}\eta_Q\cos 2\phi - \frac{3}{8}\eta_Q^2\cos^2 2\phi$$

$$B(\phi) = -\frac{30}{8} - \frac{\eta_Q^2}{2} + 2\eta_Q\cos 2\phi - \frac{3}{4}\eta_Q^2\cos^2 2\phi$$

$$C(\phi) = -\frac{3}{8} + \frac{\eta_Q^2}{2} + \frac{1}{4}\eta_Q\cos 2\phi - \frac{3}{8}\eta_Q^2\cos^2 2\phi$$

$$\eta_Q = \frac{V_{11} - V_{22}}{V_{33}} \qquad |V_{33}| \geqslant |V_{22}| \geqslant |V_{11}|$$

$$V_{33} = eq$$

in which V_{11}, V_{22} and V_{33} are the values of the three principal elements of the electric field gradient tensor, eQ is the quadrupole moment of the nucleus, and θ and ϕ are Euler angles relating the magnetic field B_0 to the PAS of the electric field gradient tensor of the nucleus.

In the presence of an anisotropic nuclear shielding interaction, the Hamiltonian ($\mathcal{H}_{CS}$) can be expressed as[43]

$$\mathcal{H}_{CS} = \omega_0[\sigma_{11}\sin^2\theta\sin^2\phi + \sigma_{22}\sin^2\theta\cos^2\phi + \sigma_{33}\cos^2\theta]I_z \tag{6}$$

Further, we rearrange Eq. (6) using δ instead of σ as follows:

$$\mathcal{H}_{CS} = \omega_0\left(\delta_0 + \frac{\Delta\delta}{2}[(3\cos^2\theta - 1) - \eta\sin^2\eta\cos 2\phi]\right)I_z \tag{7}$$

where

$$\delta_{iso} = \tfrac{1}{3}(\delta_{11} + \delta_{22} + \delta_{33})$$

$$\Delta\delta = \delta_{iso} - \delta_{33}$$

$$\eta = \frac{\delta_{11} - \delta_{22}}{\Delta\delta}$$

$$\delta_{11} \geqslant \delta_{22} \geqslant \delta_{33}$$

in which δ_{iso} is the isotropic chemical shift, η is the shielding asymmetry parameter and $\Delta\delta$ is the anisotropic parameter. The total Hamiltonian expressed by Baugher *et al.*[43] is simply the sum of Eqs (5) and (7).

For the more general case, one has to consider the second-rank tensor properties of both the quadrupolar and shielding tensors. One cannot simply add two tensor quantities without considering the relative orientation of one tensor with respect to the other. In this case, there is no reason to believe that the PAS for the anisotropic shielding tensor will be coincident with that of the quadrupolar tensor. Hence, the first step in the analysis is to place the tensors in a common reference frame. As the quadrupolar interaction is more dominant for ^{17}O, it is convenient to express the shielding tensor in the frame of the quadrupolar tensor. Thus, the quadrupolar resonance frequency is considered to be the same as that in Eq. (5). The shielding Hamiltonian ($\mathcal{H}_{CS}$), transformed to the quadrupolar PAS frame, expressed in terms of its value in the shielding frame is

$$\mathcal{H}_{CS} - \omega_0\delta_{iso}I_z = \left(\frac{\omega_0 I_z\Delta\delta}{2}\right)\left[(3\cos^2\theta - 1)\left(\frac{3\cos^2\beta - 1}{2} - \frac{\eta}{2}\sin^2\beta\cos 2\gamma\right)\right.$$
$$\left. + \sin 2\theta\cos(\phi + \alpha)\left\{-\frac{3}{2}\sin 2\beta - \eta\sin\beta\cos\beta\cos 2\gamma\right\}\right.$$

$$+ \sin 2\theta \sin(\phi + \alpha)\{\eta \sin\beta \sin 2\gamma\}$$

$$+ \frac{1}{2}\sin^2\theta \cos 2(\phi + \alpha)\{3\sin^2\beta - \eta\cos 2\gamma(1 + \cos^2\beta)\}$$

$$+ \frac{1}{2}\sin^2\theta \sin^2(\phi + \alpha)\{2\eta\cos\beta \sin 2\gamma\}\Bigg] \tag{8}$$

Note that when $(\alpha, \beta, \gamma) = (0, 0, 0)$, Eq. (8) reduces to Eq. (7). In our lineshape simulations the Hamiltonian of the system is the sum of Eqs (5) and (8) as well as the Zeeman term.

From these Hamiltonians, the central transitions $(-1/2, 1/2)$ will be at the positions given by

$$\delta = \delta_{CS} + \delta_{Q\pm 1/2} \tag{9}$$

where

$$\delta_{CS} = \delta_{iso} + \left(\frac{\Delta\delta}{2}\right)\Bigg[(3\cos^2\theta - 1)\left(\frac{3\cos^2\beta - 1}{2} - \frac{\eta}{2}\sin^2\beta\cos 2\gamma\right)$$

$$+ \sin 2\theta\cos(\phi + \alpha)\left\{-\frac{3}{2}\sin 2\beta - \eta\sin\beta\cos\beta\cos 2\gamma\right\}$$

$$+ \sin 2\theta\cos(\phi + \alpha)\{\eta\sin\beta\sin 2\gamma\}$$

$$+ \frac{1}{2}\sin^2\theta\cos 2(\phi + \alpha)\{3\sin^2\beta - \eta\cos 2\gamma(1 + \cos^2\beta)\}$$

$$+ \frac{1}{2}\sin^2\theta\sin 2(\phi + \alpha)\{2\eta\cos\beta\sin 2\gamma\}\Bigg] \tag{10}$$

$$\delta_{Q\pm 1/2} = -\frac{R}{6\omega_0^2}[A(\phi)\cos^4\theta + B(\phi)\cos^2\theta + C(\phi)] \times 10^6 \tag{11}$$

The static powder spectrum can be calculated by integration over all possible orientations using Eqs (4) and (9). Using a Sun 4 SPARC Station for the calculations, it takes about one minute to obtain a simulated spectrum.

2.4. MO calculations of nuclear shielding

The ^{13}C chemical shift obtained from solid-state NMR is closely related to the electronic structure of a molecule, and therefore includes information about the three-dimensional structure of the molecule. In order to reveal the correlation between the structures of peptides and the ^{13}C chemical shifts, ^{13}C shielding calculations have been carried out using finite perturbation theory with intermediate neglect of differential overlap (FPT-INDO)[7,8] and by the

coupled Hartree–Fock method using *ab initio* gauge-invariant atomic orbitals (GIAO-CHF).[9,10] FPT-INDO calculations enable us to understand what kinds of physical phenomena contribute fundamentally to chemical shifts in molecules; it is much easier to perform this calculation than the *ab initio* methods. On the other hand, the *ab initio* GIAO-CHF method is more suitable for highly accurate shielding calculations, and so becomes the methodology for the determination of a molecular structure compared with the observation of chemical shifts. In each procedure, the total shielding constant is estimated as the sum of diamagnetic (σ^{d}) and paramagnetic (σ^{p}) contributions.

$$\sigma = \sigma^{d} + \sigma^{p} \tag{12}$$

Finite perturbation theory with the INDO MO method (FPT-INDO)

Here we describe the FPT within the INDO framework for calculating the ^{13}C shielding constant. The FPT-INDO theory has the advantage of allowing the calculation of the paramagnetic term without the explicit wavefunctions of excited states and the one-electron excitation energies, which are difficult to obtain to high accuracy by the usual semiempirical MO approximations. In the FPT-INDO calculations, however, the contributions from AOs centred on two different nuclei are not involved. *N*-Acetyl-*N'*-methyl-L-alanine amide (Ac-L-Ala-NHMe) (having the same skeletal bonds as a peptide) forming hydrogen bonds with two formamide molecules as a model supermolecule (Fig. 1a) has been often employed. The bond lengths and bond angles proposed by Momany *et al.*[11] have been used.

Coupled Hartree–Fock method employing the 4-31G ab initio *MO method with gauge-invariant atomic orbitals (4-31G-GIAO-CHF)*

The model molecule, Ac-L-Ala-NHMe, is shown in Fig. 1b. All the bond lengths in this model molecule were optimized by the *ab initio* 4-31G MO method. The calculated shielding values were converted to chemical shifts as given in ppm relative to methane. (The calculated ^{13}C shielding of methane by the 4-31G/4-31G basis set[12] is 207.2 ppm and the observed ^{13}C chemical shift is −2.1 ppm relative to trimethylsilane (TMS).) Finally, the calculated chemical shifts can be given relative to TMS.

3. HYDROGEN-BOND LENGTH AND NMR CHEMICAL SHIFT

3.1. Hydrogen-bonding effect on the ^{13}C chemical shift of the carbonyl-carbon in several amino acid residues

Figure 2 shows the 67.80 MHz ^{13}C CP-MAS NMR spectrum of Ala-Ser in the solid state as a typical example. The carbonyl-carbon of the C-terminal

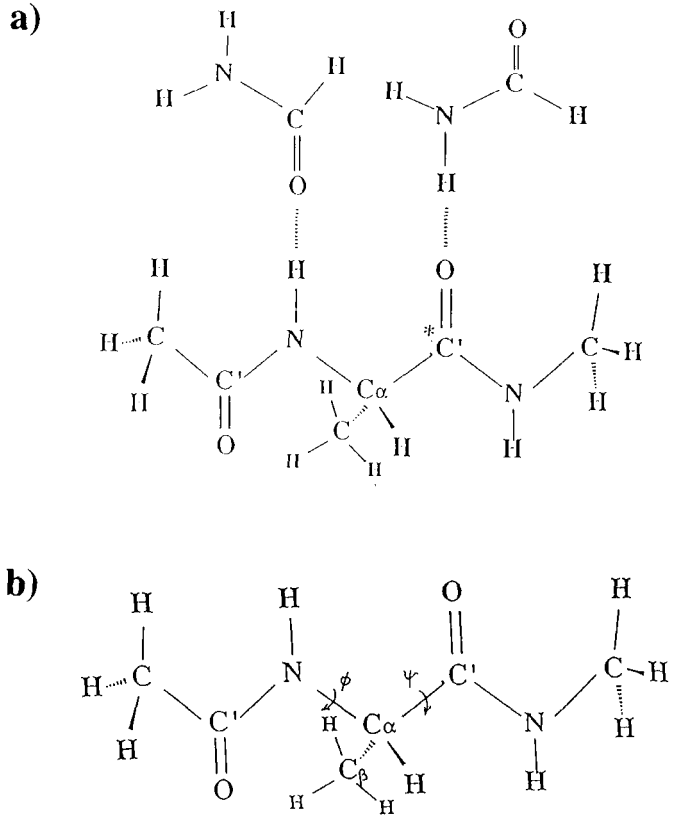

Fig. 1. Molecular structure of *N*-acetyl-*N'*-methyl-L-alanine amide, hydrogen-bonded (a) with and (b) without two formamide molecules. The chemical shielding calculation is made for the carbonyl marked by *.

carboxylic group is deshielded by several ppm and appears as a rather sharp peak relative to the internal amide carbonyl-carbon signal.[14] The isotropic ^{13}C chemical shifts of the L-Ala carbonyl-carbons measured are listed in Table 1, together with the geometrical parameters obtained by X-ray diffraction studies.[15–20] Some of the geometrical parameters are calculated using the unit-cell parameters and fractional coordinates reported in the literature.

Figure 3 shows plots of the observed isotropic ^{13}C chemical shifts (δ_{iso}) of the L-Ala carbonyl-carbon against the N···O separation ($R_{N\cdots O}$), where $R_{N\cdots O}$ gives a measure of hydrogen-bond length. It is found that a decrease of $R_{N\cdots O}$ leads to a decrease in shielding shift, and there exists an approximately linear relationship between the ^{13}C chemical shift and $R_{N\cdots O}$. It is noted that not only in oligopeptides (dimers or trimers) but also in the polypeptide ((L-Ala)$_n$ with the α_R-helix form) the L-Ala carbonyl-carbon chemical shifts give a similar

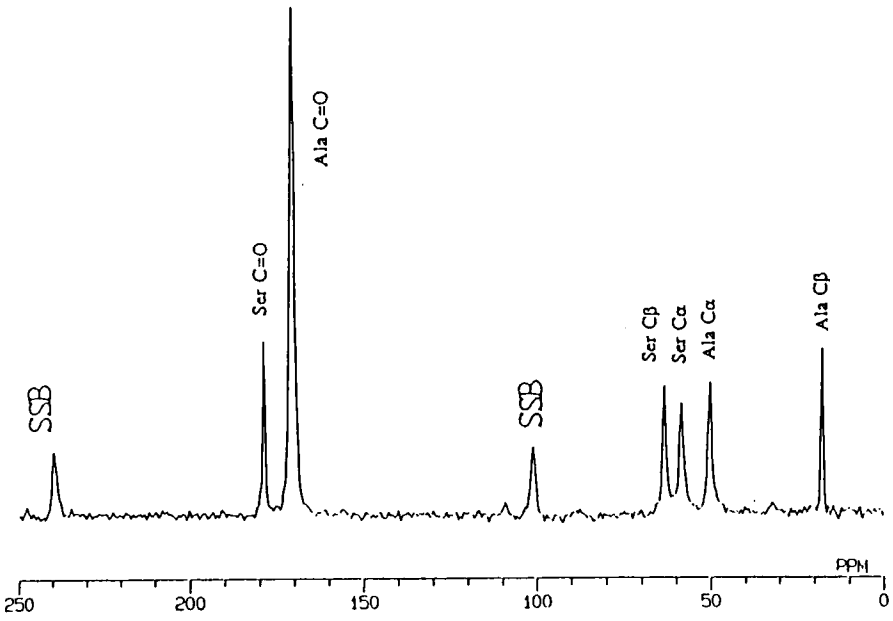

Fig. 2. 67.8 MHz cross polarization magic-angle spinning (CP-MAS) NMR spectrum for [5%, 1-^{13}C]Ala-Ser, as a typical example. The solid-state NMR measurements are performed under the following conditions: the RF field intensity for the carbon channel is 56 kHz; the contact time for the matched cross polarization between ^{1}H and ^{13}C is 2 ms; heteronuclear dipolar decoupling during the acquisition period is carried out at an intensity of 56 kHz. The number of data points collected is 2048; before Fourier transformation, the FID is zero-filled; the total data points are 8192. SSB denotes a spinning sideband.

hydrogen-bond length dependence. This suggests that the ^{13}C chemical shifts of any L-Ala carbonyl-carbon accepting the hydrogen bond that is formed between the amide ⟩C=O and amide ⟩N—H are strongly influenced by the hydrogen-bond length. This relationship is expressed as

$$\delta_{iso}(\text{ppm}) = 237.5 - 21.7R_{N\cdots O}\ (\text{Å}) \tag{13}$$

Equation (13) indicates that the hydrogen-bond length can be determined through the observation of the ^{13}C chemical shifts of the L-Ala carbonyl-carbons in peptides and polypeptides.

However, the relationship between the observed solid-state ^{13}C chemical shifts of the Gly carbonyl-carbon and $R_{N\cdots O}$ has been determined by Ando *et al.*[21] and expresssed as

$$\delta_{iso}(\text{ppm}) = 206.0 - 12.4R_{N\cdots O}\ (\text{Å}) \tag{14}$$

Table 1. Observed ^{13}C chemical shifts of the L-alanine-residue carbonyl-carbons of some oligopeptides in the solid state as determined by ^{13}C CP-MAS NMR and geometrical parameters.

Sample	^{13}C Chemical shift (ppm)				Geometrical parameters[c]				
					N···O length (Å)	C=O···N angle (°)	Dihedral angles (°)		
	δ_{iso}	δ_{11}	δ_{22}	δ_{33}			ϕ	ψ	ω
Ac-Ala-NHMe	175.9	245	186	96	2.92	138.3	−84.3	159.0	173.3
	177.0	241	196	94	2.72	132.4	−87.6	154.8	171.9
Ac-Ala-Aib-OMe[b]	174.7	–	–	–	2.93	154.5	−134.0	122.2	−174.1
	171.7	–	–	–	2.97	152.2	−129.8	121.5	−179.5
Ala-Gly-Gly·H_2O	172.6	245	179	93	3.00	150.2	–	160.0	172.4
Ala-Ser	170.1	249	172	89	3.04	156.3	–	124.8	−178.0
Ala-Pro-Gly·H_2O	169.3	235	178	95	3.157	155.2	–	153.2	177.0
$(Ala)_n^a$	176.8	243	194	94	2.87	–	−57.4	−47.5	−179.8

[a]With the α-helix form.
[b]Aib: aminoisobutyric acid.
[c]Determined by X-ray diffraction.

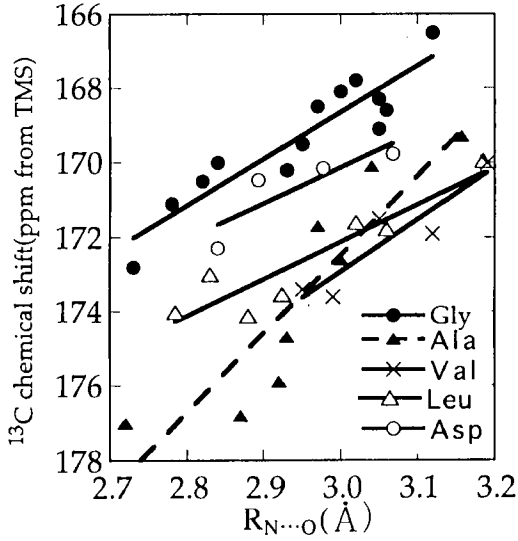

Fig. 3. Plots of ^{13}C chemical shifts for the carbonyl-carbons in Gly, L-Ala, L-Val, D,L-Leu and L-Asp residues in peptides in the solid state, against the N···O separation ($R_{N\cdots O}$).

As can be seen from these two relationships, Eqs (13) and (14), the slope of the variation of the ^{13}C chemical shift of the L-Ala carbonyl-carbon against $R_{N\cdots O}$ is 1.7 times larger than that of the Gly carbonyl-carbon. This shows that the $R_{N\cdots O}$ dependence of the former is much larger than that of the latter. Recently, the same NMR experiments were performed for several peptides that contain a bulky side-chain such as L-valine (Val), D- and L-leucine (Leu), and L-aspartic acid (Asp) residues.[45] These data are also plotted in Fig. 3. From these results, expressions are obtained for the relationships between δ_{iso} and $R_{N\cdots O}$ as determined by least mean squares methods. These are given in ppm relative to TMS by

$$\delta_{iso}\ (\text{ppm}) = 215.4 - 14.2R_{N\cdots O}\ (\text{Å}) \quad \text{for L-Val} \tag{15}$$

$$\delta_{iso}\ (\text{ppm}) = 202.2 - 10.0R_{N\cdots O}\ (\text{Å}) \quad \text{for L-Leu} \tag{16}$$

$$\delta_{iso}\ (\text{ppm}) = 199.0 - 9.6R_{N\cdots O}\ (\text{Å}) \quad \text{for L-Asp} \tag{17}$$

It is found that the slope of the variation of δ_{iso} against the hydrogen-bond length for these amino acid residues decreases in the order L-Ala > L-Val > Gly > L-Leu ≈ L-Asp. The magnitude of the intercept decreases in the same order as the slope. Therefore, we can say that the equations for these relationships are quite characteristic for the individual amino acid residues. Most recently, Take *et al.*[110] have studied L-phenylalanine residues hydrogen-

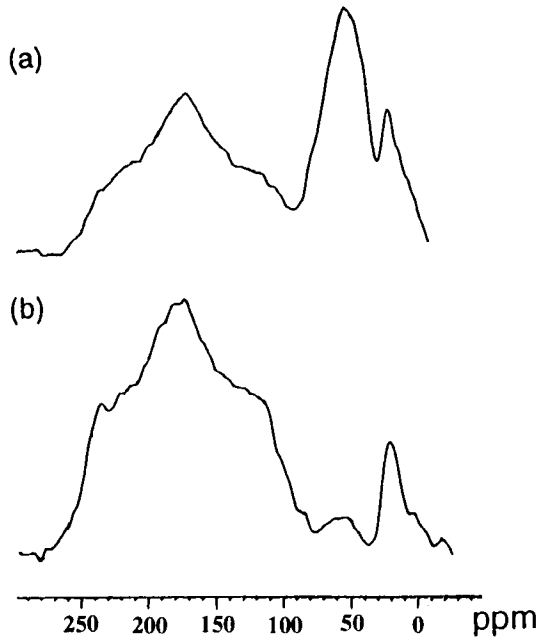

Fig. 4. 67.8 MHz (a) CP-static and (b) the dipolar-dephased CP-static spectra for [5%, 1-^{13}C]Ala-Ser in the solid state, as a typical example. The other conditions for NMR measurements are the same as those in Fig. 2.

bonded in peptides and polypeptides. It is found that the amide carbonyl ^{13}C chemical shift is strongly affected by the orientation of the aromatic ring and the hydrogen-bond length.

The principal values of the ^{13}C chemical shift tensor of the L-alanine carbonyl-carbon in peptides

It is expected that the principal values of the ^{13}C chemical shift tensors (δ_{11}, δ_{22} and δ_{33} in order of increasing shielding) will, in principle, be more valuable as parameters for obtaining detailed information on hydrogen-bonding, to be related to electronic structure, than will the isotropic ^{13}C chemical shift ($\delta_{iso} = (\delta_{11} + \delta_{22} + \delta_{33})/3$).

Figures 4a and 4b show the 67.80 MHz ^{13}C NMR powder pattern spectra of [5%, 1-^{13}C]Ala-Ser measured by CP-MAS and by the dipolar dephasing (DDph) pulse technique,[22] respectively. From these spectra, one can see the severe overlap between the carbonyl-carbon and C_α carbon powder spectra. Even when one uses the DDph pulse sequence, it is realized that it is not

necessarily easy to determine the exact principal values for the ^{13}C chemical shift tensor because of the overlap of the powder patterns of more than two sites due to the carbonyl-carbons of several amino acid residues, which arises from the low concentration of the carbonyl-^{13}C-labelled L-Ala residue. For this, it is useful to apply the spinning-sideband (SSB) analysis,[5,6,23] namely, the Herzfeld–Berger analysis, to determine the exact principal values of the ^{13}C-labelled L-Ala carbonyl-carbons.

Figures 5a–e show the 67.80 MHz ^{13}C CP-MAS spectra for several peptides with spinning frequencies around 1.6 kHz. The above-mentioned spinning-sideband analysis is carried out to determine the principal values of the ^{13}C chemical shift tensor. Figures 5f–j show the calculated MAS SSB spectra for these peptides. The errors in δ_{11}, δ_{22}, and δ_{33} from the SSB spectrum simulation are estimated as <1.5 ppm, <0.7 ppm, and <1.5 ppm, respectively.

Table 1 lists the determined principal values of the ^{13}C chemical shift tensors of the L-alanine residue carbonyl-carbons of some oligopeptides. The plots of δ_{11}, δ_{22} and δ_{33} against the N···O separation are shown in Figs 6a–c, respectively. Cross and coworkers have reported solid-state NMR measurements of gramicidin A, and determined the principal values for the chemical shift tensor of L-alanine carbonyl-carbon.[111] These data are included in Fig. 6. From this plot, it is found that the experimental δ_{22} values are the most sensitive to a change in $R_{N\cdots O}$, and the δ_{22} values shift linearly to high frequencies with a decrease of $R_{N\cdots O}$ except for the δ_{22} value of Ala-Pro-Gly·H_2O. In the case of Ala-Pro-Gly·H_2O, the covalent bond between the Ala and Pro residues does not form the peptide bond but the imide bond. The electronic structure of the L-Ala carbonyl-carbon in Ala-Pro-Gly·H_2O is thought to be different from that of the L-Ala carbonyl-carbon forming the peptide bond and, hence, the chemical shift for the L-Ala carbonyl-carbon might be sensitive to both $R_{N\cdots O}$ and the nature of the bonds involved. A decrease of $R_{N\cdots O}$ leads to a slight decrease in δ_{11}, except for Ala-Pro-Gly·H_2O. The experimental δ_{33} values are almost independent of $R_{N\cdots O}$ with some scatter of the data. From the above results, it can be concluded that the large high-frequency shift of the isotropic ^{13}C chemical shifts, δ_{iso}, with decreasing $R_{N\cdots O}$ comes from the behaviour of the δ_{22} component in overcoming that of the δ_{11} component.

^{13}C shielding constant calculation by the FPT-INDO method

Figures 7a–d show the calculated isotropic shielding constants (σ_{iso}) and the tensor components of the paramagnetic terms (σ_{11}, σ_{22} and σ_{33}) for the L-Ala carbonyl-carbon of the model compound (Fig. 1a) as a function of $R_{N\cdots O}$. The calculated values are expressed in ppm with sign opposite to that of the experimental chemical shifts. Note that a negative sign for the calculated shielding constant denotes deshielding, in contrast to the positive sign of the experimental chemical shift values. An isotropic shielding constant and its tensor component are usually represented as the sum of the diamagnetic and

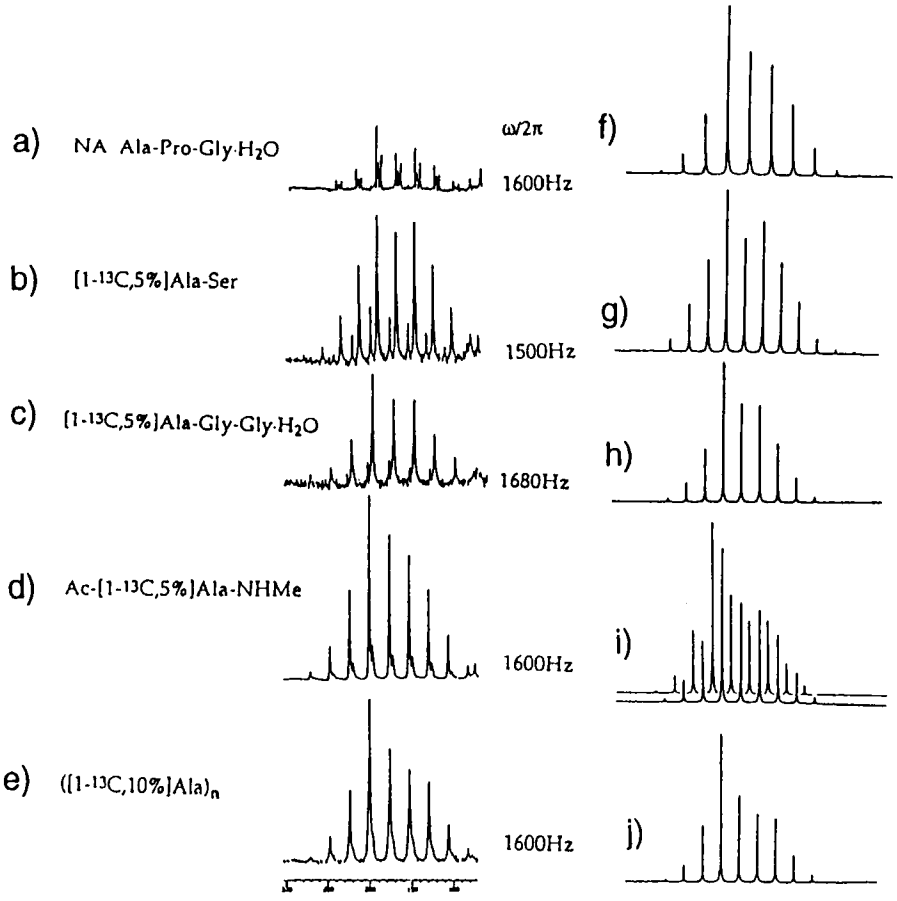

Fig. 5. ^{13}C cross polarization magic-angle spinning (CP-MAS) NMR spectra (left) for the several peptides that contain L-alanine residues, and the MAS spectrum simulation (right) for each L-alanine residue carbonyl-carbon using the principal values of determined chemical shift tensors. The RF field intensity for the carbon channel is 56 kHz; the contact time for the matched cross polarization between ^{1}H and ^{13}C is 2 ms; the heteronuclear dipolar decoupling during acquisition period is carried out at an intensity of 56 kHz. The delay time before acquisition is set at 34.8 μs; the gate for ^{13}C channel is opened at 20.0 μs after CP contact duration. The number of data collected is 2048; before Fourier transformation, the FIDs are zero-filled and the total data points are 8192. (a) Natural abundance Ala-Pro-Gly·H_2O; (b) [5%, 1-^{13}C]Ala-Ser; (c) [5%, 1-^{13}C]Ala-Gly-Gly·H_2O; (d) Ac-[5%, 1-^{13}C]Ala-NHMe; (e) ([10%, 1-^{13}C]Ala)$_n$. In the spectrum simulation procedures, 4851 orientations of chemical shift tensors with respect to the external magnetic field are accumulated.

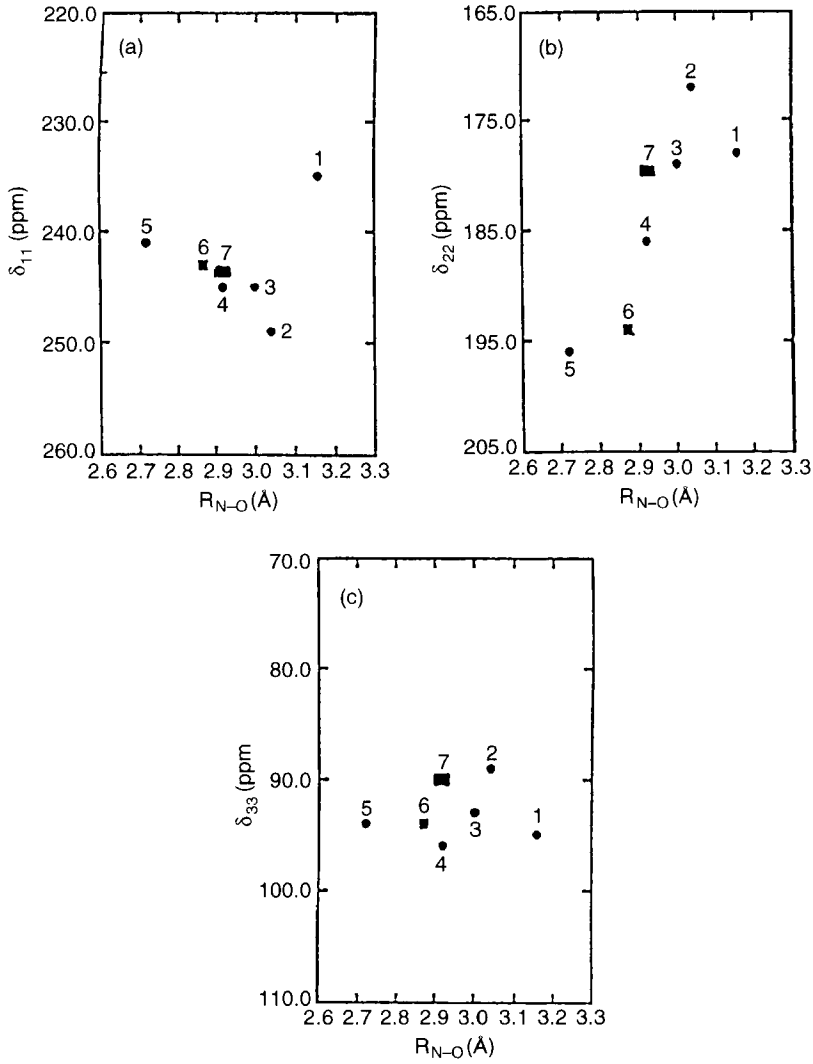

Fig. 6. Plots of the observed principal values of the ^{13}C chemical shift tensors (a) δ_{11}, (b) δ_{22}, and (c) δ_{33} against the N···O separation ($R_{N\cdots O}$): (1) Natural abundance Ala-Pro-Gly·H_2O; (2) [5%,1-^{13}C]Ala-Ser; (3) [5%,1-^{13}C]Ala-Gly-Gly·H_2O; (4, 5) Ac-[5%,1-^{13}C]Ala-NHMe; (6) ([10%,1-^{13}C]Ala)$_n$; (7) Ala-5 in gramicidin A, see Ref. 111.

the paramagnetic terms. However, the relative change for the ^{13}C shielding tensors is predominantly governed by the paramagnetic term.

Figure 7a shows the $R_{N\cdots O}$ dependence of the calculated isotropic ^{13}C shielding constant (σ_{iso}) of the central L-Ala carbonyl-carbon of the model compound with the α-helix, β-sheet, and 3_1-helix form. In the large $R_{N\cdots O}$ region, the values of σ_{iso} depend significantly on conformational changes. However, in the short $R_{N\cdots O}$ region, the change in $R_{N\cdots O}$ dominates the change in σ_{iso}. Therefore, the experimental finding that the isotropic ^{13}C chemical shift moves linearly to high frequencies with a decrease of $R_{N\cdots O}$ should be explained by the calculated results in the short $R_{N\cdots O}$ region. As the semiempirical INDO MO approximation adopted here neglects some two-centre electron integrals, the intermolecular interactions are considered to be reasonably reproduced in the short $R_{N\cdots O}$ region.[24]

The variation of the total electronic energy also supports this view as shown in Fig. 8, where the total energy minimum appears at around the $R_{N\cdots O}$ value of 2.3–2.5 Å.

As shown in Fig. 7a, a decrease of $R_{N\cdots O}$ leads to a decrease of σ_{iso} in the short $R_{N\cdots O}$ region ($R_{N\cdots O}$ = 2.3–2.5 Å). In this region, the effect of changes in hydrogen-bond length on the ^{13}C chemical shift is much larger than that in the main-chain dihedral angles. These results agree with the experimental results.

Figures 7b–d show the $R_{N\cdots O}$ dependence of the calculated principal values of the ^{13}C shielding tensor (σ_{11}, σ_{22} and σ_{33}). It is shown that a decrease of $R_{N\cdots O}$ leads to a reduction in σ_{22} and an increase in σ_{11}. σ_{33} is not sensitive to changes in $R_{N\cdots O}$. The magnitude of change for σ_{22} is much larger than those for σ_{11} and σ_{33}. These results agree with the experimental ones. If we look carefully at the calculations and experiments, the effect of changes in the main-chain dihedral angles on σ_{11} and σ_{22} from calculation is relatively larger than that from the experimental results. The difference between experiment and calculation is probably due to the fact that the calculation is carried out under the assumption that the hydrogen-bond angle ($\angle$N–O–C) is 180°. To explain the experimental behaviour, the calculation of the magnetic shielding requires a more accurate model that takes account not only of the main-chain dihedral angles and the hydrogen-bond length but also of the hydrogen-bond angle.

$R_{N\cdots O}$ dependence of the calculated electron densities on the carbonyl-carbons of the L-Ala and Gly residues

Figures 9a and 9b show the $R_{N\cdots O}$ dependence of the calculated electron densities on the carbonyl carbons of the L-Ala and Gly residues, respectively. The ^{13}C chemical shift is closely related to the electron density on the carbon atom. In general, the smaller the electron density on the carbon atom the lower the nuclear shielding. As shown in this figure, a decrease of $R_{N\cdots O}$ leads to a decrease of the electron density. However, it appears that the variation in the

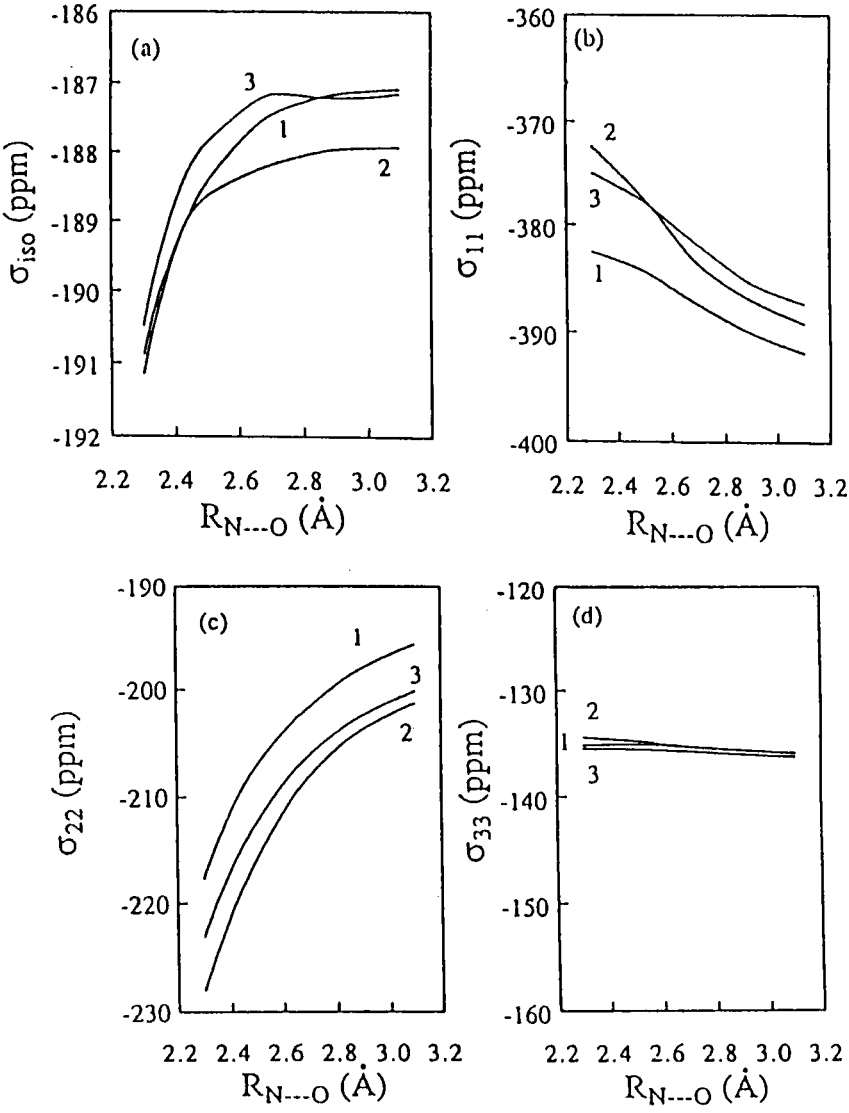

Fig. 7. Variation of the calculated ^{13}C shielding constants and the tensor components of the paramagnetic term with respect to the N···O separation $R_{N\cdots O}$ for (a) isotropic shielding constant σ_{iso}, (b) σ_{11}, (c) σ_{22} and (d) σ_{33}; (1) α_R-helix; (2) β_A-sheet; (3) 3_1-helix.

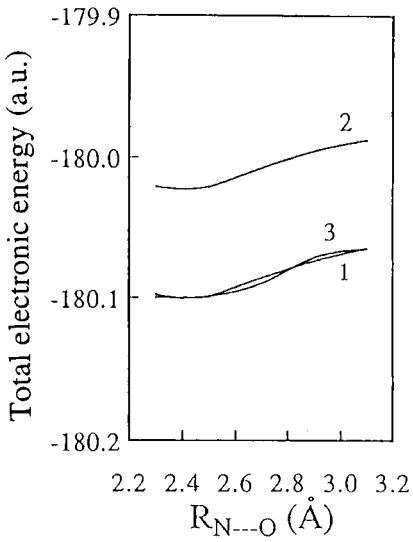

Fig. 8. Variation of the calculated total energy against the N···O separation $R_{N\cdots O}$ for *N*-acetyl-*N'*-methyl-L-alanine amide forming hydrogen bonds with two formamide molecules: (1) α_R-helix; (2) β_A-sheet; (3) 3_1-helix.

electron density on the L-Ala carbonyl-carbon is smaller than that on the Gly carbonyl-carbon, and conversely, the change of the experimental ^{13}C chemical shifts of the L-Ala carbonyl-carbon is larger than that of the Gly. This cannot be understood through the behaviour of electron density. Therefore, ^{13}C nuclear shielding calculations are required to understand the experimental behaviour.

The direction of the principal axes of the L-Ala carbonyl-shielding tensor

Figures 10a–c show the directions of the principal axis system of the ^{13}C shielding tensors for L-Ala carbonyl-carbon, as determined by theoretical calculations, where the value of $R_{N\cdots O}$ of the model compounds considered here is 2.3 Å and the main-chain dihedral angles are those of the α_R-helix ($\phi = -57°$, $\psi = -48°$), β_A-sheet ($\phi = -139°$, $\psi = 135°$), and 3_1-helix ($\phi = -88°$, $\psi = 155°$) forms, respectively. Figure 10d shows the direction of the principal axes for the shielding tensor determined by the NMR study of a [1-^{13}C]Ala-[^{15}N]Ala powder sample.[25] The σ_{22} component nearly lies along the amide carbonyl bond, and the σ_{11} is in the amide sp^2 plane and lies along the direction normal to the carbonyl bond. The σ_{33} component is aligned in the direction perpendicular to the amide sp^2 plane. The calculated directions of the principal axes do not conflict with the previous experimental results.[25] Thus, it is found that the σ_{22} value for the principal axis parallel to the carbonyl bond is the most sensitive to changes of $R_{N\cdots O}$.

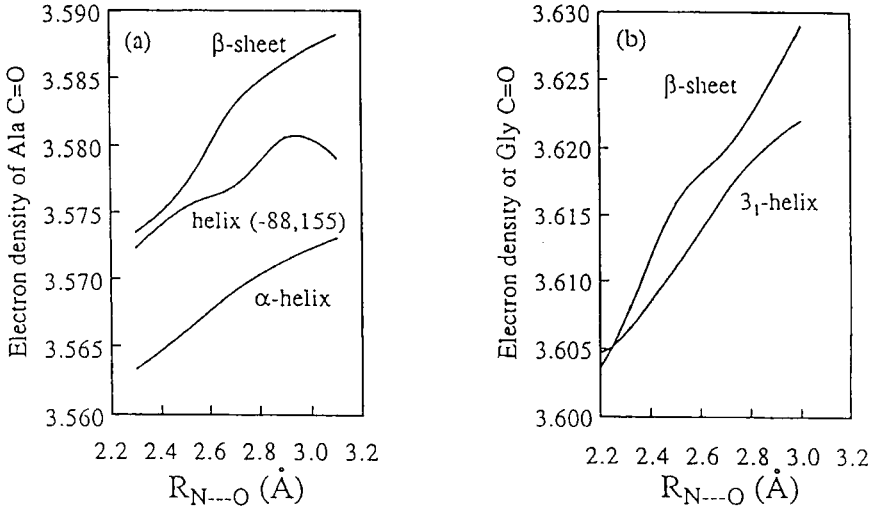

Fig. 9. Variation of the calculated electron density against the N···O separation $R_{N\cdots O}$ for (a) L-Ala carbonyl-carbon and (b) Gly carbonyl-carbon.

Application of Eqs (13)–(16) to determination of the hydrogen-bond length in solid polypeptides

Table 2 shows the values of $R_{N\cdots O}$ for some solid polypeptides, determined using Eqs (13)–(17), from the observation of the amide carbonyl-carbon chemical shift; listed here are solid polyglycine[$(Gly)_n$], poly(L-alanine) [$(L\text{-}Ala)_n$], poly(L-valine) [$(L\text{-}Val)_n$], and poly(L-leucine) [$L\text{-}Leu)_n$] with several conformations such as right-handed α-helix (α_R-helix), β-sheet, 3_1-helix.

In these homopolypeptides, the $R_{N\cdots O}$ values determined for the β-sheet form are constant in the range 3.02–3.07 Å (average 3.04 Å), regardless of amino acid residue species. The $R_{N\cdots O}$ value for the 3_1-helix in $(Gly)_n$ is 2.76 Å; only one result for the 3_1-helix form is available. Although the $R_{N\cdots O}$ values for the α_R-helix form are distributed more widely in the range 2.65–2.82 Å (average 2.76 Å) than for the β-sheet form, the $R_{N\cdots O}$ value for the β-sheet form is much longer than that for α_R-helix and 3_1-helix forms. Further, from the table, it can be seen that the $R_{N\cdots O}$ values of 3.02 Å for the β-sheet form and 2.76 Å for the 3_1-helix form in $(Gly)_n$ are very close to the corresponding $R_{N\cdots O}$ values of 2.95 Å and 2.73 Å, respectively, determined by X-ray diffraction. Also, the $R_{N\cdots O}$ values of 2.78 Å for the α_R-helix form in $(L\text{-}Val)_n$ and of 2.89 Å for the α_R-helix form in $(L\text{-}Ala)_n$ are not far from the $R_{N\cdots O}$ values of 2.89 Å and 2.87 Å, respectively, as determined by X-ray diffraction. According to the X-ray diffraction results on $(L\text{-}Ala)_n$, the $R_{N\cdots O}$ value for the β-sheet

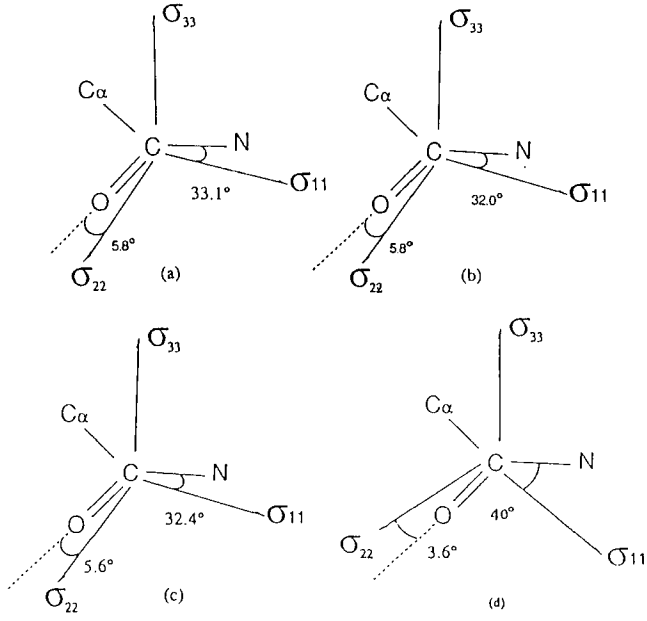

Fig. 10. Orientation of the principal axes of the calculated and observed ^{13}C nuclear shielding tensors for the L-alanine residue carbonyl-carbon: (a) α_R-helix; (b) β_A-sheet; (c) 3_1-helix; (d) [1-^{13}C]Ala-[^{15}N]Ala.

form is smaller by 0.06 Å than that for the α_R-helix form. This shows that only the NMR results for (L-Ala)$_n$ conflict with the X-ray diffraction results. Re-investigation would be needed to determine whether X-ray diffraction for the β-sheet form underestimates the hydrogen-bond length.

Now we are concerned with the $R_{N\cdots O}$ values for a Gly residue incorporated into (L-Ala)$_n$, (L-Leu)$_n$, (L-Val)$_n$, and poly(β-benzyl-L-aspartate) [L-Asp(OBzl)$_n$] as shown in Table 3. From the table, it can be seen that the $R_{N\cdots O}$ value for the α_R-helix form is in the range 2.74–2.82 Å (average 2.78 Å) and that of the β-sheet form is 3.02 Å. The $R_{N\cdots O}$ value for the β-sheet form agrees with that for homopolypeptides as mentioned above. Also, the $R_{N\cdots O}$ values for the α_R-helix are fairly widely distributed; these results are quite similar to those for homopolypeptides. Moreover, the average value is almost the same as that for the homopolypeptides. This indicates that the glycine residue is completely incorporated into the homopolypeptides with the α_R-helix and β-sheet forms. The $R_{N\cdots O}$ value for the ω_L-helix form, for which the dihedral angles (ϕ, ψ) are very close to those of the α_L-helix form, is larger by 0.07 Å than for the α_R-helix. This indicates that the α_R-helical stability is somewhat higher than the ω_L-helical stability.

Table 2. N···O separations for some homopolypeptides obtained using Eqs (13)–(16) and the amide carbonyl ^{13}C chemical shift.

Sample conformation	Amide carbonyl ^{13}C chemical shift δ (ppm)	N···O separation (Å)[a]	(Å)[b]
$(Gly)_n$			
β-sheet	168.5[c]	3.02	2.95[d]
3_1-helix	171.8[c]	2.76	2.73[e]
$(Ala)_n$			
α_R-helix	176.8	2.82	2.87[f]
β-sheet	172.8	3.02	2.83[g]
$(Val)_n$			
α_R-helix	174.9	2.78	2.89[h]
β-sheet	172.8	3.00	
$(Leu)_n$			
α_R-helix	175.7	2.65	
β-sheet	171.5	3.07	

[a]Determination using Eqs (13)–(16) and carbonyl ^{13}C chemical shift.
[b]Determined by X-ray diffraction.
[c]See Ref. 47.
[d]Ref. 51.
[e]Ref. 52.
[f]Ref. 20.
[g]Ref. 53.
[h]Ref. 54.

Verification of hydrogen-bonding structure in proteins: basic pancreatic trypsin inhibitor (BPTI): ribonuclease H from E. coli *(RNaseH)*

Using two- and three-dimensional NMR and the isotopic labelling techniques, Yamazaki and Nagayama have carried out the assignments of backbone carbons of a large protein, ribonuclease H (RNase H) extracted from *E. coli*, which consists of 155 amino acid residues and has a molecular mass of 17.6 kDa.[26] The sample is dissolved in a 0.1 mol/L deuterated acetate buffer of 80% H_2O/20% D_2O (pH 5.5). It is also found that the structure of RNase H determined by NMR agrees with that obtained from the X-ray diffraction study.[27,28] From these results, it is obvious that the main-chain conformation of RNase H in the solution state is quite similar to that of the crystalline RNase H.

^{13}C chemical shifts of the carbonyl-carbons of the L*-Ala residues in RNase H*

Figure 11 shows the plots of the ^{13}C chemical shifts of the L-alanine residue carbonyl-carbons in RNase H against the $R_{N\cdots O}$ values obtained from the X-ray

Table 3. N···O separations for Gly residue incorporated into some polypeptides obtained using Eq. (14) and the amide carbonyl ^{13}C chemical shift.

Sample conformation	Amide carbonyl ^{13}C chemical shift δ (ppm)[a]	N···O separation (Å)
$(Ala, Gly)_n$		
α_R-helix	171.7	2.82
$(Leu, Gly)_n$		
α_R-helix	171.4	2.79
$(Val, Gly)_n$		
β-sheet	168.5	3.02
$(Asp(OBzl), Gly)_n$		
α_R-helix	172.0	2.74
ω_L-helix	171.1	2.81

[a]See Ref. 47.

diffraction study. The solid straight line in Fig. 11 was obtained from Eq. (13). In this figure, there are many data that have large deviations from the solid straight line given by Eq. (13). It is thought that this is not caused by the difference between the secondary structure in the solid state and that in aqueous solution, but by the lack of accuracy of $R_{N\cdots O}$ as determined by X-ray diffraction. Since structural analysis of proteins by X-ray diffraction gives covalent bond lengths to an accuracy of 10^{-2} Å, the main-chain dihedral angles can be determined to sufficient accuracy.[28] In the case of a small protein such as BPTI, the hydrogen-bond length can be determined accurately.[29,30] Therefore, the result for the carbonyl-carbon of alanine-48 (A48) in BPTI lies on the solid straight line as shown in Fig. 11. However, through-space internuclear distances such as the hydrogen-bond lengths in large proteins (such as RNaseH) determined by X-ray diffraction might include a large experimental error (about 0.3 Å), which results in accumulated errors for the main-chain dihedral angles.[28] This means that for the structural elucidation of large proteins it is useful to utilize the chemical shift of the carbonyl-carbon as a fingerprint of hydrogen-bond length.

3.2. Hydrogen-bonded structure and ^{13}C NMR chemical shift tensor of amino acid residue carbonyl-carbons of peptides and polypeptides

Kameda *et al.*[48] have studied hydrogen-bonding effects on the principal values of the ^{13}C chemical shift tensor for Gly, Val, Leu and Asp residue carbonyl-carbons of peptides and polypeptides in the crystalline state and have

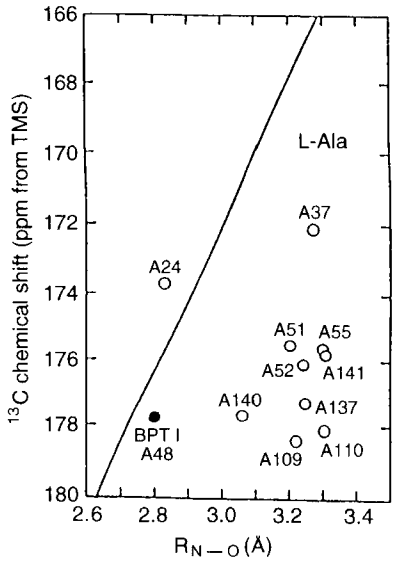

Fig. 11. Plots of the observed chemical shifts of the L-alanine residue carbonyl-carbons in RNaseH and BPTI in the aqueous solution against ($R_{N\cdots O}$). The straight line is the correlation between the observed ^{13}C chemical shifts of the L-alanine residue carbonyl-carbons in some peptides in the solid state and their $R_{N\cdots O}$ values reported previously.

elucidated the relationship between the tensor components and hydrogen-bond length. The ^{13}C shielding of the amino acid residue carbonyl-carbon of a peptide model compound is calculated by finite perturbation theory (FPT)[8,48–50] within the INDO framework.

Correlation between the hydrogen-bond length and ^{13}C chemical shift tensor components of Gly, Val, Leu and Asp residue carbonyl-carbons

A typical 67.8 MHz ^{13}C CP-MAS spectrum of poly(Gly) with 3_1-helix form at the spinning rate of 1.75 kHz is shown in Fig. 12. The other remaining samples give similar sideband spectra. The determined δ_{11}, δ_{22} and δ_{33} components of the poly(Gly) with the 3_1-helix form are 247, 182 and 91 ppm, respectively. The experimental errors in δ_{11}, δ_{22} and δ_{33} are $<$1.7 ppm, $<$0.7 ppm, and $<$1.7 ppm, respectively. The tensor components of the other samples are determined in the same manner. The determined isotropic ^{13}C chemical shifts and tensor components for Gly, Val, Leu and Asp residue carbonyl carbons in oligopeptides are listed in Table 4, together with the $R_{N\cdots O}$ values determined by X-ray diffraction, in addition to those of the Ala residue as reported previously by Asakawa *et al.*[44] It has been reported that δ_{11} is in the amide sp^2 plane and lies along the direction normal to the C=O bond; the δ_{22} component lies almost

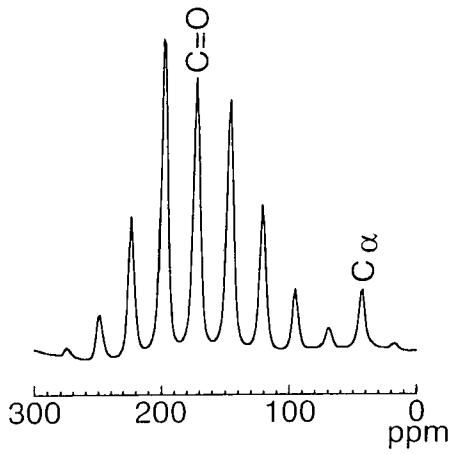

Fig. 12. A 67.8 MHz ^{13}C CP-MAS NMR spectrum of polyglycine with 3_1-helix form in the solid state. The magic angle spinning rate is 1.75 kHz.

along the amide C=O bond; and the δ_{33} component is aligned perpendicularly to the amide sp^2 plane.[55]

Figure 13 shows plots of the ^{13}C chemical shift tensor components (δ_{11}, δ_{22} and δ_{33}) against $R_{N\cdots O}$ for Gly, Ala, Val, Leu and Asp residues. The δ_{22} value for Gly, Leu and Ala residues moves linearly to high frequencies with a decrease in $R_{N\cdots O}$.[44] The slope and intercept of the variation of the plot of δ_{22} against $R_{N\cdots O}$ vary depending on the amino acid residue. The slope of the variation of δ_{22} against $R_{N\cdots O}$ for the Ala residues in peptides is larger than those for the other amino acid residues. This shows that the value of δ_{22} for the Ala residue is more sensitive to a change in $R_{N\cdots O}$ than for the other amino acid residues. The expression for the relationship determined by the least mean squares method for oligopeptides containing a Gly residue is

$$\delta_{22} = 262.9 - 30.2R_{N\cdots O}\ (\text{Å}) \tag{18}$$

where δ_{22} and $R_{N\cdots O}$ are in ppm and Å, respectively. This relationship indicates that $R_{N\cdots O}$ can be determined through the observation of δ_{22} for the carbonyl carbon of the Gly residue in oligopeptides within an error of <0.7 ppm. It should be noted that the Gly C=O carbon chemical shifts for poly(Gly) with the β-sheet form and the 3_1-helix form are located on a straight line as expressed by Eq. (14). This shows that this relationship can be applied to polypeptides. Next, we are concerned with values of δ_{11} and δ_{33}. As seen from Fig. 14, the experimental data for δ_{11} and δ_{33} of the Gly, Ala and Leu residues scatter widely. The δ_{11} and δ_{33} values are insensitive to changes in $R_{N\cdots O}$, but it seems that δ_{11} and δ_{33} move slightly to low and high frequencies, respectively,

Table 4. Observed isotropic ^{13}C chemical shifts and tensor components of the Gly, L-Val, L-Leu, L-Asp and L-Ala residues in peptides and polypeptides, and the N···O separations determined by X-ray diffraction.

	Carbonyl ^{13}C chemical shift (ppm)					N···O separation (Å)	
Sample[a]	δ_{iso}	δ_{11}	δ_{22}	δ_{33}	$\delta_{11} + \delta_{33}$	$R_{N\cdots O}$[b]	Reference
Gly residue							
Gly*-Gly	168.1	242	174	88	331	2.97	75
Cl Ac-Gly*-Gly	170.1	244	176	91	335	2.82	105
Ala-Gly*-Gly	170.6	240	177	94	334	2.93	106
Val-Gly*-Gly	169.2	245	170	93	338	3.05	78
Gly*-Gly·HNO_3	168.3	248	168	89	337	3.12	77
Poly(Gly) β-sheet	169.6	245	173	91	336	2.91	51
Poly(Gly) 3_1-helix	173.2	247	182	91	338	2.73	52
Poly(Ala, Gly*) α-helix	173.0	243	181	95	338	–	–
Poly(Ala, Gly*) β-sheet	168.8	241	171	95	336	–	–
Poly(Leu, Gly*) α-helix	172.8	241	180	97	338	–	–
Poly(Val, Gly*) β-sheet	169.6	240	169	99	340	–	–
Val residue							
Val*-Gly-Gly	169.2	245	170	93	338	3.05	78
Leu residue							
Boc-Pro-ILe*-Gly	173.0	249	183	88	336	2.83	107
DL-Leu*-Gly-Gly	172.0	246	178	92	338	3.06	108
Asp residue							
Asp*-Gly	170.3	242	175	93	336	2.98	109
Ala residue							
Ac-Ala*-NHMe	177.0	241	196	94	335	2.72	15
	175.9	245	189	96	341	2.92	
Poly(Ala) α-helix	176.8	243	194	94	337	2.87	20
Ala*-Gly-Gly	172.6	245	179	93	338	3.00	17
Ala*-Ser	170.1	249	172	89	338	3.04	18

[a]Amide carbonyl ^{13}C chemical shifts for the asterisk-marked amino acid residues were measured.
[b]Amide–amide hydrogen-bond length (Å) between nitrogen and oxygen atoms in a hydrogen bond.

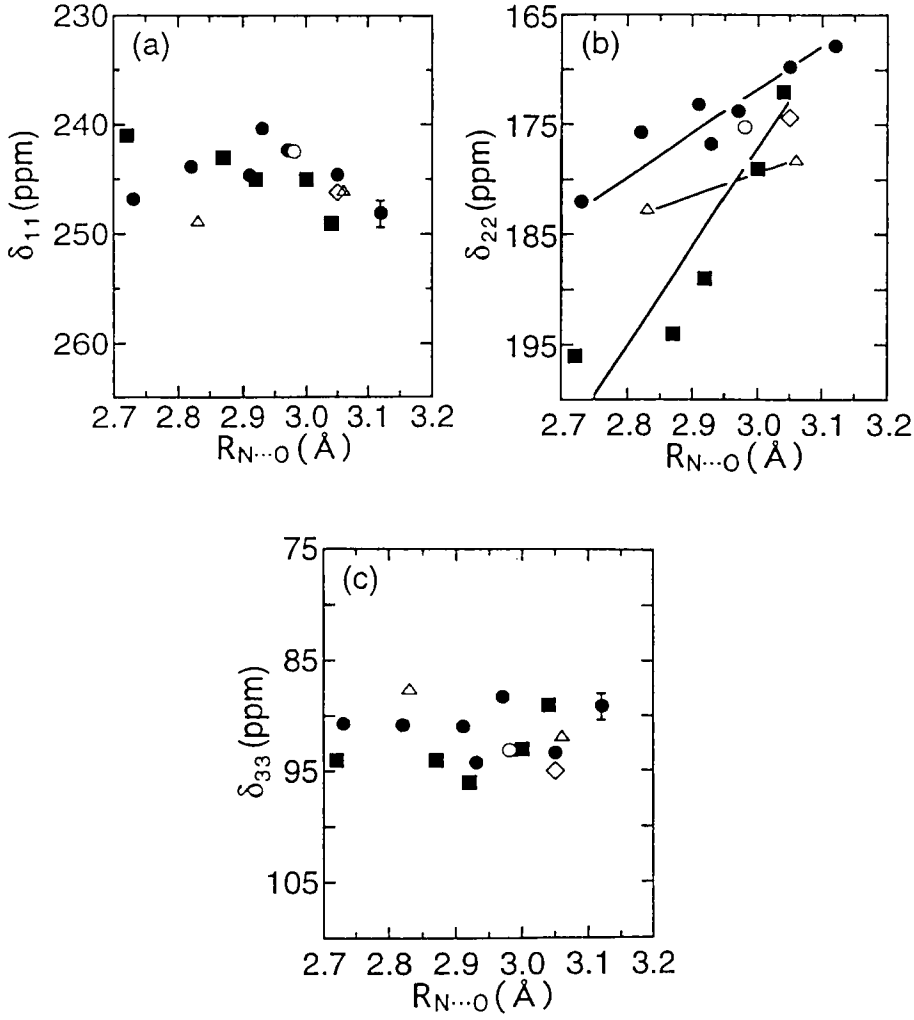

Fig. 13. Plots of the observed ^{13}C chemical shift tensor components for (a) δ_{11}, (b) δ_{22} and (c) δ_{33} for the amide carbonyl-carbons in the Gly (●), Ala (■), Val (◇), Leu (△) and Asp (○) residues in peptides against the N···O separation ($R_{N\cdots O}$). The experimental errors of δ_{11} and δ_{33} are indicated by error bars.

with a decrease in $R_{N\cdots O}$. In order to clarify the relation between δ_{11} and δ_{33}, δ_{33} is plotted against δ_{11} as shown in Fig. 14. The slope of the linear relationship between the δ_{11} and δ_{33} values is about -1. When δ_{11} moves to high frequencies, δ_{33} moves to low frequencies by the same magnitude. Therefore, the sum of δ_{11} and δ_{33} is almost constant (337.5 ± 3.5 ppm) and is independent of the amino acid residue, except for Gly-Gly. This leads to the experimental finding that

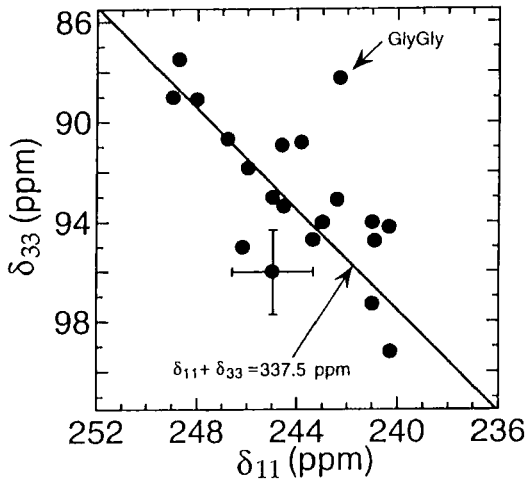

Fig. 14. Plots of the observed δ_{33} against δ_{11} for various peptides. The experimental errors of δ_{11} and δ_{33} are indicated by error bars. The slope of the line is expressed by $\delta_{11} + \delta_{33} = 337.5$ ppm.

there is a linear relationship between δ_{iso} and δ_{22} as expressed by Eq. (19):

$$\delta_{iso} = \tfrac{1}{3}\delta_{22} + 112.5 \text{ ppm} \qquad \text{(relative to TMS)} \qquad (19)$$

Therefore, it can be said that the large high-frequency shift in δ_{iso}, with a decrease in $R_{N\cdots O}$, is predominantly governed by the decrease in δ_{22}. Similar relationships have been reported by Oas *et al.* for peptides containing the Gly amino acid residue.[56]

Application of Eq. (18) to the determination of the hydrogen-bond length in Gly-containing polypeptides

Here we are concerned with the application of Eqs (13) and (18) to the determination of the $R_{N\cdots O}$ value for the guest Gly residue incorporated into host copolypeptides. As reported previously, it is determined from the reference data of poly(Ala) with the α_R-helix form that the Ala residue in poly(Ala, Gly*) takes the α_R-helix form.[57–59] However, we still have the problem of whether the guest Gly residue incorporated into host polypeptides takes the same conformation as the host amino acid residues. The $R_{N\cdots O}$ values of the guest Gly residue in some host polypeptides determined using Eq. (18) from the observation of the δ_{22} values of Gly residues are listed in Table 5, together with the $R_{N\cdots O}$ values determined using Eqs (13)–(16) through the observation of the value of δ_{iso} as reported by Tsuchiya *et al.*[45]

The ^{13}C chemical shift tensor component δ_{22} for the Gly residue leads to the

Table 5. N···O separations for some polypeptides and copolypeptides incorporating Gly residues determined using Eqs. (13)–(18) through observation of the ^{13}C chemical shift tensor component δ_{22} and the isotropic chemical shift.

Sample	Conformation	N···O separation (Å)				
		$R^{I}_{N\cdots O}$[a]	$R^{II}_{N\cdots O}$[b]	$R^{III}_{N\cdots O}$[c]	$R^{IV}_{N\cdots O}$[d]	$R^{V}_{N\cdots O}$[e]
Poly(Leu)	α-helix	–	–	2.7		
Poly(Leu, Gly*)	α-helix	2.7	2.8	–		
Poly(Val)	β-sheet	–	–		3.0	
Poly(Val, Gly*)	β-sheet	3.1	3.0		–	
Poly(Ala)	α-helix	–	–			2.8
Poly(Ala, Gly*)	α-helix	2.7	2.8			–
Poly(Ala)	β-sheet	–	–			3.0
Poly(Ala, Gly*)	β-sheet	3.0	3.1			–

[a]Determined using Eq. (18) and ^{13}C chemical shift tensor component δ_{22} for the Gly residue in copolypeptides.
[b]Determined using Eq. (14) and isotropic ^{13}C chemical shift for the Gly residue.
[c]Determined using Eq. (16) and isotropic ^{13}C chemical shift for the Leu residue.
[d]Determined using Eq. (15) and isotropic ^{13}C chemical shift for the Val residue.
[e]Determined using Eq. (13) and isotropic ^{13}C chemical shift for the Ala residue.

result that the hydrogen-bond lengths of the guest Gly residue ($R^{I}_{N\cdots O}$) in poly(Leu, Gly*) and poly(Ala, Gly*), of which the host Leu and Ala residues take the α_R-helix form, are 2.7 Å as estimated by using Eq. (18). This value is in agreement with the values for the lengths of 2.7 and 2.8 Å for the host Leu and Ala residues $R^{III}_{N\cdots O}$ and $R^{V}_{N\cdots O}$ respectively, determined using Eqs (13) and (16) through the observation of the δ_{iso} for Leu and Ala residues in homopoly(Leu) and poly(Ala), respectively, with the α_R-helix form. Moreover, the $R^{I}_{N\cdots O}$ values of the guest Gly residue in poly(Leu, Gly*) and poly(Ala, Gly*) are very close to the value of 2.8 Å for the guest Gly residue ($R^{II}_{N\cdots O}$) determined using Eq. (14) through the observation of the δ_{iso} value for the Gly residue in poly(Leu, Gly*) and poly(Ala, Gly*). This indicates that the guest Gly residue is completely incorporated into host polypeptides with the α_R-helix form. In the case of poly(Val, Gly*) and poly(Ala, Gly*) with the β-sheet form, similar results are obtained. It can therefore be concluded that the guest Gly residue is completely incorporated into the host polypeptides with β-sheet form. These results indicate that the hydrogen-bond length for the host residue in copolypeptides and proteins can be determined through the observation of δ_{22} for the Gly residue in addition to the method using δ_{iso}.

^{13}C shielding calculation on a hydrogen-bonded peptide model compound

FPT-INDO calculations on ^{13}C shielding tensors of some model peptides have been carried out to shed light on the relationships obtained between the tensor

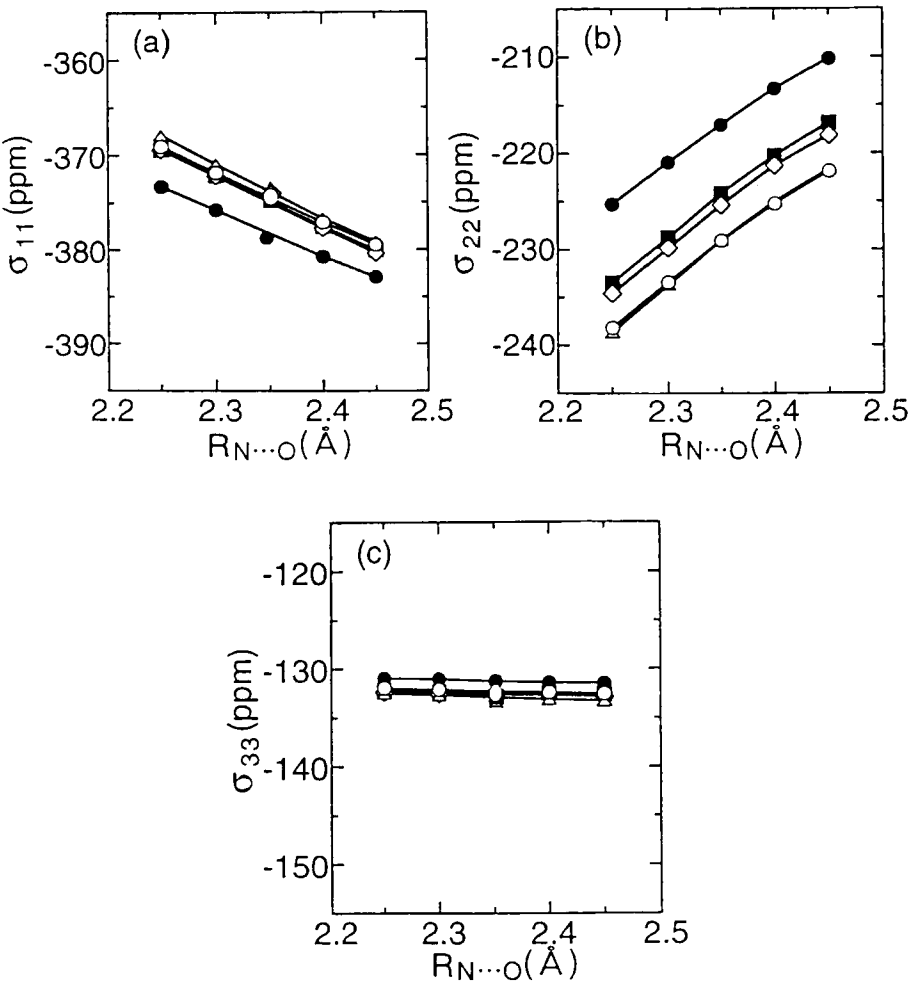

Fig. 15. Plots of the calculated ^{13}C nuclear shielding tensor components (a) σ_{11}, (b) σ_{22} and (c) σ_{33} for amide carbonyl-carbon in Gly (●), Ala (■), Val (◇), Leu (△) and Asp (○) residues in peptide model compounds against the N···O separation ($R_{N\cdots O}$).

components and hydrogen-bond length. Figure 15 shows the $R_{N\cdots O}$ dependence of the calculated values of σ_{11}, σ_{22} and σ_{33} for the Gly, Ala, Val, Leu and Asp carbonyl-carbons. The negative sign for the calculated shielding constant denotes deshielding, which corresponds to a positive sign for the chemical shift change.

It is known that for the semi-empirical INDO MO approximation adopted the intermolecular interactions are well reproduced in the region of small

$R_{N\cdots O}$ values.[24] Therefore, in the calculation, the total energy minimum appears around the $R_{N\cdots O}$ value of 2.3–2.5 Å as shown in Fig. 8. For this reason, the experiment is compared with the results of the calculations in the region of small $R_{N\cdots O}$ values. From this figure, it is found that σ_{22} is the most sensitive to a change of $R_{N\cdots O}$ and moves linearly to high frequencies with a decrease in $R_{N\cdots O}$. Correspondingly σ_{11} moves increases with a decrease of $R_{N\cdots O}$, whereas σ_{33} is insensitive to changes in $R_{N\cdots O}$. The results of the theoretical calculations agree well with the experimental results. Such agreement indicates that the ^{13}C chemical shift changes originate predominantly from the change of the electronic state of the amino carbonyl groups caused by the hydrogen-bond length variation. Further, the amino acid residue dependence of the calculated tensor components is similar to the experimental one.

3.3. Hydrogen-bonded structure and ^{15}N NMR chemical shift for the amide nitrogen in glycine-containing peptides

High-resolution ^{15}N NMR spectroscopy has been applied increasingly to the investigation of peptides, polypeptides and proteins in the solid state.[62–73] Shoji *et al.*[74] have demonstrated that the isotropic ^{15}N chemical shifts of a number of homopolypeptides in the solid state, as determined by the cross polarization–magic angle spinning (CP-MAS) NMR method, are significantly displaced by as much as 1.2–10.0 ppm, according to their particular conformation, such as the α-helix and β-sheet forms.[74] Such a large chemical shift difference may come from changes in the hydrogen-bond length and angle and through a change in the dihedral angles (θ, ϕ).

^{15}N NMR chemical shifts of the glycine amide nitrogen of peptides in the solid state

The ^{15}N chemical shift values of the glycine residues of some oligopeptides are tabulated in Table 6, together with geometrical parameters obtained by X-ray diffraction studies. $^{15}NH_4NO_3$ is conventionally used as standard reference.[83] Some of the geometrical parameters were calculated by using the unit cell parameters and fractional coordinates given in the literature.[75–83] The ^{15}N chemical shifts and the geometrical parameters of t-butyloxycarbonyl-glycylglycylglycine benzyl ester (Boc-Gly-Gly-Gly-OBzl) are inferred from the results of Hiyama *et al.*[83] Figure 16 shows the plot of the observed ^{15}N chemical shifts of Gly NH against the N···O separation ($R_{N\cdots O}$). However, it is found that there is no clear relationship between $R_{N\cdots O}$ and ^{15}N chemical shifts. This is different from the case of ^{13}C chemical shifts of the carbonyl-carbons associated with the hydrogen bond reported previously,[14,15] where the ^{13}C signals of the carbonyl carbons are linearly deshielded with a decrease in $R_{N\cdots O}$.

Table 6. ^{15}N chemical shift of glycine residue amide nitrogens for oligopeptides containing a glycine residue as determined by ^{15}N CP/MAS NMR (from $^{15}NH_4NO_3$) and the geometrical parameters of the glycine residue amide nitrogen of GlyGly* peptides.

Sample	^{15}N chemical shift,[c] δ (ppm)	Dihedral angle (°)		Hydrogen bond length and angle				Reference
		ϕ	ψ	N···O length (Å)	H···O length (Å)	N—H length (Å)	N—H···O angle (°)	
Gly-Gly*	95.3	157.1	10.7	2.94	1.97	1.02	158	75
Gly-Gly*·HNO_3	89.4	165.6	176.9	3.12	2.38	0.76	165	76
Gly-Gly*·H_2O·HCl	91.0	−79.6	3.8	3.30[a]	2.30	0.79	162	77
Ala-Gly-Gly*	88.3	170.9	175.2	3.00	2.19	0.84	160	78
Val-Gly-Gly*	94.4	−146.6	−4.3	3.05	2.19	0.93	152	79
Pro-Gly-Gly*	89.4	−110.5	175.1	2.89	2.07	0.85	165	80
Sar-Gly-Gly*	89.0	−85.4	−177.5	3.06	2.23	0.85	167	81
Tyr-Gly-Gly*	92.3	−103.9	−152.6	2.88	2.13	0.86	144	82
Boc-Gly-Gly-Gly*-OBzl	92.8[b]	−77.8	−178.4	2.92	2.10	0.92	157	83

[a]The glycine residue participates in H···Cl type of hydrogen bond.
[b]This value is converted to the $^{15}NH_4NO_3$ aq. reference from Ref. 83.
[c]For amide nitrogen of Gly residue marked by *.

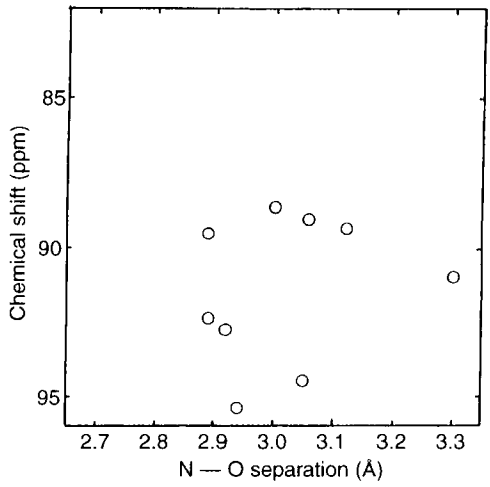

Fig. 16. Plots of the observed ^{15}N chemical shift of oligopeptides in the solid state against the N···O separation ($R_{N\cdots O}$).

Figure 17 shows the plot of the observed ^{15}N chemical shifts of the glycine residue in X-Gly-Gly against the N—H bond length (R_{N-H}) associated with a hydrogen bond. It is found that there is a clear relationship between these parameters and the decrease of R_{N-H} leads to a linear increase in shielding. The expression for this relationship is

$$\delta_{iso} = 57.73 + 39.32R_{N-H}\ (\text{Å}) \tag{20}$$

Such a trend is very different from that obtained from the corresponding ^{13}C NMR study. Amide ^{15}N chemical shifts are closely related to the length of the N—H bond but are not related to the N···O separation. This implies that the ^{15}N chemical shift value gives useful information about the length of the N—H hydrogen bond. It seems that the hydrogen bond angle ($\angle$N—H···O) is also related to the ^{15}N chemical shift.

The structure of the two hydrogen-bonded *N*-methyl acetamides used as a model system is shown in Fig. 18. First, the geometrical parameters of an *N*-methyl acetamide molecule were optimized using the *ab initio* STO-3G MO method. Next, for two hydrogen-bonded *N*-methyl acetamides, the bond length N—H is optimized as a function of the N···O separation. Figure 19 shows the relationship between the minimized bond length N—H or the total energy and the N···O separation as determined by *ab initio* MO calculations. It is shown that at $R_{N\cdots O} < 2.97$ Å, an increase of $R_{N\cdots O}$ leads to a decrease of R_{N-H}. However, at $R_{N\cdots O} > 2.97$ Å, an increase of $R_{N\cdots O}$ leads to a decrease of R_{N-H}. In the model used in this work, the $R_{N\cdots O}$ values are between 2.85 and

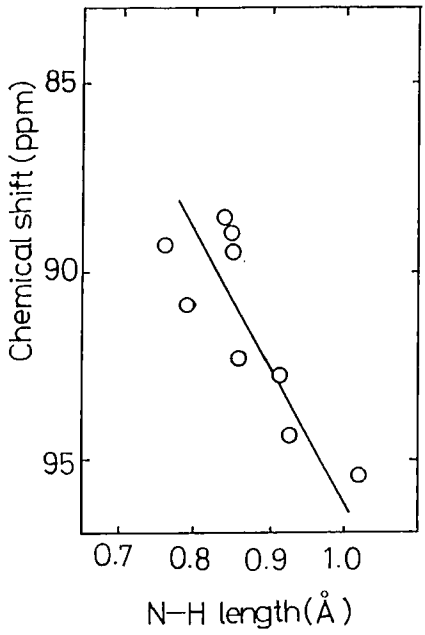

Fig. 17. Plots of the observed ^{15}N chemical shift of oligopeptides in the solid state against the N—H bond length (R_{N-H}).

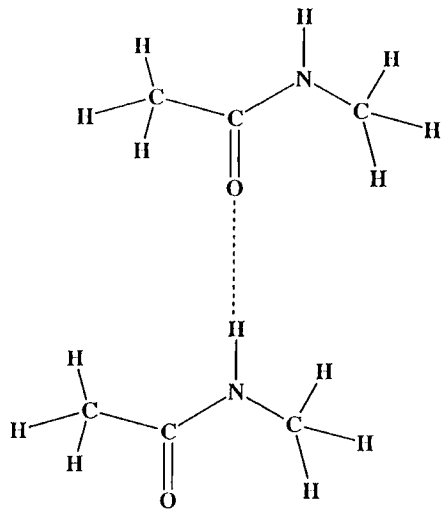

Fig. 18. Molecular structure of the two hydrogen-bonded *N*-methylacetamides used as model compounds for STO-3G MO calculation.

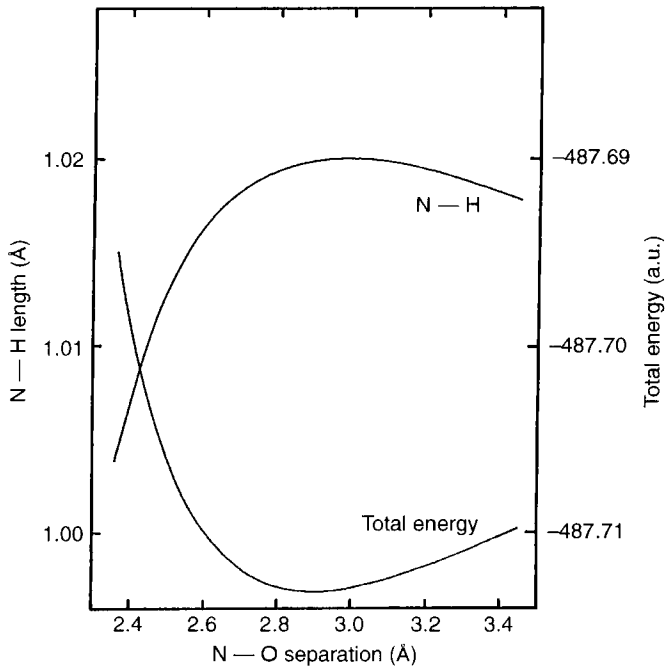

Fig. 19. Plots of the calculated NH bond length (R_{N-H}) and total energy against the separation ($R_{N\cdots O}$).

3.30 Å. Therefore, it can be concluded that the R_{N-H} values decrease with an increase of $R_{N\cdots O}$. This is in agreement with neutron diffraction studies (Fig. 20).[84]

From the above results there is an apparent relationship between the hydrogen-bond length $R_{N\cdots O}$ and the bond length R_{N-H}.

^{15}N shielding calculation

Figures 21 and 22 show as a function of N—H separation the calculated isotropic shielding (σ_{iso}) and the paramagnetic terms of the tensor components ($\sigma_{11}, \sigma_{22}, \sigma_{33}$, from high to low frequencies) of Gly obtained for the model compound *N*-acetyl-*N'*-methylglycineamide. The calculated values are all expressed in ppm and opposite in sign to the chemical shift data given in Table 6. Note that the negative sign for the calculated shielding denotes deshielding, which corresponds to a positive sign for the change in chemical shift values. A shielding value, or tensor component, is usually represented as the sum of diamagnetic and paramagnetic terms. However, the anisotropic behaviour of the shielding tensor can be explained predominantly by the paramagnetic term, since the diamagnetic term is isotropic.

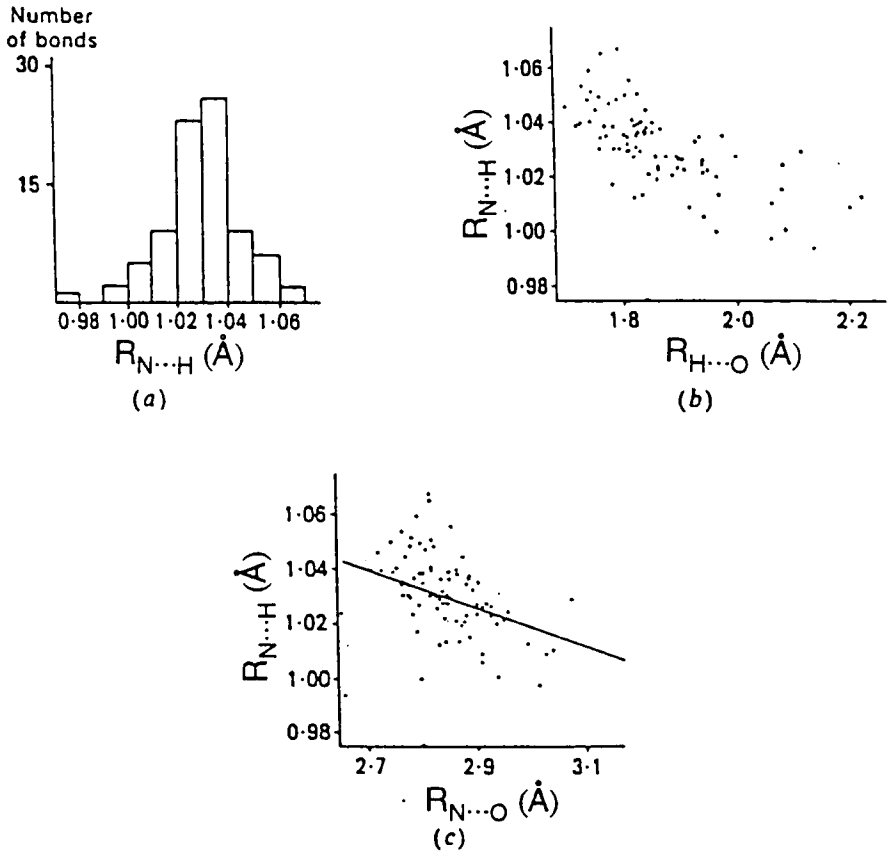

Fig. 20. (a) Distribution of R_{N-H} for the 83 bonds determined by neutron diffraction. (b) Scatterplot of R_{N-H} against $R_{H\cdots O}$. (c) Scatterplot of R_{N-H} against $R_{N\cdots O}$; the least-squares regression line is also shown (Ref. 84).

From Fig. 21 it is seen that a decrease of R_{N-H} leads to very large increase of σ_{iso}; for example, a decrease of 0.4 Å in R_{N-H} leads to a shielding increase of about 30 ppm. This agrees with the observed results. This implies that the observed shielding increase is a consequence of the changes in the electronic state expressed through a decrease of the N—H bond length. Figure 22 shows that a decrease of R_{N-H} leads to an increase in σ_{11}, σ_{22} and σ_{33}. The magnitudes for changes of the principal values of the shielding occur in the order $\sigma_{22} > \sigma_{33} > \sigma_{11}$. The direction of the principal axes of the Gly NH ^{15}N shielding tensor components, as determined by an NMR study of a Boc-Gly-Gly-Gly-OBzl single crystal,[83] are shown in Fig. 23.

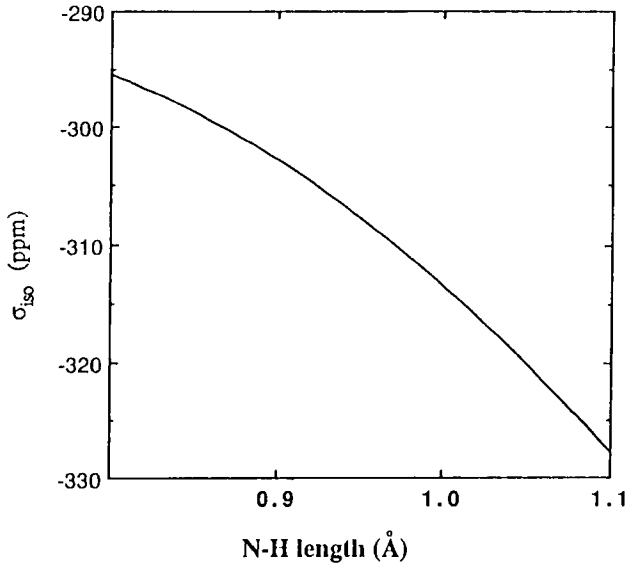

Fig. 21. Plots of the calculated ^{15}N isotropic shielding against the N—H bond length (R_{N-H}) from the FPT-INDO method.

The σ_{11} component lies approximately along the N—H bond, and the σ_{33} component lies aproximately along the N—C′ bond. The σ_{22} component is aligned in the direction perpendicular to the peptide plane. From this, it can be inferred that the σ_{22} and σ_{33} components, rather than the σ_{11} component, are sensitive to R_{N-H} changes. This is due to the fact that the σ_{22} component lies approximately along the direction of the nitrogen lone-pair electrons and the electron density is very high in this direction. The σ_{33} component lies approximately along the N—C′ bond into which lone-pair electrons of the nitrogen atom transfer, and so the bond order becomes very high. Consequently, the σ_{22} and σ_{33} components are sensitive to changes in R_{N-H}.

^{15}N NMR chemical shifts of the glycine residue of BocGly peptides in the solid state

All of the isotropic ^{15}N chemical shift values (σ_{iso}) and the principal values of the ^{15}N chemical shift tensors σ_{11}, σ_{22} and σ_{33} are tabulated in Table 7. The geometrical parameters obtained by X-ray diffraction studies[85–89] are given in Table 8, where some of the geometrical parameters are estimated by using the unit-cell parameters and fractional coordinates given in the literature. The values of $R_{N\cdots O}$ for the peptides used in this work are in the range from 2.95 to 3.08 Å. However, the hydrogen bond angles $\angle C{=}O\cdots N$ are in the range from 113° to 155°. Figure 24 shows the plot of the observed isotropic ^{15}N nuclear

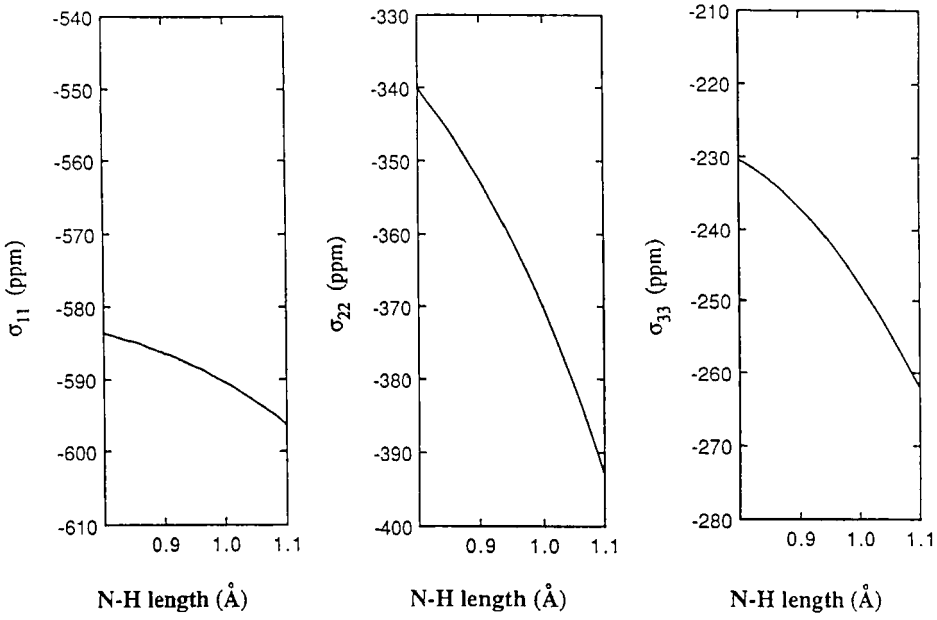

Fig. 22. Plots of the calculated ^{15}N shielding tensor components against the N—H bond length (R_{N-H}) from the FPT-INDO method.

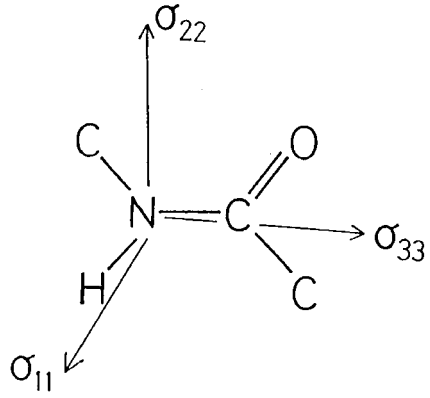

Fig. 23. Orientation of the principal axes of the ^{15}N shielding tensors of the glycine residue amide nitrogen as determined in the literature.

Table 7. Observed ^{15}N isotropic chemical shifts and nuclear shielding tensor components of glycine amide nitrogen of Boc-Gly* peptides (ppm from $^{15}NH_4NO_3$ aq.).

Sample	δ_{iso}	δ_{11}	δ_{22}	δ_{33}
Boc-Gly	59.75	127.0	51.2	1.1
Boc-Gly-Ala	61.61	121.5	52.2	11.1
Boc-Gly-Phe	54.04	112.7	56.1	−6.7
Boc-Gly-Aib[a]	57.70	127.0	49.1	−3.0
Boc-Gly-Pro-OBzl	53.06	117.2	50.6	−8.6

[a]Aib: aminoisobutyric acid.

shieldings (δ_{iso}) of Gly NH against the value of $R_{N\cdots O}$. It is found that there is a clear relationship between δ_{iso} and $R_{N\cdots O}$, and a decrease of $R_{N\cdots O}$ leads to a decrease in shielding. This trend is similar to that found for the carbonyl ^{13}C nuclear shielding and $R_{N\cdots O}$. Figures 25a–c show the plots of the observed principal values (δ_{11}, δ_{22} and δ_{33}) of the ^{15}N nuclear shielding tensor of Gly NH against $R_{N\cdots O}$. It is found that δ_{11} and δ_{33} are more sensitive than δ_{22} to changes in $R_{N\cdots O}$. A change of 0.2 Å in $R_{N\cdots O}$ leads to a change of 20 ppm in δ_{11} and δ_{33}, although the change in δ_{22} is 5 ppm. However, only δ_{33} decreases linearly with decrease of $R_{N\cdots O}$; for δ_{11} and δ_{22} there is no clear relationship with $R_{N\cdots O}$. These results show that such behaviour is governed not only by the hydrogen-bond length, but also by the hydrogen bond angle.

Theoretical calculation of ^{15}N shielding

To obtain a deeper understanding between the experimental finding that the isotropic ^{15}N chemical shift and the principal value of σ_{33} depend upon the hydrogen-bond length, theoretical calculations of ^{15}N chemical shifts have been carried out by the FPT-INDO method. Figures 26 and 27a–c show, respectively, the calculated isotropic ^{15}N shielding (σ_{iso}) and the paramagnetic terms of the shielding tensor components (σ_{11}, σ_{22} and σ_{33}) of Gly NH in the model compound. The calculated values are all expressed in ppm with sign opposite to that of the experimental chemical shift values shown in Table 7.

As shown in Fig. 26, a decrease of $R_{N\cdots O}$ leads to a decrease of σ_{iso}. This agrees with the experimental results. Such a relationship suggests that the isotropic ^{15}N chemical shift value can be used in the estimation of $R_{N\cdots O}$. This is similar to the case of the carbonyl ^{13}C chemical shift reported previously.

Figures 27a–c show the $R_{N\cdots O}$ dependence of the calculated principal values of ^{15}N nuclear shielding tensor (σ_{11}, σ_{22} and σ_{33}). It is shown that a decrease of $R_{N\cdots O}$ leads to decrease of σ_{11}, σ_{22} and σ_{33}. The magnitudes for changes of the shielding are in the order $\sigma_{11} > \sigma_{33} > \sigma_{22}$. Such an order for shielding changes agrees with the observed order. Further, a linear decrease of σ_{33} with a decrease of $R_{N\cdots O}$ agrees with observation. However, experimentally there

Table 8. The geometrical parameters of the glycine residue amide nitrogen of Boc-Gly peptides.

Sample	Dihedral angle (°)			Hydrogen bond length and angle				Reference
	ω	ϕ	ψ	N···O length (Å)	H···O length (Å)	N–H···O angle (°)	N–O=C angle (°)	
Boc-Gly	174.0	−61.5	−15.1	3.01	–	–	113.1	85
Boc-Gly-Ala	178.8	−125.6	45.0	2.95	2.02	161.1	–	86
Boc-Gly-Phe	−176.9	−88.0	−14.5	3.08	–	–	155.4	87
Boc-Gly-Aib[a]	−159.4	89.5	165.1	3.08	–	–	116.4	88
Boc-Gly-Pro-OBzl	172.2	−109.5	164.4	3.01	2.24	163.4	136.7	89

[a]Aib: aminoisobutyric acid.

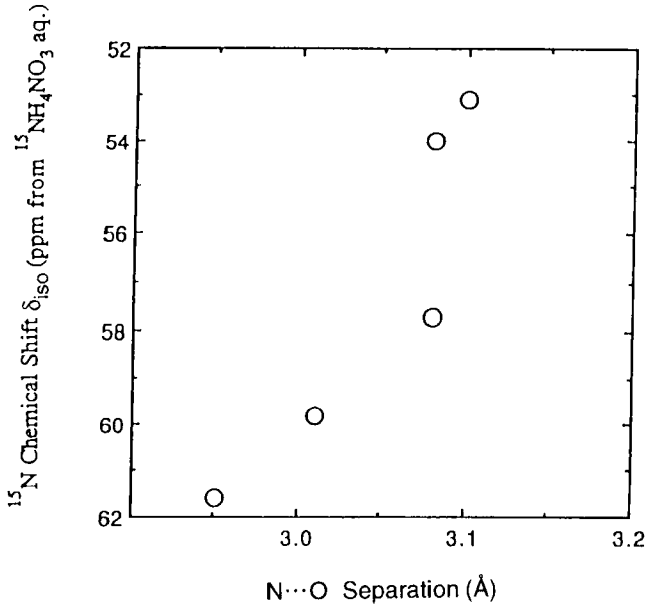

Fig. 24. Plots of the observed isotropic ^{15}N chemical shifts (δ_{iso}) in the solid state against the N···O separation ($R_{N\cdots O}$).

is no relationship between $R_{N\cdots O}$ and σ_{11} or σ_{22}, but in the calculation there is a relationship. Where does this discrepancy come from? In the above calculation, only the hydrogen-bond length is taken into account. For more complete understanding of hydrogen-bonding, another important factor such as the hydrogen-bond angle (that is the distortion from the linearity of the hydrogen bond) should be taken into account. For this reason, the ^{15}N chemical shift was calculated as a function of the hydrogen bond angle ($\angle$N—H···O) using the model compound given in Fig. 28. The H···O length is fixed at 1.75 Å and the hydrogen bond angle ($\angle$N—H···O) is varied.

Figures 29 and 30a–c show, respectively, the plots of σ_{iso}, and σ_{11}, σ_{22} and σ_{33} against the angle θ. From Fig. 29 it is apparent that a change of the angle θ from 140° to 220° leads to change of 5 ppm in σ_{iso} compared with the value of about 20 ppm induced by a change of $R_{N\cdots O}$ from 2.4 to 3.2 Å. Hence the angular dependence is not as sensitive as the distance dependence.

From Fig. 30 we see that the magnitudes of changes in σ_{11} and σ_{22} are about 10 and 4 ppm, respectively, in going from $\theta = 140°$ to 220°. In contrast, σ_{11} and σ_{22} change by about 30 and 4 ppm, respectively, as $R_{N\cdots O}$ change from 2.4 to 3.2 Å. The magnitude of change in σ_{33} is about 1 ppm in going from $\theta = 140°$ to 220° and about 15 ppm as $R_{N\cdots O}$ among from 2.4 to 3.2 Å. Thus, σ_{11} and σ_{22} are relatively sensitive to a change in θ, but σ_{33} is relatively insensitive to

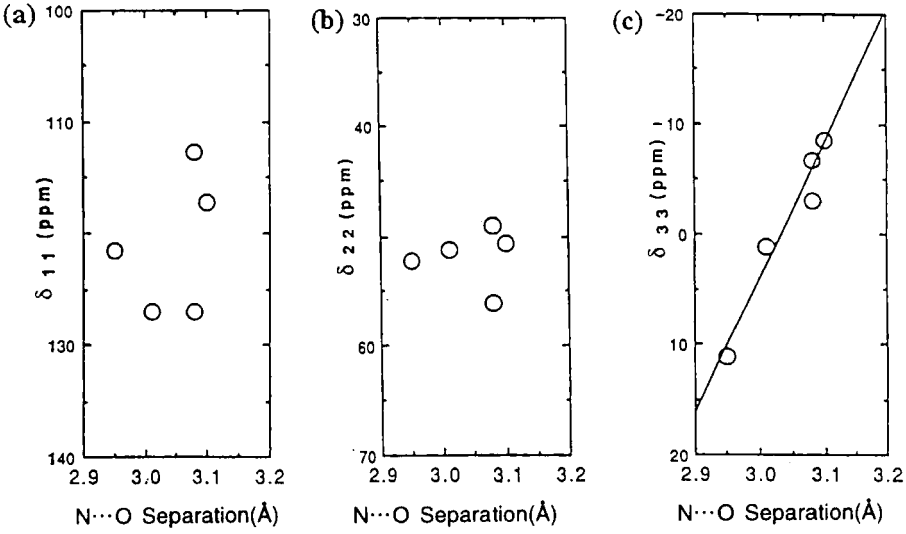

Fig. 25. Plots of the observed principal values of the ^{15}N nuclear shielding tensor (a) δ_{11}, (b) δ_{22} and (c) δ_{33}, in the solid state against the N···O separation ($R_{N\cdots O}$).

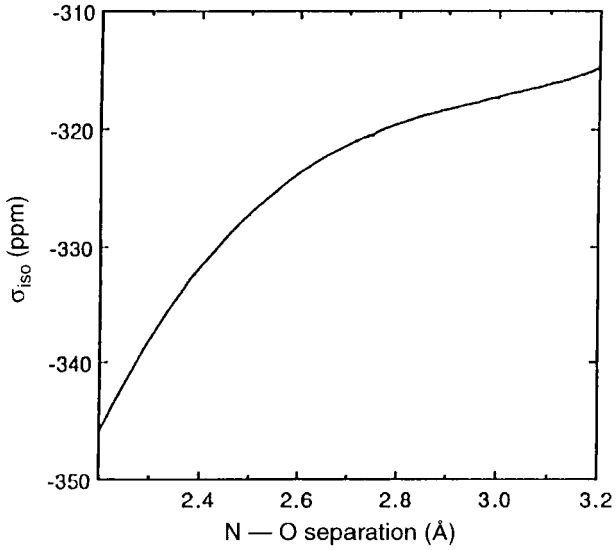

Fig. 26. Variation of the calculated isotropic ^{15}N shielding (σ_{iso}) with the N···O separation ($R_{N\cdots O}$).

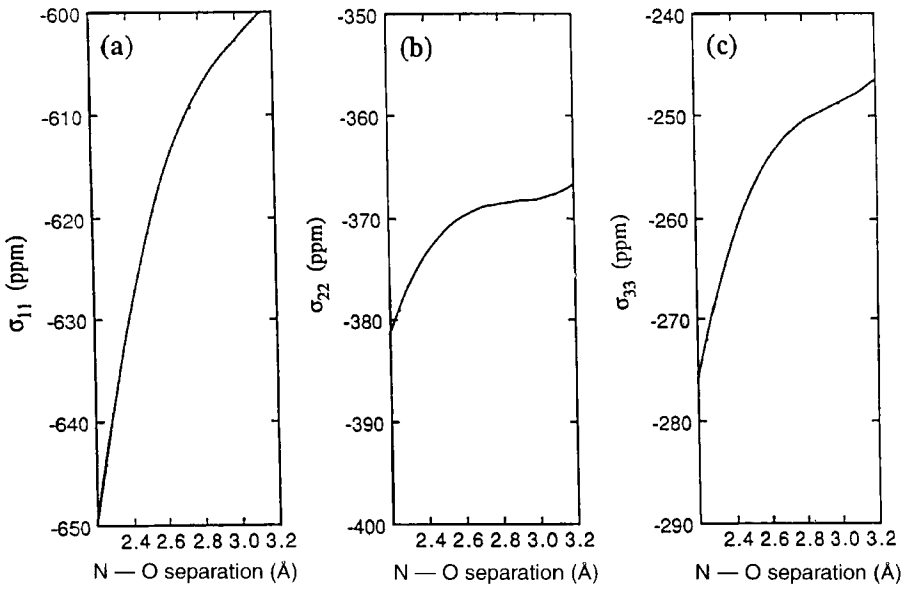

Fig. 27. Variation of the calculated ^{15}N shielding tensor components with the N···O separation ($R_{N\cdots O}$): (a) σ_{11}; (b) σ_{22}; (c) σ_{33}.

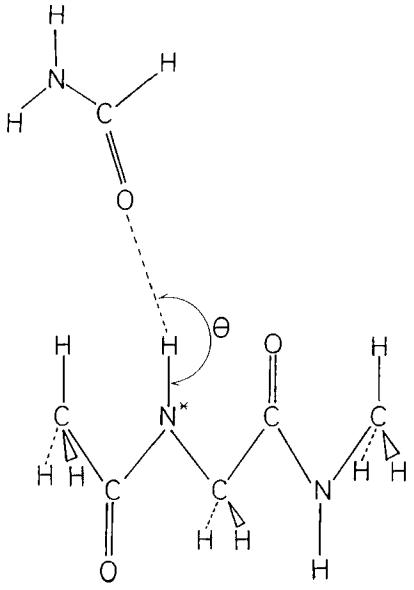

Fig. 28. Molecular structure of *N*-acetyl-*N'*-methylglycine amide hydrogen-bonded with a formamide molecule.

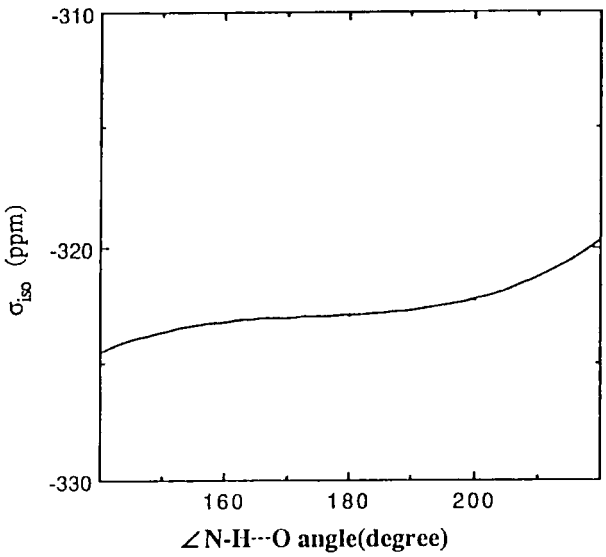

Fig. 29. Variation of the calculated isotropic ^{15}N shielding (σ_{iso}) with the hydrogen bond angle $\angle N{-}H\cdots O$ (θ).

change of θ when compared with the $R_{N\cdots O}$ dependence of σ_{11} and σ_{22}. From these results we may understand the experimental finding that there is a relationship between hydrogen-bond length and the values of σ_{33} and σ_{iso} in spite of the distribution in the hydrogen bond angles but there is no clear relationship between $R_{N\cdots O}$ and σ_{11} or σ_{22}.

3.4 Hydrogen-bonded structure and the ^{17}O NMR of glycine- and L-alanine-containing peptides and polypeptides

The oxygen atom is one of the more important atoms forming hydrogen-bonded structures in peptides and polypeptides. However, solid-state ^{17}O NMR study of peptides and polypeptides has not been carried out, owing to the very weak sensitivity of solid-state ^{17}O NMR measurement, which has two origins. One is that the ^{17}O nucleus has a very low natural abundance of 0.037%. The other is that the ^{17}O nuclear spin quantum number (I) is 5/2; thus the nucleus is quadrupolar and the ^{17}O signal is broadened by nuclear quadrupolar effects in the solid. Solution-state ^{17}O NMR spectroscopy has been successfully employed to elucidate a number of structural problems in organic chemistry,[90–93] because the ^{17}O signal becomes very sharp owing to the removal of some quadrupolar interactions by isotropic fast reorientation in solution. For example, as the oxygen atom is directly associated with the

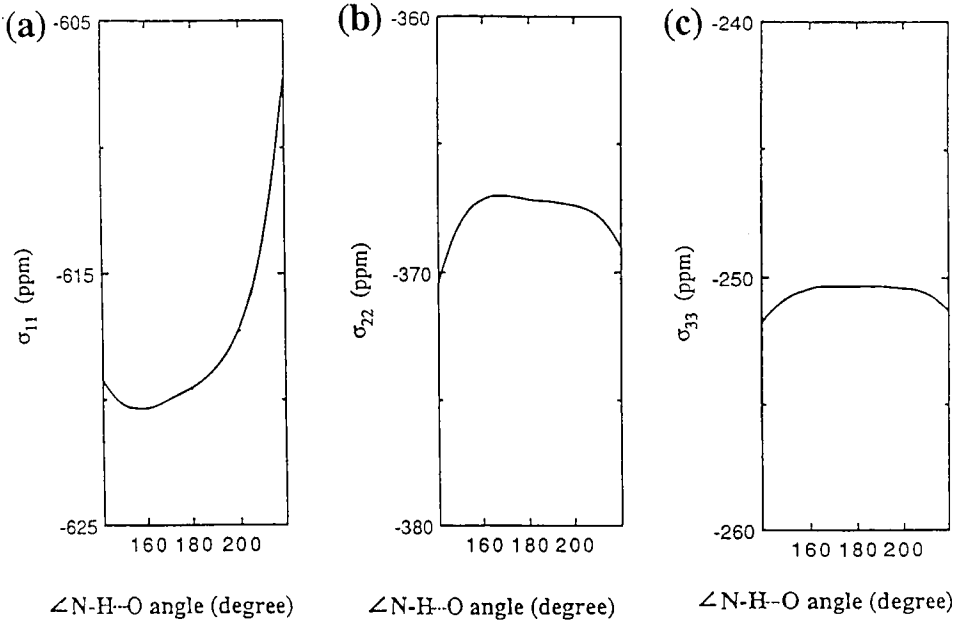

Fig. 30. Variation of the calculated ^{15}N shielding tensor components with the hydrogen bond angle $\angle N{-}H\cdots O$ (θ): (a) σ_{11}; (b) σ_{22}; (c) σ_{33}.

formation of hydrogen bonds, hydrogen-bonding of the carbonyl group in various compounds often results in large low-frequency shifts of the carbonyl ^{17}O NMR signal.[94,95] From these results, solution-state ^{17}O NMR has been established as a means of performing structural characterizations; it can be anticipated that solid-state ^{17}O NMR will provide an understanding of the hydrogen-bonding structure in solid peptides and polypeptides as described previously.[96] In this section, solid-state ^{17}O NMR spectra of $[Gly]_n$ form I (PG I), $[Gly]_n$ form II (PG II), glycylglycine (GlyGly) and glycylglycine nitrate ($GlyGly \cdot HNO_3$) are discussed with a view to understanding the relationship between the hydrogen-bonding structure and the ^{17}O NMR parameters.

Static ^{17}O spectra of the ^{17}O-labelled peptides and polypeptides

Static ^{17}O CP NMR spectra of GlyGly were observed at 36.6, 54.2 and 67.8 MHz as shown in Fig. 31.[40] The spectra at 36.6 and 54.2 MHz consist of two major split signals, but that at 67.8 MHz becomes one major signal. Such splitting comes from the quadrupolar interaction. By computer simulation, the quadrupolar coupling constant e^2qQ/h was determined to be 8.55 MHz. This value is much larger than that for the amide ^{14}N nitrogen nuclei (1.11 MHz). It is seen that the ^{17}O NMR spectra depend strongly on the measurement

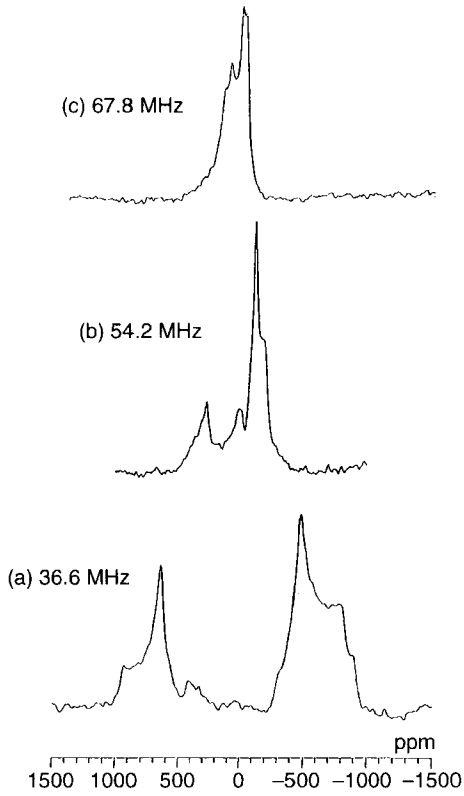

Fig. 31. ^{17}O CP Static NMR spectra of Gly-Gly in the solid state.

frequencies because the quadrupolar effect depends on the measurement frequencies and the broadening of ^{17}O NMR signal is increased by the quadrupolar effect as the measurement frequency is decreased. Consequently, high-frequency measurements are needed for quadrupolar nuclei such as ^{17}O.

Figure 32 shows the 67.8 MHz static ^{17}O CP NMR spectra of PG I, PG II, GlyGly and GlyGly·HNO_3. Computer simulations were performed for superimposition of theoretically calculated spectra on to the experimental spectra. To determine the ^{17}O NMR parameters unequivocally, computer simulations are carried out for frequencies of 36.6, 54.2 and 67.8 MHz. For example, Fig. 33 shows 67.8, 54.2 and 36.6 MHz static ^{17}O CP NMR spectra of GlyGly together with theoretically calculated spectra, and Fig. 34 shows 67.8 MHz static ^{17}O CP NMR spectra of PG I, PG II, GlyGly and GlyGly·HNO_3 together with theoretically calculated spectra. The ^{17}O NMR parameters of PG I, PG II, GlyGly and GlyGly·HNO_3 obtained by computer simulation are shown in

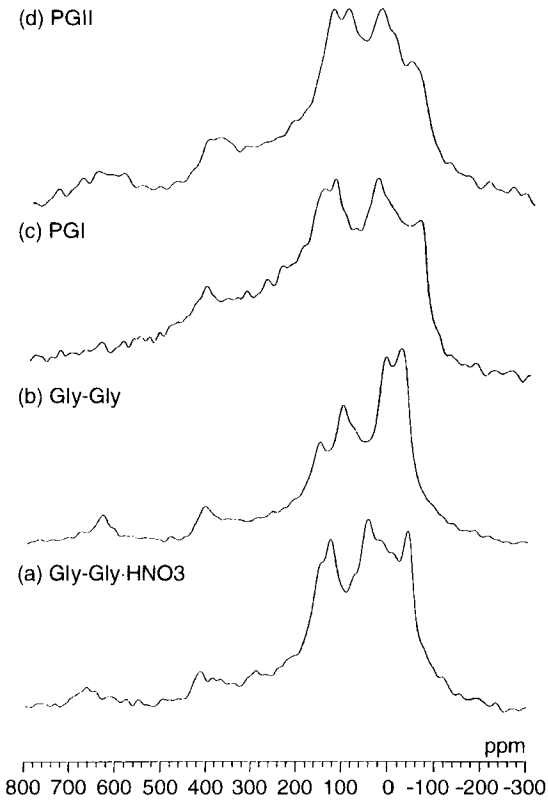

Fig. 32. 67.8 MHz ^{17}O CP static NMR spectra of (a) Gly-Gly·HNO_3, (b) GlyGly; (c) PG I and (d) PG II.

Table 9. From these results, the δ_{11}, δ_{22} and δ_{33} values of the samples vary from 546 to 574 ppm, 382 to 425 ppm, and −132 to −101 ppm, respectively. The magnitude of the chemical shift change is much larger than those of the carbonyl ^{13}C and amide ^{15}N chemical shifts. Each $\Delta\delta$ value, defined as $\Delta\delta = \delta_{iso} - \delta_{33}$, is about 400 ppm, much larger than those for the carbonyl ^{13}C and amide ^{15}N chemical shifts, which are about 170 and 100 ppm, respectively. Each η value, defined as $\eta = (\delta_{11} - \delta_{22})/\Delta\delta$, is constant ~0.4. These values are common to the carbonyl-oxygen atoms in peptides. Although the chemical shift tensor is axially symmetric ($\delta_{11} = \delta_{22}$) for the case of the carbonyl-oxygen of L-alanine as reported by Fiat *et al.*,[97,98] the chemical shift tensor of the carbonyl-oxygen in the peptides considered here is not axially symmetric. The e^2qQ/h values change from 8.30 to 8.75 MHz. These values are larger than the corresponding value for L-leucine, which is 8.0 MHz at 190 K.[98] The h_Q values of polypeptides such as PG I and II are 0.26 and 0.29; the corresponding values

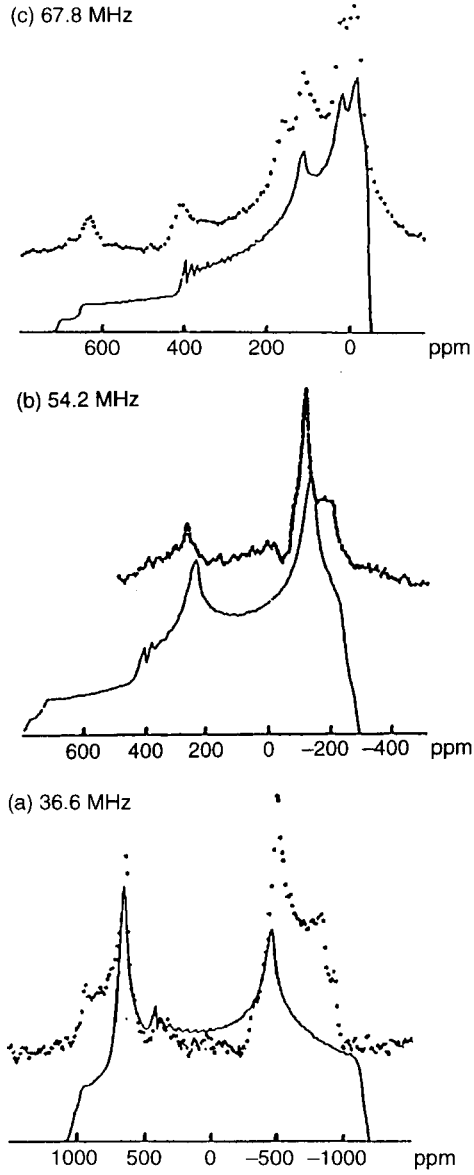

Fig. 33. ^{17}O CP static NMR spectra of Gly-Gly together with theoretically simulated spectra.

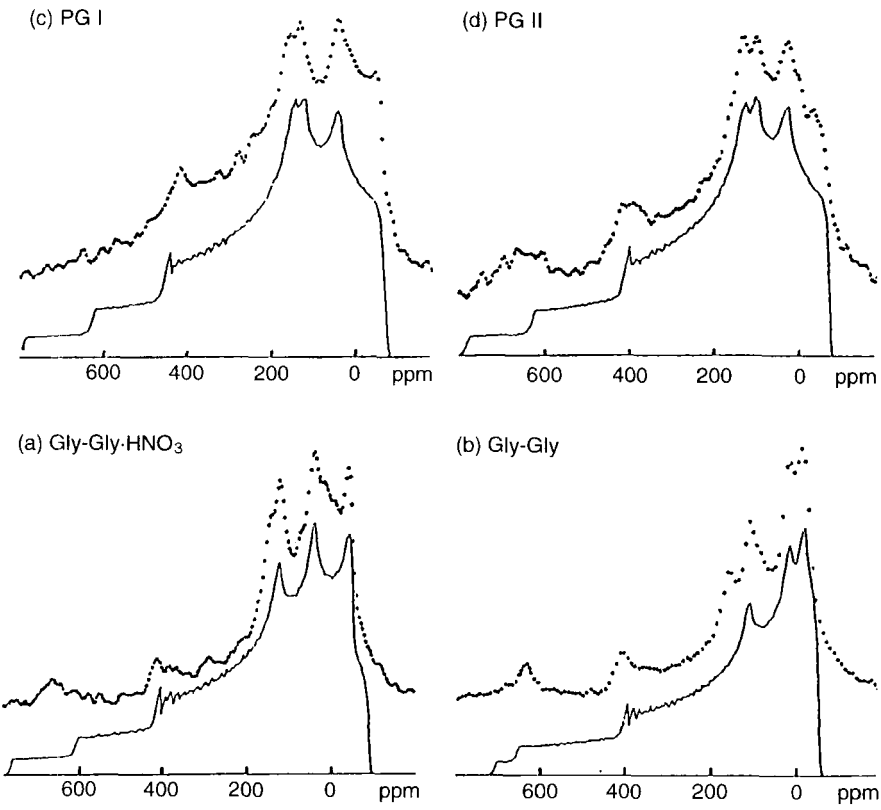

Fig. 34. 67.8 MHz ^{17}O CP static NMR spectra of (a) Gly-Gly·HNO_3, (b) Gly-Gly, (c) PG I, and (d) PG II, together with theoretically simulated spectra.

for oligopeptides such as GlyGly and GlyGly·HNO_3 are 0.45 and 0.47, respectively. The difference may arise from a difference in molecular packing between these samples. Further, it is found that the PAS of the quadrupolar tensor and the PAS of the ^{17}O nuclear shielding tensors for the carbonyl oxygens of peptides and polypeptides are not coincidental with each other. The relationship between these two sets of PAS is shown in Fig. 35 for PG II. From these experimental results, each of the above NMR parameters is seen to be strongly influenced by the electronic structure of the molecule.

The direction of the principal axes of the electric field gradient tensor and the nuclear shielding of the carbonyl-oxygen of peptides and polypeptides

So far there have been few studies aimed at determining the direction of the PAS of the electric field gradient tensor and the nuclear shielding tensor of

Table 9. Determined ^{17}O NMR parameters of solid peptides containing a Gly residue.

Sample	e^2qQ/h (MHz)	η_Q	Chemical shift (ppm)						Angle Δ (°)[c]		
			δ_{11}	δ_{22}	δ_{33}	δ_{iso}	$\Delta\delta^a$	η^b	α	β	γ
Polypeptides											
PG II	8.30	0.29	562	410	−108	288	396	0.38	92	89	−81
PG I	8.55	0.26	574	425	−101	299	400	0.37	100	91	−79
Oligopeptides											
GlyGly	8.55	0.45	546	382	−132	265	397	0.41	94	90	−87
GlyGly·HNO_3	8.75	0.47	559	408	−127	280	407	0.37	94	89	−81

[a] $\Delta\delta = \delta_{iso} - \delta_{33}$.
[b] $\eta = (\delta_{11} - \delta_{22})/\Delta\delta$.
[c] Angle Δ indicates the Euler angles between the principal axes of the quadrupolar tensor and the chemical shift tensor.

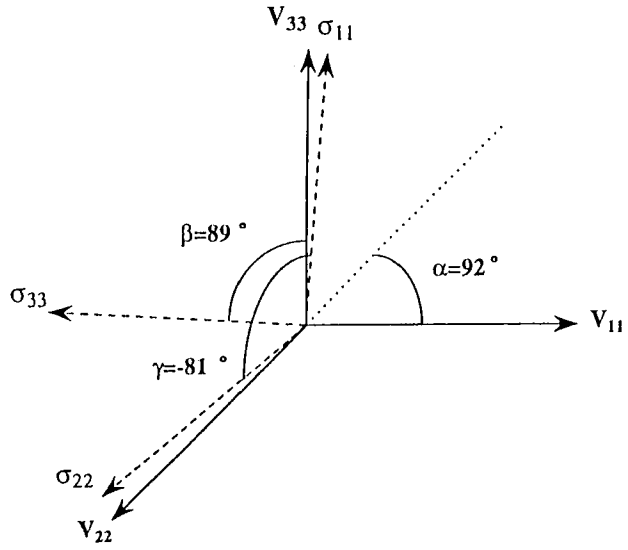

Fig. 35. The relationship between the PAS of the quadrupolar (V) and chemical shift (σ) tensors on the carbonyl-oxygen for PG II.

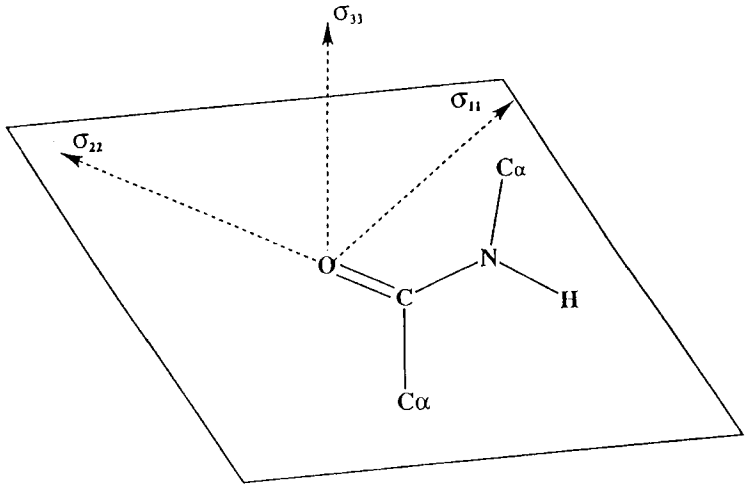

Fig. 36. The direction of the PAS of the nuclear shielding tensor of the carbonyl-oxygen obtained from the FPT-MNDO-PM3 method.

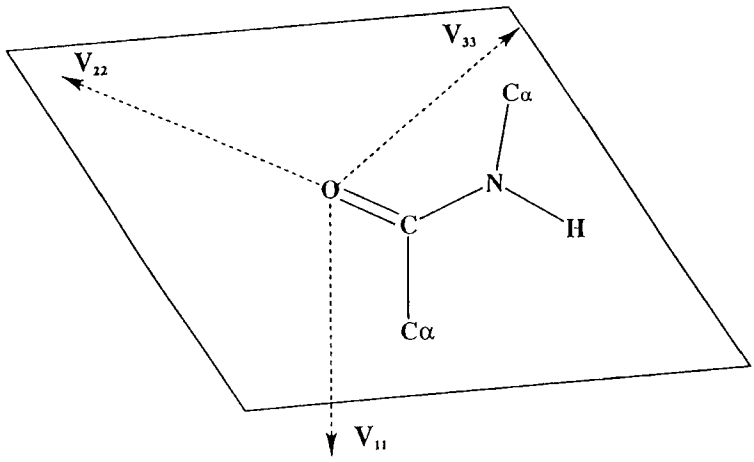

Fig. 37. The direction of the PAS of the electric field gradient of the carbonyl-oxygen obtained from the FPT-MNDO-PM3 method.

carbonyl-oxygen atoms of peptides and polypeptides from NMR experiments. The direction of the PAS of the nuclear shielding of the carbonyl oxygen of peptides and polypeptides is determined as shown in Fig. 36 employing FPT-MNDO-PM3 methods. It is shown that the σ_{22} component lies approximately along the C=O bond, the σ_{11} component is aligned in the direction perpendicular to the C=O bond on the peptide plane, and σ_{33}, which is the most shielded component, is aligned in the direction perpendicular to the peptide plane.

The direction of the PAS of the electric field gradient tensor of the carbonyl-oxygen is shown in Fig. 37 employing the FPT-MNDO-PM3 method. It is shown that the V_{22} component lies approximately along the C=O bond, the V_{33} component is aligned in the direction perpendicular to the C=O bond in the peptide plane, and the V_{11} component is aligned in the direction perpendicular to the peptide plane. These results show that the largest component V_{33} of the electric field gradient lies along the molecular chain direction. The relationship between the electric field gradient tensor and the nuclear shielding obtained by this calculation agrees with the experimental results as shown in Fig. 34.

Nuclear quadrupolar coupling constant (e^2qQ/h) of carbonyl-oxygen atoms of peptides and polypeptides

The geometric parameters and hydrogen-bonding geometrical parameters of some peptides and polypeptides containing a glycine residue are shown in Table 10. Some of the geometric parameters are calculated by using the

unit-cell parameters and fractional coordinates as determined by X-ray diffraction.[77,99-101] Figure 38 shows a plot of the observed e^2qQ/h values against the hydrogen-bond length.

The e^2qQ/h values decrease linearly with a decrease in the separation ($R_{N\cdots O}$) in Å. This relationship can be expressed by

$$\frac{e^2qQ}{h}(\text{MHz}) = 5.15 + 1.16R_{N\cdots O} \tag{21}$$

This experimental result shows that a decrease of the hydrogen-bond length leads to a decrease in electric field gradient (q). The q value is very sensitive to a change in hydrogen-bond length. From this relation it is apparent that hydrogen-bond length can be determined by the observation of the e^2qQ/h value.

^{17}O NMR chemical shifts of the carbonyl-oxygen of peptides and polypeptides

From Table 9, it is apparent that there is large difference in the ^{17}O chemical shift values between peptides and polypeptides. Figure 39 shows the plot of the

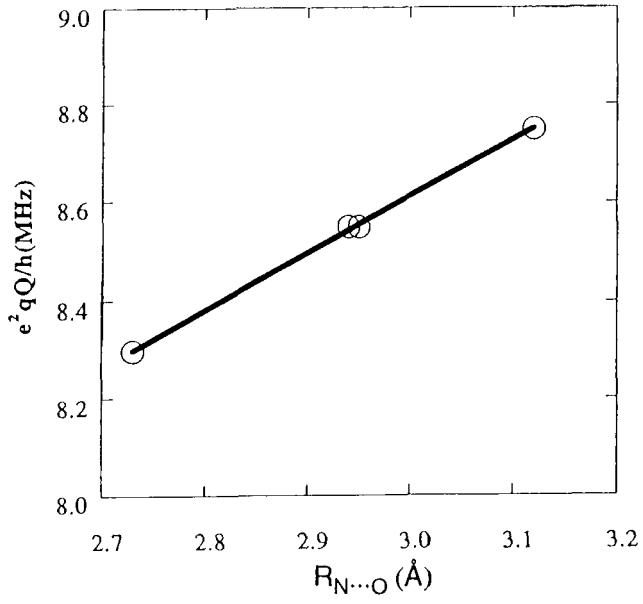

Fig. 38. Plots of the e^2qQ/h against the N···O separation ($R_{N\cdots O}$).

Table 10. The geometrical parameters of some peptides containing a Gly residue.

Sample	Dihedral angle (°)		N···O (Å)	H···O (Å)	∠C=O···N (°)	∠N–H···O (°)	N–C=O···H (°)	C=O···H–N (°)	Reference
	ϕ	ψ							
PG II	−78.0	145.8	2.73	1.84	159	146	−47	157	52
PG I	−149.9	146.5	2.95	2.16	149	133	68	−173	51
Gly-Gly	157.1	151.0	2.94	1.97	157	157	−161	−145	75
Gly-Gly·HNO_3	165.6	148.9	3.12	2.38	162	165	3	−156	77

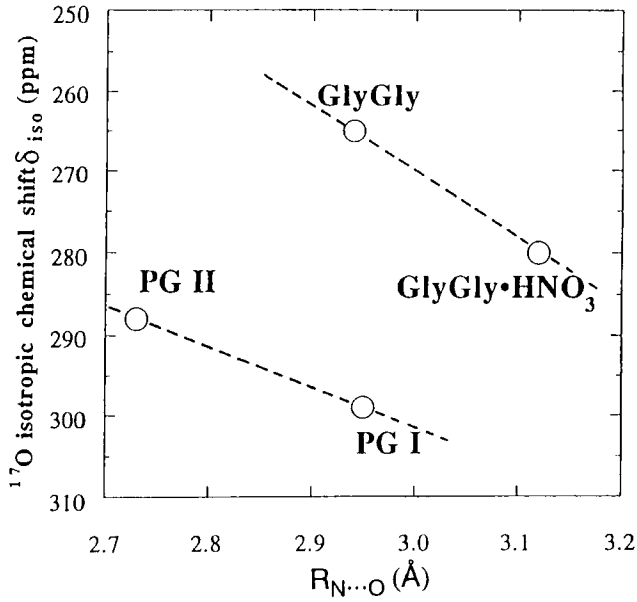

Fig. 39. Plots of the ^{17}O isotropic chemical shift against the N···O separation ($R_{N\cdots O}$).

observed isotropic ^{17}O chemical shift values (δ_{iso}) against the separation ($R_{N\cdots O}$). The δ_{iso} values in both the peptides and polypeptides move to low frequencies with a decrease in the separation ($R_{N\cdots O}$). Figures 40a–c show plots of the observed principal values of ^{17}O chemical shifts against the separation ($R_{N\cdots O}$).

Every principal chemical shift value in both peptides and polypeptides moves to low frequencies with decrease in the separation ($R_{N\cdots O}$). What is the origin of the difference of the chemical shift between peptides and polypeptides? Two possible origins are considered. The first is that the difference between peptides and polypeptides comes from the hydrogen-bond angle and hydrogen-bond dihedral angle, which are closely related to the ^{17}O chemical shift. The second is the difference in molecular packing between them.

The spatial locations of these samples are shown in Fig. 41, using the geometrical parameters given in Table 10. Figure 41 shows the dihedral angle N—C=O···H (defined by ξ here), giving a measure of the location of the amide group on the peptide plane. In the case of GlyGly ($\xi = -160°$) and GlyGly·HNO_3 ($\xi = 3°$), the amide-group-related hydrogen-bonding is nearly in the peptide plane and carbon, oxygen, hydrogen and nitrogen atoms related to hydrogen-bonding are located in the peptide plane. On the other hand, in the case of PG I ($\xi = 68°$) and II ($\xi = -47°$), the amide group-related hydrogen-bonding is away from the peptide plane. Consequently it appears that the location of the amide group affects the δ value.

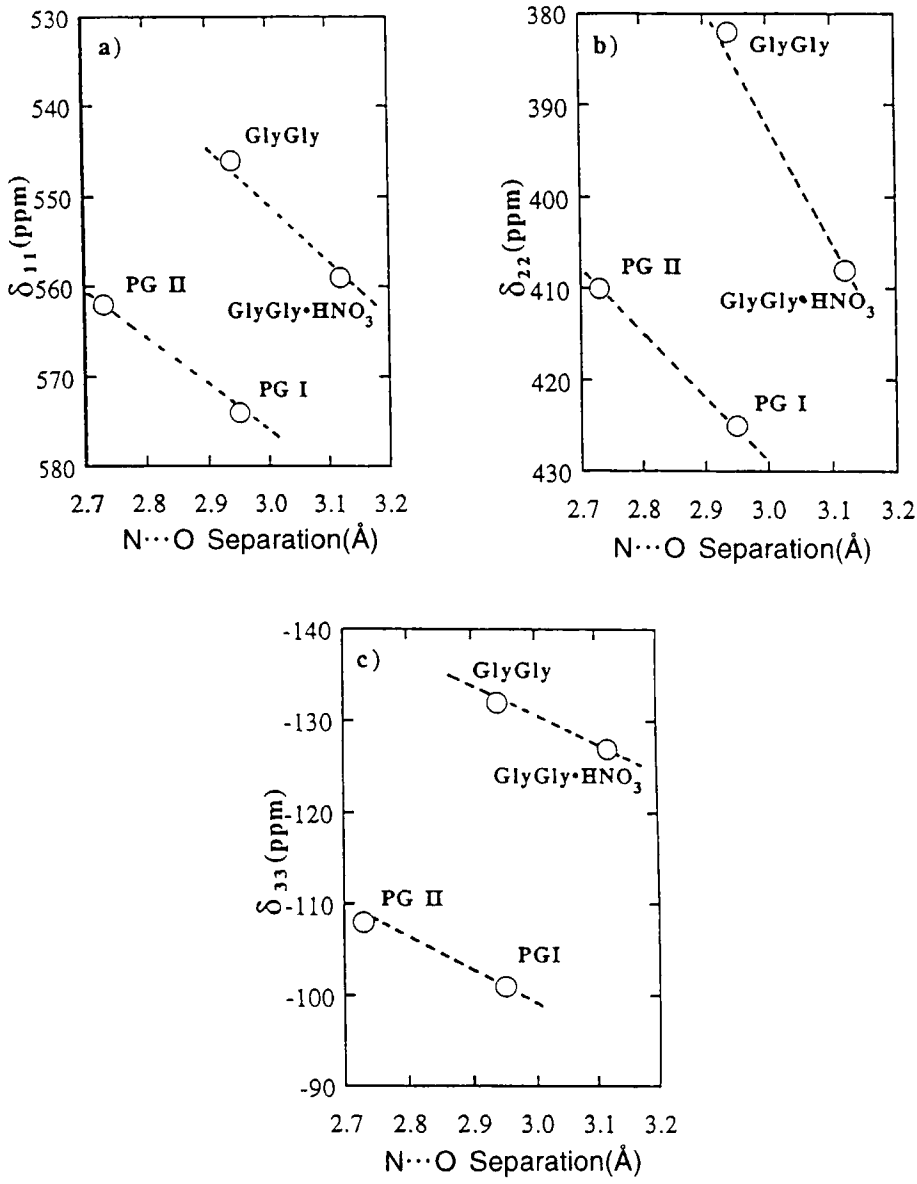

Fig. 40. Plots of the principal values of ^{17}O chemical shift, (a) δ_{11}, (b) δ_{22} and (c) δ_{33}, against the N···O separation ($R_{N\cdots O}$).

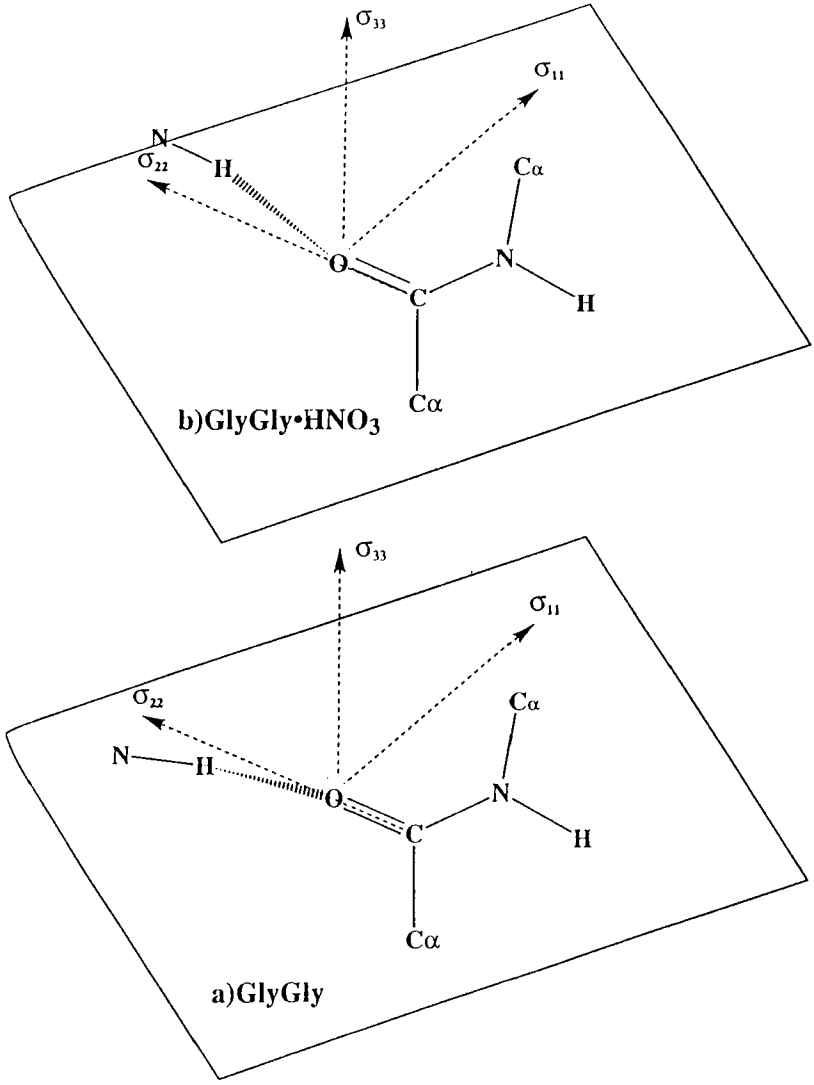

Fig. 41. The hydrogen-bonding spatial location of peptides.

4. MAIN-CHAIN DIHEDRAL ANGLES AND ^{13}C NMR CHEMICAL SHIFTS

4.1. ^{13}C chemical shifts of the L-alanine C_α- and C_β-atoms in peptides in the solid state

Figure 42 shows the 67.8 MHz CP-MAS ^{13}C spectra for Ac-L-Ala-NHMe in the solid state. From the X-ray diffraction study of the Ac-L-Ala-NHMe crystal, it has been found that the unit cell contains two molecules whose conformations are not magnetically identical. In Fig. 42, for the carbonyl-, C_α- and C_β-carbons, two signals are observed which come from two different conformations. The observed chemical shifts for L-alanine residue C_α- and C_β-carbons, with their geometrical parameters as determined by X-ray diffraction studies[20,31–35] are summarized. Some of the geometrical parameters are calculated using the unit-cell parameters and the fractional coordinates. Table 11 shows that the L-alanine residue in the peptides takes dihedral angles (ϕ, ψ) corresponding to several conformations such as α_R-helix, β_A-sheet, 3_{10}-helix, etc. The ^{13}C signal of the L-alanine C_α-carbon in poly(L-alanine), which forms the α_R-helix conformation, appears at lower frequency by several ppm relative to the signals of the other conformations. However, the ^{13}C chemical shift of the L-alanine C_β-carbon in the β_A-sheet conformation is at 21.0 ppm, and thus appears at high frequency relative to those for the other conformations. The ^{13}C chemical shift of the L-alanine C_α-carbon for the β_A-sheet conformation is 48.7 ppm, which is shielded relative to those for the other conformations. However, the ^{13}C chemical shift for poly(L-alanine), which forms the α_R-helix

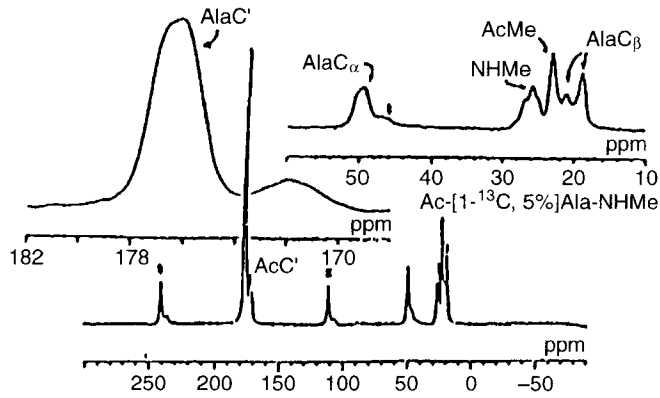

Fig. 42. 67.8 MHz CP-MAS ^{13}C spectra for *N*-acetyl-*N'*-methyl-L-alanine amide in the solid state. The conditions for NMR measurements are the same as those for Fig. 2.

Table 11. Observed chemical shifts for solid peptides that contain an L-alanine residue by ^{13}C CP-MAS NMR measurements, and their main-chain dihedral angles for the L-alanine residue portions determined by X-ray diffraction studies.

Sample	Chemical shift (ppm from TMS) C_α	C_β	ϕ (°)	ψ (°)	Secondary structure
$(Ala)_n$	53.0	15.5	−54.7	−47.5	α_R-helix
	48.7	21.0	−138.8	134.7	β_A-sheet
$(D,L\text{-Ala})_n$[a]	50.1	15.9	54.7	47.5	α_L-helix
$(Ala\text{-}Gly\text{-}Gly)_n$ I	49.7	22.6			β-sheet
$(Ala\text{-}Gly\text{-}Gly)_n$ II	49.7	18.4	−90.0	150.0	3_1-helix[e]
$(Ala\text{-}Ala\text{-}Gly)_n$	50.1	21.4			β-sheet
$(Ala\text{-}Gly)_n$ I[b]	49.5	21.0			β-sheet
$(Ala\text{-}Gly)_n$ II[c]	51.5	17.6			Unknown[f]
$(Pro\text{-}Ala\text{-}Gly)_n$	49.3	18.6			Triple-helix[e]
Ac-Ala-NHMe[d]	49.3	18.8	−84.3	159.0	3_1-helix like[g]
	50.4	21.2	−87.6	154.8	
Boc-Ala-Aib-OH[h]	52.3	17.4	−66.3	−24.1	3^R_{10}-helix
Boc-Ala-Pro-OH	49.2	17.2	−95.4	153.6	3_1-helix-like[g]

[a] $(D,L\text{-Ala})_n$ denotes copolymer of D- and L-alanine.
[b] $(Ala\text{-}Gly)_n$ form I is a model compound for silk II.
[c] $(Ala\text{-}Gly)_n$ form II is a model compound for silk I.
[d] There are two conformers in a unit cell.
[e] $(Ala\text{-}Gly\text{-}Gly)_n$ form II and $(Pro\text{-}Ala\text{-}Gly)_n$ are model compounds for collagen.
[f] Some X-ray crystallographic structures[13,14] were presented by other groups. However, arguments about the structure for $(Ala\text{-}Gly)_n$ and silk I have been raised.[7]
[g] The secondary structures for these samples are not exactly 3_1-helix conformation because the hydrogen-bonding structures are not the same as for the 3_1-helix for polypeptides.
[h] Aib: aminoisobutyric acid.

conformation, is 53.0 ppm, which is shielded by several ppm relative to the other conformations. The ^{13}C chemical shifts of the L-alanine C_α- and C_β-carbons for the other specified conformations are intermediate values between those for the α_R-helix and the β_A-sheet conformations. We recognize from these results that the ^{13}C chemical shifts of the C_α- and C_β-carbons in the L-alanine residue in peptides relates closely to the main-chain conformation. However, since the term "main-chain conformation" of a peptide implies not only the main-chain dihedral angles (ϕ, ψ) but also its hydrogen-bonding structure (hydrogen-bond length and angle), it is not yet apparent whether the ^{13}C chemical shifts of the L-alanine C_α- and C_β-carbons should be governed by the dihedral angles for the L-alanine residue moiety.

Nuclear shielding calculation by the FPT-INDO and 4-31G-GIAO-CHF methods: dihedral angle (ϕ, ψ) dependence of the ^{13}C chemical shifts of the L-alanine residue C_α- and C_β-atoms

The correlation between the chemical shifts and the main-chain dihedral angles of peptides has been investigated by nuclear shielding calculations by the FPT-INDO and *ab initio* GIAO-CHF methods, the latter with a 4-31G basis set.[60]

An *N*-acetyl-*N'*-methyl-L-alanine amide (Ac-L-Ala-NHMe) molecule was employed as a model (Fig. 1b). All of the geometrical parameters of this molecule, except for the C—H bond lengths in the acetyl methyl group and the amide methyl group, are optimized by the *ab initio* molecular orbital method with the 4-31G basis set. Using the optimized geometries of this molecule, the carbon nuclear shieldings[9,10] were calculated.[61] In contrast, standard geometrical parameters are used for the FPT-INDO calculation.

Table 11 shows the main-chain conformation and the observed ^{13}C chemical shifts for a series of peptides that contain the L-alanine residue. As mentioned, "main-chain conformation" of peptides implies not only the main-chain dihedral angles but also the hydrogen-bonded structure. Since the L-alanine residue in a protein does not necessarily form a hydrogen bond, it is still important to estimate the contribution of the main-chain dihedral angles to the chemical shift of the L-alanine residue C_α- and C_β-atoms. The shielding map obtained is fairly close to that produced by the *ab initio* MO method. Figure 43a shows the dihedral angle (ϕ, ψ) dependence of the calculated isotropic chemical shift for the L-alanine residue C_β-atoms.

The isotropic shieldings for C_β are 186.4 ppm for the main-chain dihedral angles that correspond to the β_A-sheet conformation, 189.4 ppm for the α_R-helix, 189.6 ppm for the α_L-helix, 188.7 ppm for the 3_1-helix, and 186.5 ppm for silk I and $(Ala\text{-}Gly)_n$ form II. By comparison, the observed isotropic chemical shifts are 21.0 ppm for the β_A-sheet, 15.5 ppm for the α_R-helix, 15.9 ppm for the α_L-helix, 18.4 ppm for 3_1-helix (we employ the chemical shift values for $(Ala\text{-}Gly\text{-}Gly)_n$ that forms a collagen-like helix), and 17.6 ppm for $(Ala\text{-}Gly)_n$ form II. It is found that changes of the main-chain dihedral angles dominate the isotropic chemical shift behaviour of the L-alanine residue C_β-atom, except for silk I and $(Ala\text{-}Gly)_n$ form II. Saito, Ando, and coworkers[36] have previously presented a structural model of silk I and/or $(Ala\text{-}Gly)_n$ form II that is known as a crankshaft model. In addition, they have predicted that the structure of silk I and/or $(Ala\text{-}Gly)_n$ form II might be a loose fourfold helical conformation, which was originally proposed by the X-ray diffraction study of Konishi and Kurokawa.[37] From the calculated structure, the loose helix model is found to be unacceptable. Thus, at present it is difficult to deduce with certainly values for the main-chain dihedral angles.

In order to elucidate the isotropic chemical shift behaviour, we have calculated the principal values of the nuclear shielding tensor. The dihedral

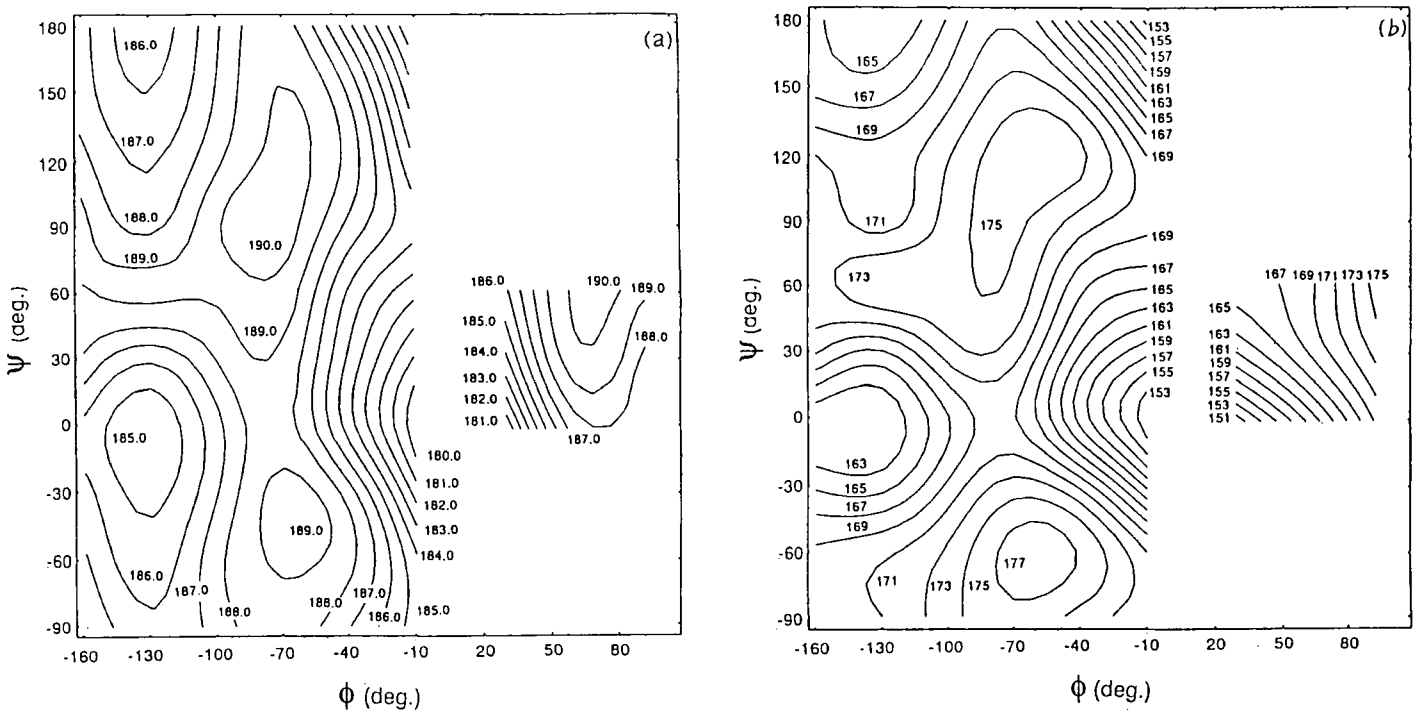

Fig. 43. The dependences on the dihedral angles (ϕ, ψ), of the nuclear shielding constants for the L-alanine residue C_α- and C_β-atoms in peptides. Chemical shielding calculations are carried out using the GIAO-CHF method with the 4-31G *ab initio* basis set. 4-31G optimized geometries are employed for the model molecule, *N*-acetyl-*N'*-methyl-L-alanine amide. (a) Isotropic, (b) σ_{11}, (c) σ_{22}, and (d) σ_{33} for the C_β-carbon (in ppm). (e) Isotropic, (f) σ_{11}, (g) σ_{22}, and (h) σ_{33} for the C_α-carbon (in ppm).

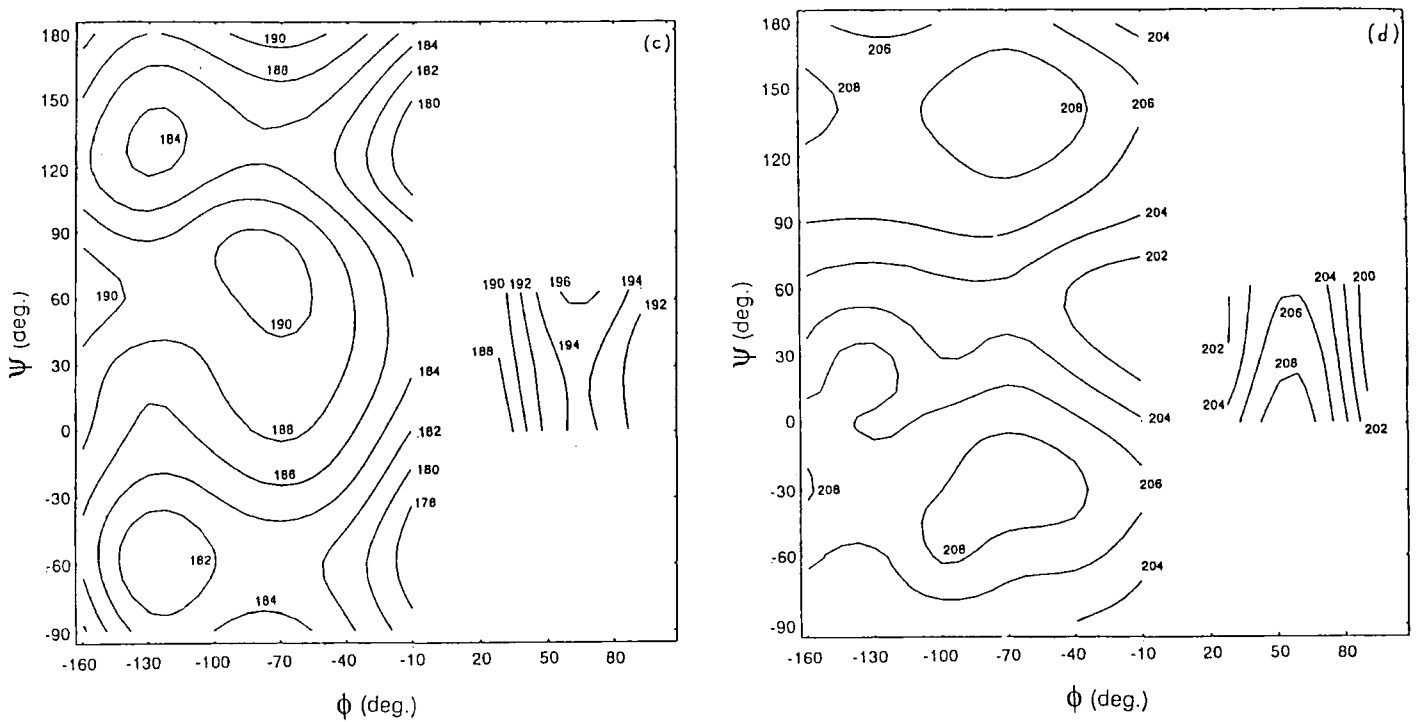

Fig. 43. continued

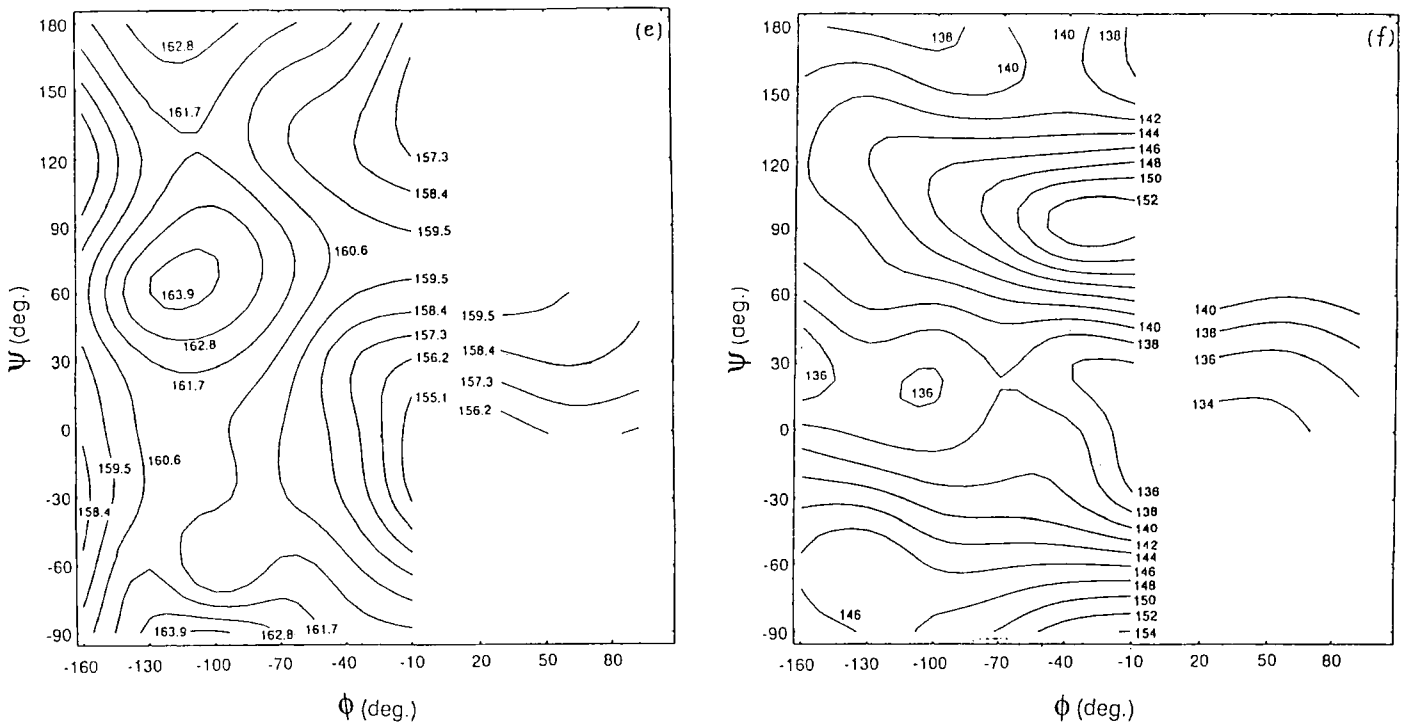

Fig. 43. continued

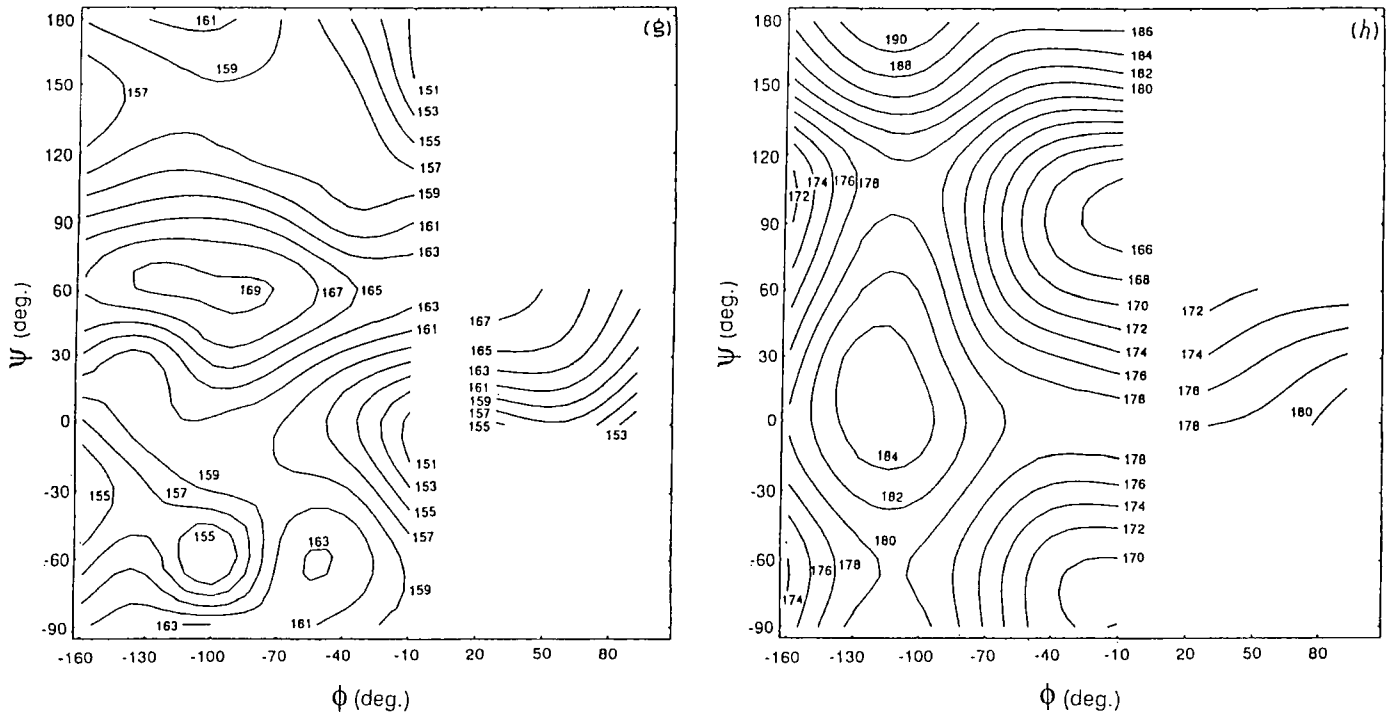

Fig. 43. continued

angle (ϕ, ψ) dependences of σ_{11}, σ_{22} and σ_{33} (in order of increasing shielding) are shown in Figs 43b–d. From these figures the fact that the isotropic C_β chemical shift for the α_R-helix appears at a lower frequency (15.5 ppm) than that for the β_A-sheet (21.0 ppm) is rationalized by the explicit differences found for σ_{11} ($\Delta\sigma_{11} \approx 9$ ppm). Careful investigation of the nuclear shielding tensor shows that the paramagnetic contribution to σ_{11} dominates the total σ_{11} value. The 2p orbital for the C_α-carbon, which is influenced by the angular momentum operator L_κ and which contributes to the C_α—C_β bond, provides the most effective contribution to the paramagnetic contribution to σ_{11}, since the coupling integral, $\langle\phi_\nu|\mathbf{L}_\kappa/r_B^3|\phi_\lambda\rangle$, is dominated by a contribution from the 2p orbital perpendicular to the σ_{11} direction. In the 4-31G optimized geometries, the distance between the C_α- and C_β-atoms is 1.51 Å for the β_A-sheet and 1.53 Å for the α_R-helix; thus changes in the value of σ_{11} are explained by the differences in the length of the C_α—C_β bond that arise from the changes in the main-chain dihedral angles.

Figures 43e–h show the dependence of the isotropic nuclear shielding for the C_α on the main-chain dihedral angles. From Fig. 43e, the isotropic nuclear shielding for C_α is 160.4 ppm for the β_A-sheet, 159.6 ppm for the α_R-helix, 159.2 ppm for the α_L-helix, 161.4 ppm for the 3_1-helix, and 157.9 ppm for silk I and $(Ala\text{-}Gly)_n$ form II. The corresponding observed isotropic chemical shifts are 48.7 ppm for the β_A-sheet, 53.0 ppm for the α_R-helix, 50.1 ppm for the α_L-helix, 49.7 ppm for the 3_1-helix, and 51.5 ppm for $(Ala\text{-}Gly)_n$ form II, respectively. Although it is obvious that there exists a main-chain dihedral angle dependence on chemical shift for the C_α-atom, it seems to be more complicated than that for the C_β-atom, since the orientation of the chemical shift tensor for C_α with respect to the molecular fixed frame is different from one set of values of (ϕ, ψ) to another, and also because, in the case in which the L-alanine residue carbonyl or amide group forms the hydrogen bond, the hydrogen-bonded structure can also affect the behaviour of the chemical shift for C_α. As regards the structure of $(Ala\text{-}Gly)_n$ form II and silk I, chemical shift calculation including hydrogen-bonding is required.

For further insight into the C_α chemical shift behaviour, principal values of the nuclear shielding tensor were calculated.[60,61] From Figs 43f–h, it is obvious that all of the principal values are quite sensitive to change in the dihedral angles (ϕ, ψ). In particular, the value of σ_{33} is the most sensitive to (ϕ, ψ) differences. For almost all values of (ϕ, ψ), the principal axis of σ_{33} is aligned along the C_α—C' bond, but with about 30° deviation, and is also nearly perpendicular to the C_α—C_β bond. Since it is generally known that a bond extension causes a shielding decrease,[38] it is predicted that the C_α—C' bond length differences associated with dihedral angle variations contribute dominantly to the σ_{33} changes. However, the C_α—C' bond lengths in the 4-31G energy-optimized geometry are 1.512 Å for the β_A-sheet and 1.516 Å for the α_R-helix; thus the bond length difference is 0.004 Å. It seems that this bond length difference is too small to be responsible for the behaviour of σ_{33}. For

the values of σ_{33} of C_α, it is found that the diamagnetic contribution dominates changes in the total σ_{33} value; therefore, the most crucial factor for this behaviour is a change in the geometric parameters of the C_α moiety along the σ_{33} axis of model compounds which have several main-chain dihedral angles.

It should be noted that the other principal values, σ_{11} and σ_{22}, change the orientation of their principal axes from one set of (ϕ, ψ) values to another. One of the complexities concerning the orientation of chemical shift tensors is discussed in the next section. Another complexity, the hydrogen-bonding effect, seems to be rather intricate because the chemical shift for C_α, especially the principal values of the chemical shift tensor, is greatly affected by differences not only in $R_{N\cdots O}$ and $R_{H\cdots O}$ but also in the hydrogen-bond angles (for example, $\angle N\cdots O{=}C$ and $\angle H\cdots O{=}C$). The hydrogen-bonding effect on the C_α chemical shift is estimated from solid-state NMR measurements combined with GIAO-CHF nuclear shielding calculations.

The orientation of the PAS of the calculated nuclear shielding tensor with respect to the molecular fixed frame

As mentioned above, the principal values of the chemical shift tensor give information about the three-dimensional electronic state of a molecule. However, in order to understand the behaviour of the principal values, one needs information about the orientation of the PAS of a chemical shift tensor with respect to the molecular fixed frame.

Figures 44a–d show the calculated orientations of the principal axis systems of the nuclear shielding tensors of the L-alanine C_β-atoms in some peptides whose L-alanine moieties have different main-chain dihedral angles $(\phi, \psi) = (-57.4°, -47.5°)$ (α_R-helix), $(-138.8°, 134.7°)$ (β_A-sheet), $(-66.3°, -24.1°)$ (3_{10}-helix), and $(-84.3°, 159.0°)$ (3_1-helix). Figures 44a–d show that the σ_{33} component lies nearly along the $C_\alpha{-}C_\beta$ bond for all of the peptides considered here, and also that the σ_{11} component is nearly perpendicular to the plane which is defined by C_β, C_α, and the N atoms in the L-alanine residue. In contrast, the σ_{22} component is parallel with respect to the plane. These results agree with the direction of σ_{33} of C_β in the L-alanine amino acid determined experimentally by Naito *et al.*[39] As seen from Table 12, the value of the σ_{11} component, for dihedral angles corresponding to the β_A-sheet conformation, is 37.06 ppm. This shows a deshielding of about 9 ppm with respect to the value found for the α_R-helix conformation. This result means that the value of σ_{11} dominates the shielding decrease of the C_β-atom for the β_A-sheet conformation. Since the σ_{11} does not lie along a specified chemical bond, it is not easy to comprehend intuitively the chemical shift tensor behaviour of C_β. However, it is obvious that the through-space interaction between the C_β-methyl group and its surroundings might be important in understanding the behaviour of σ_{11}.

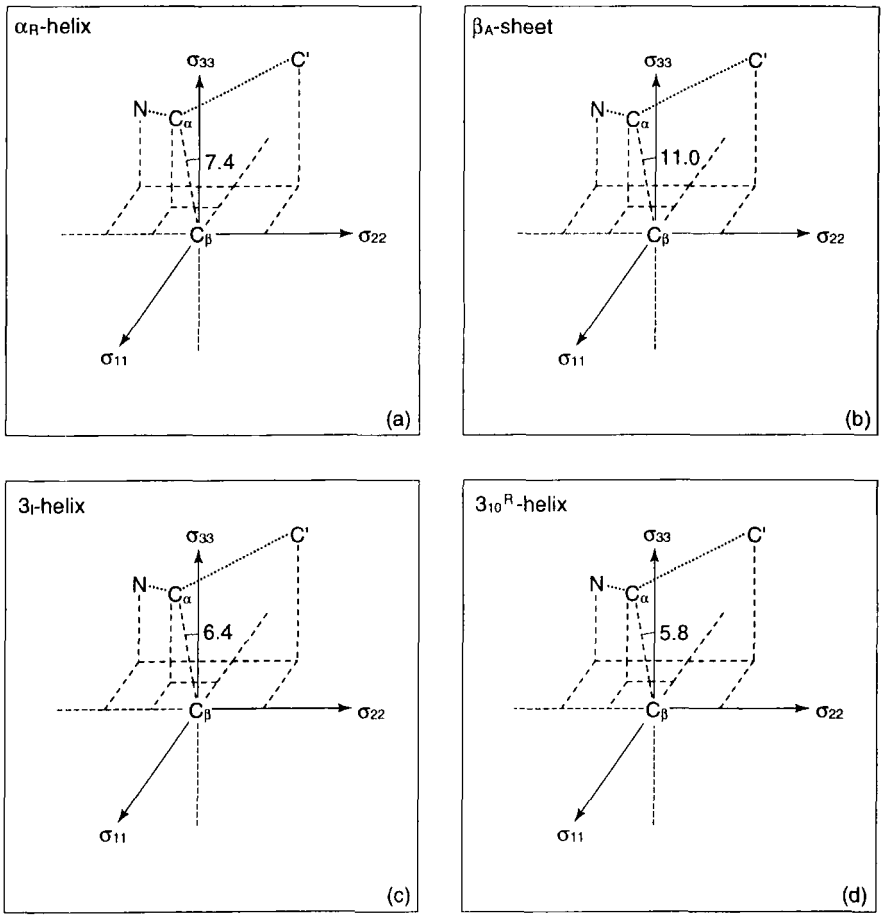

Fig. 44. Orientation of the principal axes of the calculated ^{13}C nuclear shielding for the L-alanine residue. C_α-carbons: (a) $(\phi, \psi) = (-57.4°, -47.5°)$ (α_R-helix); (b) $(-138.8°, 134.7°)$ (β_A-sheet); (c) $(-66.3°, -24.1°)$ (3^R_{10}-helix); (d) $(-84.3°, 159.0°)$ (3_I-helix). C_β-carbon: (e) $(\phi, \psi) = (-57.4°, -47.5°)$ (α_R-helix); (f) $(-138.8°, 134.7°)$ (β_A-sheet); (g) $(-66.3°, -24.1°)$ (3^R_{10}-helix); (h) $(-84.3°, 159.0°)$ (3_I-helix).

Figures 44e–h show the calculated orientations of the PAS of the nuclear shielding tensors of the L-alanine C_α-atoms in peptides with respect to the molecular frame. As is seen from these figures, the calculated orientation of the PAS for C_α is quite different from sample to sample. For all of the dihedral angles employed in the calculations, the σ_{33} component of the ^{13}C nuclear shielding tensor of the L-alanine C_α always lies along the C_α–C' bond. However, for the dihedral angles $(\phi, \psi) = (-57.4°, -47.5°)$ (α_R-helix),

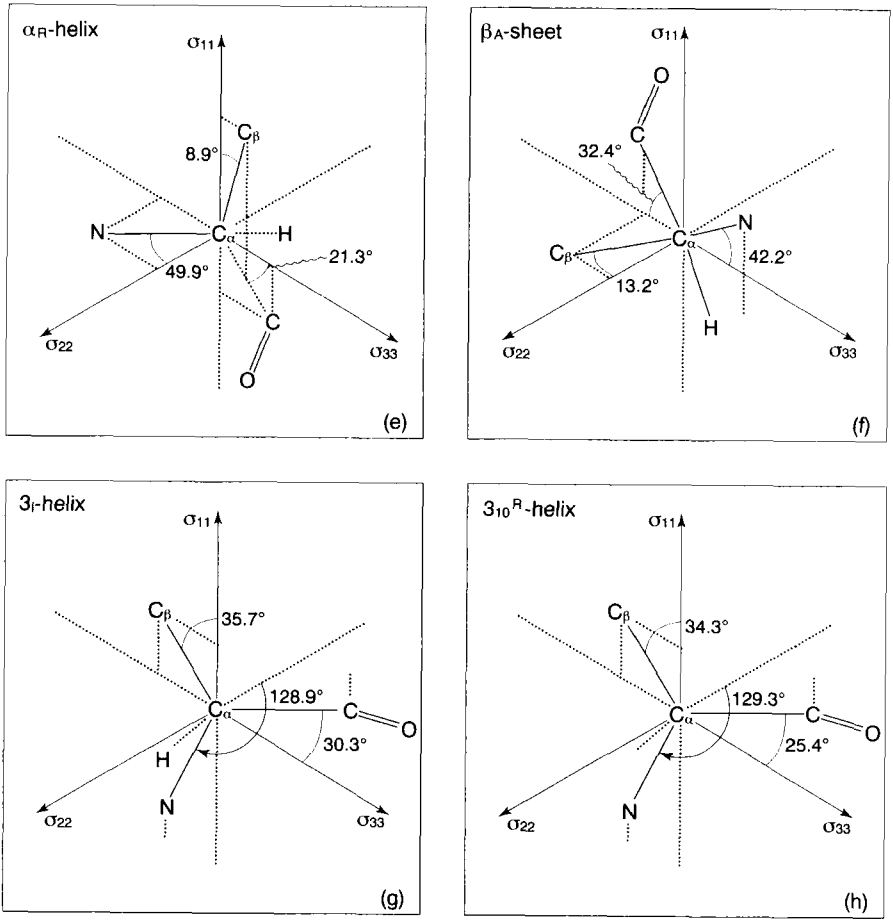

Fig. 44. continued

(−66.3°, −24.1°) (3_{10}-helix), and (−84.3°, 159.0°) (3_1-helix), the σ_{11} component lies along a direction which deviates slightly from the C_α—C_β bond; for the dihedral angles $(\phi, \psi) = (-138.8°, 134.7°)$ (β_A-sheet), the σ_{22} component is along this direction. As shown in Table 12, the principal value that lies nearly along the C_α—C_β bond is 47.53 ppm for the β_A-sheet form, 61.93 ppm for the α_R-helix form, 64.74 ppm for the 3_{10}-helix form, and 65.79 ppm for $(\phi, \psi) = (-84.3°, 159.0°)$ (3_1-helix). Changes of the dihedral angles cause large deviations in the nuclear shielding tensor element that is along the C_α—C_β bond. Moreover, since the value of σ_{33} depends on changes from one dihedral angle to another, it is obvious that there exists an explicit dihedral angle

Table 12. Calculated ^{13}C chemical shielding for the C_α- and C_β-atoms of the L-alanine residue by the 4-31G-GIAO-CHF method.

	^{13}C chemical shielding (ppm)							
	C_α				C_β			
Sample	σ_{iso}	σ_{11}	σ_{22}	σ_{33}	σ_{iso}	σ_{11}	σ_{22}	σ_{33}
α_R-helix	45.52	61.93	43.69	30.93	15.72	28.16	22.14	−3.16
β_A-sheet	44.73	62.02	47.53	24.64	18.74	37.06	21.70	−2.53
3_1-helix	43.62	65.79	46.46	18.91	15.94	33.80	17.97	−3.49
3^R_{10}-helix	45.71	64.74	45.04	26.37	15.84	32.47	19.03	−4.00

dependency for the value of σ_{33}. Consequently, if the carbonyl group in the L-alanine residue forms a hydrogen bond, the σ_{33} value will probably be affected. The principal values of the nuclear shielding tensor of the L-alanine C_α-carbon in peptides have not yet been measured, because the nuclear shielding anisotropy is not so large that we can accurately evaluate it. Measurement of the principal values of the nuclear shielding tensor for the L-alanine C_α-atom remains as a future task.

4.2. Applications to the structural elucidation of some proteins: Basic pancreatic trypsin inhibitor (BPTI); ribonuclease H from *E. coli* (RNaseH)

^{13}C chemical shifts of C_β for the L-Ala residues in RNase H

The correlation between the ^{13}C chemical shifts of peptides and their backbone conformations is of great interest for structural elucidation studies. We have calculated the isotropic ^{13}C chemical shift of the C_β-atoms in the L-alanine residue using the GIAO-CHF method; the calculated shifts are shown in Table 13. A comparison of the calculated and experimental ^{13}C chemical shifts is given in Fig. 45. From this it is clear that the isotropic ^{13}C chemical shift of the L-alanine C_β is apparently related to the main-chain dihedral angles of the L-alanine residue of RNase H in aqueous solution. In this figure, the observed chemical shift behaviour of the L-alanine residue C_β is generally similar to that of the RNase H in aqueous solution. From this comparison between the experimental and calculated chemical shifts, one appreciates that there are some data that deviate from the dashed line. This may be produced by a difference between the solution and the crystalline structure of the protein, or by the interaction between the L-alanine C_β-atom and its surrounding, solvent molecules (H_2O) or side-chains of the adjacent amino acid residues. For

Table 13. Geometrical parameters of L-alanine residues in RNase H and BPTI determined by X-ray diffraction, and ^{13}C NMR chemical shifts of the carbonyl-, C_α- and C_β-atoms in the corresponding residues.

Amino acid residue[a]	Dihedral angle (°)				Observed chemical shift (ppm)			Calculated chemical shift (ppm)	
	ϕ	ψ	ω	$R_{N\cdots O}$	C′	C_α	C_β	C_α	C_β
A24	−144.6	134.7	178.7	2.83	173.7	49.2	21.3	49.55	22.74
A37	−160.5	150.4	179.9	3.27	172.1	50.2	19.7	50.13	21.61
A51	−55.2	−46.1	−179.1	3.20	175.5	53.3	19.3	49.76	19.88
A52	−71.3	−35.4	−178.6	3.24	176.1	52.7	15.3	49.52	19.90
A55	−65.8	−49.2	178.1	3.30	175.6	52.7	17.2	49.27	19.83
A58	−81.0	−11.5	176.8	–	176.1	51.2	17.2	49.34	20.93
A93	−62.4	−22.9	−179.0	–	175.8	53.1	16.0	50.07	20.14
A109	−53.5	−49.9	−177.5	3.22	178.4	52.9	15.8	49.66	20.00
A110	−72.2	−25.6	180.0	3.30	178.1	52.7	16.5	49.66	20.11
A125	−66.5	123.7	−179.8	–	176.1	50.8	16.4	49.74	19.06
A137	−53.7	−57.3	179.8	3.25	177.3	53.5	16.6	49.29	20.17
A139	−67.4	−38.4	177.7	–	178.9	52.9	15.7	49.60	19.77
A140	−67.6	−41.7	−179.0	3.06	177.7	52.7	15.3	49.51	19.76
A141	−60.5	−22.9	−178.9	3.31	175.8	52.7	16.0	50.14	20.20
A16	−76.2	172.0	170.6	–	–	50.5	18.5		
A25	−62.3	−28.0	177.0	–	–	53.0	17.5		
A27	−82.9	−23.1	−178.7	–	176.3	50.5	19.0		
A40	−62.5	151.1	170.6	–	176.9	52.5	18.5		
A48	−61.7	−35.9	−179.4	2.80	177.9	53.5	16.0		

[a]A = Alanine.

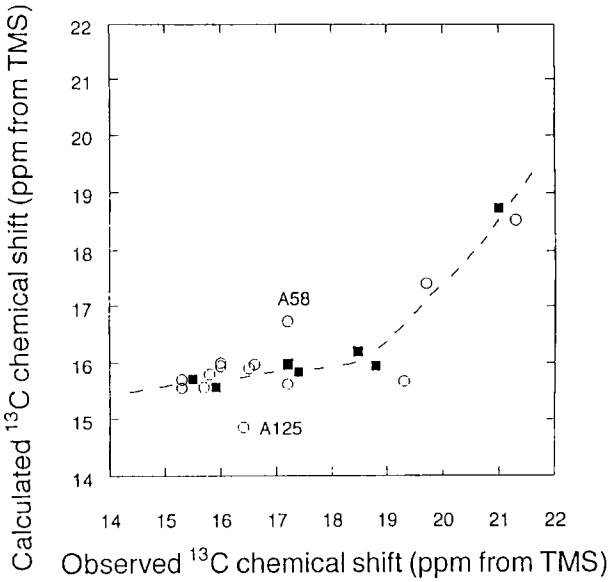

Fig. 45. Comparison of the calculated chemical shifts with the observed shifts of the L-alanine residue C_β-atoms of some peptides in the solid state (solid squares) and in RNaseH in the solution state (open circles).

example, the data for A51, A58, and A125 as shown in Fig. 45 deviate from the correlation curve; where A_i indicates the *i*th L-alanine residue. These L-alanine residues do not form any hydrogen bond in the protein; that is, the solvent molecules or side-chains of adjacent residues can be proximate to the C_β-methyl group. From such a situation, it is thought that the isotropic chemical shifts for the A51, A58 and A125 C_β-atoms are affected by not only their main-chain dihedral angles but also by the above-mentioned interactions. It is important in studying the functional aspects of a protein to detect these interactions. The detection of such interactions in solution can only be done by a comparison of solid-state NMR measurements and chemical shift calculations, as well as solution NMR and X-ray diffraction studies.

^{13}C chemical shifts of the C_α-atoms of the L-Ala residues in RNase H

Chemical shift calculations for the L-alanine residue C_α-atoms have been carried out by the GIAO-CHF method with a 4-31G basis set. In this calculation, *N*-acetyl-*N'*-methyl-L-alanine amide (Ac-L-Ala-NHMe) with the dihedral angles (ϕ, ψ) is employed. The experimental and calculated isotropic chemical shifts are shown in Table 13. A comparison between the experimental

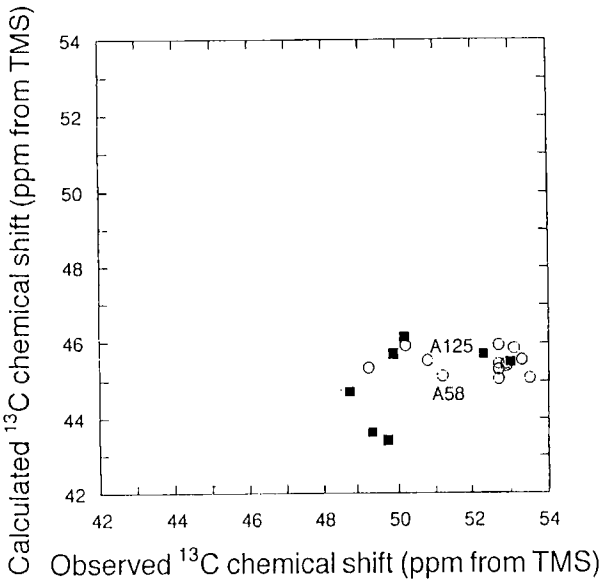

Fig. 46. Comparison of the calculated chemical shifts with the observed shifts of the L-alanine residue C_α-carbons in some peptides in the solid state (solid squares) and in RNaseH in the solution state (open circles).

and the calculated ^{13}C chemical shifts is shown in Fig. 46. From this figure it is found that there is no clear relationship between the experimental and the calculated chemical shifts. This is because we carried out the calculation without taking account of hydrogen-bonding effects. Although we have tried to perform calculations taking hydrogen-bonding into account, we have so far suffered from being unable to obtain the self-consistent field (SCF) convergence.

4.3. The relationship between the helical conformation and ^{13}C NMR chemical shift of the carbonyl-carbons of polypeptides in the solid state

It has been demonstrated that the ^{13}C chemical shift contour map for the C_β-carbon reasonably explains the experimental ^{13}C chemical shift behaviour for the L-alanine residue with the α-helix, β-sheet, etc. However, from the experimental results reported previously,[44,45,47,102] it has been shown that the ^{13}C chemical shifts of the amino carbonyl-carbons of various amino acid residues such as those of glycine (Gly), L-Ala, L-valine (L-Val), L-leucine (L-Leu) and L-asparatic acid (L-Asp) residues are closely related to the

hydrogen-bond length. From these previous results, it can be appreciated that the ^{13}C chemical shift of the amide carbonyl-carbon in polypeptides is closely related not only to the main-chain conformation but also to the hydrogen-bond length. In the helical region it is apparent from the structural requirement that in the helical conformation formed by intramolecular interactions there is a close relationship between the dihedral angles (ϕ, ψ) and hydrogen-bond length for the peptides and polypeptides. Therefore, if in the right-handed helix region (the dihedral angles ($\phi = -110°$ to $-20°$ and $\psi = -110°$ to $-20°$)) the dihedral angles (ϕ, ψ) are fixed, the hydrogen-bond length and angle are immediately determined. This means that the conformation dependence of the ^{13}C chemical shift of the amide carbonyl-carbon comes from the hydrogen-bond length variation through a change of the dihedral angles (ϕ, ψ). With this in mind, the ^{13}C chemical shift contour map of the amide carbonyl-carbon of some amino acid residues is produced as a function of the dihedral angles (ϕ, ψ) in the vicinity of the helix region using the relationship between the ^{13}C chemical shift and hydrogen-bond length reported previously. This contour map has been used to explain satisfactorily the experimental ^{13}C chemical shift behaviour.

Calculation of the hydrogen-bond lengths and angles as functions of the dihedral angles (ϕ, ψ)

Polypeptides with a helical conformation form intramolecular hydrogen bonds that stabilize the conformation. The hydrogen-bond length and angle are closely related to the main-chain helical conformation with specified dihedral angles (ϕ, ψ) in the vicinity of the α-helix form. Thus, when standard geometries are used for the bond lengths and bond angles,[103] the main-chain conformation and also the hydrogen-bond length and angle can immediately be determined by giving the dihedral angles (ϕ, ψ).[104]

In geometrical calculations on intramolecular separation ($R_{N\cdots O}$) between nitrogen and oxygen atoms in the $\rangle C{=}O\cdots H{-}N\langle$ form and hydrogen-bond angle ($\angle C{=}O\cdots N$), we have adopted a pentapeptide molecule as a model for polypeptides. The α-helical conformation for the pentapeptide is shown in Fig. 47, where the dotted line shows the intramolecular hydrogen bond. The bond lengths and angles are assumed to be the same for all of the amino acid residues except for $\angle C(=O)-C_\alpha-N$. The bond lengths for the $N-C_\alpha$, $C_\alpha-C(=O)$, $C(=O)-N$ and $C=O$ bonds are assumed to be 1.453, 1.530, 1.325 and 1.230 Å, respectively, and the bond angles for $\angle C_\alpha-C(=O)-N$, $\angle O-C-N$, $\angle C_\alpha-C=O$ and $\angle C(=O)-N-C_\alpha$ are assumed to be 115.0°, 124.5°, 120.5° and 121.0°, respectively.[103] As the bond angle Θ, we use 111.0° for the Gly residue and 109.3° for the L-Ala, L-Leu, L-Val and L-Asp residues.[103] The angle ω is fixed to be 180° for all of the amino acid residues.

Using these bond lengths and angles, the hydrogen-bond length and angle for any specified helix forms in polypeptides can be calculated as a function of

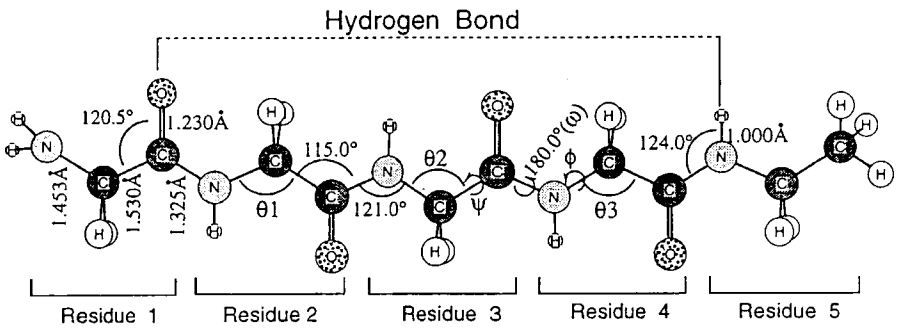

Fig. 47. Molecular structure of pentapeptide molecule. The possible hydrogen bond obtained by forming the α-helix form is shown by the dashed line. The definition of the dihedral angles (ϕ, ψ) is indicated. For the bond angle Θ ($\angle$C(=O)$-$C$_\alpha$$-$N), 111.0° is used for the Gly residue and 109.3° for the L-Ala, L-Leu, L-Val and L-Asp residues.

the dihedral angles (ϕ, ψ) in the skeletal bonds. The calculations were carried out at intervals of 1° by changing the dihedral angles (ϕ, ψ) from $-110°$ to $-20°$ in the vicinity of the right-handed α-helix form ($\phi = -57.4°$ and $\psi = -47.5°$). The hydrogen-bond lengths and bond angles obtained are shown as the contour maps of functions of the dihedral angles (ϕ, ψ) in Figs. 48 and 49, respectively.

Calculation of the ^{13}C NMR chemical shift contour map as a function of the dihedral angles (ϕ, ψ)

In previous work on the effect of hydrogen-bonding on the ^{13}C chemical shift of the amide carbonyl-carbon in solid polypeptides and oligopeptides,[44,45,47,102] it has been demonstrated that the isotropic chemical shifts (δ_{iso}) of the Gly, L-Ala, L-Val, L-Leu and L-Asp residues are predominantly governed by $R_{N\cdots O}$, the separation between the nitrogen and oxygen atoms in the hydrogen bond, and move linearly to high frequency with a decrease in $R_{N\cdots O}$ as expressed in ppm by Eqs (36)–(41).

Using these relationships, the $R_{N\cdots O}$ values of polypeptides in the solid state have been determined through the observation of the carbonyl ^{13}C chemical shift. Further, it has been shown that the $R_{N\cdots O}$ values for the guest Gly residue incorporated into host polypeptides and proteins are successfully determined through the observation of the carbonyl ^{13}C chemical shift.[45,102] Using Eqs (13)–(18) and the calculated $R_{N\cdots O}$ contour map (Fig. 48), the ^{13}C chemical shift contour map was produced as a function of the dihedral angles (ϕ, ψ) as shown in Fig. 49. On the basis of these contour maps, the main-chain helical conformation is analysed below.

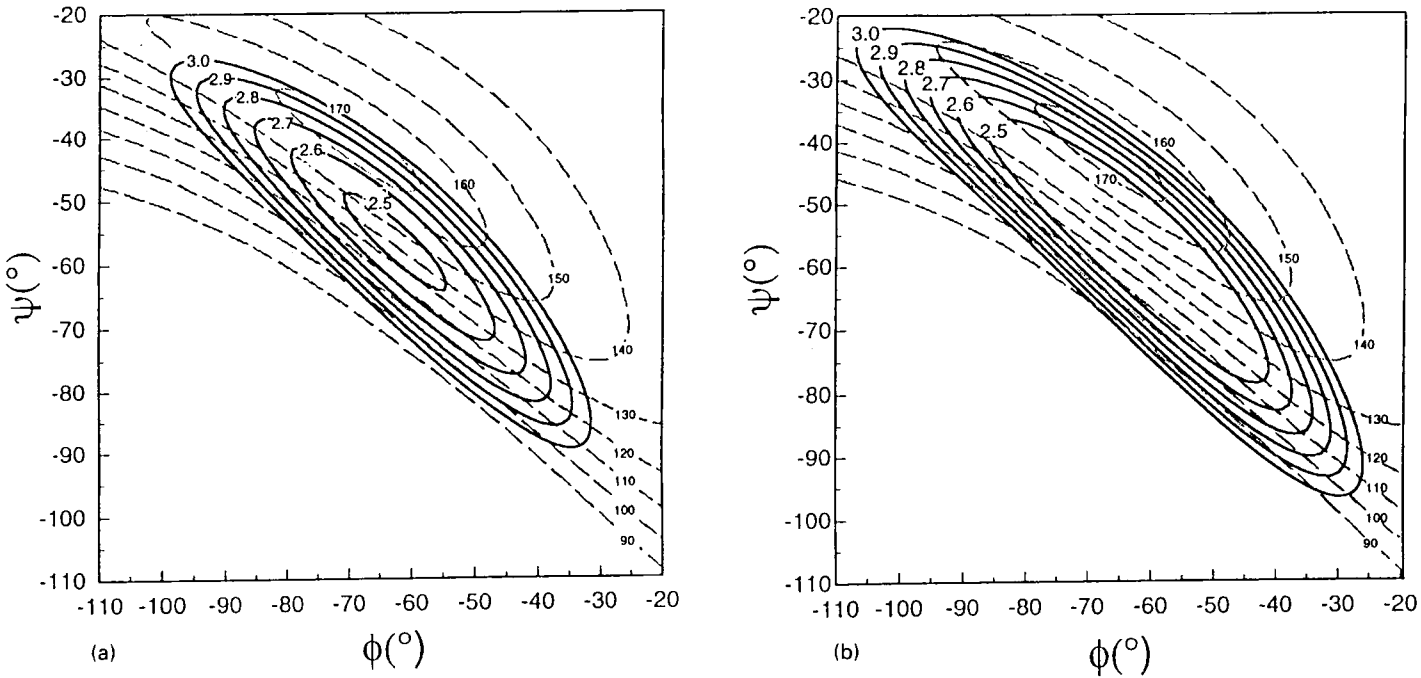

Fig. 48. The separation ($R_{N\cdots O}$) and angle contour maps as functions of the dihedral angles (ϕ, ψ) for (a) the Gly residue and (b) the L-Ala, L-Leu, L-Val and L-Asp residues. The $R_{N\cdots O}$ value and angle contour lines are represented by the solid and dotted lines, respectively. $R_{N\cdots O}$ and angle are expressed in Å and degrees, respectively.

^{13}C chemical shift contour maps for the carbonyl-carbon of the Gly, L-Ala, L-Leu, L-Val and L-Asp residues

The bold solid lines in Figs 48a and 48b show the $R_{N\cdots O}$ contour maps as functions of the dihedral angles (ϕ, ψ) for the Gly residue, and for the L-Ala, L-Leu, L-Val and L-Asp residues in the vicinity of the right-handed α_R-helix form, respectively. $R_{N\cdots O}$ is expressed in angstroms at 0.3 Å intervals in the range from 2.5 to 3.0 Å. It can be seen that each of the contour lines on the map distributes from the top left ($\phi = -110°$, $\psi = -20°$) to the bottom right ($\phi = -20°$, $\psi = -110°$) in Figs. 48a and 48b, and the region of the contour line decreases with a decrease in $R_{N\cdots O}$.

As the angle ∠N—Ca—C(=O) of the Gly residue is different from that of the L-Ala, L-Leu, L-Val and L-Asp residues, the $R_{N\cdots O}$ contour map for the Gly residue (Fig. 48a) is somewhat different from that of the L-Ala, L-Leu, L-Val and L-Asp residues (Fig. 48b). For example, the region of the contour line for the Gly residue, as shown in Fig. 48a, is smaller compared with the maps for the L-Ala, L-Leu, L-Val and L-Asp residues at the same value of $R_{N\cdots O}$.

As shown in Figs. 48 and 49, as the dihedral angles (ϕ, ψ) are varied, the hydrogen-bond angle changes together with change of $R_{N\cdots O}$. The broken lines in Figs. 48a and 48b show the hydrogen-bond angle (∠C=O···N) contour map as a function of the dihedral angles (ϕ, ψ). The angle ∠C=O···N is expressed in degrees at 20° intervals in the range from 90° to 180°. As seen from these figures, the deviation of the dihedral angles (ϕ, ψ) from ($\phi = -57.4°$, $\psi = -47.5°$) (the α-helix form) leads to a deviation of the angle ∠C=O···N from 180° (the linear hydrogen bond). Further, it is seen that the hydrogen-bond angle (∠C=O···N) contour map for the Gly residue is similar to that for the L-Ala, L-Leu, L-Val and L-Asp residues. This is different from the case of the $R_{N\cdots O}$ contour map.

Using Eq. (14) and the calculated $R_{N\cdots O}$ map for the Gly residue (Fig. 49a), the δ_{iso} contour maps for polyglycine (poly(Gly)) were produced as functions of the dihedral angles (ϕ, ψ) as shown in Fig. 49a. Similarly, using Eqs. (13)–(17) and the calculated $R_{N\cdots O}$ maps for the L-Ala, L-Leu, L-Val, and L-Asp residues (Fig. 48b), the δ_{iso} contour maps for poly(L-Ala) were produced as functions of the dihedral angles (ϕ, ψ) as shown in Fig. 49b. The δ_{iso} value for the amide carbonyl-carbon of poly(L-Ala) with the α-helix form is 176.8 ppm,[77] and the dihedral angles (ϕ, ψ) determined by X-ray diffraction are $\phi = -57.4°$ and $\psi = -47.5°$.[20] The data point for the α-helix form fixed with $\delta_{iso} = 176.8$ ppm and ($\phi = -57.4°$, $\psi = -47.5°$) (indicated by "c") is correctly placed on the predicted contour maps as shown in Fig. 49b. From this result, the possible dihedral angles (ϕ, ψ) for unknown conformations of polypeptides can be predicted by the δ_{iso} contour maps (Figs. 49a and 49b) for the amide carbonyl-carbon.

The hydrogen-bond angle is within a specified range for a given hydrogen-bond form. Most of the ∠C=O···N values for oligopeptides and

polypeptides used in our previous work[44,45,47,102] are within the range 145° to 165°, and the mean value and standard deviation are 156° and +4°, respectively. From this limitation, the acceptable region in the δ_{iso} contour maps is between the hydrogen-bond angle contour lines at $\angle C{=}O\cdots N = 152°$ and 160°, and so the optimum dihedral angles (ϕ, ψ) are predicted to be at the crossing point of the hydrogen-bond angle contour line at $\angle C{=}O\cdots N = 156°$ and the ^{13}C chemical shift contour line. The probable dihedral angles (ϕ, ψ) of poly(L-Ala) with the α-helix form are at the crossing point between the hydrogen-bond angle contour line at $\angle C{=}O\cdots N = 156°$ and the δ_{iso} contour line at 176.8 ppm. There are two crossing points, as seen from this contour map, but the point in the vicinity of $\phi = -57.4°$ and $\psi = -47.5°$ is acceptable for the α-helix as indicated by "a" in Fig. 49b. Thus, the predicted dihedral angles (ϕ, ψ) are not far from the dihedral angles ($\phi = -57.4°$, $\psi = -47.5°$) corresponding to the α-helix form indicated by "c" in Fig. 49b. Moreover, using Eq. (18) and the calculated $R_{N\cdots O}$ map for the Gly residue (Fig. 48a), the δ_{22} contour map for poly(Gly) was produced as a function of the dihedral angles (ϕ, ψ) as shown in Fig. 49c.

Application of the contour ^{13}C chemical shift map to the elucidation of the conformational behaviour of a small protein (BPTI)

Values of the dihedral angles (ϕ, ψ) and $R_{N\cdots O}$ of BPTI are accurately determined by X-ray diffraction,[29,41,42] and the assignments of the ^{13}C NMR signals for the C_α and amide carbonyl-carbons are made by solution NMR measurements.[30] In BPTI, the 47th to 56th amino acid residues, Ser(47)–Ala(48)–Glu(49)–Asp(50)–Cys(51)–Met(52)–Arg(53)–Thr(54)–Cys(55)–Gly(56), take the α_R-helix conformation. The oxygen atom in the amide group of the Ala(48) residue with the α_R-helix forms an intermolecular hydrogen bond with the nitrogen atom in the amide carbonyl group of the Met(52) residue. The δ_{iso} value for the amide carbonyl-carbon of Ala(48) is 177.9 ppm,[46] and the dihedral angles (ϕ, ψ) determined by X-ray diffraction are ($\phi = -61.7°$, $\psi = -35.9°$).[42] From the crossing point between the δ_{iso} contour line at 177.9 ppm and the hydrogen-bond angle contour line at 156° in Fig. 49b, the dihedral angles (ϕ, ψ) for Ala(48) in BPTI are predicted to be ($\phi = -45°$, $\psi = -61°$). These are very close to the dihedral angles ($\phi = -61.7°$, $\psi = -35.9°$) determined by X-ray diffraction. This means that the ^{13}C chemical shift contour map is very useful for analysing the conformations of polypeptides and proteins through the observation of the ^{13}C chemical shift of the amide carbonyl-carbons.

Finally, it can be concluded that the ^{13}C chemical shift contour maps are very useful for predicting the dihedral angles (ϕ, ψ) of polypeptides and proteins in the solid state through the ^{13}C shifts of the amide carbonyl-carbons of the Gly, L-Ala, L-Leu, L-Val and L-Asp residues.

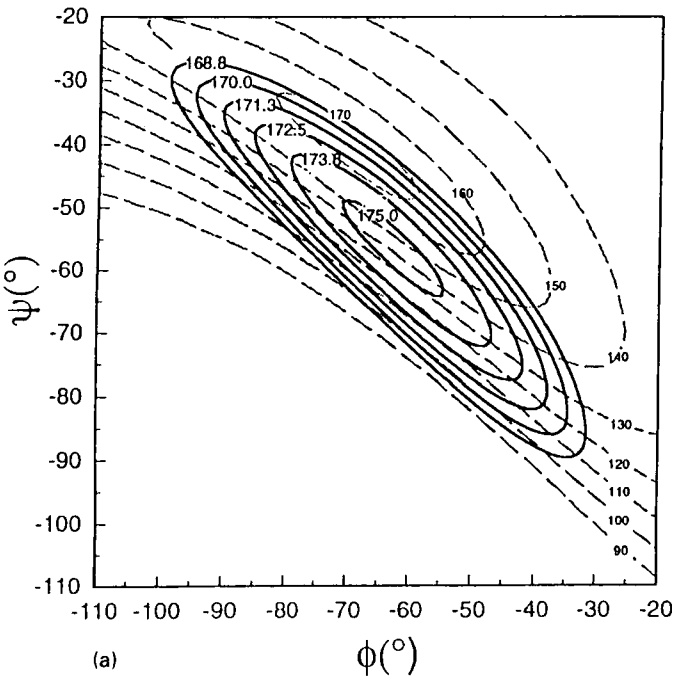
-20
-30
-40
-50
-60
-70
-80
-90
-100
-110
ψ(°)
-110 -100 -90 -80 -70 -60 -50 -40 -30 -20
φ(°)
168.8
170.0
171.3
172.5
173.8
175.0
170
160
150
140
130
120
110
100
90

(a)

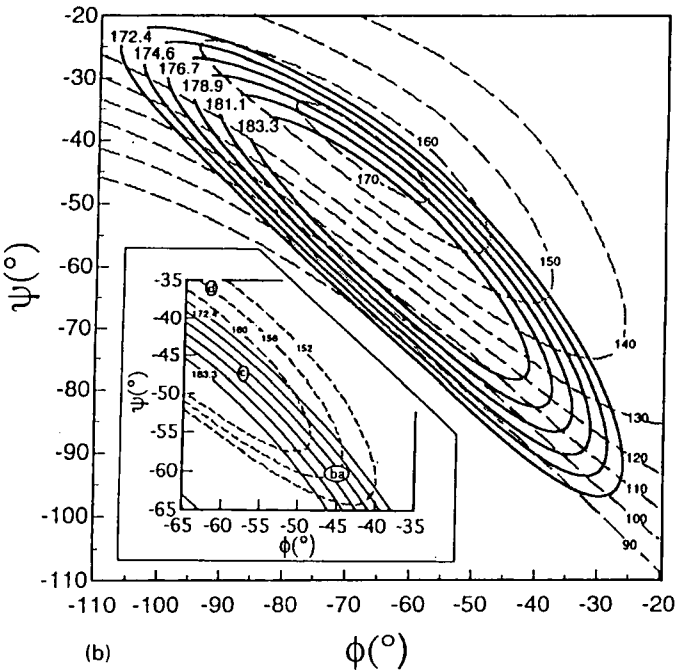
-20
-30
-40
-50
-60
-70
-80
-90
-100
-110
ψ(°)
-110 -100 -90 -80 -70 -60 -50 -40 -30 -20
φ(°)
172.4
174.6
176.7
178.9
181.1
183.3
160
170
150
140
130
120
110
100
90
-35
-40
-45
-50
-55
-60
-65
-65 -60 -55 -50 -45 -40 -35
ψ(°)
φ(°)
θ
θ
ba

(b)

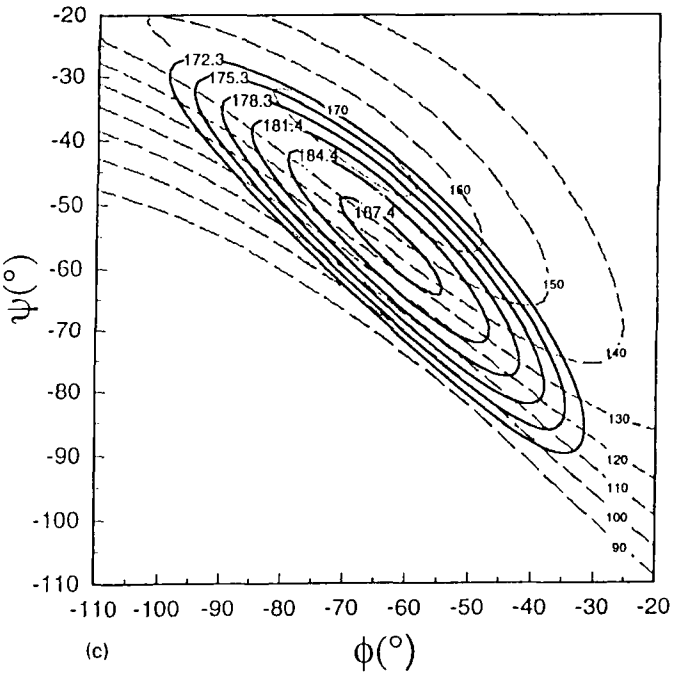

Fig. 49. The δ_{iso} contour maps for (a) Gly and (b) L-Ala residue carbonyl-carbons and (c) the δ_{22} contour map for the Gly residue carbonyl-carbon as functions of the dihedral angles (ϕ, ψ). Magnification of the range of the dihedral angles (ϕ, ψ) from $\phi = -65°$ to $-35°$ and from $\psi = -65°$ to $-35°$ is shown in the lower left of (b). The labels a and b indicate the predicted dihedral angles (ϕ, ψ) for poly(L-Ala) and any specified amino acid residue sequence with α_R-helix form in BPTI, respectively, obtained from the δ_{iso} for L-Ala and Eq. (36). The labels c and d indicate the dihedral angles (ϕ, ψ) for poly(L-Ala) and BPTI with α_R-helix form, respectively, obtained by X-ray diffraction.

5. CONCLUSIONS

As discussed, it is concluded that solid-state high-resolution NMR spectroscopy combined with quantum-chemical calculation is a very useful methodology for elucidating the hydrogen-bonded structure of peptides and polypeptides, including proteins, in the solid state.

REFERENCES

1. R. R. Ernst, G. Bodenhausen and A. Wokaun, *Principles of Nuclear Magnetic Resonance in One and Two Dimensions*, Oxford University Press, New York, 1987.
2. E. R. Andrew, A. Bradbury and R. G. Eades, *Nature*, 1958, **182**, 1659. I. J. Lowe, *Phys. Rev. Lett.*, 1959, **2**, 285.
3. A. Pines, M. G. Gibby and J. S. Waugh, *J. Chem. Phys.*, 1972, **56**, 1776.
4. N. Bloembergen and T. J. Rowland, *Acta Metall.*, 1953, **1**, 731.
5. J. Herzfeld and A. Berger, *J. Chem. Phys.*, 1980, **73**, 6021.
6. J. Fenzke, B. Maess and H. Pfeifer, *J. Magn. Reson.*, 1990, **88**, 172.
7. P. D. Ellis, G. E. Maciel and J. W. McIver, Jr, *J. Am. Chem. Soc.*, 1972, **94**, 4069.
8. I. Ando and G. A. Webb, *Theory of NMR Parameters*, Academic Press, London, 1983.
9. R. Ditchfield, *Mol. Phys.*, 1974, **27**, 789.
10. K. Wolinski, J. F. Hinton and P. Pulay, *J. Am. Chem. Soc.*, 1990, **112**, 8251.
11. F. A. Momany, R. F. McGuire, J. F. Yan and H. A. Scheraga, *J. Phys. Chem.*, 1971, **75**, 2286.
12. H. Kurosu, G. A. Webb and I. Ando, *Magn. Reson. Chem.*, 1992, **30**, 1122.
13. N. Izumiya, T. Kato, M. Ohno and H. Aoyagi, *Peptide Synthesis*, Marzen, Tokyo, 1975.
14. O. W. Howarth, *Prog. NMR Spectrosc.*, 1978, **12**, 1.
15. Y. Harada and Y. Iiyaka, *Acta Crystallogr.*, 1974, **B30**, 1452.
16. G. Valle, M. Crisma, F. Formaggio, C. Toniolo and C. Jung, *Justus Liebigs Ann. Chem.*, 1987, 1055.
17. V. Lalitha and E. Subramanian, *Indian J. Pure Appl. Phys.*, 1985, **23**, 506.
18. P. G. Jones, L. Falvello and O. Kennard, *Acta Crystallogr.*, 1978, **B34**, 1939.
19. S. Wo, P. Declercq, B. Tinant and M. V. Meerssche, *Bull. Soc. Chim. Belg.*, 1987, **96**, 515.
20. S. Arnott and S. D. Dover, *J. Mol. Biol.*, 1967, **30**, 209.
21. S. Ando, I. Ando, A. Shoji and T. Ozaki, *J. Am. Chem. Soc.*, 1988, **110**, 3380.
22. S. J. Opella and M. H. Frey, *J. Am. Chem. Soc.*, 1979, **101**, 5854.
23. S. Vega, E. T. Olejniczak and R. G. Griffin, *J. Chem. Phys.*, 1984, **80**, 4832.
24. K. Morokuma, *Chem. Phys. Lett.*, 1971, **19**, 129.
25. C. J. Hartzell, M. Whitfield, T. G. Oas and G. P. Drobny, *J. Am. Chem. Soc.*, 1987, **109**, 5966.
26. T. Yamazaki, M. Yoshida and K. Nagayama, *Biochemistry*, 1993, **32**, 5656.
27. W. Yang, W. A. Hendrickson, R. J. Crouch and Y. Satow, *Science*, 1990, **249**, 1398.
28. K. Katayanagi, M. Miyagawa, M. Matsushima, M. Ishikawa, S. Kanaya, H. Nakamura, M. Ikehara, T. Matsuzaki and K. Morikawa, *J. Mol. Biol.*, 1992, **223**, 1029.
29. S. Deisenhofer and W. Steigemann, *Acta Crystallogr. Sect. B*, 1975, **31**, 238.
30. E. Tuchen and P. E. Hansen, *Biochemistry*, 1988, **27**, 8568.
31. Y. Harada and Y. Iitaka, *Acta Crystollogr. Sect. B*, 1974, **30**, 1452.
32. R. Bosh, K. P. Voges, G. Jung and W. Winter, *Acta Crystallogr. Sect. C*, 1983, **39**, 481.
33. M. E. Kamwaya, O. Oster and H. Bradaczek, *Acta Crystallogr. Sect. B*, 1982, **38**, 172.
34. S. Arnott and S. D. Dover, *J. Mol. Biol.*, 1967, **30**, 209.
35. S. Arnott, S. D. Dover and A. Elliott, *J. Mol. Biol.*, 1967, **30**, 201.

36. B. Lotz and H. D. Keith, *J. Mol. Biol.*, 1971, **61**, 201.
37. T. Konishi and M. Kurokawa, *Sen'i Gakkaishii*, 1968, **24**, 550.
38. D. B. Chesnut, *Annu. Rep. NMR Spectrosc.*, 1989, **21**, 51.
39. A. Naito, S. Ganapathy, K. Akasaka and C. A. McDowell, *J. Chem. Phys.*, **74**, 3190.
40. S. Kuroki, A. Takahashi, I. Ando, A. Shoji and T. Ozaki, *J. Mol. Struct.*, 1994, **323**, 197.
41. A. Wlodawer, J. Deisenhofer and R. Huber, *J. Mol. Biol.*, 1987, **193**, 145.
42. A. Wlodawer, J. Nachman, G. L. Gilliland, W. Gallagher and C. Woodward, *J. Mol. Biol.*, 1987, **198**, 469.
43. J. F. Baugher, P. C. Taylor, T. Oja and P. J. Bray, *J. Chem. Phys.*, 1969, **50**, 4914.
44. N. Asakawa, S. Kuroki, H. Kurosu, I. Ando, A. Shoji and T. Ozaki, *J. Am. Chem. Soc.*, 1992, **114**, 3261.
45. K. Tsuchiya, A. Takahashi, N. Takeda, N. Asakawa, S. Kuroki, I. Ando, A. Shoji and T. Ozaki, *J. Mol. Struct.*, 1995, **350**, 233.
46. E. Tuchen and P. E. Hansen, *Biochemistry*, 1988, **27**, 8568.
47. S. Ando, T. Yamanobe, I. Ando, A. Shoji, T. Ozaki, R. Tabeta and H. Saito, *J. Am. Chem. Soc.*, 1985, **107**, 7648.
48. T. Kameda and I. Ando, *J. Mol. Struct.*, 1997, **412**, 197.
49. P. D. Ellis, G. E. Maciel and J. M. McIver, Jr, *J. Am. Chem. Soc.*, 1972, **94**, 4069.
50. M. Kondo, I. Ando, R. Chujo and A. Nishioka, *J. Magn. Reson.*, 1976, **24**, 315.
51. B. J. Lotz, *J. Mol. Biol.*, 1974, **87**, 169.
52. G. N. Ramachandran, V. Sasisekharan and C. Ramakrishnan, *Biochim. Biophys. Acta*, 1966, **112**, 168.
53. S. Arnott and A. L. Wonacott, *J. Mol. Biol.*, 1965, **21**, 371.
54. S. Arnott, S. D. Dover and A. Elliott, *J. Mol. Biol.*, 1967, **30**, 201.
55. R. E. Stark, L. W. Jelinski, D. J. Ruben, D. A. Torcha and R. G. Griffin, *J. Magnetic Reson.*, 1983, **55**, 266.
56. T. G. Oas, C. J. Hartzell, T. J. McMahon, G. P. Drobny and F. W. Dahlquist, *J. Am. Chem. Soc.*, 1987, **109**, 5956.
57. H. Saito, R. Tabeta, A. Shoji, T. Ozaki and I. Ando, *Macromolecules*, **16**, 1983, 1050.
58. T. Taki, S. Yamashita, M. Satoh, A. Shibata, T. Yamashita, R. Tabeta and H. Saito, *Chem. Lett.*, 1981, 1803.
59. H. R. Kricheldorf and D. Muller, *Macromolecules*, 1983, **16**, 615.
60. N. Asakawa, H. Kurosu, I. Ando, A. Shoji and T. Ozaki, *J. Mol. Struct.*, 1994, **317**, 119.
61. N. Asakawa, H. Kurosu and I. Ando, *J. Mol. Struct.*, 1994, **323**, 279.
62. G. A. Webb and M. Witanowski, *Proc. Indian Acad. Sci. (Chem. Sci.)*, 1985, **94**, 241.
63. G. Harbison, J. Herzfeld and R. J. Griffin, *J. Am. Chem. Soc.*, 1981, **103**, 4752.
64. T. A. Cross, J. A. Diverdi and S. T. Opella, *J. Am. Chem. Soc.*, 1982, **104**, 1759.
65. T. A. Cross, M. H. Fray and S. T. Opella, *J. Am. Chem. Soc.*, 1983, **105**, 7471.
66. H. G. Forster, D. Muller and H. R. Kricheldorf, *Int. J. Biol. Macromol.*, 1983, **5**, 101.
67. T. H. Huang, W. W. Achovchin, R. G. Griffin and C. M. Dobson, *Biochemistry*, 1984, **23**, 5933.
68. E. O. Stejeskal, J. Schaefer and R. A. MaKay, *J. Magn. Reson.*, 1984, **57**, 471.
69. C. N. Matthews, R. Ludicky, J. Schaefer, E. O. Stejeskal and R. A. MaKay, *Origins Life*, 1984, **14**, 243.
70. T. A Cross and S. T. Opella, *J. Mol. Biol.*, 1985, **182**, 367.
71. B. A. Choi, J. E. Roberts, J. N. S. Evans and M. F. Roberts, *Biochemistry*, 1986, **25**, 557.
72. J. Schaefer, J. R. Garbow, G. E. Jacob, T. M. Forest and G. E. Willsin, Jr, *Biochem. Biophys. Res. Commun.*, 1986, **137**, 736.
73. P. L. Stewart, K. G. Valentine and S. J. Opella, *J. Magn. Reson.*, 1987, **71**, 45.
74. (a) A. Shoji, T. Ozaki, T. Fujito, K. Deguchi and I. Ando, *Macromolecules*, 1987, **20**, 2441. (b) A. Shoji, T. Ozaki, T. Fujito, K. Deguchi, S. Ando and I. Ando, *Macromolecules*, 1989, **22**, 2860.

(c) A. Shoji, T. Ozaki, T. Fujito, K. Deguchi, S. Ando and I. Ando, *J. Am. Chem. Soc.*, 1990, **112**, 4693.
75. A. B. Biswas, E. W. Hughes, B. D. Sharma and J. N. Willson, *Acta Crystallogr.*, 1968, **B24**, 40.
76. T. F. Koetzle, W. C. Hamilton and R. Parthasarathy, *Acta Crystallogr.*, 1972, **B28**, 2083.
77. S. N. Rao and R. Parthasarathy, *Acta Crystallogr.*, 1973, **B29**, 2379.
78. V. Lathitha, R. Murali and E. Subramanian, *Int. J. Peptide Protein Res.*, 1986, **27**, 472.
79. V. Lalitha, E. Subramanian and R. Parthasarathy, *Int. J. Peptide Protein Res.*, 1986, **27**, 223.
80. V. Lalitha, E. Subramanian and J. Bordener, *Indian J. Pure Appl. Phys.*, 1977, **99**(2), 595.
81. J. P. Glusker, H. L. Carrell, H. M. Berman, B. Gallen and R. M. Peck, *J. Am. Chem. Soc.*, 1988, **110**, 2378.
82. W. M. Carson and M. L. Hackert, *Acta Crystallogr.*, 1978, **B34**, 1275.
83. Y. Hiyama, C. Niu, J. V. Silverton, A. Bavoso and D. A. Torchia, *J. Am. Chem. Soc.*, 1988, **110**, 2378.
84. R. Taylor, O. Kennard and W. Versichel, *Acta Crystallogr.*, 1984, **B40**, 280.
85. G. Valle, G. M. Bonora and C. Toniolo, *Gazz. Chim. Ital.*, 1984, **114**, 341.
86. P. M. Gadret, J. M. Leger and A. Carpy, *Acta Crystallogr.*, 1977, **B33**, 1067.
87. R. Murali, E. Subramanian and R. Parthasarathy, *Int. J. Peptide Protein Res.*, 1986, **27**, 478.
88. G. D. Smith, V. Z. Pletnev, W. L. Duax, T. M. Baiasubramanian, H. E. Bosshard, E. W. Czerwinski, N. E. Kendrick, F. S. Mathews and G. R. Marshall, *J. Am. Chem. Soc.*, 1981, **103**, 1493.
89. R. E. Marsh and M. R. N. Murthy, *J. Am. Chem. Soc.*, 1977, **99**, 1251.
90. D. W. Boykin, ed., *^{17}O NMR Spectroscopy in Organic Chemistry*, CRC Press, Boca Raton, FL, 1991.
91. A. L. Baumstark and D. W. Boykin, in *Advances in Oxygenated Processes*, vol. III (ed. A. L. Baumstark), pp. 141–176, JAI Press, 1991.
92. W. G. Klemperer, in *The Multinuclear Approach to NMR Spectroscopy* (ed. J. B. Lambert and F. G. Riddell), pp. 245–260, Dordrecht, Holland, 1983.
93. J. P. Kintzinger, in *Newly Accessible Nuclei*, vol. 2 (ed. P. Laszlo), pp. 79–104, Academic Press, New York, 1983.
94. D. W. Boykin and A. L. Baumstark, *New J. Chem.*, 1992, **16**, 357.
95. D. W. Boykin and A. Kumar, *J. Heterocyclic Chem.*, 1992, **29**, 1.
96. S. Kuroki, I. Ando, A. Shoji and T. Ozaki, *J. Chem. Soc., Chem. Commun.*, 1992 (5), 433.
97. R. Goc, E. Ponnusomy, J. Tritt-Goc and D. Fiat, *Int. J. Peptide Protein Res.*, 1988, **31**, 130.
98. R. Goc, J. Tritt-Goc and D. Fiat, *Bull. Magn. Reson.*, 1989, **11**, 238.
99. W. T. Astbury, C. H. Dalgleish, S. E. Darmon and G. B. B. M. Sutherland, *Nature*, 1948, **69**, 596.
100. F. H. C. Crich and A. Rich, *Nature*, 1955, **176**, 780.
101. A. Kevick, A. R. Al-Karaghouli and T. F. Koetzle, *Acta Crystallogr.*, 1977, **B33**, 3796.
102. T. Kameda, N. Takeda, S. Kuroki, H. Kurosu, S. Ando, A. Shoji and T. Ozaki, *J. Mol. Struct.*, 1996, **384**, 17.
103. F. A. Momany, R. F. MacGuire, A. W. Burgess and H. A. Sheraga, *J. Phys. Chem.*, 1975, **79**, 2361.
104. A. G. Walton, in *Polypeptides and Protein Structure* (ed. R. Glasgow), Elsevier-North Holland, Amsterdam, 1981.
105. S. T. Rao, *Crystallogr. Commun.*, 1973, **2**, 257.
106. V. Lathitha, E. Subramanian and J. Bordner, *Indian J. Pure Appl. Phys.*, 1985, **23**, 506.
107. Y. Yamada, I. Tanaka and T. Ashida, *Acta Crystallogr., Sect. B*, 1980, **36**, 331.
108. K. N. Goswami, V. S. Yadava and V. M. Padmanabhan, *Acta Crystallogr., Sect. B*, 1977, **33**, 1280.

109. D. S. Eggleston, E. J. Valente and D. J. Hodson, *Acta Crystallogr., Sect. B*, 1981, **37**, 1428.
110. H. Take, S. Kuroki, N. Asakawa, H. Kurosu and I. Ando, *Polymer Preprints, Japan*, 1992, **41**, 3436.
111. Q. Teng, M. Igbal, T. A. Cross, *J. Am. Chem. Soc.*, 1992, **114**, 5312.

This Page Intentionally Left Blank

NMR Imaging

WILLIAM S. PRICE

Water Research Institute, Sengen 2-1-6, Tsukuba, Ibaraki 305, Japan

ANNUAL REPORTS ON NMR SPECTROSCOPY
VOLUME 35 ISBN 0-12-505335-5

Copyright © 1998 Academic Press Limited
All rights of reproduction in any form reserved

This chapter extends upon the chapter 'Gradient NMR' (Annual Reports on NMR Spectroscopy ***32****, 51–142 (1996)) and covers the use of gradients for providing spatially dependent information. The chapter provides a general coverage of nonclinically oriented imaging especially high-resolution imaging (i.e., NMR microscopy), and surveys the types of experiments that are currently feasible and their applications. The chapter begins with a conceptual introduction to imaging followed by a discussion of the "building blocks" of imaging pulse sequences. In subsequent sections, the physical phenomena that produce contrast in images are considered as well as the pulse sequences that can be used to incorporate these sources of contrast into the image. The technical and hardware aspects of imaging are presented as well as a discussion of artefacts and complications in imaging. In the final section some examples of the applications to which imaging has been applied are surveyed.*

1. INTRODUCTION

NMR imaging has been recognized as a powerful diagnostic tool in medicine for more than two decades. In medical imaging systems the resolution is generally of the order of 1 mm^3. More recently and with the advent of smaller imaging systems (e.g., radiofrequency and gradient coils built especially for NMR tube size samples), ever higher levels of resolution are being obtained. In fact, the major NMR instrument makers now offer imaging accessories for many commercial spectrometers. Levels of resolution with volume element (voxel) sizes less than $(100\ \mu m)^3$ are now very commonplace. High-resolution imaging is generally termed NMR microscopy as the human eye cannot resolve voxels smaller than $(100\ \mu m)^3$. Presently, the highest resolution obtained is under $(10\ \mu m)^3$. The proton is still the predominant choice for imaging owing to its higher sensitivity and magnetogyric ratio. Other common nuclei are ^2H, ^{17}O, ^{19}F, ^{23}Na and ^{31}P. However, with the increasingly higher fields and more sensitive imaging probes, the range of feasible nuclei for imaging studies is increasing. Nonmedical imaging generally has fewer restrictions on the amount of time for which the sample may be imaged and on the experimental conditions such as RF irradiation limits.

NMR imaging is essentially the use of one or more magnetic (B_0) or radiofrequency (B_1) gradients to provide a well-defined spatial dependence to nuclear spin dynamics. A spatial image of the sample can then be reconstructed from the NMR signals acquired. The actual appearance of the image depends not only upon the spin density but also upon sources of contrast (e.g. local field fluctuations, molecular rotational dynamics and molecular translational motion), which modulate the image intensity and thus impart a signature of the local environment of the spin on to the image. In the case of biological studies, NMR microscopy provides excellent soft-tissue contrast and can make use of a number of endogenous contrast mechanisms that are directly related to tissue biochemistry, pathology and physiology. Although NMR microscopy can never compete with, for example, electron microscopy in terms of spatial resolution, it is the additional sources of contrast and the fact that the image results from the density of the particular type of spin being observed (e.g. ^{1}H) or even a particular molecule, together with the noninvasive nature of NMR, that set NMR imaging apart from all other forms of optical microscopy and tomography.[1]

Owing to the increasingly higher resolution obtainable and its ability to provide information on the spatial distribution of chemical species, spatially localized velocity and self-diffusion measurements, all in a noninvasive manner, imaging is becoming a standard tool with myriad applications in many areas of science. Areas of application include biotechnology, fluid dynamics, the food industry, natural product processing, petrochemicals, fluid dynamics, plant physiology, porous materials, the morphology and dynamics of polymeric materials and molecular dynamics.

This chapter extends upon the earlier contribution in the series, "Gradient NMR".[2] Whereas the earlier chapter was mainly concerned with the behaviour of nuclear spins under the influence of a single gradient, this chapter is concerned with the theory and applications of more than one gradient. The purpose of this chapter is threefold: (1) to provide a general coverage of selected areas in imaging so as to provide a "flavour" of what sort of information can be obtained; (2) to describe what type of experiments are currently feasible; and (3) since it is not possible to adequately survey either the methods or applications of imaging in a single chapter, to provide pointers to other sources of information. NMR imaging actually includes a number of subdisciplines including localized spectroscopy in which imaging techniques are used to provide spectroscopic information from a limited region of a whole sample (i.e. *v*olume *o*f *i*nterest: VOI), medical imaging, solid-state imaging and imaging of diffusion and flow. Particular emphasis will be placed on recent developments in imaging techniques, with a bias towards those that involve higher-resolution (i.e. microscopy) and nonmedical applications. Historical aspects can be found elsewhere.[3,4] Since NMR imaging is now such a huge area of research, the following areas are either beyond the scope of the present chapter or will be only mentioned in passing: imaging using surface coils and

localized spectroscopy,[5] ESR and EPR imaging[6] and force detection imaging.[7] The area of solid-state imaging was reviewed by Cory[8] in this series, and this chapter will not attempt to cover this area in any depth.

In Section 2, a conceptual introduction to imaging is presented, while in Section 3 the "building blocks" of imaging pulse sequences are discussed. In Section 4, the physical phenomena that produce contrast in images are considered. However, diffusion and flow as sources of contrast are considered separately in Section 6. Some representative imaging pulse sequences are presented in Section 5, with attention paid to how the contrast factors are incorporated. The technical and hardware aspects of imaging are presented in Section 7. Discussion of artefacts and complications is delayed until Section 8 since these can result from the sample, the pulse sequence or the hardware. Finally, in Section 9, some examples of the applications to which imaging has been applied are surveyed.

1.1. Literature sources

It should be noted that the recent *Encyclopedia of Nuclear Magnetic Resonance*[9] has chapters devoted to nearly every conceivable area of imaging and its applications. Reviews on specific areas of imaging are listed in the relevant sections in this chapter. While the common thread in imaging is the use of gradients, the common thread in the imaging literature is the plethora of acronyms, some for the same imaging technique, which results in maximum confusion for the reader.

The most complete treatment of imaging theory and techniques is that by Callaghan.[3] The book edited by Blümich and Kuhn[10] includes chapters dealing with many aspects of theory and application. More medically oriented books on magnetic resonance imaging (MRI) are by Mansfield and Morris,[11] Foster and Hutchison,[12] and Morris.[13] There have been numerous review articles on NMR imaging and microscopy[1,14–17] and also reviews on gradients featuring sections on imaging.[18,19] There have also been a few reviews on specific areas which are either totally or partially devoted to imaging applications. Many of these are listed in Section 9. The review by Gladden[20] specializes in applications to engineering. The area of solid-state imaging forms a very large body of work and there have been a number of reviews.[8,21–27]

2. BASIC IMAGING PRINCIPLES

This section attempts to provide a conceptual background to the imaging process sufficient to render the remainder of the chapter comprehensible and to provide an overview of how imaging (and this chapter) fits together. Crooks[28] has provided a succinct overview of image reconstruction methods including the factors leading to contrast.

Most of the work described in this chapter is based on variants of imaging techniques that produce images of all points within a plane, that is the projection reconstruction[29] and Fourier imaging[30] techniques. As will be seen below, imaging can be performed using B_0 and/or B_1 gradients. The properties of B_1 gradients are generally analogous to those of B_0 gradients except that whereas a B_0 gradient has a spatially dependent effect on the resonant frequency, B_1 gradients have a spatially dependent effect on the nutation angles.[18] As most of the current imaging studies are based on B_0 gradients, they represent the primary focus of the present chapter. However, it should be emphasized that under some circumstances B_1 gradients have advantages and these will be pointed out in the relevant sections.

At the most elementary level, the image can be thought of as a map of the spatial nuclear spin density, $\rho(\mathbf{r})$. Imaging is the technique by which the behaviour of the spins can be modulated by using cogent combinations of delays, radiofrequency (RF) pulses and gradients to obtain information on $\rho(\mathbf{r})$. The fundamental equation for describing NMR imaging is the Larmor equation, which for a single quantum transition in the presence of a static field of strength $\mathbf{B}_0$ (T) and a (normally linear) gradient $\mathbf{G}$ (T m^{-1}) is given by

$$\omega(\mathbf{r}) = \underbrace{\gamma\mathbf{B}_0}_{\substack{\text{spatially} \\ \text{homogeneous}}} + \underbrace{\gamma\mathbf{G}\cdot\mathbf{r}}_{\substack{\text{spatially} \\ \text{inhomogeneous}}} \tag{1}$$

where ω (rad s^{-1}) is the Larmor frequency, γ (rad T^{-1} s^{-1}) is the gyromagnetic ratio and we have neglected the small effect of the shielding constant. Thus, as depicted in Fig. 1, a spatially well-defined gradient applied to the nuclear spin results in a spatially dependent Larmor frequency (that is, spatial displacements in the direction of the gradient become frequency displacements). It is convenient to define a quantity

$$\mathbf{k} = (2\pi)^{-1}\gamma\mathbf{G}t \tag{2}$$

Thus $\mathbf{k}$ has units of m^{-1} and can be thought of as a reciprocal space vector. From Eq. (2) it can be seen that $\mathbf{k}$-space can be traversed by either changing the magnitude of G or altering the duration, t, of the application of G. The direction of the traverse is given by the direction of G. We can express the observed signal, $S(\mathbf{k})$, as a function of $\mathbf{k}$ as

$$S(\mathbf{k}) = \int \rho(\mathbf{r}) e^{i2\pi\mathbf{k}\cdot\mathbf{r}} d\mathbf{r} \tag{3}$$

Thus, from Eq. (3) it can be seen that $\rho(\mathbf{r})$ in the conjugate $\mathbf{r}$-space can be reconstructed from $S(\mathbf{k})$ by Fourier transformation, that is

$$\rho(\mathbf{r}) = \int S(\mathbf{k}) e^{-i2\pi\mathbf{k}\cdot\mathbf{r}} \, d\mathbf{k} \tag{4}$$

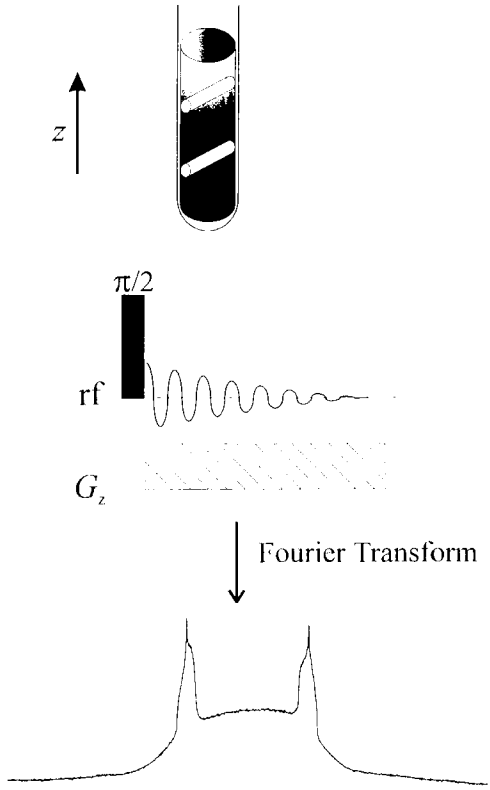

Fig. 1. An example of the use of a gradient and an RF pulse to produce a one-dimensional "image" or profile of an NMR tube containing water and a Teflon plug with two holes in it. The static field and the applied gradient are oriented down the tube (i.e. the z direction). In the absence of the gradient, all water protons, neglecting the small susceptibility and imperfections in B_0, have the same Larmor frequency. If a gradient is applied, the Larmor frequency becomes a function of the z position and thus the signal acquired shows two peaks corresponding to regions of high (NMR-visible) proton density, i.e. the water in the holes.

While conceptually correct, Eqs (3) and (4) do not indicate how to fill the void between theory and practice in imaging. Imaging involves a number of steps (see Fig. 2). In essence $\rho(\mathbf{r})$ is a three-dimensional (3D) quantity and thus we require three orthogonal gradients (i.e. one for each spatial dimension) in order to obtain the observed image, $\rho_I(\mathbf{r})$. Typically, not all of the image is sampled and even then, and as is usually the case, only a two-dimensional (2D) slice through the sample is acquired. A combination of gradients and (selective) RF pulses is used to acquire an image of (a section of) $\rho(\mathbf{r})$ into $\mathbf{k}$-space in the form of the signal $S(\mathbf{k})$. Depending on the experimental conditions used

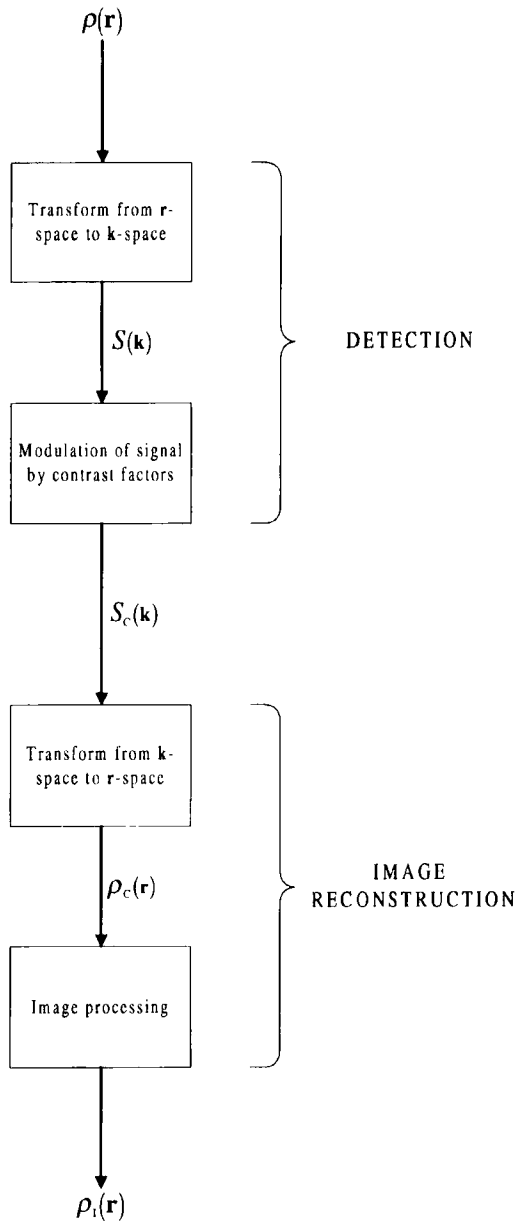

Fig. 2. A schematic representation of the imaging process. The spin density in **r**-space is transformed into a **k**-space representation using the imaging pulse sequence (i.e. gradients, delays and RF pulses). Depending on the sample and the pulse sequence employed, the signal acquired, $S_c(\mathbf{k})$, is modulated by contrast factors according to the properties of the sample. The image is then reconstructed from the acquired data set using a conjugate (e.g. Fourier) transform. Finally, the image may be further enhanced using image processing to give the final image, $\rho_i(\mathbf{r})$. (After Callaghan.[3])

(i.e. delays, gradient and RF pulses), the signal $S(\mathbf{k})$ will be modified such that nuclei with some distinctive property (chemical shift, relaxation behaviour, dipolar or scalar couplings, flow or diffusion, etc.) will have an unequal weighting in the signal (i.e. the signal will not just be a function of the population density of the observed nuclei). We will denote the signal modified to include the effects of contrast as $S_C(\mathbf{k})$. $S_C(\mathbf{k})$ is then transformed to give the nuclear spin density including the effects of a contrast factor $C(\mathbf{r})$, $\rho_C(\mathbf{r}) = C(\mathbf{r})\rho(\mathbf{r})$. Finally, $\rho_C(\mathbf{r})$ is processed (i.e. image processing), which may include the application of digital filters, etc., to give the displayed image $\rho_I(\mathbf{r})$.[3]

In Section 3 we consider in detail the building blocks (e.g. including volume selection, selective excitation) of imaging pulse sequences that can be used to transform from $\rho(\mathbf{r})$ to $S_C(\mathbf{k})$. In Section 4 image contrast is considered and how it can be incorporated into the acquired signal (i.e. $S_C(\mathbf{k})$). In Section 5 reconstruction of the image is considered (i.e. $S(\mathbf{k}) \rightarrow \rho_I(\mathbf{r})$).

3. SPATIAL ENCODING AND DECODING

3.1. Introduction

In this section the ways in which a combination of gradients and RF pulses can be used to transform from **r**-space to **k**-space are considered. There are three common ways in which a gradient can be used to impart a spatial dependence into the acquired NMR signal, (1) slice selection, (2) frequency-encoding and (3) phase-encoding, and these will be discussed in Sections 3.2–3.4, respectively. In Section 3.5 selective RF pulses are considered, and finally in Section 3.6 two typical imaging sequences are described. Mulkern[31] has provided a detailed summary of the in-plane spatial encoding process.

3.2. Slice selection

A slice of a sample can be selectively excited by the simultaneous application of a well-defined gradient through the sample to achieve a spatially dependent Larmor frequency (i.e. Eq. (1) and Fig. 1) with a frequency-selective (i.e. "soft") RF pulse (see Fig. 3). The slice thickness (Δz) will depend on the strength of the applied gradient and the frequency selectivity of the RF pulse, $\Delta\omega_{B_1}$ (see Section 3.5),

$$\Delta z = \frac{\Delta\omega_{B_1}}{\gamma G_z} \tag{5}$$

Further, the slice position is determined by the frequency (ω_{B_1}) of the excitation field $\mathbf{B}_1(t)$ with respect to the Larmor frequency ($\omega_0 = \gamma \mathbf{B}_0$) resulting from the static (polarizing) field, $\mathbf{B}_0$

$$z = \frac{\omega_{B_1} - \omega_0}{\gamma G_z} \tag{6}$$

The concept of slice selection is shown schematically in Fig. 3. It should be

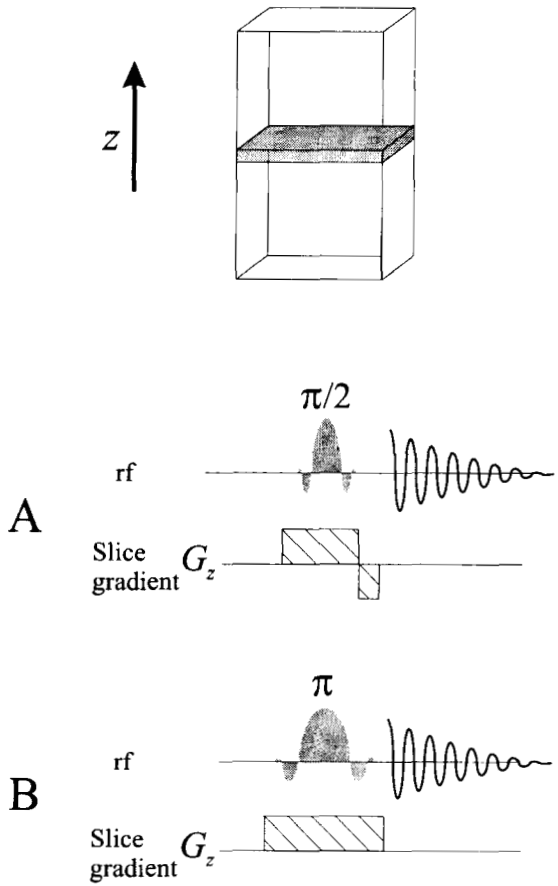

Fig. 3. Two possible slice selection schemes using selective RF pulses (denoted by the approximate sinc function shapes) together with a gradient applied perpendicular to the slice of interest. In scheme (A) the magnetization in the slice is rotated into the xy plane. Since the transverse magnetization is dephased during the slice selection, a short, negative gradient is applied immediately after the RF pulse to refocus the magnetization. (B) Slice selection using a π pulse. The magnetization is automatically refocused.

noted that any arbitrarily oriented plane can be selected by imposing a gradient normal to the required image plane.

The magnetization components within the excited frequency range are completely dephased immediately after the RF pulse and, consequently, the signal originating from different positions within the slice along the gradient direction will interfere destructively with one another. Thus, in the simplest case it is necessary to apply a negative gradient for a short period of time immediately after the RF pulse to refocus the magnetization (see Fig. 3A). A π pulse (see Fig. 3B), however, is self-refocusing. Other refocusing methods such as prefocused pulses[32–34] are possible and these have been considered in detail by Callaghan.[3]

3.3. Frequency encoding

If an NMR signal is acquired in the presence of a gradient, then the frequencies contained in the NMR signal will have a spatial dependence (see Eq. (1)) or, conversely, the spatial dimension along the direction of the gradient is frequency-encoded. In the simplest implementation, a gradient is applied immediately after the excitation pulse and the free induction decay (FID) is acquired in the presence of this gradient, subsequent Fourier transformation of the FID gives the one-dimensional (1D) profile $\rho(z)$ in the direction of the gradient, which we have taken to be z in this case (see Fig. 1). When used in this way, the applied gradient is termed the *frequency-encoding* or *readout* gradient. It is clear that frequency-encoding can be performed in a single scan.

The simplistic pulse sequence featured in Fig. 1 is susceptible to the effects of eddy currents generated by the rapid switching of the gradient (see Section 7.5), which distort the FID and consequently the resulting image. A common means of circumventing this problem is to use an echo sequence such that by the start of signal acquisition the perturbations of the magnetic field due to the eddy currents have become negligible. There are two types of echoes that can be used: (1) spin-echoes (see Fig. 4A) and (2) gradient-echoes (see Fig. 4B). Hennig has presented a detailed discussion of the echoes and their place in imaging.[35,36] It is important to understand the distinction between a gradient- and a spin-echo. In the case of a gradient-echo, at the time of signal acquisition only the gradient-induced phase has been refocused. In the case of the spin-echo, not only is the gradient-induced dispersion refocused but, by virtue of the inclusion of the π RF pulse, chemical shifts and frequency dispersion due to residual B_0 inhomogeneity and susceptibility effects in heterogeneous samples are also refocused. Whether this difference is significant in practice depends on the experimental conditions.

In a more general case when unequal gradient strengths are used during the defocusing and refocusing periods, refocusing occurs when the "area" of the

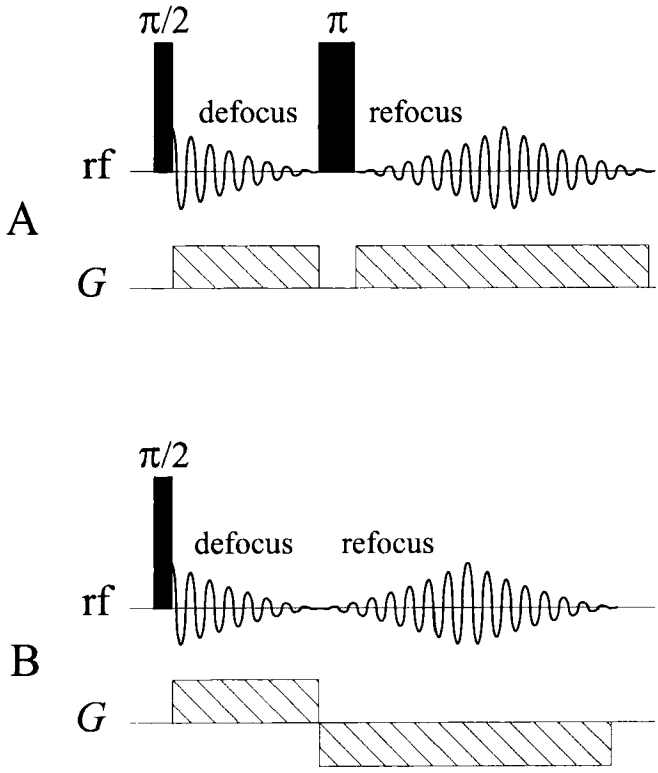

Fig. 4. (A) Gradient- and (B) spin-echo schemes for frequency encoding. Both sequences contain two gradient pulses. In the case of the gradient-echo, the gradient pulses are antiphase, while in the spin-echo sequence the sign of the applied gradient in the second half of the sequence is effectively negated by the π pulse. In a gradient-echo, only the phase dispersion resulting from the gradient pulses is refocused by the beginning of signal acquisition. In the spin-echo sequence, not only is the gradient-induced dispersion refocused but also chemical shift effects and dispersion due to magnetic inhomogeneities in the sample.

gradient in the defocusing period equals that of the refocusing period,

$$\int_{\text{defocusing}} G(t)\,\mathrm{d}t = \int_{\text{refocusing}} G(t)\,\mathrm{d}t \tag{7}$$

In Eq. (7) the gradient is written as $G(t)$ to emphasize that the gradient itself may be a time-dependent function.

3.4. Phase encoding

The third method of obtaining spatial information is to consider a spatially dependent phase change. If a gradient is applied for a fixed time, t, prior to signal acquisition then the phase of the signal, ϕ, is spatially dependent,

$$\phi(\mathbf{r}) = \int_0^t (\gamma \mathbf{B}_0 + \gamma \mathbf{G} \cdot \mathbf{r})\, dt \tag{8}$$

where the integrand is identically given by $\omega(\mathbf{r})$ as in Eq. (1). Since $\mathbf{B}_0$ is (effectively) homogeneous through the sample, it does not contribute to the spatial dependence. In this case the gradient is referred to as a phase-encoding gradient. In contradistinction to frequency encoding, in phase encoding it is necessary to observe an appropriately phase-encoded signal multiple times.

3.5. Selective excitation

In Section 3.2 it was noted that the slice thickness was a function of the selectivity of the RF pulse in the presence of the slice selection gradient. The selectivity of a rectangular RF pulse can be increased merely by lengthening the pulse and using a reduced power; however, this approach is limited as it results in a sinc function-shaped excitation profile. Also, to achieve the desired selectivity, the pulse duration will eventually become too long and relaxation effects may become significant during the pulse. Selective RF pulses can be grouped into amplitude-modulated and frequency- (or phase-) modulated pulses. There have been a number of reviews on shaped pulses, selective excitation and design techniques.[37-39]

When considering the use of a selective pulse, a number of factors must be considered including the excitation profile and the phase of the excited magnetization, the duration of the pulse and its vulnerability to machine limitations such as RF inhomogeneity. Finally, it is necessary to consider whether it is technically possible to produce the pulse and whether it will cause excessive heating of the sample (although this is normally not a problem with nonbiological samples). In NMR microscopy, the RF homogeneity is normally quite good and, as a result, amplitude-modulated pulses are typically used. The exact magnetization excitation pattern resulting from an RF pulse can in general be calculated from the Bloch equations. However, the reverse problem of how to find the form of the time-domain RF excitation needed to achieve the desired frequency domain is not straightforward, owing to the nonlinearity of the Bloch equations. Insight into the problem can be gained by assuming that the magnetization behaves as a linear system in response to an RF pulse. Under this condition and certain restrictions, the frequency domain excitation pattern

generated by an arbitrarily shaped pulse is directly proportional to the Fourier transform of the pulse. Thus, to obtain a rectangular excitation profile, the shape of the time-domain RF pulse should be modulated according to the Fourier transform of a (rectangular) sinc function. However, time restraints require the selective pulse to be as short as possible, and the selective pulse used for slice selection is one that is amplitude-modulated as a sinc function and truncated over a finite interval of time. A number of approaches for optimizing amplitude-modulated pulses have appeared in the literature, including optimal control theory (see the review by Warren and Silver[37]) and Shinnar-Le Roux (SLR) pulse design (see the review by Maudsley and Matson[38]).

Frequency-modulated (or adiabatic) pulses operate according to a spin-locking mechanism in which the spins follow the direction of the effective $\mathbf{B}_1$ field. An advantage of frequency-modulated pulses is that they are able to maintain both selectivity and tip angle over a range of RF power. Consequently they have found application in surface coil studies.

3.6. Typical 2D and 3D imaging sequences and nomenclature

3.6.1. Introduction

Using the different spatial encoding techniques outlined in Sections 3.2 to 3.4, it is possible to construct many imaging schemes (see, for example, Section 5). After exciting a single slice through the sample, there comes a choice of how to sample **k**-space. The geometry in which the plane is sampled is known as the "raster" and how it is sampled will affect both the efficiency of the sampling procedure and the reconstruction procedure. If the slice is sampled in a Cartesian raster, the imaging process is termed *Fourier imaging*; alternatively, if the slice is sampled in a polar raster, it is termed *projection reconstruction*.

3.6.2. Fourier imaging

Imaging is by nature a three-dimensional (3D) experiment and as a consequence requires three orthogonal gradients (see Eq. (1)) to locate a spin in laboratory space. However, the acquisition of a full 3D data set comes with substantial time and memory requirements. It is more typical to acquire a two-dimensional slice through the sample. This dramatically reduces the size of the acquired data set from the order of N^3 to N^2 where N is the number of discrete points sampled. A simple sequence for Fourier imaging is depicted in Fig. 5. This can be likened to a two-dimensional NMR experiment as it comprises clear preparation, evolution and detection periods. During the preparation period the magnetization is allowed to reach a steady-state condition (N.b., time constraints normally preclude full relaxation in imaging

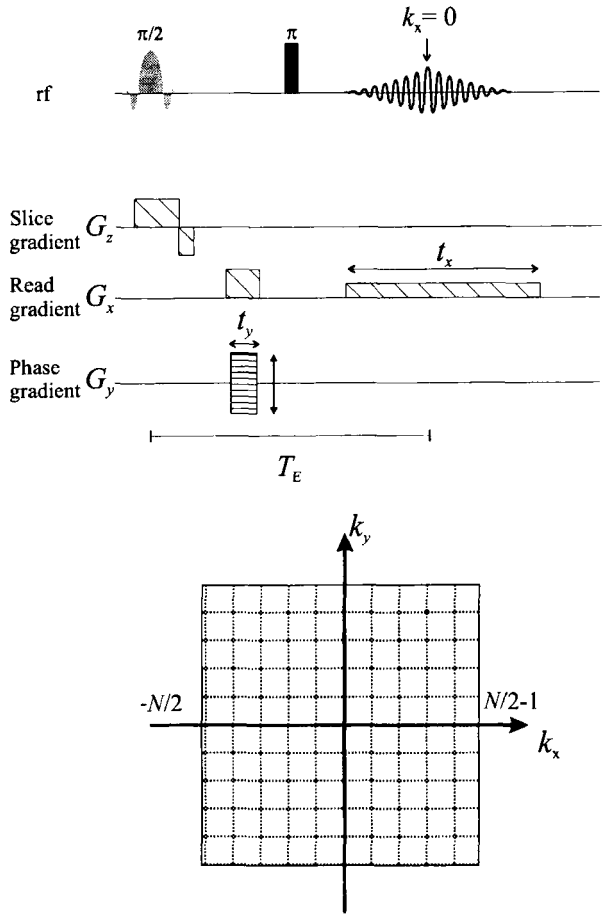

Fig. 5. A basic two-dimensional Fourier imaging sequence. A slice is first selected using a gradient-echo by applying a selective RF pulse in the presence of the slice gradient (G_z) as shown in Fig. 3. The slice is then sampled in **k**-space with two orthogonal gradients (i.e. G_y, the phase gradient, and G_x, the read gradient) producing a Cartesian raster which subdivides the slice into a "matrix" with 256×256 elements. In this example, N data points are sampled from $k_x = -(1/2\pi)\gamma G_x(\frac{1}{2}N)T$ to $k_x = (1/2\pi)\gamma G_x(\frac{1}{2}N - 1)T$ and thus all four quadrants of **k**-space are sampled. Alternatively, the read gradient could be started later and only the second half of the echo acquired, which would then correspond to sampling from $k_x = 0$ to $k_x = (1/2\pi)\gamma G_x(N - 1)T$. T_E denotes the echo time. The precursor read gradient before the π pulse causes a delayed "spin-echo" to be formed so that the origin of **k**-space is shifted away from the leading edge of the gradient.

experiments). A slice is selected by applying a selective RF pulse in the presence of the slice gradient (i.e, G_z). This (two-dimensional) slice or "imaging plane" is then sampled using two other orthogonal gradients. One gradient (i.e., G_y) serves to phase-encode the magnetization with information on the y coordinate (see Eq. (8)). During the detection period (i.e. acquisition) the FID is frequency-encoded owing to the presence of the third orthogonal gradient (i.e. the read gradient, G_x). A series of FIDs are collected while either incrementing or decrementing G_y by a set amount (ΔG_y) in successive experiments. The recycle delay, T_R, is the time from the beginning of one sequence to the start of the next and the echo time, T_E, is defined in Fig. 5. It should be noted that the choice of x, y and z gradients for read, phase and slice gradients is purely arbitrary and any permutation is possible. Thus, this method samples **k**-space in a Cartesian coordinate system in the xy plane with the units of the abscissa (k_x) and the ordinate (k_y) being $(2\pi)^{-1}\gamma G_x t_x$ and $(2\pi)^{-1}\gamma G_y t_y$, respectively, as depicted in Fig. 5. Normally, a fixed phase period is used and the gradient magnitude is varied so that the time of the experiment stays constant. This procedure is also known as "spin warp imaging". Thus, ignoring the average across the slice (i.e. the integral over the slice thickness) and neglecting the effects of spin relaxation, the signal in a two-dimensional image (a two-dimensional version of Eq. (3)) is

$$S(k_x, k_y) = \iint \rho(x, y)\, e^{i2\pi(k_x x + k_y y)}\, dx\, dy \tag{9}$$

Two-dimensional Fourier transformation of the data (Eq. (9)) will return the image (i.e. $\rho(x, y)$). **k**-Space is sampled with a finite number of points (suitable for fast Fourier transformation), for example 256×256. $\rho(x,y)$ should be a real function and thus $S(k_x, k_y)$ should satisfy the symmetry $S(-k_x, -k_y) = S^*(k_x, k_y)$, where * denotes complex conjugate.

It is an appropriate juncture to consider the maximum spatial distances (commonly known as *f*ield *o*f *v*iew; FOV) represented along each dimension in the final image (see Fig. 5). The FOV in each direction are independent of each other and are determined by their respective sampling frequencies. The FOV in the frequency-encoded x direction and the phase-encoded y direction are given by

$$\Delta x = \frac{2\pi}{\gamma G_x (\Delta t_x)} \tag{10}$$

and

$$\Delta y = \frac{2\pi}{\gamma (\Delta G_y) t_y} \tag{11}$$

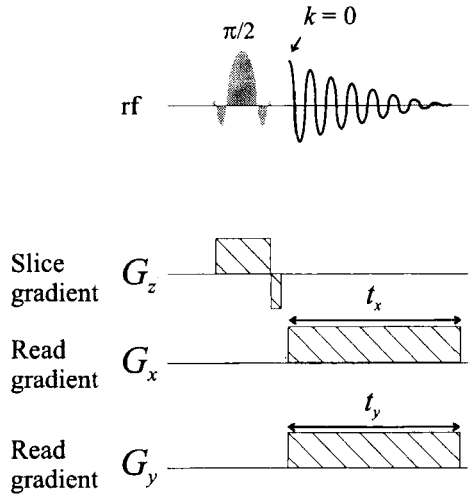

Fig. 6. An example of a projection reconstruction sequence. The desired slice is first selected with a gradient-echo. During signal acquisition, two orthogonal gradients are applied simultaneously to sample the N^2 points on the imaging plane with a polar raster.

respectively, where Δt_x is the time between data point acquisitions in the FID (i.e. the dwell time). The digital resolution for a particular gradient direction in the final image is given by Δx (or Δy)/N, where N, in the case of frequency encoding, is the number of complex data points sampled per FID. For the case of phase encoding, N is the number of phase-encoded FIDs acquired.

3.6.3. Projection reconstruction

Projection–reconstruction techniques have recently been reviewed by Glover and Pauly.[40] In some circumstances it may be more efficient to sample **k**-space using polar coordinates. Experimentally this is realized by applying G_x and G_y simultaneously which is equivalent to a gradient of constant amplitude $G(=\sqrt{G_x^2 + G_y^2})$ rotated around the polar angle given by $\tan \varphi = G_y/G_x$ with φ varying from 0 to 2π (see Fig. 6). Acquisition is performed during the gradient application and no echo procedure is required. This is particularly advantageous for samples with short relaxation times. However, the transformation from **k**-space to **r**-space now has the form (this can be compared with Eq. (9) where a Cartesian raster was used)

$$S(k, \varphi) = \iint \rho(x, y)\, e^{i2\pi \mathbf{k}\cdot\mathbf{r}}\, dx\, dy \tag{12}$$

In the polar raster, the lower frequency components (i.e. the inner part of the

raster) are sampled more densely than the outer (higher frequency) region. $\rho(x, y)$ is determined using the filtered back-projection technique.[41]

4. IMAGE CONTRAST AND QUANTITATION

4.1. Introduction

Contrast in NMR images results from spatial variations in the spin density of the observed nucleus and the chemical and physical environment of the nucleus.[42] The chemical environment of the nucleus is reflected in the NMR observables of the chemical shift, spin–spin coupling constants (J) and internuclear dipolar interactions, whereas the physical environment (i.e. the molecular dynamics of the nucleus) effects the nuclear magnetization. Hence the physical environment can be probed through its effects on the nuclear spin relaxation (i.e. longitudinal, spin–spin and apparent spin–spin relaxation times) and transport properties (i.e. flow and diffusion). Ultimately, however, the imaging pulse sequence must be engineered in such a way that the desired contrast factor(s) affects the (observed) transverse magnetization. Further, efforts must be made so that the contrast observed in an image can unambiguously be related to its source; that is, care must be taken to avoid, or at least recognize, artefacts. Artefacts are mentioned in passing in Section 5 and in detail in Section 8. Thus, adding contrast in imaging is essentially the modulation of the transverse magnetization to reflect one or more elements of the environment of the nucleus.

It is the sources of contrast and the ability, in some cases, to selectively alter the contrast that is one of the great strengths of NMR imaging. Conversely, however, the additional sources of image contrast beyond the pure spin density is precisely the reason why it is generally difficult to relate the NMR image intensity directly to the nuclear spin density. Thus, for example in biological samples, the observed water proton density can be inconsistent with the known proton density.[43] In this section, the sources of contrast are examined, with the exception of motion as a form of contrast, which will be considered in Section 6, and diffusive edge enhancement, discussed in Section 8.3.2. In Section 3 the effects of contrast were ignored. Including such effects, Eq. (3) is written

$$S(\mathbf{k}) = \int \rho(\mathbf{r}) E_c(\mathbf{r})\, e^{i2\pi \mathbf{k}\cdot\mathbf{r}} d\mathbf{r} \tag{13}$$

where $E_c(\mathbf{r})$ is the normalized and combined contrast factor.[42] Thus, image reconstruction returns $\rho(\mathbf{r})E_c(\mathbf{r})$. $E_c(\mathbf{r})$ is the product of several factors and is given by[42]

$$E_c(\mathbf{r}) = E_c(T_x)\, E_c(\delta_i) E_c(\mathbf{q}) \tag{14}$$

where $E_c(T_x)(x = 1, 2 \text{ or } 1\rho)$ is the contrast factor representing the effects of spin–lattice, spin–spin or spin–lattice relaxation in the rotating frame. $E_c(\delta_i)$ represents chemical shift effects and $E_c(\mathbf{q})$ is the contrast factor for molecular motion, which contains contributions from self-diffusion and flow. The factors included in Eq. (14) are primary contrast factors as they can all be included into the Bloch equations. In addition to the primary contrast factors, there are also secondary contrast factors such as temperature and susceptibility differences which appear as perturbations of the primary contrast factors.

The fundamental approach for applying contrast is to precondition the magnetization prior to the imaging (i.e. spatial localization) step in the pulse sequence. However, the method employed depends on the desired degree of quantitation. The higher the degree of quantitation, the more time required. There are three general approaches (qualitative → quantitative) for incorporating contrast factors: (1) a one-shot scheme, (2) a two-image scheme and (3) a multiple slicing scheme. In a one-shot scheme, the pulse sequence is designed such that only spins that are responsible for a particular contrast produce the final signal. For example, a chemical shift imaging sequence can be made to select just one resonance frequency. In a two-image scheme, two imaging experiments are performed using different experimental conditions that result in different contrasts. One image is then compared (e.g. by subtraction) to the other on a pixel (image picture element) by pixel basis. The final experimental scheme is the use of multiple slice imaging, in which multiple images are acquired under different contrast conditions. Thus, each 2D image is a slice along the "contrast direction" (e.g. see Section 6.3.2). Then a 1D data array can be formed from the same respective pixel in each image.

In the following sections we consider the different origins of (inherent) contrast in NMR imaging. The use of contrast agents (e.g. Ref. 44) is not considered.

4.2. Chemical shift

In our discussion of basic imaging principles in Section 2, it was simplistically assumed that in the absence of a field gradient the frequency domain signal consisted of only one peak at zero frequency (see Eq. (8)). However, if we consider the possibility of there being more than one resonance in the spectrum then Eq. (8) becomes[42]

$$\omega(\mathbf{r}) = \gamma(\mathbf{B}_0 + \mathbf{G}\cdot\mathbf{r} + \delta_i \mathbf{B}_0 \times 10^{-6}) \tag{15}$$

where δ_i is the chemical shift of the ith species. The last term in Eq. (15) can be a source of artefacts (see Section 8.3.2); however, it can also provide valuable information (see Section 5.1.3). In this case the chemical shift can provide an extra dimension and thus the ultimate form of a chemical shift

imaging (CSI) data set is four-dimensional (three for the spatial axes and one chemical shift axis).

4.3. Relaxation contrast

Relaxation contrasts are intrinsic in all imaging experiments and provide information on motions with a time scale on the order of the rotational correlation times of the observed spins. T_1, T_2 and $T_{1\rho}$ probe different motional time scales and thus, by appropriate choice of contrast method, images can be made to reflect particular motions.[45] T_1 filters are sensitive to motions with correlation times between 10^{-8} and 10^{-12} s. The dipolar filter can be used to probe motions with correlation times faster than 10^{-5} s.[46] By changing the strength of the spin-locking field, the $T_{1\rho}$ filter can be used to probe motions with correlation times between 10^{-4} and 10^{-2} s.

In biological systems, the relaxation times of the water protons are very common sources of contrast. The relaxation times reflect the relaxation of the macromolecular phase and the exchange (i.e. magnetization transfer) between the aqueous and macromolecular phases (i.e. hydration effects).[47–50]

4.4. Susceptibility

Susceptibility differences in heterogeneous samples induce local magnetic field gradients across boundaries. These local gradients degrade the homogeneity of the applied magnetic field at and around such interfaces. As will be discussed in Section 8.3, this can significantly reduce the T_2 of spins in the affected region, resulting in image artefacts and distortion, but it also provides a source of contrast in its own right. Since the effect of magnetic susceptibility is field dependent, the problems (or degree of contrast) associated with susceptibility differences become more pronounced at higher fields. The oxygenation state of haemoglobin can also lead to a change in susceptibility as blood changes between the deoxygenated (paramagnetic) state to the oxygenated (diamagnetic) state. The contrast arising from this process is commonly termed BOLD (*b*lood *o*xygen *l*evel *d*ependent) contrast (e.g. see Ref. 51).

4.5. Temperature

As temperature increases, so does molecular motion. Consequently, molecular diffusion coefficients and relaxation times increase with temperature. Similarly, the chemical shifts of some resonances are temperature dependent (e.g. methanol[52]). Thus, diffusion coefficients, relaxation times and chemical shifts can be used to measure sample temperature indirectly in imaging. Of these, the

most general method is to monitor diffusion[53] and the interpretation of the data is also the simplest for this case. Doran *et al.*[54] have concisely summarized the three different approaches.

4.6. Quantitation of image density

From the above discussion of contrast factors it is clear that it is not possible to obtain a true "density" image since it is impossible to remove all of the contrast factors apart from the spin density. Suitable choices of imaging sequences can serve to lessen contrast contributions and this will become clear in subsequent sections. In the case of relaxation, by obtaining relaxation maps (see Section 4.3) it is possible to extrapolate the image intensity such that there is no relaxation contrast (i.e. $T_R = \infty$ and $T_E = 0$). Such an approach is of importance in biological tissues where the inherent heterogeneity and susceptibility differences result in large relaxation contrast in images.

5. IMAGE RECONSTRUCTION TECHNIQUES

5.1. B_0 gradient-based sequences

5.1.1. 3D imaging

Sometimes it is desired to acquire a full 3D data set, or in the case of samples with short T_2 values to avoid the time-consuming slice selection procedure and thereby avoid some signal loss. In full 3D imaging, the slice selection procedure is removed and either a phase- or frequency-encoding gradient is employed in the third orthogonal direction; the imaging of the other two dimensions is then performed as before with Fourier imaging or projection reconstruction.

5.1.2. Echo summation and multislice imaging

The minimization of the total image acquisition time or the maximization of the signal-to-noise ratio (S/N) is generally a very important aspect of imaging experiments. One method of improving S/N when T_2 is longer than the acquisition time such that coherent transverse magnetization remains, is to refocus the magnetization using a phase-inverting π pulse and then repeat the imaging sequence, for example a Carr–Purcell–Meiboom–Gill (CPMG) train of echoes.

Another efficient experimental technique is to use multislicing. A simple method is to replace the nonselective π pulse with a slice-selective π pulse in the Fourier imaging sequence (see Fig. 7A). In this case, since the magnetization is only perturbed in one slice at a time, the imaging of other slices can be

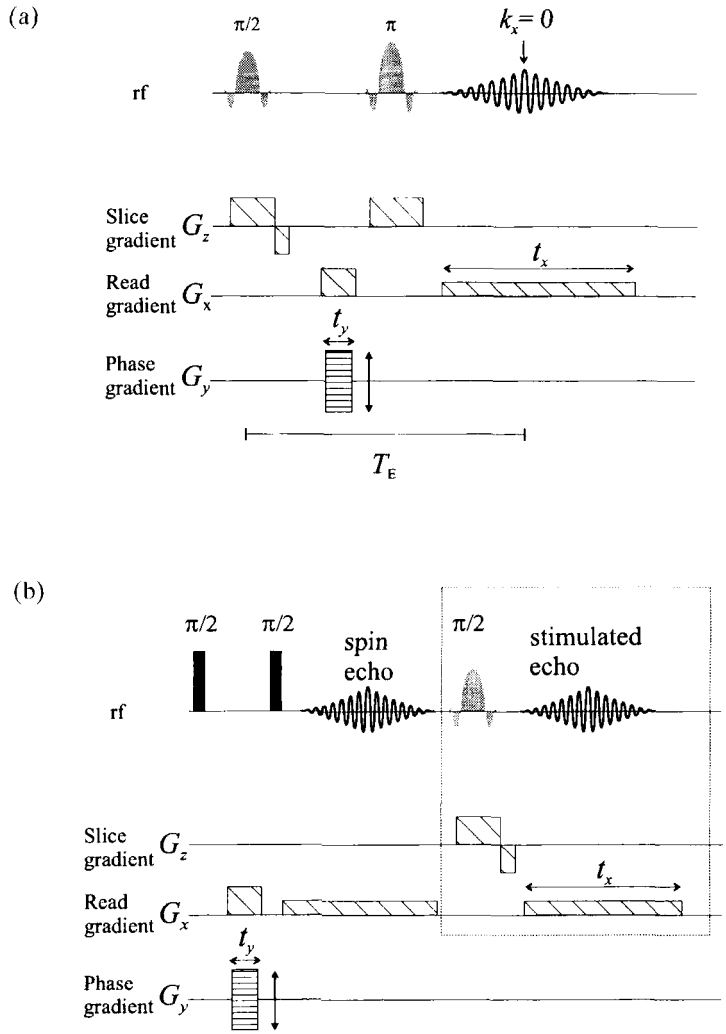

Fig. 7. Multislice imaging sequences: (A) a simple variant of the two-dimensional Fourier imaging sequence given in Fig. 5 where the "hard" π pulse is replaced by a slice-selective π pulse; (B) a stimulated-echo-based sequence. In (B) the first two hard $\pi/2$ pulses store the phase-encoded magnetization along the z axis and the third (slice-selective) pulse results in the formation of a stimulated echo, which is measured. The transmitter frequency is then shifted and the slice selection and acquisition part of the sequence (enclosed by the dotted box) are repeated for the adjacent slices. The spin-echo can also be observed to obtain a "transmission" image of pixels projected normal to the slice axis.

conducted while the spins in other slices are relaxing. However, selective π pulses are subject to nonlinearity artefacts. This process can be reduced by judicious choice of the order of the interleaving. Multislice imaging methods involving stimulated echoes are generally superior as they obviate the π pulse problem. This approach has been termed STEAM (*st*imulated *e*cho *a*cquisition *m*ode; see Fig. 7B); further details can be found elsewhere.[3,55]

5.1.3. Chemical shift imaging (CSI)

Chemical shift imaging is a combination of spectroscopy and imaging. In this technique the distribution of different substances is mapped so that the pixel intensity is a function of the space variable and of the chemical shift (see Section 4.2). Most techniques are variants of Fourier imaging sequence where the chemical shift and spatial information are sampled in **k**-space. Chemical shift selectivity may be obtained by (1) selective excitation or saturation, (2) phase encoding of the chemical shift in the evolution period, or (3) detection in the absence of gradients. CSI techniques, especially the acquisition of all four dimensions, are expensive in terms of acquisition time and memory. Consequently, it is normal to acquire only some subset of the data. One extreme is to observe the full chemical shift information but for only a single voxel (i.e. localized spectroscopy). The other extreme is to acquire all spatial dimensions but to limit the acquisition to a very narrow chemical shift range (i.e. the shift of interest) and perform *che*mical *s*hift-*s*elective (CHESS) imaging (see Fig. 8). Numerous methods have been proposed. The different chemical shift imaging techniques based on spin-echo imaging sequences have been reviewed by Rumpel and Pope.[56] The STEAM sequence provides a straightforward approach to CHESS imaging[57] (see Fig. 9), where the first (selective) RF pulse is used for chemical shift selective excitation, the second (selective) pulse for slice selection and the third for producing a stimulated echo. Great care must be taken to avoid image contamination from residual signal from a resonance other than that of interest. Xia and Jelinsky[58] have proposed a new variant of the CHESS sequence, CD-CHESS, that allows greater suppression of unwanted resonances.

Selective excitation techniques are more suited to measurements at high field owing to the greater dispersity in the spectrum and correspondingly less stringent requirements on the selectivity of the excitation. Selective saturation or selective inversion[59] of the unwanted resonance is more applicable for imaging at lower field. In some circumstances multiple quantum filters (see Section 5.1.5) can also be used for suppression of unwanted resonances.

5.1.4. Relaxation time imaging

T_1 contrast occurs when T_R is insufficient to allow full thermal relaxation. An inversion recovery preparation period before the main imaging sequence

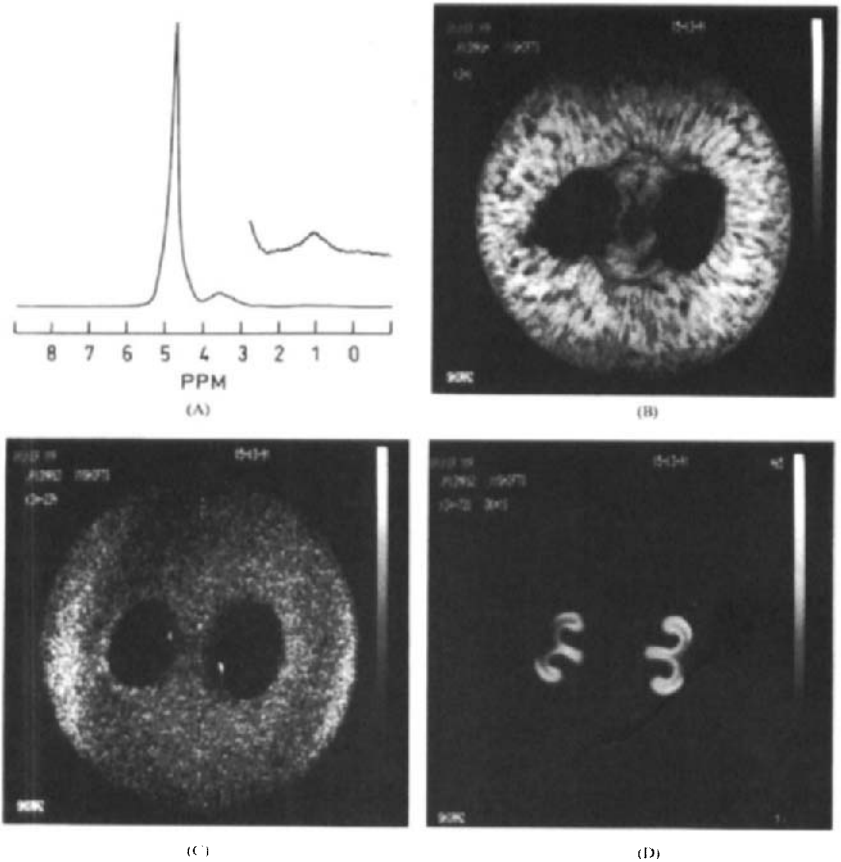

Fig. 8. (A) Conventional ^1H spectrum of a shiraz berry grape showing the resonances from water (4.8 ppm), glucose and fructose at 3.6 ppm and oil (1.1 ppm; expanded scale). (B) Water image, (C) sugar image and (D) oil image. (Reproduced with permission from Pope *et al.*[206])

introduces T_1-weighting, but it also introduces the possibility of bulk flow effects. Similar to T_1 contrast, T_2 contrast occurs if the echo time (i.e. T_E) in the imaging sequence is long compared with T_2. Relaxation times can be mapped by performing a pixel-by-pixel analysis of the corresponding pixels in images acquired with either different values of T_R in the case of T_1 contrast or of T_E in the case of T_2 contrast.

Owing to the effects of magnetic susceptibility differences in the sample and the imaging gradients, T_2 and diffusion effects are strongly coupled together (see Section 8.3). Accurate T_2 relaxation time measurements in NMR microscopy are complicated by the diffusional losses in signal intensity due to the necessity for using large gradients. In an echo-based imaging sequence, the pairs of gradient pulses (i.e. read-gradient-dephase and read gradient) on

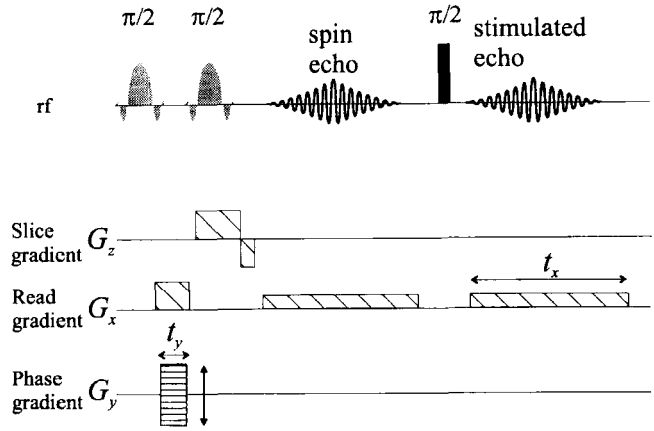

Fig. 9. Chemical shift-selective imaging using a stimulated-echo-based sequence. The first selective $\pi/2$ pulse is applied in the absence of gradients to effect chemical shift selection. The second $\pi/2$ pulse is applied for slice selection leading to a spin-echo, and after the third (hard) π pulse a stimulated echo is formed.[57]

opposite sides of the π pulse (see Section 6.3)[60] effectively form a pulsed field gradient (PFG) spin-echo sequence (see Section 6), and thus if T_E is increased to measure the T_2 decay the signal loss due to diffusion will also increase. Consequently, the measured T_2 will be an underestimate.[61] Careful consideration must be given to the imaging sequence used to measure T_2 (or, conversely, diffusion). Two approaches are presented in Fig. 10; in the first by Hsu *et al.*[62,63] the spin-echo imaging sequence is modified so that the read gradient does not form a PFG sequence; in the second approach by Haase *et al.*[60] a magnetization preparation period is used before the imaging part of the sequence so that the effects of T_2 relaxation and diffusion in the sequence can be uncoupled.

5.1.5. Zero- and multiple-quantum imaging

Zero-quantum coherence can be a practical solution for obtaining separate chemical shift resolved images of samples in which the single-quantum transitions are not otherwise able to be resolved owing to internal gradients since the homonuclear zero-quantum coherence is independent of magnetic field inhomogeneity. Multiple-quantum filters are an easy way to separate nuclei on the basis of the number of scalar coupling partners. In particular, double-quantum filtration can be used for water suppression. This is of particular consequence in imaging since the lines do not have to be resolved from each other and no selective pulses are required. Multiple-quantum coherence phase encoding can be used to effectively increase the gradient strength (consider Eq. (1)), but generally at the expense of increasing the

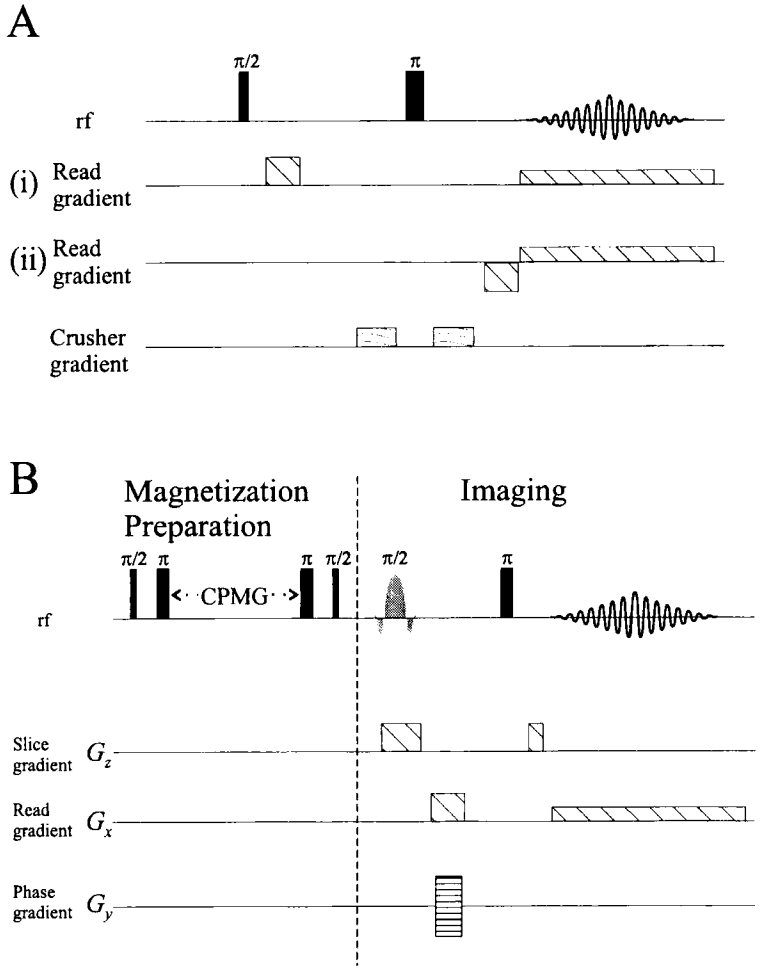

Fig. 10. Examples of sequences for measuring T_2 while minimizing the effects of diffusion. (A) In the 1D spin-echo imaging sequence the read-dephasing gradient is normally placed (i) before the π pulse; however, the diffusional loss is alleviated by (ii) placing the read-dephasing gradient after the π pulse and immediately before the read gradient.[63] The crusher gradients are common to either version of the sequence and serve to eliminate refocusing or imperfectly inverted magnetization. (B) A "magnetization-prepared" spin-echo imaging sequence.[60] A CPMG sequence is prefixed to the spin-echo sequence to provide T_2-weighting to the magnetization. Since the imaging part of the sequence is unchanged (i.e. T_E is constant) the effects of diffusion during the imaging sequence are kept constant and can be neglected in the relaxation analysis when considering the effects of the CPMG.

experimental time. Although multiple-quantum filters have many useful features, they suffer from poor signal efficiency owing to leakage pathways, and multiplets with differing J values will have different amplitudes in the final (detected) single-quantum coherence, leading to problems in obtaining quantitative results from images. Chandrakumar and Velan[64] have presented an imaging method in which the frequency-encoded direction is single-quantum encoded and the others are multiple-quantum phase-encoded. Consequently, the images exhibit a characteristic form factor reflecting the modification due to the n-quantum phase-encoding. Importantly, this increased resolution in the phase-encoded direction(s) does not require an increased bandwidth since the signal is acquired using a conventional bandwidth as required for single-quantum frequency encoding. They note that their method enables the measurement of images with contrast controlled by multiple-quantum coherence relaxation and diffusion coefficients. Zero- and multiple-quantum imaging was considered in detail by Callaghan[3] and has been reviewed by Norwood and Hall.[65]

5.1.6. Fast imaging (EPI, FLASH, etc.)

Obtaining an image quickly has enormous significance in the medical and biological fields, where motional artefacts are a real problem, but it also has significance for multiparameter data sets and multidimensional imaging. What is needed is a rapid means for sampling **k**-space. Two common approaches are to measure all of **k**-space using a series of echoes after a single excitation (i.e. a single shot) or to sample **k**-space more quickly (i.e. reduce T_R). The *e*cho *p*lanar *i*maging (EPI) technique[66] falls into the first category and the *f*ast *l*ow *a*ngle *sh*ot (FLASH) technique[67] belongs to the second category. It should be stressed, though, that the rapid sampling of **k**-space comes at the expense of reduced S/N. FLASH is less efficient than EPI owing to the need to repeat the selective excitation process. Other approaches are alternative **k**-space trajectories and the reduction of the number of **k**-space lines (e.g. Refs. 68–72). Hafner has presented a simple fast imaging scheme termed *b*ack-projection *l*ow-*a*ngle *sh*ot (BLAST), which is applicable to solids as well as liquid-like materials.[73] There is a vast number of acronyms for fast gradient-echo sequences, and some attempts have been made to correlate the different acronyms to their proper generic sequence.[36,74]

FLASH. The main features of FLASH imaging have recently been surveyed by Haase.[74,75] The method is an extension of the gradient-echo pulse sequence in which a single gradient-echo is preceded by a low angle ($\sim 5°$) slice-selective RF pulse together with a fast repetition time (see Fig. 11). The longitudinal magnetization approaches a saturation value that determines the signal intensity. The minimum gradient-echo time is hardware dependent and is typically of the order of 1 ms, and the minimum repetition time of a

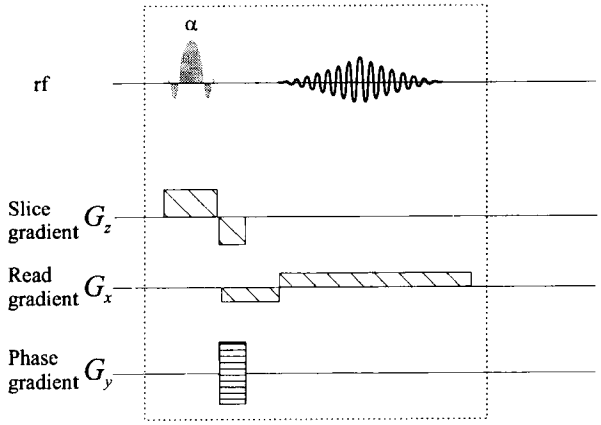

Fig. 11. The FLASH pulse sequence.[67] A very low-angle slice-selective pulse is used ($\alpha \sim 5°$) to excite the magnetization, which is detected in the form of a gradient-echo after reversal of the read gradient. The sequence (dashed box) is rapidly repeated using different values of the phase-encoding gradient so that all of **k**-space is traversed. No relaxation delay is used between subsequent scans.

gradient-echo imaging experiment is twice this long. Hence a 128×128 pixel image can be obtained in 250 ms; assuming that there is sufficient signal to noise. Haase[74,75] has discussed the artefacts that are likely to occur in FLASH imaging; these include susceptibility to artefacts arising from magnetic field inhomogeneities, distortion of the slice profile, flow artefacts and chemical shift artefacts.

A train of RF pulses with a repetition time smaller than T_2 results in a constant signal with an echo-like signal before the pulse and an FID after the pulse; this is commonly termed steady-state free precession (SSFP).[76] The echo part can be refocused by inverting the gradient pulses after the acquisition of the gradient-echo and before the next pulse, or removed by "spoiling methods" using gradient (also known as "crusher") pulses or phase scrambling. For "spoiled" gradient-echo imaging with large flip angles, the signal strength is proportional to T_R/T_1; for low flip angles the signal is dominated by the spin density. If the echo is refocused and large flip angles are used, the signal is proportional to T_2/T_1, and for smaller flip angles to the spin density. Hence, by manipulating these effects, contrast can be added to the image. Refocused gradient-echo imaging leads to T_2-weighting, while "spoiled" gradient-echo imaging leads to T_1-weighting or, in both cases, if low flip angles are used, to the spin density.

As noted by Haase,[75] it is difficult to obtain quantitative data on relaxation, flow and diffusion using standard fast gradient-echo sequences. However, the situation is alleviated by using magnetization-prepared (or snapshot- or

turbo-) fast gradient-echo sequences.[60,77,78] In these sequences, the magnetization is altered in a specific way before the acquisition of the whole image using short T_R values. The contrast in the image is then dependent on the manipulations in the magnetization preparation period (i.e. the preparation part and the imaging part of the sequence are separated; see, for example, Fig. 10B). Such preparation can involve single inversion for T_1-weighted images, a $\pi/2$–π–$\pi/2$ (DEFT) sequence for T_2 weighting, chemical shift imaging or DEFT pulse sequence in combination with diffusion or flow encoding gradients.[60,77,78]

Echo planar and hybrid methods. Although EPI was proposed early in the history of NMR imaging by Mansfield,[66] technical limitations prevented its wide acceptance. EPI is a Fourier imaging technique and has recently been reviewed.[79] In EPI a single train of very rapid gradient-echoes with different phase encoding is acquired after a slice-selective excitation pulse. A sufficiently large effective transverse relaxation time, T_2^*, is necessary to prevent too rapid decay of the magnetization during the echo train. A number of variants of EPI exist. EPI techniques have the advantage that all of the echoes needed to form an image are collected within a single shot of 25–100 ms.

π-EPI (PEPI)[80] is a modified version of EPI in which the gradient reversals are replaced by π pulses; hence the effects of magnetic inhomogeneities are greatly reduced since they are periodically refocused (i.e. the image depends on T_2, not T_2^*). Guilfoyle *et al.*[81] have proposed a 3D version of π-EPI; while it is no longer a single-shot technique, it does allow an $N \times N \times N$ image to be obtained in N acquisitions.

From the discussion in this and the preceding section, it can be surmised that imaging sequences that are hybrids of both the FLASH and EPI approaches will give better results. Deichmann *et al.*[82] have considered the optimization of such sequences (see Fig. 12) as a function of T_1 and T_2^*.

5.1.7. Heteronuclei

While almost all imaging has been conducted using protons, primarily for reasons of superior sensitivity, some other nuclei are candidates at natural abundance (e.g. ^{7}Li, ^{14}N, ^{19}F, ^{23}Na, ^{29}Si and ^{31}P), although generally with lower spatial resolution. It is not only the S/N which determines the success of imaging with heteronuclei but also T_2 and T_1 as they determine the minimum repetition time. For example, Link and Seelig[83] have compared the different imaging sequences suitable for deuterium imaging. The lower sensitivity of deuterium ($\sim$ 1/100 the sensitivity of protons) is partly compensated by its more favourable relaxation properties. The lower γ of deuterium also means that larger gradients are required if resolutions comparable to those observed with protons are to be obtained with the same acquisition time. However, the

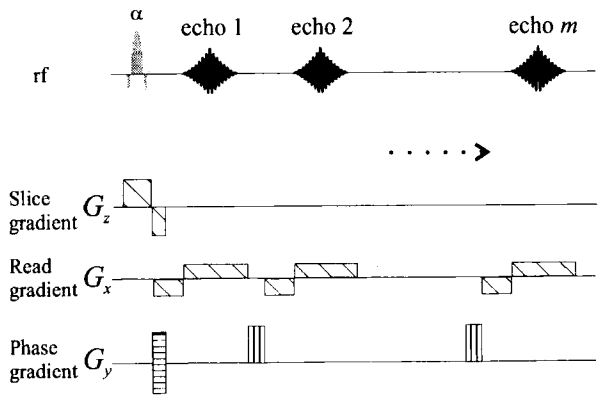

Fig. 12. A hybrid FLASH-EPI sequence.[82] A small-angle slice-selective excitation pulse (α) is used as in FLASH and then a series of m gradient-echoes with different phase encoding are acquired. The optimal value of m depends on the values of T_1 and T_2^*. The sequence is repeated until the required number of echoes is acquired. If $m = 1$ the sequence would correspond to the FLASH sequence as shown in Fig. 11.

smaller γ also means that deuterons are less sensitive to magnetic susceptibility problems than are protons. As a consequence, the deuterium signal decays more slowly.

It is possible to image some other nuclei if isotopic enrichment is used (e.g. ^{13}C, ^{15}N and ^{17}O). The situation can be vastly improved if the heteronuclei are close to protons (e.g. hydrocarbon compounds) so that heteronuclear polarization transfer methods can be used. In this case it may be possible to image with proton sensitivity. Kimmich *et al.*[84] have demonstrated that proton-detected ^{13}C imaging can be performed using multiple-quantum filters[85] or cyclic J cross polarization-based spectral editing.[86]

The use of hyperpolarized atoms offers a novel solution to the signal-to-noise limitations that plague imaging since it can yield up to a 10^5-fold enhancement in detectability (see Fig. 13). Navon *et al.*[87,88] have investigated the use of hyperpolarized ^{129}Xe in imaging experiments. The hyperpolarized gas can be imaged directly or indirectly through the environment of the gas (see Plates 1 and 2). They have coined the term *s*pin *p*olarization-*i*nduced NOE (SPINOE) to describe the process where NOEs transfer enhanced polarization from hyperpolarized gas (e.g. ^{129}Xe) to the solution phase without the need for radiofrequency irradiation. This technique has many potential applications such as a contrast agent in materials science,[89] and can be used with ^3He. The nature of the hyperpolarized nuclei, and in particular the fact that the large nonequilibrium polarization is nonrenewable, dictates that special consideration must be given to the imaging method used.[90] Zhao *et al.*[90] have reported

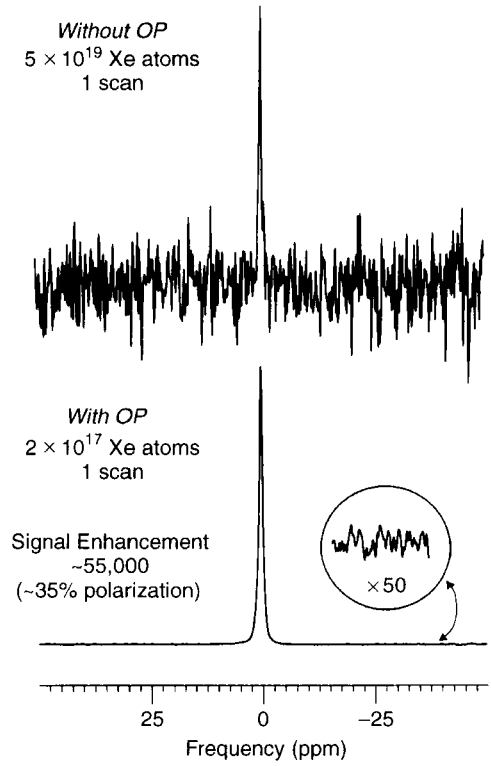

Fig. 13. Optical pumping enhancement of ^{129}Xe gas. (Reproduced with permission from A. Pines.)

the use of gradient-echo imaging approaches suitable for use with hyperpolarized ^{129}Xe. Recently, Skalla *et al.*[91] obtained images of spatial distributions of (optically) spin-polarized Rb atoms in a vapour cell.

5.2. B_1 gradient-based sequences

B_1 gradients have a number of interesting features compared with B_0 gradients, namely negligibly small rise and fall times, the fact that they do not generate eddy currents and that they are technically simple to produce. A number of reviews have been devoted to them.[18,19,92,93] The disadvantages of B_1 gradients are that it is difficult to generate independent gradients along three spatial directions and that it is difficult to generate strong B_1 gradients.

5.2.1. *Rotating-frame spectroscopic imaging*

The rotating-frame imaging (RFI) experiment was first proposed by Hoult.[94] This is essentially a two-dimensional experiment in which one dimension is along the direction of the B_1 gradient and the other dimension provides chemical shift information. In the simplest case, the B_1 gradient is applied (in the z-direction) for a time t_1, which is incremented followed by acquisition during t_2. This gives a two-dimensional data set,

$$S(t_1, t_2) = \sin(2\pi z k)\cos(2\pi \nu t_2) \tag{16}$$

where z and ν are the position and resonance frequency, respectively, and k is now given by (the B_1 analog of Eq. (2))

$$\mathbf{k} = (2\pi)^{-1}\gamma \mathbf{G}_1 t \tag{17}$$

Double Fourier transformation of Eq. (16) results in the chemical shift information along one dimension and the spatial information along the other. Since this method employs only a single gradient coil, the sample must be rotated and the RFI process repeated at each orientation if a plane is to be imaged. This method is consequently very slow.

5.2.2. *Rapid rotating-frame imaging*

A more time-efficient scheme has been devised for 2D imaging by B_1 gradients[95] (see Fig. 14). It is sometimes referred to by the acronym RIPT (*r*apid rotating-frame *i*maging with an RF *p*ulse *t*rain). Using a purposely designed saddle coil that produces a significant B_1 variation along z, slice selection in the z direction is achieved by a DANTE-type pulse train.[96] Owing to the inevitable leakage between the gradient coil and the detection coil, the read B_1 gradient cannot be on during acquisition; the solution is to apply the read gradient in the form of pulses separated by acquisition windows and thereby acquire a pseudo-FID point by point.[97–99] The signal is damped according to an effective relaxation rate constant,[100]

$$\frac{1}{T_{1,2}} = \frac{(1/T_1) + (1/T_2)}{2} \tag{18}$$

Of particular significance is the dependence on T_2 and not T_2^*. During the acquisition windows the effects of T_1 and T_2^* are operative depending on the orientation of the magnetization. However, the effects of T_2^* and internal B_0 gradients are partly compensated by an averaging process since the nutation encoding normally involves a large number of periods.[95] The xy plane is then sampled using projections along the gradient axis collected for different

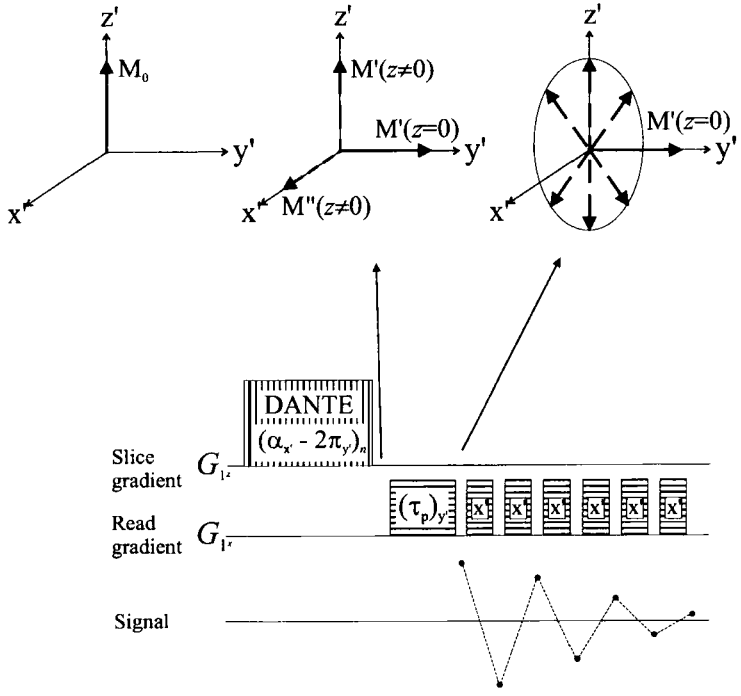

Fig. 14. A pulse sequence for one-dimensional B_1 gradient encoding (after Maffei *et al.*[95]). A DANTE-like pulse train (the tip angles α and 2π refer to the magnetization at $z = 0$, with $n\alpha = \pi/2$) is used to rotate the magnetization of interest ($z = 0$) along the y axis using the slice gradient (G_{1z}). The selected magnetization (denoted by $M(z = 0)$) is then spin-locked during the gradient "purge" pulse of duration τ_p, while the unwanted magnetization (denoted by $M'(z \neq 0)$ and $M''(z \neq 0)$) is spread in the xz plane and does not contribute to the pseudo-FID obtained during the off periods of the application of the read gradient (G_{1x}). The data points of the pseudo-FID are denoted by solid circles. A schematic diagram of the RF coil arrangements used to generate the slice selection and read gradients is given in Fig. 22. N.b., lower-case letters with a prime refer to the rotating frame.

orientations of the sample with respect to the z axis. If the angle α describes the rotation of the object with respect to x axis of the laboratory frame, the signal can be expressed as[95]

$$S(k, \alpha) = \iint \rho(x, y) \cos[2\pi k(x \cos\alpha + y \sin\alpha + D_{B_1})] \, dx \, dy \qquad (19)$$

where D_{B_1} is the distance between the axis about which the sample is rotated and the virtual point of zero B_1. Using this technique a typical measuring time is of the order of 10 min,[101] assuming that about one hundred projections are

necessary to acquire the image and also waiting a sufficient relaxation time between the acquisition of successive projections. The filtered back-projection algorithm is used to reconstruct the image of the xy plane. Although this imaging procedure is more efficient than RFI, it is at the expense of losing chemical shift information. T_1 contrast can easily be performed as in conventional B_0 imaging and T_2 contrast can be incorporated by including an echo sequence prior to the slice selection. This method also requires less power than RFI.[98] Complications arising from the intermixing of off-resonance peaks with the on-resonance signal have been considered.[102] Recently, Raulet *et al.*[101] have investigated a more time-efficient EPI-like modification to the above-mentioned B_1 imaging method.

5.2.3. Chemical shift imaging

Bowers *et al.*[99] performed chemical shift imaging relying on the frequency-selective excitation and B_1-independent inversion properties of hyperbolic secant RF pulses. By combining the DANTE-Z approach[103] for selecting a given resonance in a multiline spectrum with imaging by B_1 gradients, Valtier *et al.*[104] were able to perform chemical shift imaging.

5.3. Volume selection

For completeness, in this section the different techniques of volume selection are briefly explained; more detailed accounts can be found elsewhere (e.g. Ref. 105). A simple, but inaccurate, means of obtaining such information is via the homogeneity of the RF coil. Such methods typically involve the use of single surface coils and thus the technique is normally limited to superficial regions of the sample. Surface coil spectroscopy is outside the scope of this chapter and a review of its use and application may be found elsewhere.[106] Volume selection typically proceeds in one of three ways: (1) excitation of spins inside the VOI or its complement (2) destruction outside the VOI, or (3) difference techniques.

A simple example of the first approach is to use the STEAM sequence (see Fig. 7B) modified such that each selective $\pi/2$ pulse is applied in the presence of a different orthogonal gradient and thereby directly excite spins in the VOI. Of particular significance is that such methods result in localization in a single scan. In the complementary approach of destruction outside the VOI, different combinations of RF pulses (e.g. pulse-trains, sandwiches or three pulses) are successively applied in the presence of field gradients to retain only magnetization in the region of interest. The final approach is that of a difference technique such that by a process of addition and subtraction the VOI is selected. A common difference technique is *i*mage *s*elected *in vivo* *s*pectroscopy (ISIS)[107] in which a combination of selective inversion pulses is applied

with special phase cycling which result in inversion of the longitudinal magnetization in the selected planes. Since only inversion pulses are involved, the signals are not T_2-weighted.

5.4. Solid-state techniques

5.4.1. Introduction

The imaging of solids and near solids presents special difficulties in imaging owing to two problems: (1) much larger natural line widths and (2) the longitudinal relaxation rate not being correspondingly short. This area of imaging has been comprehensively reviewed by Cory[8] in this series. Consequently, in this section we give only brief coverage to solid-state imaging with emphasis on some of the more recent developments. There have been two general approaches to imaging in the solid state: (1) using some method to increase the effective T_2, that is line-narrowing techniques which attempt to reduce the anisotropy of the interaction Hamiltonians; or (2) brute force methods where the larger natural line widths are left unchanged and the imaging method is adapted to work with the much smaller T_2 values. The very short T_2 values also complicate slice selection processes and some methods have been proposed (see the reviews by Kimmich[108] and Blümler and Blümich[26]). The stray field imaging technique inherently includes slice selection.

The line-narrowing techniques can be classified into two groups depending upon the space chosen to produce the averaging of the interaction Hamiltonians (mainly the dipolar interaction): (1) averaging in real space (i.e. *m*agic *a*ngle *s*pinning; MAS) and (2) techniques in which the narrowing is performed in spin space by RF excitation (e.g. multipulse, magic echo and magic angle in the rotating frame). Maraviglia *et al.*[109] have provided a detailed coverage of the methods for manipulating line widths in solid-state imaging. The application of relaxation filters to solid-state imaging has been reviewed.[25,45]

5.4.2. Multipulse line narrowing

These approaches are based on nullifying the interactions that result in line broadening (e.g. dipolar interactions between neighbouring spins). However, these also cancel the effect of magnetic inhomogeneities. Thus, it is necessary to separate the natural and the applied inhomogeneity (i.e. the applied gradients). Two approaches have been proposed and both require that the imaging gradients are off during the application of the RF pulses. The first approach is the 6-pulse ZIG ZAG sequence[110] in which the RF pulses coincide at the zero crossing of an oscillatory field gradient. In the second, very technically difficult, approach the gradients are applied in very short bursts between the RF pulses.[111]

5.4.3. *Magic angle spinning*

In this method the sample is rotated at the magic angle (54.7°) with respect to the static field to average the dipole–dipole interactions at the same time imaging gradients are applied that match the frequency and phase of the MAS rotor. However, it is normally necessary to combine some form of multipulse line-narrowing procedure to produce sufficiently narrow lines. A weak point of this approach is that many samples cannot withstand the centrifugal forces involved in the MAS experiment. However, this approach does retain (limited) chemical shift information (e.g. Refs 112, 113).

5.4.4. *Rotating-frame imaging*

In this technique the radiofrequency is applied at a suitable amplitude and frequency to produce an effective field, $\mathbf{B}_{\text{eff}}$ at the *m*agic *a*ngle to the *r*otating *f*rame (hence the acronym MARF).[114] This results in line narrowing since the magnetization is spin-locked at the magic angle. The $\mathbf{B}_0$ and $\mathbf{B}_1$ fields are modulated to establish a gradient in the resonance offset while maintaining $\mathbf{B}_{\text{eff}}$ at the magic angle. This method produces narrower lines than the MAS methods and the sample is static but the sensitivity is much lower.

5.4.5. *Magic sandwich echo (MSE) imaging*

In this approach, also known as magic echo phase encoding (MEPSI), an extended FID is produced using a train of magic echoes.[115–120] The imaging gradients are applied and acquisition is performed during various windows in the pulse sequence. Matsui *et al.*[117] have achieved resolutions of 50 μm with this technique. Hafner *et al.*[121] have extended the magic echo technique to three dimensions and were able to obtain a resolution of $(300\ \mu\text{m})^3$.

5.4.6. *Constant-time imaging (CTI)*

In constant-time imaging (also known as single-point imaging) all of the spatial information is obtained using phase-encoding gradients (see Fig. 15). The method allows the observation of images from samples with very short relaxation times. In fact, it is possible to image samples where the T_2 is less than the typical gradient switching times (~0.2 ms for many microimaging probe heads). In this sequence a single short RF pulse is applied to create transverse magnetization in the presence of the gradients. At the end of the phase-encoding time, the phase and amplitude of the magnetization are measured. This procedure is then repeated for different values of the phase-encoding gradient. Since this method relies on pure phase encoding, it is slow, but as it does not record the time evolution of the magnetization, chemical shift, magnetic susceptibility, and dipolar and quadrupolar distortions are not

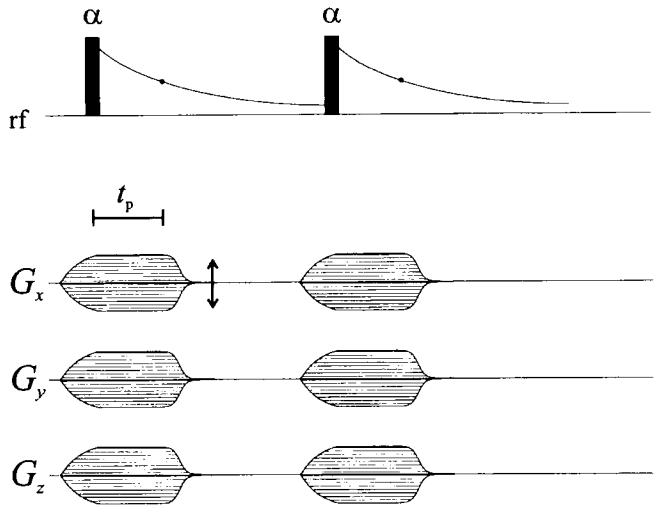

Fig. 15. A 3D CTI imaging sequence (after Gravina and Cory[122]). This simple sequence can be implemented on a liquid-state NMR spectrometer with microimaging probe. A short RF pulse (α) excites the magnetization after the gradients have been turned on. A single point is acquired after a fixed duration t_p. The sequence is then repeated with different values of the phase-encoding gradients.

observed. Further, neglecting the effects of diffusion, the resolution is a function only of the gradient strength. The duration of the RF pulse must be short to achieve even excitation of the gradient-broadened spectrum. Additionally, the bandwidth of the receiver needs to be made sufficiently large. If either condition is not met, the signal acquired when the gradient is strongest (i.e. high **k** values) will be attenuated, resulting in blurring of sharp edges in the spatial image and a resolution less than that predicted on the basis of the gradient alone.

Gravina and Cory have described a version of the CTI experiment that can be implemented on a standard liquid NMR spectrometer with a microimaging probe head.[122] They derived expressions for the resolution and S/N of this technique and compared the efficiency of the CTI technique to frequency-encoding techniques. While CTI provides distortion-free images for a large range of samples and the diffusion-limited resolution is twice as fine as that of a spin-echo technique with frequency encoding, the sensitivity is less than that of the frequency-encoded methods. They concluded that CTI is the method of choice when the sample T_2 is less than the gradient stabilization time. Compared to other imaging experiments, CTI is generally performed with a very high gradient duty cycle. More recently, a ramped gradient version of the CTI sequence that is much faster and enables the introduction of quantitative T_1 contrast or suppression has been presented.[123]

5.4.7. *Fringe (or stray) field methods*

The *str*ay *f*ield *i*maging (STRAFI) technique is a conceptually and experimentally simple method.[124] STRAFI makes use of the linear region of the stray field gradient outside the centre of a superconducting magnet, and this gradient can be in excess of 50 T m^{-1}. Spins in a thin slice orthogonal to the gradient are excited by a nonselective RF pulse. Since the gradient is so large, the nonselective RF pulse is effectively a selective pulse with the excited slice having a thickness of typically 7–70 μm. As the gradient is static, the sample has to be mechanically moved through the gradient. The FID is extremely short owing to the gradient broadening and so a train of solid echoes (i.e. $(\pi/2)_x$–τ–[$(\pi/2)_y$–τ–echo–τ]$_n$) is used to preserve the magnetization (~ spin locking). This also overcomes the problem of spectrometer dead time. Also, since the echo is produced by pulses of the same length, the width of the selected slice is constant. Typically the sample is moved on the order of 50 μm between pulse sequences. T_1 saturation effects are obviated since the sample is moved through the sensitive slice during the imaging process and hence the repetition rate can be made very fast. From moving the sample through the gradient and exciting slices, a 1D profile can be obtained. Two- and three-dimensional data sets can be obtained by combining sample rotation and translation. The image is reconstructed using the back-projection algorithm.

The multiple echoes can be used either for signal averaging or for producing a series of spin relaxation-weighted profiles. The very strong gradient and sample movement have the effect of modulating the amplitude of successive echoes. This modulation has been explained quantitatively.[125] It was shown in a later work[126] that it is also possible to use the spin-echo sequence $(\pi/2)_x$–τ–[π_y–τ–echo–τ]$_n$, where the intensity of the π pulse is double that of the $\pi/2$ to maintain the constant slice width. This echo sequence affords a considerably improved S/N for soft solids.

It has been pointed out that the very large gradient is usually the dominant factor in determining the line width and so that the other interactions such as magnetic susceptibility,[127] dipolar interactions and even electron nuclear interactions can be neglected. This leads to the concept of a "high-gradient" approximation.[128] The STRAFI technique even allows the imaging of paramagnetic solids.[128]

5.4.8. *Oscillating gradients*

This is also a direct approach and is most applicable to semisolids. An oscillating gradient with a period T, which must be of the order of T_2, is applied and a $\pi/2$ pulse is applied at the zero crossing of the gradient field. Providing the RF pulse is short, the gradient will appear to be zero during the time of the RF pulse and all spins will be affected by the RF pulse. After one cycle of the gradient, a gradient-echo is formed and the echo data are sampled in the capture window from $T/2$ to $3T/2$. Two-dimensional images can be formed using back-projection.

This method is simple but restricted. A large receiver bandwidth must be used on account of the large gradients and, because it is based on a gradient-echo, the method is vulnerable to susceptibility artefacts. Recently a three-dimensional oscillating gradient-echo technique has been developed that uses a doubly resonant circuit for the read gradient.[129,130] It can produce three-dimensional images using an echo time under 100 μs. This method is suitable for imaging nonbiological semisolids and has particular applications for objects to which MAS and STRAFI methods cannot be applied.

5.4.9. Stochastic imaging

Blümich has reviewed the use of stochastic excitation in imaging.[131,132] This technique is suitable for both liquid and solid-state samples. The most impressive aspect of stochastic (i.e. RF noise) excitation is the low power required compared to pulse excitation.[133] The RF amplitude required is about one hundredth of that required in pulsed NMR and thus the method has particular relevance to the imaging of solids. Stochastic imaging can be divided into two approaches: (1) cross correlation and time-dependent magnetic field gradients and (2) the back-projection technique in which back-projections of the sample are derived from the linear response to stochastic (i.e. random[133] or Hadamard[131]) excitation. The Hadamard technique is fast and, significantly, results in projections free of systematic noise. As yet, there have been few examples of the use of stochastic imaging.

6. DIFFUSION AND FLOW IMAGING

6.1. Introduction

Flow (net movement) and diffusion (random movement) represent two motional forms of contrast in an image. How these two phenomena may be incorporated into the image experiment to provide contrast is the subject of this section. In the earlier chapter in this series on gradient NMR[2] the use of magnetic field gradients to study diffusion was considered in detail. The imaging of flow and diffusion forms a huge subject area in its own right and it is not possible to give more than a cursory coverage in the present chapter. More complete accounts and links to relevant literature sources can be found elsewhere.[3,53,134–139]

6.2. Flow

Flow imaging techniques can be classified into three categories: inflow/outflow, time-of-flight methods, and phase-sensitive methods. As noted by Callaghan,[3]

the range of average velocities, v, that are measurable is limited by $v_{max} \approx l/T_E$ (where l is the length of the receiver coil) from above and by the molecular self-diffusion from below. For water at room temperature the minimum velocity measurable is about 20 $\mu m s^{-1}$. (Ref. 3.)

Flow-sensitive (or steady-state techniques) rely on the build-up of longitudinal magnetization being limited by the transit time.[76,140] The RF and gradient pulses are rapidly repeated such that the saturation recovery or the steady-state free precession signal amplitude depends on the molecular motion since moving spins will not be permanently in the excitation slice. This can be achieved using either B_0 or B_1 gradients. The steady-state free precession method can be made more sensitive to slow fluid flow using the moving reference frame technique.[141,142]

Time-of-flight methods involve selectively exciting (or destroying) a particular group of spins and then following their displacement during the pulse sequence. An example of a time-of-flight pulse sequence is given in Fig. 16. This method differs from the flow-sensitive method in that the slice that is eventually imaged is different from that which was initially excited. The excited slice is chosen to be normal to the principal flow direction, whereas the detected slice can be parallel or perpendicular to the flow. A novel time-of-flight technique is the use of "tagging" pulse sequences. The basic idea is to use RF modulation (e.g. a DANTE sequence) to encode an endogenous marker onto the sample of interest and observe its evolution[143,144] (see Fig. 17). Thus, the tagging effect lasts only on the order of T_1. As will be seen in Sections 9.1 and 9.4, tagging techniques have vast potential in the field of fluid dynamics.

The phase-sensitive techniques are based on the phase shift of the transverse magnetization that occurs in the presence of a magnetic field gradient in the direction of flow.[135,138] These are the most precise of the three methods, especially in the form of dynamic NMR microscopy (see Section 6.3.2).

In flow measurements it is desirable to suppress the signal from the stationary spins, and there are a few ways of doing this[145] including (1) subtraction, in which two data sets are obtained which contain different contributions from flowing spins but the same contribution from static spins; (2) saturation of the static spins as in steady-state free precession approaches;[135] or (3) selective excitation of the flowing spins, which is considered in the subsequent paragraphs.

Before proceeding it is worth while to review briefly the connections between flow and phase. The phase shift at time t of a nuclear spin following a path $\mathbf{r}(t')$ in a gradient $\mathbf{g}(t')$ (N.b., this gradient is denoted by a lower-case $\mathbf{g}$, to emphasize that its purpose is not spatial encoding) is given by

$$\phi(t) = \gamma \int_0^t \mathbf{g}(t') \cdot \mathbf{r}(t')\, dt' \tag{20}$$

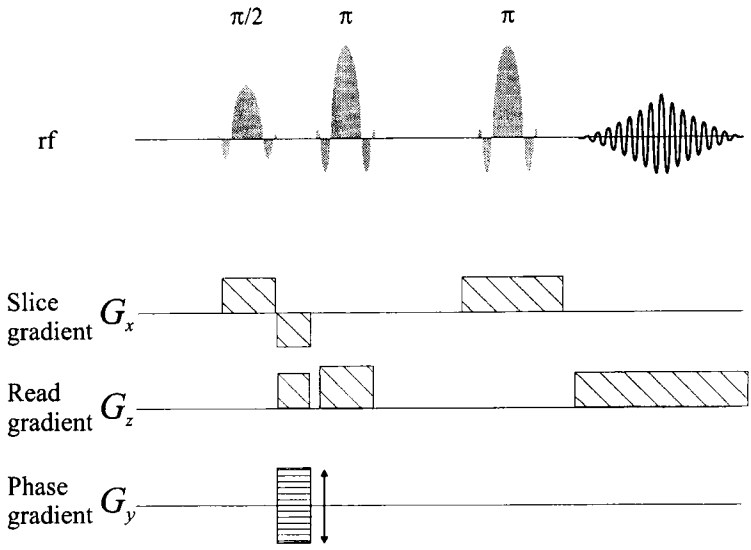

Fig. 16. An example of a time-of-flight imaging pulse sequence for measuring spin displacement. A slice selective $\pi/2$ pulse excites a yz plane parallel to the direction of flow (z). A slice-selective π pulse refocuses spins in the xy plane orthogonal to the direction of flow at $z = z_0$. This process effectively labels the spins in the xy plane at the coordinate z_0. A second selective π pulse is then applied to refocus the magnetization into the xy plane. The z axis is frequency encoded during acquisition.

Only the component of the spin's motion in the direction of the gradient, $z(t)$, is relevant and this can be expanded in a Taylor series:

$$z(t) = z_0 + \left(\frac{\partial z}{\partial t}\right)_{t=0} t + \frac{1}{2}\left(\frac{\partial^2 z}{\partial t^2}\right)_{t=0} t^2 + \cdots \tag{21}$$

The terms on the right-hand side of Eq. (21) correspond to the position z_0, velocity $v_0 = (\partial z/\partial t)_{t=0}$, acceleration, $a_0 = (\partial^2 z/\partial t^2)_{t=0}$, etc. Equation (20) can then be rewritten as

$$\phi(t) = \gamma z_0 M_0 + \gamma v_0 M_1 + \tfrac{1}{2}\gamma a_0 M_2 + \cdots \tag{22}$$

where

$$M_n = \int_0^t g_z(t')(t')^n \, dt' \tag{23}$$

M_n is termed the nth moment of $g_z(t)$ with respect to t (N.b., this should not be confused with macroscopic magnetization). Equation (22) provides the

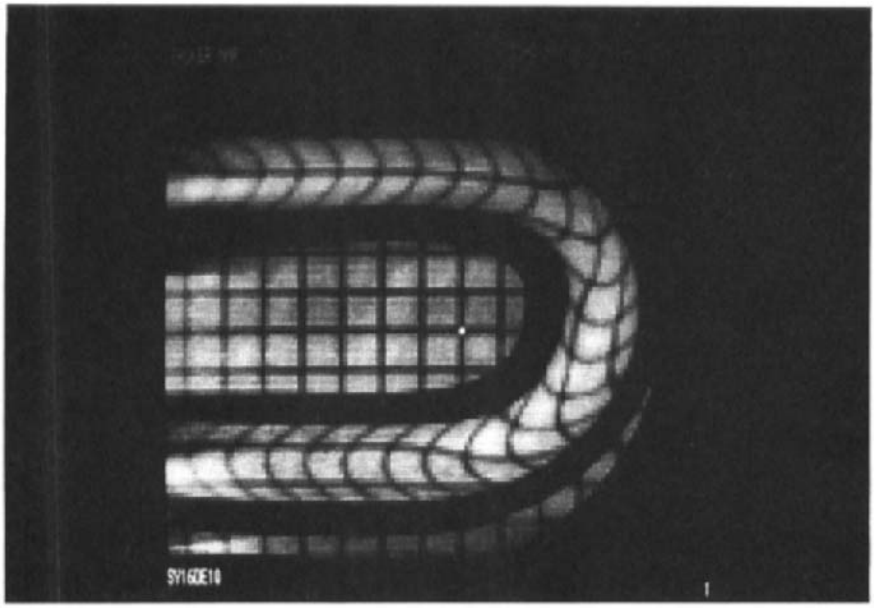

Fig. 17. An image of a U tube flow phantom obtained with a DANTE grid-tagging sequence. (From J. M. Pope and S. Yao, *Concepts Magn. Reson.*, 1993, **5**, 281. © 1993 John Wiley and Sons, Inc. Reproduced by permission of John Wiley & Sons, Inc.)

basis of so-called gradient moment nulling methods and flow compensation. By using appropriately shaped gradient pulses, certain moments can be nulled. For example, a bipolar gradient waveform encodes for flow velocity (i.e. $M_0 = 0$, $M_1 \neq 0$). Many examples of such gradient waveforms have been summarized by Pope and Yao[138] and the design methods of such waveforms have been discussed by Duerk and Simonetti.[146] A typical flow-selective excitation sequence is $(\pi/2)_x$–τ–$(\pi/2)_{-x}$ with a bipolar gradient pulse between the RF pulses. An imaging sequence incorporating such a selection sequence is shown in Fig. 18. Pope and Yao have described a series of flow-selective sequences based on binomial selective excitation in combination with flow-encoding gradients.[145] It is an appropriate stage to mention that gradient moment nulling can be employed in conventional spin-echo imaging sequences to avoid flow artefacts.

6.3. Diffusion measurements with pulsed field gradients

Diffusion can be measured using both B_0 and B_1 gradients. Two basic pulsed field gradient (PFG) sequences, one B_0-based and the other B_1-based, for

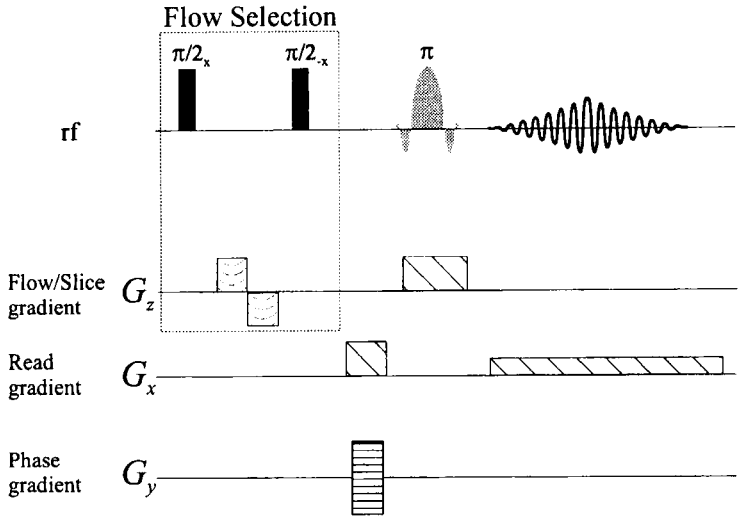

Fig. 18. An example of a single slice imaging sequence with a flow-selective excitation sequence (i.e. $(\pi/2)_x$–G–$(-G)$–$(\pi/2)_{-x}$). This sequence suppresses the signals from stationary spins since magnetization from stationary spins is returned to the static field direction, whereas that from moving spins acquires an additional phase change due to the effects of the gradient pulse and is consequently rotated into the transverse plane.

measuring diffusion are presented in Fig. 19. As the basis of NMR diffusion measurements was described in detail earlier in this series,[2] here it is sufficient to note that if in the period between the leading edges of the gradient pulses (Δ) there is no translational motion of the spins in the direction of the applied gradient then the dephasing effects of the first gradient pulse will be counteracted (i.e. rephased) by the effects of the second gradient pulse. A net displacement (i.e. flow) will be reflected by a net phase change of the signal and a random displacement will be reflected by attenuation of the echo signal. The degree of dephasing/rephasing is proportional to

$$\mathbf{q} = (2\pi)^{-1}\gamma\mathbf{g}\delta \tag{24}$$

where $\mathbf{q}$ defines a dynamic reciprocal space vector and is clearly similar to $\mathbf{k}$ (see Eq. (2)) except that $\mathbf{q}$ provides information on displacement whereas $\mathbf{k}$ provides information on position. In our definition of $\mathbf{q}$ we have denoted the amplitude of the gradient by $\mathbf{g}$ to emphasize that it is the amplitude of the gradient pulses in the PFG sequence. It should be emphasized that $\mathbf{g}$ is a vector quantity and it determines the direction in which the diffusion is measured.

There are a number of ways of relating the diffusion coefficient to the echo

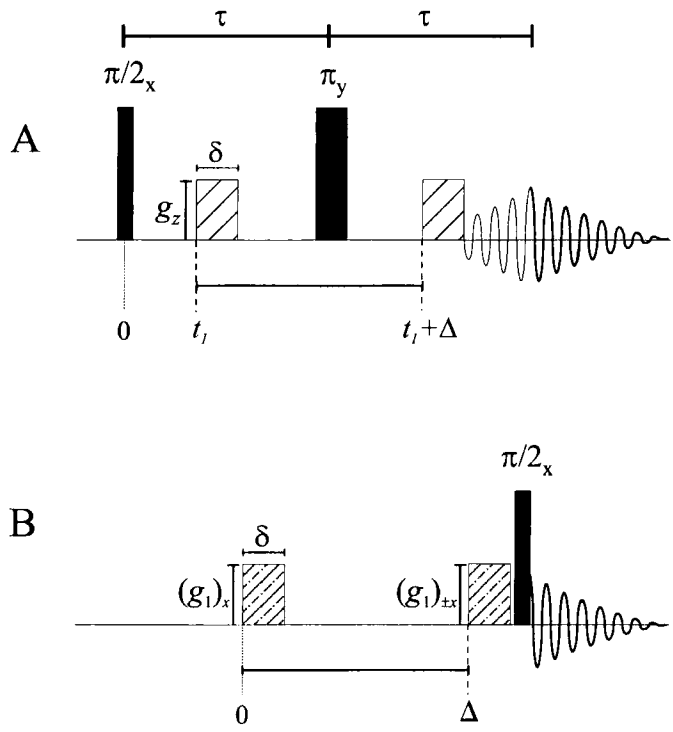

Fig. 19. (A) Basic B_0 gradient-based and (B) B_1 gradient-based sequences for measuring diffusion. In the B_1 gradient sequence, the phase of the second gradient pulse is shifted by π to ensure the cancellation of any contribution other than longitudinal magnetization prior to the read pulse. The B_1-based sequence has the advantage of being weighted by longitudinal relaxation instead of transverse relaxation. However, there is a factor of 2 loss in signal to noise due to the inherent defocusing/refocusing behaviour of the B_1 gradient pulses.

attenuation,[2] $E_\Delta(\mathbf{q})$, including the short gradient pulse approximation (SGP). In the short gradient pulse approximation we have[147,148]

$$E_\Delta(\mathbf{q}) = \iint \mathrm{d}\mathbf{r}_0\,\mathrm{d}\mathbf{r}\,\rho(\mathbf{r}_0)P(\mathbf{r}_0\mathbf{r}, t = \Delta)\,\mathrm{e}^{\mathrm{i}2\pi\mathbf{q}\cdot(\mathbf{r}-\mathbf{r}_0)} \tag{25}$$

where $\rho(\mathbf{r}_0)$ is the equilibrium spin density, $P(\mathbf{r}_0, \mathbf{r}, t)$ is the Green's function or diffusion propagator,[147,149] which is the conditional probability of finding a particle, initially at a position $\mathbf{r}_0$, at a position $\mathbf{r}$ after a time t. $P(\mathbf{r}_0, \mathbf{r}, t)$ satisfies the (isotropic) diffusion equation (e.g. see Ref. 150), subject to the initial condition $P(\mathbf{r}_0, \mathbf{r}, 0) = \delta\ (\mathbf{r}_0 - \mathbf{r})$ (N.b., δ is the Dirac delta function) and

appropriate boundary conditions. In some materials (liquid crystals, ordered biological tissue, etc.) the diffusion is anisotropic and the scalar diffusion coefficient must be replaced by a Cartesian tensor.

For the case of (three-dimensional) diffusion in an isotropic and homogeneous medium (i.e. boundary condition $P \rightarrow 0$ as $r \rightarrow \infty$), $P(\mathbf{r}_0, \mathbf{r}, t)$ is given by[150]

$$P(\mathbf{r}_0, \mathbf{r}, t) = (4\pi Dt)^{-3/2} \exp\left(-\frac{(\mathbf{r} - \mathbf{r}_0)^2}{4Dt}\right) \tag{26}$$

Equation (26) states that the radial distribution function of the spins in an infinitely large system with regard to an arbitrary reference time is Gaussian. Using Eq. (26), the solution to Eq. (25) becomes

$$E_\Delta(q) = \exp(-4\pi^2 q^2 D\Delta) \tag{27}$$

which describes a pure attenuation; including the effects of flow in the z direction (v_z) the solution becomes

$$E_\Delta(q) = \exp(-4\pi^2 q^2 D\Delta + \mathrm{i}2\pi q v_z) \tag{28}$$

The second term in the exponential in Eq. (28) produces a phase shift due to flow in the direction of the applied gradient.

The solution of the diffusion equation becomes much more complicated when the displacement of the particle is affected by its boundaries and $P(\mathbf{r}_0, \mathbf{r}, t)$ is no longer Gaussian. When the PFG method is used to measure diffusion in free solution, the value of Δ chosen has no particular significance, as is clear from Eq. (27). However, in the case of restricted diffusion the effects of the geometry on the motion of the species must be accounted for. Consequently, if the boundary effects are not properly accounted for, an apparent diffusion coefficient, D_{app}, will be measured instead of D.

6.3.1. "Diffusive diffraction" and imaging molecular motion

If a spin is trapped within a fully enclosing pore, then in the long-time limit ($\Delta \rightarrow \infty$) all memory will be lost of the starting position (and, therefore, the diffusional process) and so

$$P(\mathbf{r}_0, \mathbf{r}, \infty) = \rho(\mathbf{r}) \tag{29}$$

and we can define the average propagator,

$$\bar{P}(\mathbf{R}, \infty) = \int \mathrm{d}\mathbf{r}_0 \rho(\mathbf{r}_0) \rho(\mathbf{r}_0 + \mathbf{R}) \tag{30}$$

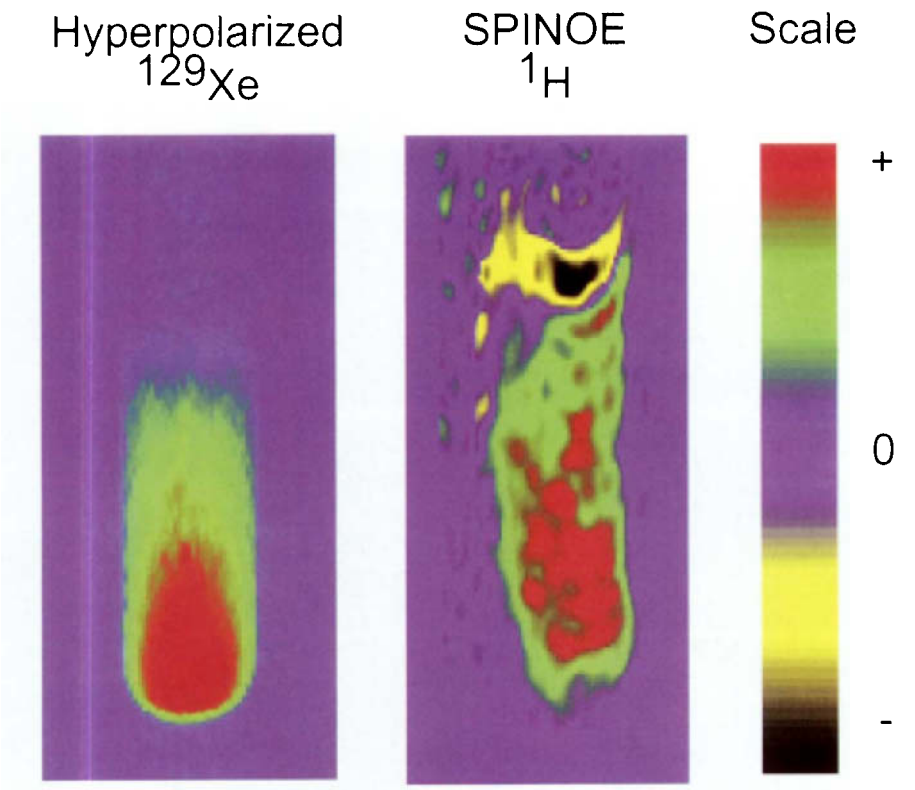

Plate 1. Example of imaging using a hyperpolarized gas. Left:"Hyperpolarized" xenon gas gives off a large magnetic resonance signal in a solution containing hydrogen atoms. Right: 2 minutes later, that signal transfers to the hydrogens. (Reproduced with permission from A. Pines.)

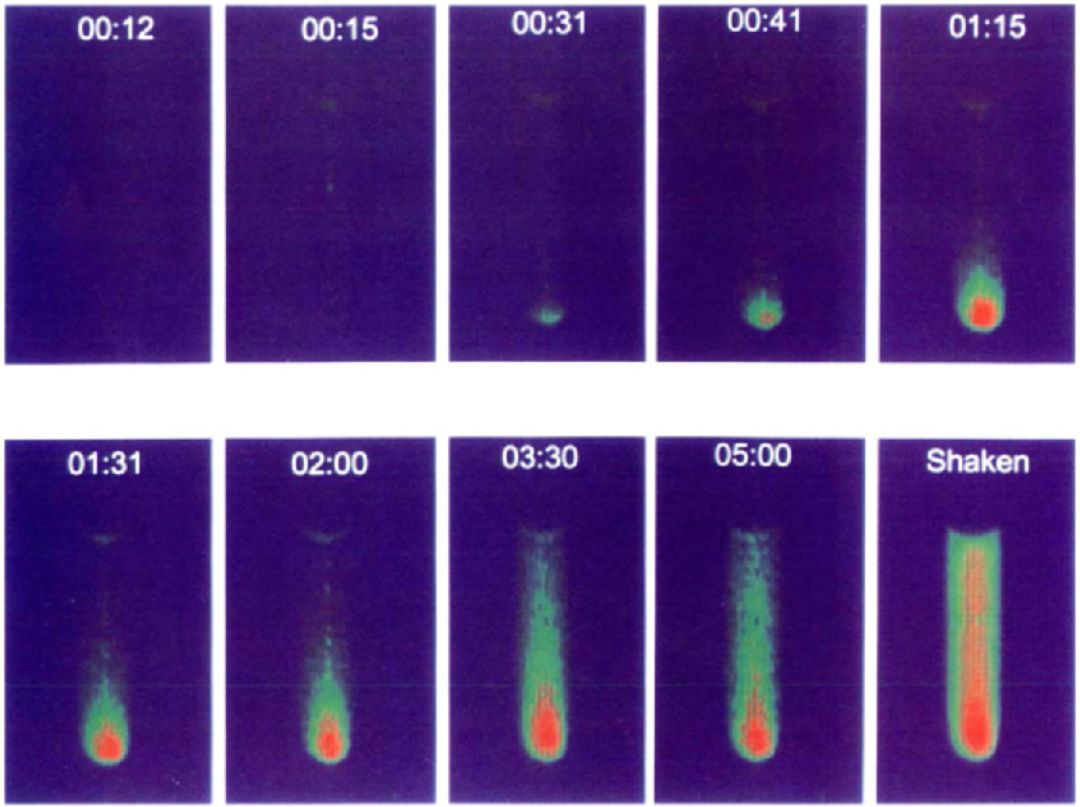

Plate 2. Time-resolved, ^{129}Xe images of ^{129}Xe dissolved in benzene, taken after exposure of the benzene to the hyperpolarized ^{129}Xe. Immediately after the Xe is added there is a concentration gradient which evolves with time. The images were taken using the FLASH technique. (Reproduced with permission from A. Pines.)

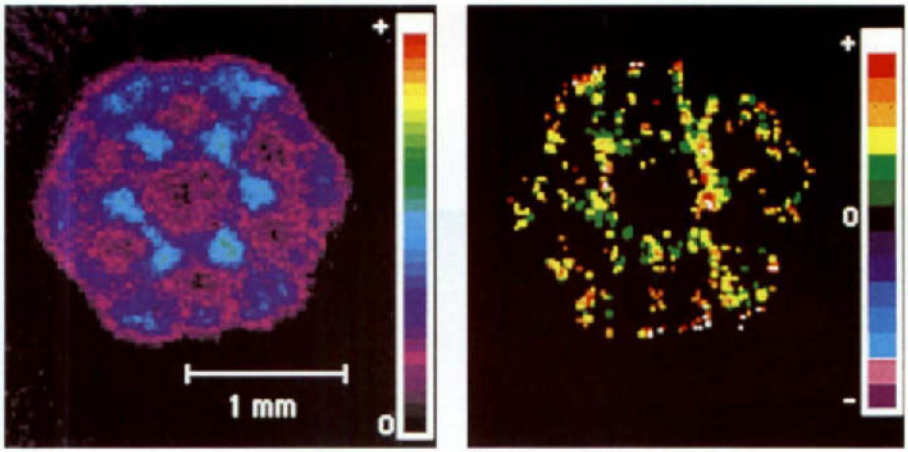

Plate 3. (a) Water proton density image of a transverse section of the stem of *Equisetum* obtained at 60 MHz. The image reveals the high water content of the vascular bundles and outer cortex. (b) Water velocity image of the stem at the same position. The maximum velocity is around 40 μms^{-1}. (Reproduced with permission from Xia *et al.*[240].)

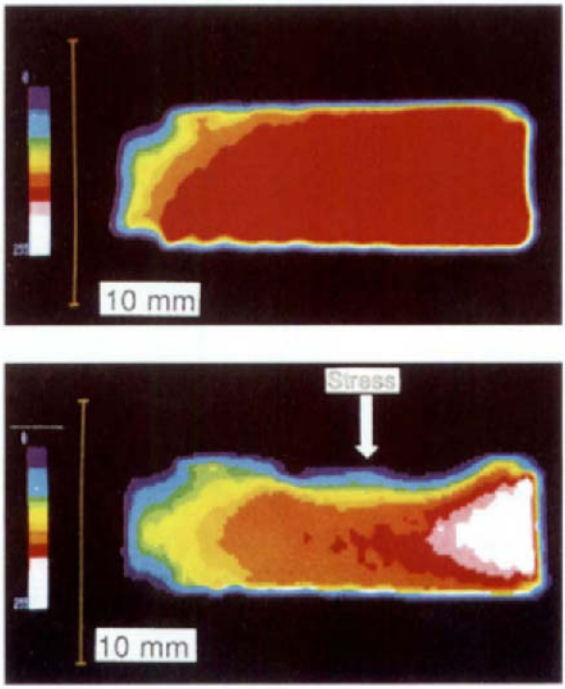

Plate 4. ^{1}H T_2 enhanced image of PMAA gel under (a) no stress and (b) a stress of 4.8 kPa. (Reproduced with permission from Yasunaga *et al.*[281].)

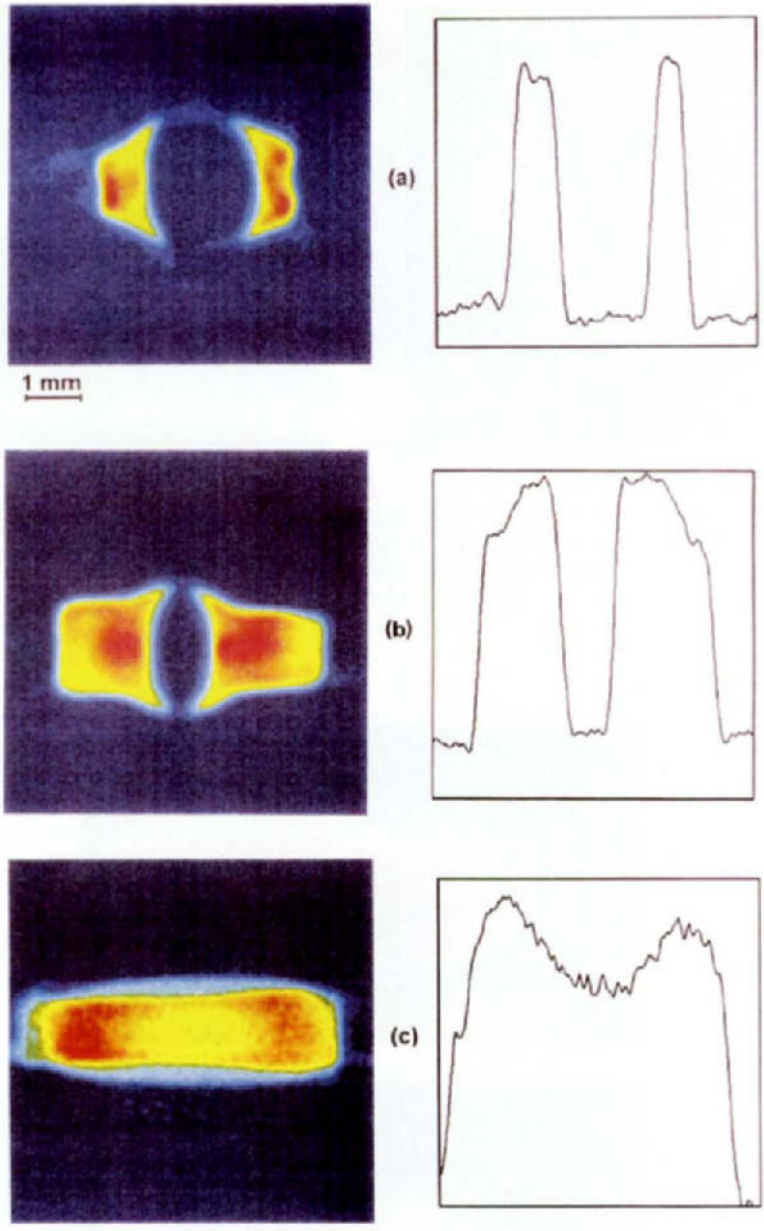

Plate 5. Solvent penetration in stretched PVC and swelling, after being immersed in toluene for (a) 14 h and (b) 30 h; (c) the final state after being immersed in trichloroethylene. Diffusion profiles (cross-sections) along the preferential solvent penetration are shown on the right. The images were acquired using radiofrequency gradients (Reproduced with permission from Valtier *et al.*[293].)

where $\mathbf{R} = \mathbf{r} - \mathbf{r}_0$. Thus, $\bar{P}(\mathbf{R}, \infty)$ is the autocorrelation function of the molecular density. From Eq. (30) and using the Wiener–Kintchine theorem,[151] it is found that $E(\mathbf{q}, \infty)$ is the power spectrum of $\rho(\mathbf{r}_0)$,[3,152,153]

$$E(\mathbf{q}, \infty) = \int d\mathbf{R}\, \bar{P}(\mathbf{R}, \infty)\, e^{i2\pi\mathbf{q}\cdot\mathbf{R}}$$
$$= |S(\mathbf{q})|^2 \tag{31}$$

where $S(\mathbf{q})$ is the Fourier transform of $\rho(\mathbf{r})$.

This is the origin of diffraction-like effects in PFG diffusion studies. $S(\mathbf{q})$ is analogous to the signal measured in conventional NMR imaging. However, whereas conventional imaging returns the phase-sensitive spatial spectrum of the restricting pore, $E(\mathbf{q}, \infty)$ measures the power spectrum, $|S(\mathbf{q})|^2$, and thus is sensitive to average features in local structure (not the motional characteristics). Further, because $E(\mathbf{q}, \infty)$ measures the power spectrum of $S(\mathbf{q})$, Fourier inversion cannot be used to obtain a direct image of the pore. However, **q**-space imaging has the potential to give much higher resolution than conventional **k**-space imaging since the signal is not acquired in the presence of a gradient and thus results from the entire sample rather than a voxel (see Fig. 20). Thus, the resolution achievable in **q**-space imaging is limited only by the magnitude of q. It is important to note that the above discussion regards "diffusive (i.e. **q**-space) diffraction" not "Mansfield (**k**-space) diffraction".[154,155] Mansfield (**k**-space) diffraction depends on the relative positions at fixed time (N.b., normal imaging returns an image of $\rho(\mathbf{r})$), whereas **q**-space diffraction depends on the relative displacements of the molecular origin during Δ.

6.3.2. Dynamic NMR microscopy

The term "dynamic NMR microscopy" has been applied to the situation in which the PFG pulse sequence (Fig. 19) is incorporated into the imaging experiment (see, for example, Fig. 21) and a sequence of high-resolution images is obtained, each with an increasingly large value of **g** that corresponds to slices in **q**-space.[3,156–158] This allows diffusion and flow to be sources of contrast in the image. Each slice in **q**-space is weighted progressively by $E_c(\mathbf{q})$ (see Section 4). The spectrum of displacements at each pixel is then calculated using Fourier methods. Hence, maps of the velocity and diffusion can be obtained simultaneously with high precision. Dynamic NMR microscopy has elements of both PFG and conventional imaging and the signal is modulated in both **k**- and **q**-space,

$$S(\mathbf{k}, \mathbf{q}) = \int \rho(\mathbf{r}) \exp(i2\pi\mathbf{k}\cdot\mathbf{r}) \int P(\mathbf{r}_0, \mathbf{r}, \Delta) \exp(i2\pi\mathbf{q}\cdot(\mathbf{r} - \mathbf{r}_0))\, d\mathbf{r}_0\, d\mathbf{r}$$
$$= \int \rho(\mathbf{r}) E_\Delta(\mathbf{q}, \mathbf{r}) \exp(i2\pi\mathbf{k}\cdot\mathbf{r})\, d\mathbf{r} \tag{32}$$

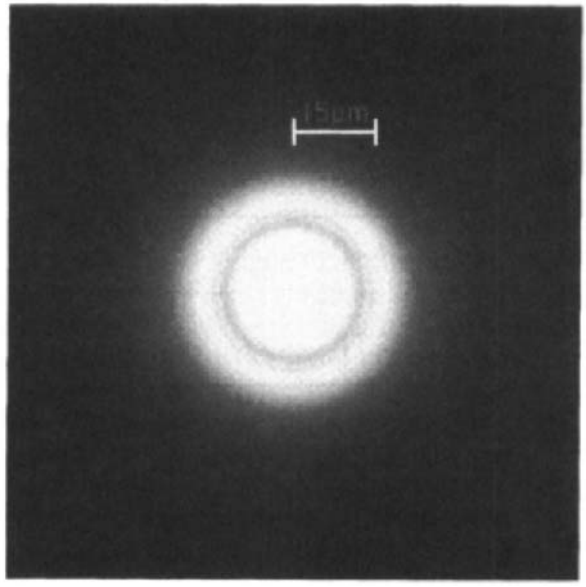

Fig. 20. "Image" of the pore autocorrelation function convoluted with the diffusion-weighted three-dimensional lattice correlation function of water in monodisperse polystyrene spheres with a pore spacing of 15.8 μm. (Reproduced with permission from Callaghan *et al.*[153].)

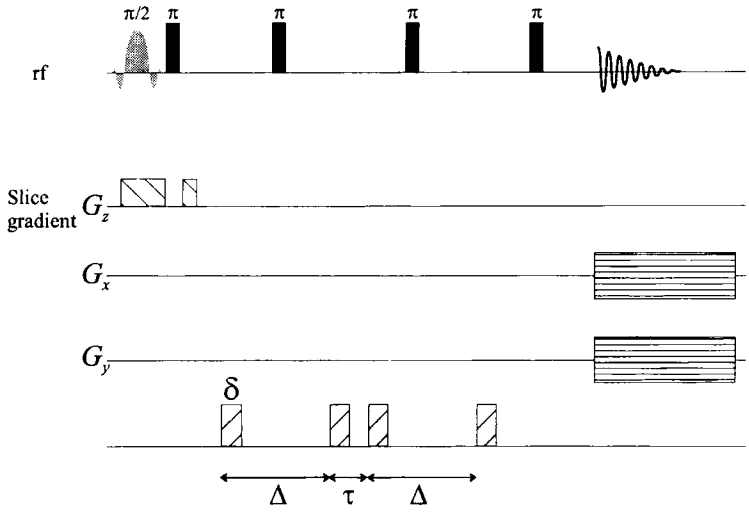

Fig. 21. An example of an imaging sequence for velocity-compensated dynamic NMR microscopy[157] which incorporates the PFG sequence given in Fig. 19A. The sequence contains two PFG trains resulting in an even echo effect so that phase shifts resulting from coherent motion are refocused. The precursor read gradient is not shown.

In Eq. (32) an infinitesimally small volume d**r** is assumed and we can consider $E_\Delta(\mathbf{q},\mathbf{r})$ as the Fourier transform of the local dynamic profile,

$$E_\Delta(\mathbf{q},\mathbf{r}) = \int \bar{P}(\mathbf{R},\Delta)\exp(\mathrm{i}2\pi\mathbf{q}\cdot\mathbf{R})\,\mathrm{d}\mathbf{R} \tag{33}$$

where $\bar{P}(\mathbf{R},\Delta)$ is really a function of the pixel coordinate. Note that $E_\Delta(\mathbf{q},\mathbf{r})$ refers to the normalized echo contribution at the pixel coordinate **r**, whilst $E_\Delta(\mathbf{q})$ refers to the whole sample. If gradients for both imaging and diffusion were used in all three spatial dimensions, the signal in Eq. (32) would be six-dimensional. However, in practice, **q** is applied in only a single dimension (along which the motion is detected; normally z). From a series of images in which **q** is incremented, $E_\Delta(\mathbf{q})$ can be calculated for each pixel. $\bar{P}(Z,\Delta)$ can be determined for each pixel in the image from Fourier transformation with respect to **q**. These functions can then be analysed to return values of v and D for each pixel.

For the case of free diffusion, $\bar{P}$ is a Gaussian curve centred at $v\Delta$ and the width of the curve is proportional to the width of the square root of the self-diffusion coefficient. The velocity and the diffusion coefficient are given by[3]

$$v = \frac{2\pi k_v n_\mathrm{D}}{N\gamma g_\mathrm{m}\delta\Delta} \tag{34}$$

$$D = \frac{(n_\mathrm{D}k_\mathrm{FWHM})^2}{(4\ln(2)/\pi^2)\gamma^2N^2g_\mathrm{m}^2\delta^2\Delta} \tag{35}$$

where N is the size of the array in the transformation, g_m is the maximum pulsed field gradient applied, $n_\mathrm{D}+1$ is the total number of increments of q in the experiment, k_v is the position of the peak and k_FWHM is the width of the peak. The use of "difference propagators" has been demonstrated to be a viable means for obtaining accurate information about velocities at the subvoxel level using dynamic NMR spectroscopy.[159] Xia and Callaghan have reported a less sophisticated and slightly less accurate but more time-efficient "one-shot" (i.e. it does not require multislicing in **q**-space) phase-encoding method of velocity microscopy.[43] Using this method they successfully measured flows down to 45 μm s^{-1}.

6.3.3. Diffusion tensor imaging

In the general case as noted in Section 6.3, the diffusion process is represented by a Cartesian tensor and thus in anisotropic systems (e.g. skeletal muscle) the scalar D_app measured will depend on the direction of the imaging gradients. In such cases the diffusive processes are better described by an apparent diffusion

tensor $\mathbf{D}_{app}$ instead of D_{app}. $\mathbf{D}_{app}$ contains information relating to the structure and orientation of the restricting geometry and the principal diffusivities.[160] Scalar imaging parameters can be derived from $\mathbf{D}_{app}$ including the mean diffusivity (= Trace($\mathbf{D}_{app}$)), diffusion anisotropy of the sample, and organization of the fibres.[161] Importantly, these features, which may be used as contrast factors, are rotationally and translationally invariant and are thus free of orientational artefacts.[160,161] Le Bihan and coworkers have developed methods to estimate $\mathbf{D}_{app}$ from 2D spin-echo images[162,163] and more recently using EPI techniques.[164]

6.4. Miscellaneous

It should be noted that diffusion imaging is also possible using other imaging techniques including steady-state free precession[140] and B_1 gradient imaging-based methods.[165] In a technique somewhat related to STRAFI, Callaghan and Stepisnik[166] have performed spatially distributed pulsed gradient spin-echo NMR experiments using a single wire through the sample. Using this technique they were able to achieve gradients on the order of $100\,T\,m^{-1}$; since the gradient is produced by a single wire instead of a (more inductive) coil, they were able to achieve very rapid switching times. They remarked that gradients well in excess of this figure should be feasible, allowing measurements of molecular displacements smaller than 10 nm and thereby bridging the gap between PFG NMR and neutron scattering. They used their technique to observe anisotropic diffusion in a liquid crystal. Randall *et al.*[167] have suggested the use of high-order primary Hahn echoes in combination with the STRAFI method to obtain diffusion maps of materials of all types, including solids.

7. TECHNICAL ASPECTS OF IMAGING

7.1. Introduction

The elements of an NMR microscope are essentially those of a normal NMR spectrometer with the addition of gradient coils and amplifiers. However, particular emphasis has to be placed on achieving very high S/N. In this section we consider the elements of the NMR microscope and some of the recent advances in the construction. A more detailed coverage of the elements of the NMR microscope may be found elsewhere.[3] Xia *et al.*[168] have presented the designs of two microscopy probes for use in plant imaging and for measurements of slow molecular diffusion. More recently Schoeniger and Blackband[169] presented the design of a microscopy probe for use at 8.5 T with the aim being to image a single cell.

7.2. Radiofrequency coils and systems

Many types of coils can be used in microscopy with specialized coils being more suited for particular tasks and sample geometries. At the most fundamental level they can be classified into volume coils or surface coils. Readers interested in the aspects of surface coils should refer to the reviews by Bosch and Ackerman[106] and Edelstein.[170] Volume coils and RF systems for imaging were also covered in the review by Edelstein.[170]

To achieve higher signal-to-noise ratios, the smallest possible RF coil size should be used so as to achieve a higher filling factor and have a high quality factor (Q).[171] There is much interest in providing better theoretical approaches for determining the magnetic and electric fields generated by RF coils.[172–174] Solenoid coils provide superior B_1 homogeneity and sensitivity as well as being easy to fabricate; however, their geometry precludes them from being coaxially placed in magnets. More recently solenoids with diameters as small as 50 μm for use in microprobes have been reported.[174] These can result in drastic reductions in the averaging time required but at a cost of a more delicate coil/sample assembly and perhaps increased distortions of the static magnetic field due to susceptibility variations around the sample.

To maintain homogeneity, solenoidal coils need to be relatively long compared to their diameter and this becomes an issue as the lower inductance required at higher fields requires a shorter solenoid, which results in reduced homogeneity. Birdcage coils are known to have high RF homogeneity but typically have been used only for whole-body applications.[175] There have been reports of the use of small birdcage resonators[176,177] for microscopy work, even for small samples with diameters of 3 mm or less.[178] These have the advantage of maintaining good homogeneity and Q at high frequencies and convenient orientation as the cylindrical axis is along B_0.

When imaging with large coils, the sample noise is larger than the coil noise. However, in the case of NMR microscopy where much smaller RF coils are employed, the converse is true and a large improvement in S/N can be obtained by reducing the coil noise. Black *et al.* have used the high-temperature superconductor YBCO.[179] At 7 T their coil had a Q of about 50 000. This approach can provide up to a 60-fold increase in S/N. This increase may, in many cases, make signal averaging unnecessary and the total imaging time then becomes dependent only on the time required to traverse **k**-space.

Superconducting coils are not only technically more difficult to manufacture but must also be kept at low temperatures (e.g. 10 K for YBCO) while maintaining the sample at room temperature. Hence, complicated Dewar arrangements must be employed to maintain the temperature differential between the two compartments. Further, owing to the very high Q, the resonant frequency of the superconducting coil is temperature dependent and thus the coil temperature must be accurately maintained.

7.3. B_0 gradient coils

The design and construction of B_0 gradient coils were summarized in an earlier chapter in this series[2] and has recently been the subject of several reviews.[180,181] Consequently, we will focus only on some very recent innovations in the field, especially those relevant to NMR microscopy. Surface gradient coils are not covered and details can be found in the review by Cho and Yi.[180] The performance requirements of current amplifiers have been considered by Callaghan[3] and more recently by Turner.[181]

An ideal B_0 gradient set would include the following properties: a large gradient for a given current input (i.e. high current efficiency); low inductance so as to allow rapid switching; minimal eddy current production; and, rather importantly, a linear gradient over a large sample volume. There are also practical considerations such as the ease of fabricating such a coil and whether it provides a convenient geometry for locating the sample. The gradient coils in modern imaging spectrometers are almost invariably shielded. In this technique a secondary set of windings has the effect of confining the gradients to the sample region and thereby preventing (or at least reducing) the generation of eddy currents in surrounding conductors.

The current efficiency of a coil increases with the number of turns in the coil, whereas the inductance increases with the square of the number of turns. This increase in inductance necessitates the use of larger voltage to maintain fast switching times, or conversely using large currents but with fewer turns in the gradient coil. Since increasing current generates many undesirable effects (overheating, mechanical vibrations and eddy currents, etc.) it is technically simpler to decrease the coil diameter than to increase the current. This has the added advantage that there is a rapid decay in the stray field amplitude with distance, so that decreasing the coil dimensions also helps to reduce eddy current problems.[182]

Gradient coil design can involve discrete windings or distributed windings. The simplest gradient coil producing a gradient in the z direction is the Maxwell pair; for transverse gradients the double saddle ("Golay") coil is commonly used. The distributed winding type of gradient coil is more difficult to design and to fabricate since, after the ideal current distribution is determined, the continuous current distribution must be approximated using a discrete number of conductors of finite length. A number of approaches have been used to determine the optimal positions of the coil windings. These approaches include the "target field" approach, "stream function" methods and matrix inversion techniques. The matrix inversion techniques related to finite-element methods are the most general in that they can be used for any shape of coil. The stream function is the integral of the current density. Equally spaced contours of the stream function provide cogent locations for the placement of the individual windings. In the target field approach the desired

field is specified and then Ampère's law is inverted to enable the calculation of the currents required.[183]

Simulated annealing methods have emerged as a powerful new method in the design of longitudinal[184] and transverse gradient coils.[185] Simulated annealing,[186] a combinatorial optimization technique, is used to find the global minimum of a gradient error function within the allowable physical constraints (dimensions, linearity, stored energy, inductance, etc.). The advantage of this technique is that real-space current elements can be modelled and manipulated in any geometry. While the method is computationally intensive, this would seem to become less significant with ever-faster computers. Adaptive simulated annealing has been used to design biplanar x and z gradient coils,[187] and coils with coaxial return paths[188] that represent a new alternative to Golay coils for producing transverse gradients.

The development of improved gradient coils with better performance characteristics is an area of great interest, with recent designs including transverse coils with low inductance and restricted length,[189] elliptic cylinder longitudinal gradient coils,[190,191] a novel semi-shielded quadrupole gradient coil[169] and coils containing wires wound in a sinusoidal distribution.[192] For solid imaging experiments involving magic angle spinning, special gradient coils generating gradients at magic angles with standard cylindrical geometries have been designed and built.[193,194]

7.4. B_1 gradient coils

B_1 gradient coil design is technically much easier than that for B_0 gradient coils. A typical arrangement for performing imaging with B_1 gradients is to use a single-turn coil to generate the read gradient ($G_1(x)$) and a saddle coil as the detection coil and possibly to generate a B_1 gradient in the z direction[195] (see Fig. 22). A single-turn gradient coil is capable of producing a uniform gradient in a region from $0.2r_{coil}$ to $0.9r_{coil}$, where r_{coil} is the coil radius.[196] The gradient strength is strongly related to the efficiency of the tuned circuit and the transmitter power. A major problem with B_1 gradients is that they are normally much weaker than those obtainable for B_0 gradients. The simplest way to increase the gradient strength is to decrease r_{coil}; by doing this Humbert *et al.*[197] achieved gradients up to $0.2\ T\ m^{-1}$. However, this gain is at the expense of gradient uniformity. Other approaches have included the use of flat coils,[198] which produced gradients up to $0.75\ T\ m^{-1}$; using a solenoid instead of a single-turn coil, with gradients as large as $3\ T\ m^{-1}$ being obtained in the fringe field;[199] and toroid cavity detectors.[200] Other interesting designs have included a cone coil suitable for spatial encoding along the B_0 axis[201] and a coaxial resonator for producing cylindrically symmetric gradients.[202]

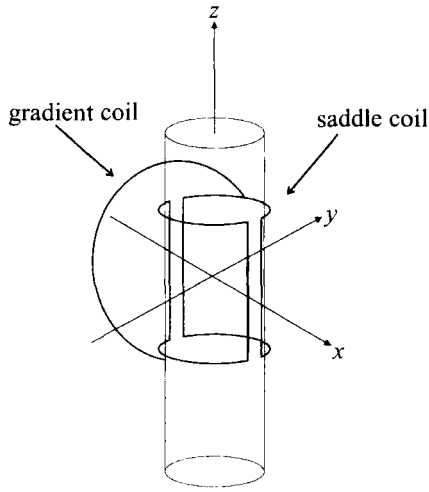

Fig. 22. A simple RF coil arrangement for the generation of B_1 gradient for encoding (after Maffei *et al.*[95]). The single-turn coil generates the RF gradient, which acts in the x direction, and the saddle coil is used to generate an RF gradient along the z direction and also for signal detection.

7.5. Miscellaneous

A few groups have reported the use and construction of apparatus for imaging at cryogenic temperatures.[203] The designs of such apparatus must meet several requirements. First, only a low power can be used to regulate the sample temperature. Second, to maintain constant sensitivity the RF coils must be thermally isolated and, conversely, to prevent sample heating. Finally, non-metallic parts are preferred near the sample not only for the obvious reason of avoiding the generation of eddy currents but also to prevent heating due to eddy currents that may be induced in conducting materials.

8. ARTEFACTS, COMPLICATIONS AND RESOLUTION

8.1. Introduction

There are numerous artefacts that can affect images, and a deeper consideration of these, especially those pertaining to nonmedical studies, is the subject of this section. We note in passing that, apart from diffusion and flow, image resolution can be limited by sample (e.g. physiological) motion, and to minimize such effects, fast imaging sequences, synchronized acquisition and post-data-processing procedures have been devised. It is important to realize

that some artefacts are image sequence-dependent. This section is particularly concerned with artefacts resulting from the effects of imperfect gradient pulses, eddy currents, magnetic inhomogeneities, diffusion, flow and chemical shifts. In the last part of this section the limits to image resolution are considered.

8.2. Applied gradients and eddy currents

The rapid switching of B_0 gradients generates eddy currents in surrounding conductors (e.g. heat shield in the Dewar, RF coils and shielding). These in turn generate secondary magnetic fields that spoil the homogeneity during the frequency encoding and result in image distortions, and in the case of diffusion gradients also contribute to gradient pulse mismatch. The eddy currents also distort the applied gradient field temporally, resulting in slower rise and settling times. A simple solution is to use "pre-emphasis", whereby the input current to the gradient coils is designed so that it compensates for the induced eddy currents. A more effective approach is the use of shielded gradient coils (see Section 7.3). It is common to use both pre-emphasis and shielded gradient coils together and, with this approach, gradient settling times of less than a few hundred microseconds are possible. Balcom *et al.*[123] have demonstrated that 1D constant-time imaging (see Section 5.4.6) can be used to measure gradient, rise, stabilization and decay.

Imperfection in gradient pulses resulting from amplifier instability or eddy currents is especially serious in the case of diffusion gradients as it can result in large artefactual losses of signal intensity. This aspect was considered in an earlier contribution.[2] However, when a PFG sequence is incorporated into an imaging sequence, as in dynamic NMR microscopy, the problems are further complicated by cross terms between the diffusion gradients and the imaging gradients. These problems are exacerbated in the case of microscopy where the imaging gradients can be as large as or larger than the size of the diffusion gradients. Neeman *et al.*[204] have considered the effect of diffusion on the signal attenuation in various spin-echo diffusion imaging sequences and derived analytical expressions for the cross terms. Thus careful experimental calibration of the gradient strength is required.[53]

8.3. Susceptibility and diffusion effects

8.3.1. Susceptibility artefacts

In high-resolution NMR great effort has been put to minimizing the residual inhomogeneity arising from imperfect shimming, and in fact the use of imaging to measure field maps is now well established as a method for sample shimming.[205] However, in the case of imaging, residual magnetic

inhomogeneity is rarely of significance, but residual inhomogeneities in heterogeneous samples (in the sense of magnetic susceptibility, χ) can be both a source of contrast and a source of artefacts, especially in biological samples owing to the presence of air bubbles.[206,207] Severe inhomogeneity problems are encountered in samples containing paramagnetic centres.[127]

Internal gradients can either add to or subtract from the applied imaging gradients since the differences in χ result in a spatially varying $B_0, \Delta B_0(\mathbf{r})$, which in turn results in a local precession frequency offset, $\gamma \Delta B_0(\mathbf{r})$. The spin warp imaging scheme (see Section 3.6.2 and Fig. 5) provides a useful model for illustrating the effects of $\Delta B_0(\mathbf{r})$. As noted in Section 3.3, a spin-echo-based sequence is much less sensitive to magnetic field inhomogeneities than a gradient-echo-based sequence since the spin-echo in the absence of diffusion will refocus (i.e. remove) the static susceptibility effects at $k = 0$ which is the centre of **k**-space and determines the overall image intensity. However, perturbations to the local magnetic field result in a residual distortion. Including the effects of $\Delta B_0(\mathbf{r})$, the raster of the spin warp imaging scheme in which the x direction of the raster is encoded using frequency encoding and the y direction using phase encoding is given by[3,208,209]

$$S(k_x, k_y) = \iint \rho(x,y) \underbrace{\exp[\mathrm{i}2\pi k_y y + \mathrm{i}\gamma \Delta B_0(x,y) t_y]}_{\text{phase encoding}} \underbrace{\exp\left[\mathrm{i}2\pi k_x \left(x + \frac{\Delta B_0(x,y)}{G_x}\right)\right]}_{\text{frequency encoding}} \mathrm{d}x\,\mathrm{d}y \tag{36}$$

Thus, $\Delta B_0(\mathbf{r})$ causes a local phase shift of

$$e^{i\gamma \Delta B_0(x,y) t_y} \tag{37}$$

and in the frequency-encoded x direction the pixels to be offset by a factor

$$\frac{\Delta B_0(x,y)}{G_x} \tag{38}$$

In a spin-echo experiment the phase shift will be refocused; or if the signal is acquired immediately after the phase-encoding step, the local phase shift can be removed by calculating a final image modulus.[209] The offset given by Eq. (38) is more troublesome and affects all imaging sequences involving frequency-encoding and, significantly, it is γ independent and depends only on the ratio of the inhomogeneity to the strength of the read gradient. From Eqs (37) and (38) it can be inferred that one, albeit time-consuming, solution would be to use only phase-encoding gradients, such as in constant-time imaging. However, from Eq. (38) it can be seen that the image distortion can be avoided by increasing the read gradient strength so that the local field offset is less than the variation in the applied field across a single voxel. Hence, different imaging

sequences will have different degrees of vulnerability to the effects of magnetic inhomogeneity and it is important to be able to recognize such effects. Chemical shift imaging techniques and particularly the selective excitation method are very sensitive to B_0 inhomogeneities, especially when attempting to resolve peaks that are close in frequency.[206]

B_1 gradients, in contradistinction to B_0 gradients, are unaffected by the effects of magnetic susceptibility since it relies on nutation rather than free precession, providing that B_1 is sufficiently strong that off-resonance effects can be neglected.[210] However, as noted above, in B_1 gradient imaging the read gradient is applied in the form of pulses separated by acquisition windows and in these windows T_2^* and the effects of internal B_0 gradients cannot be ignored. Raulet *et al.*[210] found that, at least to first order, B_1 gradient microscopy is not affected by susceptibility effects. They noted that by compensating for residual leakage between the read gradient coil and the detection coil, the acquisition windows can be shortened, thereby further reducing any susceptibility effects.

8.3.2. Diffusive relaxation and edge enhancement

Translational diffusion can affect imaging experiments in a number of ways, including shortening the apparent T_2 (i.e. diffusive relaxation) by inducing phase shifts as the spins move within spatially dependent magnetic fields.[211,212] Such fields can arise from susceptibility differences within the samples and also due to the applied imaging gradients (and it is therefore sequence specific). For example, diffusive relaxation due to the read gradient increases as the number of pixels is increased.[61,209] For a read-direction bandwidth T^{-1}, the attenuation factor at $k_x = 0$ is[213]

$$A_F(k_x = 0) = \exp(-\tfrac{4}{3}\pi^2 D k_{max}^2 (NT)) \tag{39}$$

where k_{max} is the maximum value of **k**-space employed. The signal loss associated with application of a phase-encoding gradient (i.e. G_y) pulse such as in Fourier imaging is[209]

$$A_P(k_y) = \exp(-\tfrac{4}{3}\pi^2 D k_y^2 t) \tag{40}$$

In the case of projection reconstruction where both the x and y directions are phase-encoded, $A_P(k_x, k_y)$ has the same form as Eq. (40) but k_y is replaced by k. Thus, in an imaging experiment the signal relaxation due to free diffusion ultimately limits the available resolution as it leads to a blurring of sharp features. However, there is no loss of average image amplitude since no attenuation occurs at $k = 0$. Observing Eq. (40) and recalling the definition of k (see Eq. (2)), it can be seen that for a given pixel dimension the blurring effects may be arbitrarily reduced by using a shorter phase-encode time and

correspondingly larger gradient. It should be noted that phase-encoding gradients are less susceptible to diffusive attenuation. Gradients resulting from susceptibility differences in the sample superimpose on the applied gradients,

$$\mathbf{G}^{\text{total}}(\mathbf{r}) = \mathbf{G} + \mathbf{G}^{\text{loc}}(\mathbf{r}) \tag{41}$$

leading to additional attenuation by the above mechanisms.

Callaghan *et al.*[209] noted that as a "rule of thumb" the ratio

$$\frac{\Delta x_{\text{diff}}}{\Delta x_{\text{pixel}}} \tag{42}$$

where Δx_{pixel} is the pixel dimension and Δx_{diff} is the r.m.s. displacement of the spins over the signal acquisition period, determines the significance of self-diffusion effects on imaging. In fact the $2Dk_{\max}^2(NT)$ (see Eq. (39)) is equivalent to $(\Delta x_{\text{diff}}/\Delta x_{\text{pixel}})^2$. Thus, sensitivity and resolution limitations resulting from diffusion apply only at high resolutions.

In the case of restricted diffusion the situation is rather different. Restricted diffusion results in edge enhancements that are observable only at the microscopic level.[212,214–218] Pütz *et al.*[217] proposed a mechanism whereby diffusive boundaries impermeable to water distort the lineshape function of the observed frequency spectra so as to enhance image contrast around boundaries. As pointed out by Callaghan *et al.*,[212] the edge enhancement that occurs in a spin-echo sequence arises from diffusive attenuation, and this effect will dominate the lineshape distortion effects. The edge enhancement provides an interesting source of contrast that may be used to discern features that would otherwise be too thin to resolve, such as membranes.[218] De Swiet[218] has noted that the type of phase-encoding used strongly affects the results. Callaghan *et al.*[209] have considered the complicated interplay between susceptibility and diffusion in spin warp imaging that can lead to local boundaries appearing as bright features. In this case the susceptibility-related fields modulate the net local gradient, and as a result the total gradient at any point can be larger or smaller than the read gradient, leading to relative signal enhancement or attenuation. Thus, at points where the local gradient and read gradient are equal in magnitude but of opposite sign (i.e. a gradient null point) it is possible for sharp bright spots to occur, or dark spots if the gradients are of the same sign.

8.4. Flow

It is perhaps less than surprising that flow and sample motion also lead to image artefacts in conventional spin-echo imaging sequences, although these tend to

be more serious in medical imaging. The artefacts are in two forms. First, if there is variations in flow (e.g. turbulence) across a voxel, the resulting phase dispersion will cause a loss in image intensity.[219] In this sense the turbulence can be thought of as a diffusion-like process. Second, if the spins in a voxel have a nonzero average velocity, the phase of the resulting signal will be offset by the phase shift related to M_1 (see Eqs (22) and (23)); however, providing that this difference does not change from step to step in the phase-encoding gradient, the spatial localization will be unaffected. Flow parallel to the direction of the phase-encoding gradient will result in phase-misregistration. These motional artefacts can be reduced by using flow-compensated imaging sequences in which the imaging gradients meet the condition $M_1 = 0$. Flow-related artefacts have been considered in detail elsewhere.[138,220]

8.5. Chemical shift

Slice selection can be hampered by chemical shift effects that result in localization errors.[38] If there is sufficiently high resolution, a simple imaging method will produce an image that is the superposition of the images of the individual signals that appear to be shifted in space (recall that imaging relies on making the position frequency dependent).[3] The choice of soft pulse for chemical shift selective excitation in chemical shift imaging is important in minimizing artefacts from nearby resonances.[221]

8.6. Resolution and signal to noise

To a first approximation, resolution in NMR microscopy is "sensitivity limited"[171,222] as the minimum acceptable S/N translates into the highest usable resolution (= smallest voxel). The S/N obtainable depends on a number of factors, including the electronic noise of the instrument, the resolution required (i.e. the voxel size), the experiment time and the inherent properties of the sample (e.g. relaxation characteristics, chemical shift, diffusion and susceptibility differences in a heterogeneous sample). For an isotropic voxel the number of spins per voxel reduces cubically with the resolution. For example, to go from an isotropic resolution of $(1\,\text{mm})^3$ to $(10\,\mu\text{m})^3$ and maintain the same image quality, the S/N per voxel would have to increase by a million times. The relationship between S/N and experimental variables is

$$\text{SNR} \propto \frac{B_0^2 B_1 \sqrt{n}}{\sqrt{4kT\Delta\nu(R_{\text{coil}} + R_{\text{sample}})}} \tag{43}$$

where n is the number of scans, and k is the Boltzmann constant, T is the temperature, $\Delta\nu$ is the bandwidth, R_{coil} and R_{sample} are the coil and sample

resistance, respectively. When small RF coils are used, R_{sample} is negligible. Since R_{coil} is proportional to $\sqrt{B_0}$ owing to skin effects, the overall S/N increases as $B_0^{7/4}$. The S/N can also be increased by decreasing the size of the RF coils[171,174] and thereby increasing B_1. There are many sources of noise in the NMR experiments, but in a well-designed system the sensitivity and overall noise are ultimately determined by the probe and RF preamplifier. As noted above, the Johnson noise in the receiver coil can be reduced through the use of superconducting materials and reducing the operating temperature of the receiver coil–preamplifier system.

Apart from superconducting RF coils, imaging with the sample itself at cryogenic temperatures results in enormous gains in S/N by virtue of the Boltzmann distribution. For example, Moore *et al.*,[203] after allowing for molar densities and T_1 relaxation rates, estimated a gain in S/N of about 16 for n-$^1H_2$ (n denotes the equilibrium rotational state populations at room temperature) at 14 K relative to ^1H_2O at room temperature.

The least technically demanding means of increasing S/N is simply to increase the number of averages. However, owing to time constraints, this is generally not an acceptable solution. A more prudent alternative is to use an appropriate pulse sequence suited to the sample and experimental conditions; for example, diffusion-induced signal loss can be reduced by using diffusion-reduced gradient-echo pulse sequences.[17,223]

Ideally, the best resolution is obtained using the minimum bandwidth consistent with the intrinsic line width (i.e. $1/(\pi T_2)$) equal to the pixel width in the frequency domain. This leads to an optimal gradient amplitude for a given sample dimension.[3] Resolution of a few micrometres (i.e. 1–5 μm) is theoretically obtainable with B_0 gradients of the order of a few T m^{-1} and observing proton resonances. However, as noted above, magnetic susceptibility and translational diffusion act to degrade spatial resolution, although some of these problems can be overcome using larger gradients (~6 T m^{-1}).[213]

An interaction that affects the spatial resolution results in a modulation of the signal in **k**-space. The shape of this modulation is called the modulation transfer function (MTF) and its Fourier transform is termed the point spread function (PSF). The convolution of PSF with the spatial distribution of spins determines the smallest feature that can be resolved in an image. The resolution is commonly defined by the full width at half-height (FWHH) of the PSF.[224] Using the PSF, McFarland[224] has analysed resolution in the spin warp and projection reconstruction sequences.

In B_1 microscopy the obtainable resolution depends on various factors including T_2, diffusion, S/N and the strength and quality of the B_1 gradients over the sample volume. On the basis of relaxation times, it was calculated that even with modest gradients sub-micrometre resolution is possible.[95] The major problem with B_1 gradient-based microscopy is the low gradient strengths obtainable. Woelk *et al.*[200] predicted a theoretical maximum (observing ^1H) of

6.5 μm and experimentally managed to observe 20 μm resolution using a toroidal cavity detector that produces a B_1 field gradient inversely proportional to the distance from the centre of the torus. More recently, a resolution better than 5 μm was achieved using a two-turn flat coil.[198] Canet has shown[19] that the theoretical spatial resolution in B_1 imaging under the somewhat ideal conditions of the magnetization decay during the acquisition of the pseudo-FID being described by $T_{1,2}$ (see Eq. (18)), and ignoring the effects of translational diffusion, is

$$\Delta x_{\text{pixel}} = \frac{2}{\gamma G_1 T_{1,2}} \tag{44}$$

Of particular interest is that when $T_2 \ll T_1$, $T_{1,2} \approx 2 \times T_2$, whereby a factor of 2 is gained over conventional B_0 imaging. Further, since the B_1 method does not use an echo, in contrast to many B_0 methods, there is a significant gain in S/N. The S/N can be further enhanced by using a low-pass filter with a cut-off frequency equal to the Nyquist frequency of the acquisition process.

9. AREAS OF APPLICATION

This section is intended to introduce some of the systems and areas that imaging has been applied to, especially in the areas of biology, chemistry and fluid dynamics, and some recent novel applications.

9.1. Biological studies

Biological studies, being directly related to the medical field, were an obvious and early extension of the domain of imaging applications. Biological studies have benefited from the increasingly higher resolutions obtainable, and the deeper understanding of image contrast mechanisms (and how to control them) permits different aspects of physiological processes and metabolism to be visualized noninvasively even at cellular levels.[225] The applications to plant science and agriculture have been reviewed by Sarafis *et al.*[226] ^{1}H imaging is also a very convenient means of studying freezing behaviour in plants[227] (see Fig. 23). From images acquired at 500 MHz, Bowtell *et al.*[228] were able to observe cellular detail in a geranium petiole. They achieved an in-plane resolution of 4.5 μm with a slice thickness of 100 μm. They remarked that much of the appearance of the images obtained was a consequence of signal loss due to diffusion in the local gradients that surround intercellular air spaces. Similarly, taking advantage of higher fields, images have been obtained of single-cell organisms (i.e. green algae) with spatial resolutions of 6 μm;[171] also images of single neurons isolated from the marine snail *Aplysia* with in-plane resolutions

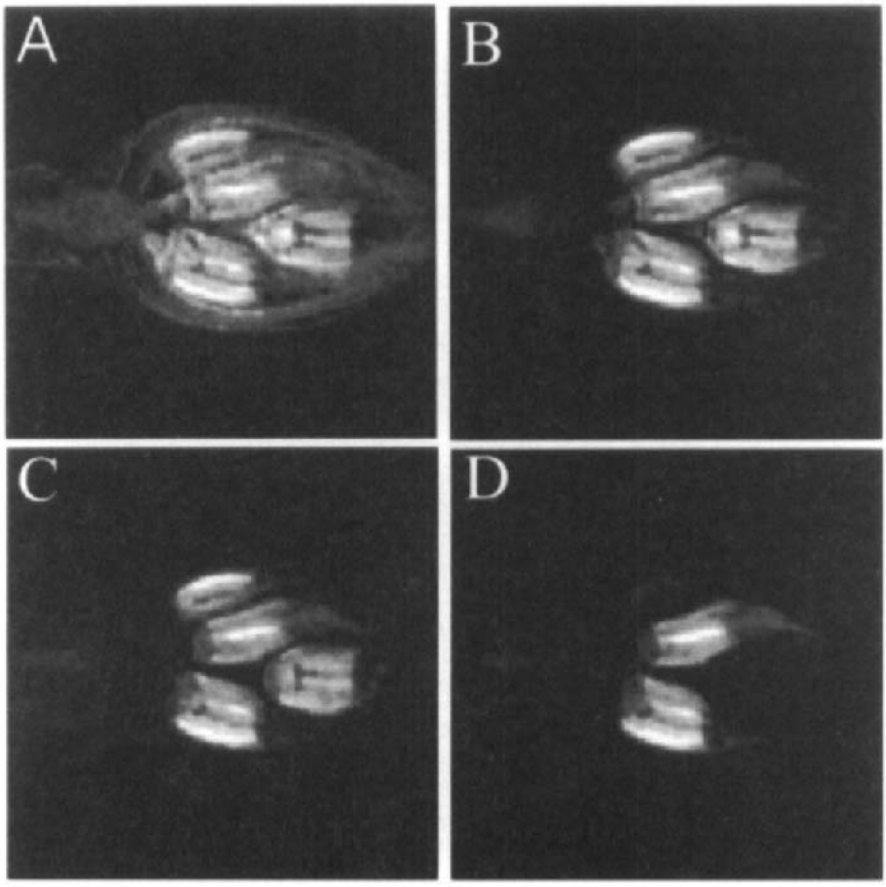

Fig. 23. Visualization of freezing behaviour in an azalea flower bud at (A) 1°C, (B) −7°C, (C) −14°C and (D) −21°C using ^{1}H NMR spin-echo images. The progression of the freezing process is clearly seen with only supercooled water remaining visible in the images below 0°C. (Modified with permission from Price *et al.*[227].)

of 20 μm have been obtained at 360 MHz[62,169] and later at 500 MHz.[229] In a pioneering study, Jacobs and Fraser[230] studied cell movement and lineages in developing frog embryos. To do this they injected a single cell at the embryonic 16-cell stage with a contrast agent. Kemp-Harper *et al.*[231] have reported three-dimensional triple-quantum filtered ^{23}Na imaging of agarose gels and in a blue mussel.

Chemical shift microscopy has found application in plant histochemistry,[232–234] with recent applications including determining the distribution of sucrose in castor bean seedlings[235] and imaging the distributions of water, oil and soluble carbohydrates.[207] Biological chemical shift microscopy applica-

tions are not only the preserve of the botanist, and Skibbe *et al.*[236] have recently reported the use of ^{1}H spin-echo and ^{31}P chemical shift-selective microscopy to study pH metabolism in (living) caterpillars.

Dynamic NMR microscopy has particular relevance to understanding physiological processes in biological tissue such as observing *in vivo* vascular flow measurements in botanical samples. Back *et al.*[237] have reviewed the biophysical applications of motional contrast. Recent studies have included observing flow in ripening kiwi fruit,[238] diffusion of cell-associated water in ripening barley seeds[239] and xylem transport and water flow in plants[238,240,241] (see Plate 3). In a fascinating study, Görke *et al.*[242] studied coherent and incoherent flow in fertilized quail and bantam eggs using multiplane tagging and gradient-echo imaging sequences. They were able consistently to observe distinct motions to and from the yolk. Further, they showed that the flow is largely of a pulsating nature with a pulsation frequency of 0.4 Hz.

In vitro imaging applications have included ^{1}H spin-echo imaging studies of the finger-like lysis patterns of blood clots[243,244] and a ^{23}Na NMR microscopy study of the sorption of sodium ions in the polyelectrolyte matrix of bovine nasal cartilage from which the ion activity coefficients and fixed charge density in cartilage were able to be determined.[245] In a later study, Potter *et al.* used an inversion recovery null-point technique to investigate the transport of divalent copper ions into cartilage.[246] They pointed out that transient diffusion studies of ion interdiffusion are a useful method for investigating the effect of matrix composition on ion transport. It was noted that had PFG measurements been used, the self-diffusion coefficient would have been measured, not the interdiffusion coefficient.

9.2. Chemical systems and materials

9.2.1. Chemical systems

Imaging provides a unique approach for studying the distribution of species in materials and the spatial dependence of chemical reactions and phase transitions. It is certain that the range of applications in this field will grow enormously in the next few years.

Mobile protons in many transition metals have liquid-like narrow lines. McFarland and Lee[247] used conventional imaging techniques to localize hydrogen spatially in the H–Pd system (see Fig. 24). They noted that NMR microimaging represents perhaps the only way of imaging protons in metal hydrides. NMR microscopy has found application in monitoring the formation of the gel layer in hydrophilic matrix pharmaceutical tablets[248,249] (see Fig. 25). Imaging has proved to be an excellent method for visualizing ice structure in saltwater ice.[250] Tallarek *et al.*[251] have used ^{1}H FLASH imaging to observe the chromatographic bands of gadolinium chelates. The images allowed the

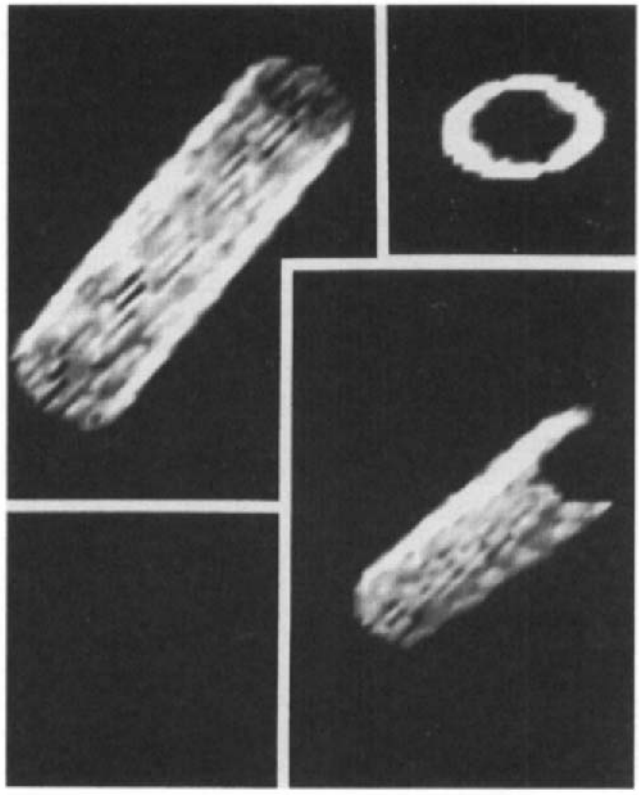

Fig. 24. Three views of a 3D ^1H NMR image of a section of H–Pd 1.0 mm in diameter. The image intensity is proportional to the proton density. The spin-echo image was obtained using a 300 ms repetition time and a 4 ms echo time. Each image element corresponds to a spatial volume of approximately 50–100 μm in linear size. As can clearly be seen, the signal is confined to the surface layer. (Reproduced with permission from McFarland and Lee[247].)

formation and resorption of fissured and/or compact zones in the column to be visualized. Hills *et al.*[252] studied drying in granular beds of nonporous particles using standard spin-echo imaging.

The noninvasive nature of NMR imaging has particular relevance to study of the delicate interactions in chemical systems. Even at cryogenic temperatures NMR imaging is noninvasive, since the NMR excitation energy corresponds to only a few millikelvins. Moore *et al.*[203] used a cryogenic imaging device to image $^1H_2$, $^2H_2$ and mixtures of these isotopes in the liquid and solid states. A three-dimensional image of solid $^1H_2$ at 13 K is shown in Fig. 26. Cryogenic imaging is likely to become a routine method for probing the spatial distribution of hydrogen isotopes inside inertial-confinement fusion targets.

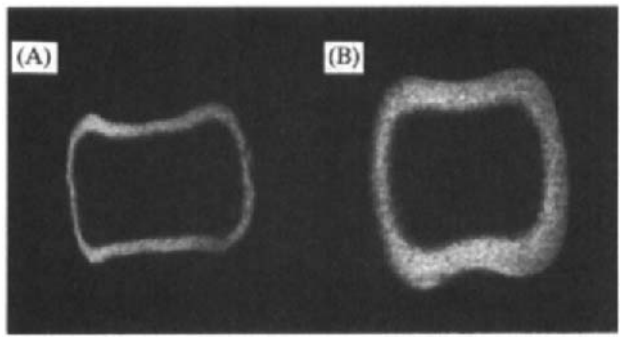

Fig. 25. 500 MHz ^{1}H NMR images showing the axial and radial growth of the gel layer of hydroxypropylmethylcellulose tablets after (A) 10 min and (B) 30 min of hydration. (Reproduced with permission from Bowtell *et al.*[249].)

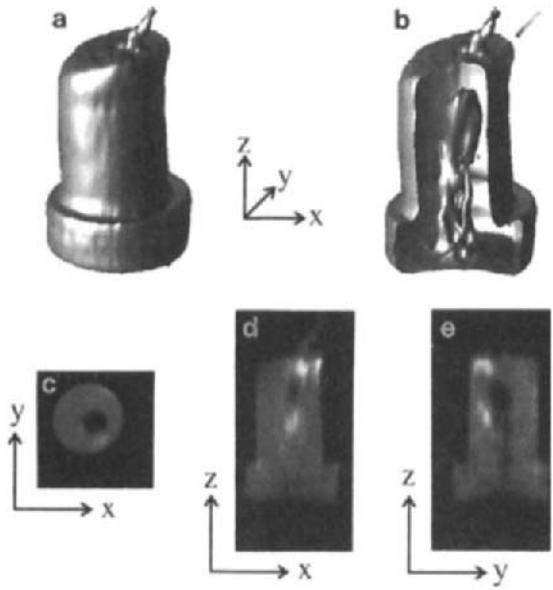

Fig. 26. Three-dimensional image of solid $^1H_2$ at 13.0 K: (a) iso-surface, (b) as for (a) but with a cutaway to enable a void within the solid to be visualized; (c–e) central slices in the indicated directions. The experimental parameters used were a total acquisition time of 12 h with an FOV of 120 μm (x) $\times$ 270 μm (y) $\times$ 500 μm (z) digitized into 128 $\times$ 64 $\times$ 64 points. (Reproduced with permission from Moore *et al.*[203].)

German and McCarthy[253] took advantage of the noninvasive properties of magnetic resonance imaging to study the structure and collapse of foams (i.e. unstable colloidal systems) from cream, egg white and beer. Kose has imaged the three-dimensional foam structures and analysed their geometric properties.[254]

Microimaging has great application in following kinetics of chemical reactions. Recent studies have dealt with following the progress of the dispersion-limited oxidation and reduction of iron in a polyacrylamide gel system,[255] Belousov–Zhabotinsky reactions[256–258] and the transport and spatial distribution of copper and heavy metal ions in calcium alginate gels.[259,260] The copper ion transport was imaged indirectly using the effects of the copper on the water proton relaxation times using an inversion recovery sequence that allowed the selective imaging of a specific relaxation time. It was noted that this technique is applicable to the study of ion-exchange kinetics *in situ* and for tracking the motion of ions under chemical and electrical potential gradients. More recently a combined magnetization transfer and null-point technique was used to study the degradation of calcium alginate gels by EDTA.[261]

Solid-state imaging has found application in following anisotropic chemical reactions, including the reactions of substituted benzoic acid crystals and powders with ammonia gas.[262,263]

9.2.2. Polymers and materials

As for chemical systems, the adoption of imaging methods in polymer and materials science was hampered by the lack of practical imaging methods. With recent advances in solid-state imaging, more and more systems, and not only those with near liquid-state line widths, are becoming experimentally accessible and with increasingly higher resolutions. For example, Barth *et al.*[264] have successfully studied rubber far below the glass transition temperature (163 K); Maas *et al.*[265] have reported the use of ^{1}H NMR imaging at 600 MHz of solid propellant materials (i.e. elastomers) in which a resolution of 8.5 μm $\times$ 8.5 μm was achieved. Imaging has also been applied to natural composites such as coal.[266] Relaxation times generally have wide variations in solid samples as well as being sensitive to temperature and pressure; thus, structural and chemical changes often provide sources of contrast in the images.[45,267]

A number of reviews have either focused on or contained sections on the application of NMR imaging to polymers.[25,268–276] Imaging has been applied to study the ageing and processing of elastomers and polymers.[45,267,277] Doran *et al.*[54] have used a fast inversion recovery imaging sequence to map the steady-state temperature distribution within a block of *cis*-polybutadiene. Importantly, and in contradistinction to traditional methods, imaging provides accurate information on the temperature distribution through the entire block. Beuf *et al.*[278] have reported a magnetic resonance imaging method for estimating the volume magnetic susceptibility of materials. Imaging has even

been used to observe dental microleakages resulting from shrinking during polymerization.[279]

The visualization of strain in materials has been revolutionized by imaging. ^{2}H NMR imaging has been used to study strain in elastomers through its effect on the quadrupole splitting.[280] In another study,[281] ^{1}H imaging was used to study the propagation of strain induced by stress in a crosslinked poly(methacrylic acid) (PMAA)/water gel. It was noted that the ^{1}H spin density and the molecular motion of water molecules in the gel are changed by altering the strength of the stress (see Plate 4).

Imaging has proved itself a valuable tool in studies of solvent penetration in polymeric materials[282] since it gives information on the evolution of the mobile components within the materials and not just at the surface. Systems studied include solvent mobility in swollen PMMA,[283,284] crosslinked polystyrenes,[285] high-molecular-mass polybutadiene,[286] the diffusion of acetone and methanol into polycarbonate,[287] cyclic sorption–desorption into poly(methyl methacrylate),[288] the ingress of water into nylon 6.6.[289] and the distribution of water in the polymer matrix of a silicon microchip.[290] Swelling kinetics in glassy and rubbery networks have also been studied using ^{1}H and ^{19}F microscopy.[291]

B_1 gradient microscopy is well suited to studying solvent penetration in polymeric materials owing to its weak sensitivity to magnetic susceptibility and its inherent applicability to samples with short T_2.[292,293] Maffei *et al.*[292] studied the penetration of toluene into poly(vinyl chloride), acetic acid into cellulose, and *n*-pentane into polystyrene. More recently, Valtier *et al.*[293] have studied solvent penetration into stretched PVC (see Plate 5) and later used B_1-based chemical shift imaging to observe the penetration of isooctane, toluene and ethanol into polyamide.[104]

Imaging has found many applications in ceramics since it allows the discrimination between amorphous, crystalline and highly plasticized binder and observation of porosity and void distributions.[294] Reviews of the application of imaging to ceramics can be found elsewhere.[295,296]

9.2.3. Porous media

Imaging has become an important tool in the study of porous media and the area has been reviewed by Gladden.[297] The investigation of the characteristics of fluids in porous media (see also Section 9.4) is important in a diverse range of applications from the absorption of water by building materials to the oil industry.[298] Packer[298] noted that imaging has great potential for supporting and evaluating production strategies and for studying fluid dynamics in the rocks themselves. In rocks the fluids comprise gas, oil, and aqueous phases. Much of the work performed in the use of imaging to study fluid displacement has been summarized by Majors *et al.*[299] and also by Nesbitt *et al.*[220] Attard *et al.*[300] used Fourier transform two- and three-dimensional saturation recovery imaging to

obtain density and T_1 images of brine-saturated sandstone core samples. They remarked on the advantage of acquiring full 3D data sets and that the long acquisition time required was not significant compared to the time required for traditional means of analysis for core samples.

Although the water content of rocks is typically far below that of biological specimens, rocks have the advantage that the imaging process can be averaged for as long as necessary to make up for the inherently lower abundance of the proton (the typically observed) nucleus. Relaxation processes (e.g. T_1, $T_{1\rho}$ and T_2) and D and v are sensitive to molecular mobility and, by appealing to these sensitivities, it is possible to use imaging to map the interactions of the fluids with the surface of the pores. Transverse relaxation in rocks is often strongly influenced by susceptibility variations on the scale of the pore dimensions. For example, sandstone often contains a considerable amount of iron oxide, which causes the line width to increase to several kilohertz. Generally only a fraction of the fluid present is detectable and the susceptibility variations also complicate attempts to measure diffusion and flow[301] and the use of chemical shift imaging to separate different phases. The imaging measurements are further complicated by the presence of more than one type of fluid in the pores, since the voxel will contain contributions from both. Owing to the inherent line broadening in rocks, chemical shift imaging is possible only in special cases.[302]

In some cases it is possible to image with a voxel size smaller than the pore size and thereby obtain direct information on the pore structure on the rock. When this is not the case, it may be possible to resort to secondary sources of information. For example, it is known that fluids in pores undergo enhanced relaxation at the rock–fluid interface (i.e. surface-mediated transport) and since self-diffusion is the means of transport within the pore, there is a relationship between the pore size and the relaxation rate.[303] For many sandstones, the fast diffusion limit applies and the relaxation has the form[304]

$$\frac{1}{T_1} \approx \rho(S/V) \approx \frac{\rho}{a} \tag{45}$$

where ρ is the surface relaxation strength ($\mathrm{m\,s^{-1}}$), S/V is the surface-to-volume ratio and a is the linear dimension of the pore. However, the pore sizes in the rock are not homogeneous and so the apparent relaxation is typically multiexponential. By imaging spin–lattice relaxation and then fitting the data for each voxel in the image to an appropriate model, information can be obtained on the pore size.

Thus, while a density image reflects the porosity in a sample and a T_1 map is related to the pore size, flow should be sensitive to both properties. Slow movements can be monitored using standard imaging techniques, whereas more rapid flows require the use of flow-sensitive techniques. The typically very low flow rates and the presence of internal gradients necessitate the use of special techniques to measure flow. For example, Guilfoyle *et al.*[80] used an

EPI-based technique that minimized the effect of background gradients to measure water flow through Bentheimer sandstone. In a later study on Bentheimer sandstone, Waggoner and Fukushima[301] modified a stimulated-echo sequence used in diffusion studies[305] to maximize velocity sensitivity and to minimize the effects of background gradients. Rajanayagam *et al.*[306] have performed quantitative flow and diffusion imaging on model porous media (glass beads). They noted that the imaging-derived flow values were systematically higher than directly measured values and that this difference results from partial volume effects. Imaging has also been used to study percolation.[307]

It is worth while noting that whereas the fast imaging-type sequences were originally used only in the domain of medical imaging, they are finding increasing application in nonmedical applications, especially in rock studies. For example, using microscopy at 11.7 T, Peters *et al.*[308] have used π-EPI[80] to obtain T_1 maps of Bentheimer sandstone in an order of magnitude less time than that required had an equivalent 3DFT experiment been used. Similarly, by using this technique they were able to measure flow rapidly using an EPI-based flow encoding procedure.[80] Mansfield and Issa[309] have used π-EPI-based sequences to measure water flow through Bentheimer sandstone. Their measurements have led them to propose a stochastic theory of flow in porous rocks. Their theory leads to a Gaussian velocity distribution that is in good agreement with their data. In a subsequent paper[310] they proposed a hydrodynamic model for flow and intervoxel coupling.

Imaging has also been applied to more straightforward aspects of porous materials, including using T_1-weighted relaxation measurements to characterize fractures and porous matrix in fractured permeable rock systems[311] and a constant-time imaging study in which the hydration of cement was studied.[312] ^{23}Na imaging was used to measure the diffusion coefficient of Na^+ and ^{1}H imaging was used to measure indirectly the diffusion of Ni^+ in sand.[313]

Hollewand and Gladden[314] used imaging to study various alumina and silica catalyst support pellets. They recorded spin-density, spin–lattice relaxation times and self-diffusion coefficients in the samples. They noted that the advantage of NMR imaging measurements is that they allow the characterization of pore structure and transport processes in the same experiment. In a later study, Cheah *et al.*[315] studied catalyst deactivation; in particular they studied the deposition of coke within alumina pellets.

9.3. Food science

Recently there have been a number of reviews and books on the application of NMR and imaging to food science, including two chapters in this series.[316–320] Consequently we will not delve into this area except to remark that the real strength of imaging in studying food is the noninvasive examination of heat and mass transport during food processing.

9.4. Fluid dynamics

Apart from the applications presented above, the ability of NMR imaging to measure diffusion and flow noninvasively has enormous potential in the fields of fluid dynamics and rheology. It is not only that it is more convenient than other methods, but that it is able to perform measurements that are simply not possible with traditional techniques.[135,321] For example, in contradistinction to many traditional methods which require a "beam" to be directed at the sample, NMR has no preferred directions and it is also possible to image only the flowing material and not the stationary material, as noted in Section 6.2. Further, it is applicable to fluids that need to be isolated. The ability of NMR to measure diffusion and flow in a non-spatially-resolved manner was covered in an earlier contribution.[2]

Magnetic resonance flow imaging has been used to study thermal convection[322] and was found to be capable of resolving details at a level comparable to optical techniques. In a later study, Weis *et al.*[323] demonstrated that the combined application of Fourier encoding velocity imaging and multistripe/multiplane tagging imaging allows the quantitative examination of thermal convection for arbitrary boundary conditions. In fact, multistripe tagging procedures have found increasing use in applications such as studying (gas–solid) granular flows,[324] studying the flow of a pair of density-stratified, immiscible fluids,[325] mapping flow streamlines[326] and, in combination with EPI, visualizing turbulent flow[327] and the study of laminar flow.[328]

Imaging has found application in studying particle migration in suspensions flowing in tubes[329] and in couette flow (e.g. flow between rotating concentric cylinders).[330,331] Dynamic NMR microscopy has been used to study shear thinning in high polymer solutions,[332] the laminar flow of water through cylindrical tubes in the vicinity of abrupt expansions and contractions,[321] couette flow,[333] the time evolution of electroosmotic flow in a capillary,[334] and to observe the "spurt-like effect" in the nonNewtonian flow of a worm-like surfactant system.[335] Microimaging has been used to observe flow profiles in hollow-fibre membrane filtration.[336] Chemical shift imaging was also used to investigate quantitatively the oil concentration polarization layers that formed during hollow-fibre membrane filtration[336] and in cross flow membrane filtration of an oil–water emulsion.[337]

Fast imaging sequences such as EPI have particular utility for studying systems in which there are irregular changes in the spin-density or the local molecular velocities and thus the entire **k**-space needs to be sampled on a time smaller than these changes.[338] Kose[219,339,340] has used an EPI-based sequence to study the instantaneous flow distribution in the equilibrium turbulent region, or "puff", in a circular pipe (see Fig. 27) and to observe the spatiotemporal structure of wavy Taylor–Couette flow.[341]

Davies *et al.*[342] have used a prefocused FLASH pulse sequence to obtain 2D images quickly with a T_1-dependent signal intensity for the study of viscous

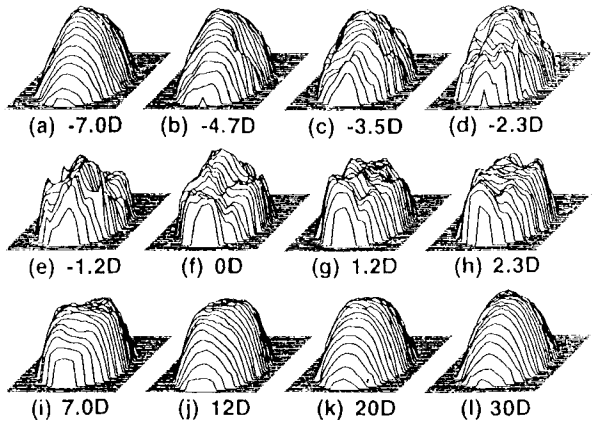

Fig. 27. Instantaneous distribution of the flow component along a pipe axis in the equilibrium puff. The numbers under each figure denote the distances in terms of the inner diameter of the pipe (D) from the upstream interface at the pipe axis. Poiseuille flow occurs near the upstream and far downstream from the upstream laminar to turbulent interface. (Reproduced with permission from Kose[340].)

fingering; in particular, they studied the miscible displacement by water of the non-Newtonian fluid carboxymethyl cellulose. Imaging has some advantages over traditional techniques (e.g. time-lapse photography) in that it can be used in systems where there is no colour contrast and that it can examine the phenomenon in three dimensions. Imaging has even been used to study the extrusion and flow of pastes.[343,344]

10. CONCLUDING REMARKS

In this chapter, I have attempted to provide an introduction to the theory and practice (and pitfalls) of magnetic resonance imaging. Particular emphasis was placed on the methods that result in higher resolution (i.e. NMR microscopy) and their diverse applications in the nonmedical sciences. In NMR imaging, the single largest problem is signal to noise, and with increasingly more sensitive NMR probes, higher static fields and innovative methods such as the use of hyperpolarized nuclei, imaging will become a standard technique for the physical sciences. In the confines of one chapter it is not possible to cover comprehensively the methods available or to survey more than a few of the applications, but it is hoped that what has been reviewed is sufficient to inspire the imagination of what systems imaging methods may be applied to.

ACKNOWLEDGEMENTS

Drs A. V. Barzykin, K. Hayamizu and M. Ishikawa are thanked for their support in the preparation of this chapter.

REFERENCES

1. P. T. Callaghan, *Proc. RMS*, 1992, **27**, 67.
2. W. S. Price, *Annual Reports on NMR Spectroscopy* (ed. G. A. Webb), Vol. 32 p. 51, Academic Press, London, 1996.
3. P. T. Callaghan, *Principles of Nuclear Magnetic Resonance Microscopy*, Clarendon Press, Oxford, 1991.
4. E. R. Andrew, *Encyclopedia of Nuclear Magnetic Resonance* (ed. D. M. Grant and R. K. Harris), p. 2462, Wiley, New York, 1996.
5. M. Decorps and D. Bourgeois, *NMR Basic Principles and Progress*, 1992, **27**, 119.
6. A. Coy, N. Kaplan and P. T. Callaghan, *J. Magn. Reson.*, 1996, **A121**, 201.
7. C. S. Yannoni, O. Züger, D. Rugar and J. A. Sidles, *Encyclopedia of Nuclear Magnetic Resonance* (ed. D. M. Grant and R. K. Harris), p. 2093, Wiley, New York, 1996.
8. D. G. Cory, *Annual Reports on NMR Spectroscopy* (ed. G. A. Webb), Vol. 24 p. 88, Academic Press, London, 1992.
9. D. M. Grant and R. K. Harris, eds, *Encylopedia of Nuclear Magnetic Resonance*, Wiley, New York, 1996.
10. B. Blümich and W. Kuhn, eds, *Magnetic Resonance Microscopy*, VCH, Berlin, 1992.
11. P. Mansfield and P. G. Morris, *NMR Imaging in Biomedicine*, Academic Press, New York, 1982.
12. M. A. Foster and J. M. S. Hutchison, *Practical NMR Imaging*, IRL Press, Oxford, 1987.
13. P. G. Morris, *Nuclear Magnetic Resonance Imaging in Medicine and Biology*, Clarendon Press, Oxford, 1986.
14. W. Kuhn, *Angew. Chem.*, 1990, **29**, 1.
15. R. A. Komoroski, *Anal. Chem.*, 1993, **65**, 1068A.
16. F. W. Wehrli, *Prog. NMR Spectrosc.*, 1995, **28**, 87.
17. X. Zhou and G. A. Johnson, *The Biomedical Engineering Handbook* (ed. J. D. Bronzino), CRC Press, Baton Rouge, 1995.
18. D. Canet and M. Décorps, *Dynamics of Solutions and Fluid Mixtures* (ed. J.-J. Delpuech), p. 309, Wiley, New York, 1995.
19. D. Canet, *Prog. NMR Spectrosc.*, 1997, **30**, 101.
20. L. F. Gladden, *Chem. Eng. Sci.*, 1994, **49**, 3339.
21. J. M. Listerud, S. W. Sinton and G. P. Drobny, *Anal. Chem.*, 1989, **61**, 23A.
22. P. Jezzard, J. J. Attard, T. A. Carpenter and L. D. Hall, *Prog. NMR Spectrosc.*, 1991, **23**, 1.
23. P. Jezzard, C. J. Wiggins, T. A. Carpenter, L. D. Hall, P. Jackson, N. J. Clayden and N. J. Walton, *Adv. Mater.*, 1992, **4**, 82.
24. W. S. Veeman, *Magnetic Resonance Microscopy* (ed. B. Blümich and W. Kuhn), p. 29, VCH, Weinheim, 1992.
25. B. Blümich and P. Blümler, *Makromol. Chem.*, 1993, **194**, 2133.
26. P. Blümler and B. Blümich, *NMR Basic Principles and Progress*, 1994, **30**, 209.
27. J. H. Strange and M. R. Halse, *Encyclopedia of Nuclear Magnetic Resonance* (eds D. M. Grant and R. K. Harris), p. 2472, Wiley, New York, 1996.
28. L. E. Crooks, *Encyclopedia of Nuclear Magnetic Resonance* (eds D. M. Grant and R. K. Harris), p. 2439, Wiley, New York, 1996.
29. P. C. Lauterbur, *Nature*, 1973, **242**, 190.

30. A. Kumar, D. Welti and R. R. Ernst, *J. Magn. Reson.*, 1975, **18**, 69.
31. R. Mulkern, *Concepts Magn. Reson.*, 1992, **4**, 307.
32. T. P. L. Roberts, T. A. Carpenter and L. D. Hall, *J. Magn. Reson.*, 1990, **89**, 595.
33. H. Geen and R. Freeman, *J. Magn. Reson.*, 1991, **93**, 93.
34. B. Newling, J. J. A. Derbyshire, T. A. Carpenter, D. Xing and L. D. Hall, *J. Magn. Reson.*, 1995, **B108**, 269.
35. J. Hennig, *Concepts Magn. Reson.*, 1991, **3**, 125.
36. J. Hennig, *Concepts Magn. Reson.*, 1991, **3**, 179.
37. W. S. Warren and M. S. Silver, *Adv. Magn. Reson.*, 1988, **12**, 247.
38. A. A. Maudsley and G. B. Matson, *Encyclopedia of Nuclear Magnetic Resonance* (ed. D. M. Grant and R. K. Harris), p. 4210, Wiley, New York, 1996.
39. P. G. Morris, *Encyclopedia of Nuclear Magnetic Resonance* (ed. D. M. Grant and R. K. Harris), p. 1390, Wiley, New York, 1996.
40. G. H. Glover and J. M. Pauly, *Encyclopedia of Nuclear Magnetic Resonance* (ed. D. M. Grant and R. K. Harris), p. 3772, Wiley, New York, 1996.
41. A. L. Robinson, *Science*, 1975, **190**, 542.
42. Y. Xia, *Concepts Magn. Reson.*, 1996, **8**, 205.
43. Y. Xia and P. T. Callaghan, *Magn. Reson. Med.*, 1992, **23**, 138.
44. R. N. Muller, *Encyclopedia of Nuclear Magnetic Resonance* (ed. D. M. Grant and R. K. Harris), p. 1438, Wiley, New York, 1996.
45. P. Blümler and B. Blümich, *Magn. Reson. Imaging*, 1992, **10**, 779.
46. N. Egger, K. Schmidt-Rohr, B. Blümich, W. D. Domke and B. Stapp, *J. Appl. Polym. Sci.*, 1992, **44**, 289.
47. S. H. Koenig, *Biophys. J.*, 1995, **69**, 593.
48. R. S. Balaban, *Encyclopedia of Nuclear Magnetic Resonance* (ed. D. M. Grant and R. K. Harris), p. 2962, Wiley, New York, 1996.
49. R. G. Bryant, *Encyclopedia of Nuclear Magnetic Resonance* (ed. D. M. Grant and R. K. Harris), p. 2954, Wiley, New York, 1996.
50. E. Liepinsh and G. Otting, *Magn. Reson. Med.*, 1996, **35**, 30.
51. S. Ogawa, R. S. Menon, D. W. Tank, S.-G. Kim, H. Merkle, J. M. Ellermann and K. Ugurbil, *Biophys. J.*, 1993, **64**, 803.
52. A. L. Van Geet, *Anal. Chem.*, 1970, **42**, 679.
53. D. Le Bihan, *Magn. Reson. Q.*, 1991, **7**, 1.
54. S. J. Doran, T. A. Carpenter and L. D. Hall, *Rev. Sci. Instrum.*, 1994, **65**, 2231.
55. J. Frahm, K.-D. Merboldt, W. Hänicke and A. Haase, *J. Magn. Reson.*, 1985, **64**, 81.
56. H. Rumpel and J. M. Pope, *Concepts Magn. Reson.*, 1993, **5**, 43.
57. A. Haase and J. Frahm, *J. Magn. Reson.*, 1985, **64**, 94.
58. Y. Xia and L. W. Jelinski, *J. Magn. Reson.*, 1995, **B107**, 1.
59. E. Kaldoudi and S. C. R. Williams, *Concepts Magn. Reson.*, 1992, **4**, 53.
60. A. Haase, M. Brandl, E. Kuchenbrod and A. Link, *J. Magn. Reson.*, 1993, **A105**, 230.
61. M. Brandl and A. Haase, *J. Magn. Reson.*, 1994, **B103**, 162.
62. J. S. Schoeniger, N. Aiken, E. Hsu and S. J. Blackband, *J. Magn. Reson.*, 1994, **B103**, 261.
63. E. W. Hsu, J. S. Schoeniger, R. Bowtell, N. R. Aiken, A. Horsman and S. J. Blackband, *J. Magn. Reson.*, 1995, **B109**, 66.
64. N. Chandrakumar and S. S. Velan, *J. Magn. Reson.*, 1993, **A104**, 115.
65. T. J. Norwood and L. D. Hall, *Encyclopedia of Nuclear Magnetic Resonance* (ed. D. M. Grant and R. K. Harris), p. 3138, Wiley, New York, 1996.
66. P. Mansfield, *J. Phys. C.*, 1977, **10**, 55.
67. A. Haase, J. Frahm, W. Matthaei, W. Hänicke and K.-D. Merboldt, *J. Magn. Reson.*, 1986, **67**, 258.
68. P. M. Glover, P. F. Tokarczuk and R. W. Bowtell, *Magn. Reson. Med.*, 1995, **34**, 74.
69. P. Irarrazabal and D. G. Nishimura, *Magn. Reson. Med.*, 1995, **33**, 656.

70. D. Graveron-Demilly, G. J. Marseille, S. Crémilleux and D. Van Ormondt, *J. Magn. Reson.*, 1996, **B112**, 119.
71. P. M. Margosian, G. DeMeester and H. Liu, *Encyclopedia of Nuclear Magnetic Resonance* (ed. D. M. Grant and R. K. Harris), p. 3462, Wiley, New York, 1996.
72. A. Macovski and C. H. Meyer, *Encyclopedia of Nuclear Magnetic Resonance* (ed. D. M. Grant and R. K. Harris), p. 4552, Wiley, New York, 1996.
73. S. Hafner, *Magn. Reson. Imaging*, 1994, **12**, 1047.
74. A. Haase, *Encyclopedia of Nuclear Magnetic Resonance* (ed. D. M. Grant and R. K. Harris), p. 5004, Wiley, New York, 1996.
75. A. Haase, *MAGMA*, 1994, **2**, 157.
76. S. Patz, *Advances in Magnetic Resonance Imaging* (ed. E. Feig), p. 73, Ablex Publishing Corp., Norwood, NJ, 1989.
77. A. Haase, *Magn. Reson. Med.*, 1990, **13**, 77.
78. P. M. Jakob, D. Matthaei, H. Stodal, U. Brinck and A. Haase, *MAGMA*, 1993, **1**, 77.
79. P. Mansfield, *Encyclopedia of Nuclear Magnetic Resonance* (ed. D. M. Grant and R. K. Harris), p. 1831, Wiley, New York, 1996.
80. D. N. Guilfoyle, P. Mansfield and K. J. Packer, *J. Magn. Reson.*, 1992, **97**, 342.
81. D. N. Guilfoyle, B. Issa and P. Mansfield, *J. Magn. Reson.*, 1996, **A119**, 151.
82. R. Deichmann, H. Adolf, U. Nöth, E. Kuchenbrod, C. Schwarzbauer and A. Haase, *Magn. Reson. Med.*, 1995, **34**, 481.
83. J. Link and J. Seelig, *J. Magn. Reson.*, 1990, **89**, 310.
84. R. Kimmich, U. Görke and J. Weis, *J. Trace Microprobe Techn.*, 1995, **13**, 285.
85. A. Knüttel, K.-H. Spohn and R. Kimmich, *J. Magn. Reson.*, 1990, **86**, 542.
86. C. Kunze and R. Kimmich, *Magn. Reson. Imaging*, 1994, **12**, 805.
87. G. Navon, Y.-Q. Song, T. Room, S. Appelt, R. E. Taylor and A. Pines, *Science*, 1996, **271**, 1848.
88. A. Bifone, Y.-Q. Song, R. Seydoux, R. E. Taylor, B. M. Goodson, T. Pietrass, T. F. Budinger, G. Navon and A. Pines, *Proc. Natl. Acad. Sci. USA*, 1996, **93**, 12932.
89. Y.-Q. Song, H. C. Gaede, T. Pietrass, G. A. Barrall, G. C. Chingas, M. R. Ayers and A. Pines, *J. Magn. Reson.*, 1995, **A115**, 127.
90. L. Zhao, R. Mulkern, C. Tseng, D. Williamson, S. Patz, R. Kraft, R. L. Walsworth, F. A. Jolesz and M. S. Albert, *J. Magn. Reson.*, 1996, **B113**, 179.
91. J. Skalla, G. Wäckerle, M. Mehring and A. Pines, *Phys. Lett. A.*, 1997, **226**, 69.
92. P. Styles, *NMR Basic Principles and Progress*, 1992, **27**, 45.
93. D. Canet, *Encyclopedia of Nuclear Magnetic Resonance* (ed. D. M. Grant and R. K. Harris), p. 3938, Wiley, New York, 1996.
94. D. I. Hoult, *J. Magn. Reson.*, 1979, **33**, 183.
95. P. Maffei, P. Mutzenhardt, A. Retournard, B. Diter, R. Raulet, J. Brondeau and D. Canet, *J. Magn. Reson.*, 1994, **A107**, 40.
96. P. Maffei, K. Elbayed, J. Brondeau and D. Canet, *J. Magn. Reson.*, 1991, **95**, 382.
97. D. Boudot, D. Canet and J. Brondeau, *J. Magn. Reson.*, 1990, **87**, 385.
98. K. R. Metz, J. P. Boehmer, J. L. Bowers and J. R. Moore, *J. Magn. Reson.*, 1994, **B103**, 152.
99. J. L. Bowers, P. M. Macdonald and K. R. Metz, *J. Magn. Reson.*, 1995, **B106**, 72.
100. H. C. Torrey, *Phys. Rev.*, 1949, **76**, 1059.
101. R. Raulet, D. Grandclaude, F. Humbert and D. Canet, *J. Magn. Reson.*, 1997, **124**, 259.
102. J. R. Moore and K. R. Metz, *J. Magn. Reson.*, 1993, **A101**, 84.
103. D. Boudot, D. Canet, J. Brondeau and J. C. Boubel, *J. Magn. Reson.*, 1989, **83**, 428.
104. M. Valtier, R. Raulet, R.-P. Eustache and D. Canet, *J. Magn. Reson.*, 1995, **A112**, 118.
105. S. Singh and R. Deslauriers, *Concepts Magn. Reson.*, 1995, **7**, 1.
106. C. S. Bosch and J. J. H. Ackerman, *NMR Basic Principles and Progress*, 1992, **27**, 3.
107. R. J. Ordridge, A. Connelly and J. A. B. Lohman, *J. Magn. Reson.*, 1986, **66**, 283.
108. R. Kimmich, D. E. Demco and S. Hafner, *Magnetic Resonance Microscopy* (ed. B. Blümich

and W. Kuhn), p. 59, VCH, Weinheim, 1992.
109. B. Maraviglia, F. De Luca, B. C. De Simone and N. Lugeri, *Encyclopedia of Nuclear Magnetic Resonance* (ed. D. M. Grant and R. K. Harris), p. 2712, Wiley, New York, 1996.
110. P. J. McDonald and P. F. Tokarczuk, *J. Phys. E.*, 1989, **22**, 948.
111. D. G. Cory, J. B. Miller, R. Turner and A. N. Garroway, *Mol. Phys.*, 1990, **70**, 331.
112. D. G. Cory, A. M. Reichwein, J. C. De Boer, J. W. M. Van Os and W. S. Veeman, *Solid State NMR of Polymers* (ed. L. Mathias), p. 343, Plenum Press, New York, 1991.
113. Y. Sun, H. Lock, T. Shinozaki and G. E. Maciel, *J. Magn. Reson.*, 1995, **A115**, 165.
114. N. Lugeri, F. De Luca and B. Maraviglia, *Magnetic Resonance Microscopy* (ed. B. Blümich and W. Kuhn), p. 103, VCH, Weinheim, 1992.
115. S. Hafner, D. E. Demco and R. Kimmich, *Meas. Sci. Technol.*, 1991, **2**, 882.
116. D. E. Demco, S. Hafner and R. Kimmich, *J. Magn. Reson.*, 1992, **96**, 307.
117. S. Matsui, Y. Ogasawara and T. Inouye, *J. Magn. Reson.*, 1993, **105**, 215.
118. F. Weigand, B. Blümich and H. W. Spiess, *Solid State Nucl. Magn. Reson.*, 1994, **3**, 59.
119. S. Hafner, D. E. Demco and R. Kimmich, *Solid State Nucl. Magn. Reson.*, 1996, **6**, 275.
120. S. Matsui, A. Uraoka and T. Inouye, *J. Magn. Reson.*, 1996, **A120**, 11.
121. S. Hafner, P. Barth and W. Kuhn, *J. Magn. Reson.*, 1994, **A108**, 21.
122. S. Gravina and D. G. Cory, *J. Magn. Reson.*, 1994, **B104**, 53.
123. B. J. Balcom, M. Bogdan and R. L. Armstrong, *J. Magn. Reson.*, 1996, **A118**, 122.
124. J. H. Iwamiya and S. W. Sinton, *Solid State Nucl. Magn. Reson.*, 1996, **6**, 333.
125. T. B. Benson and P. J. McDonald, *J. Magn. Reson.*, 1995, **A112**, 12.
126. T. B. Benson and P. J. McDonald, *J. Magn. Reson.*, 1995, **B109**, 314.
127. P. Kinchesh, E. W. Randall and K. Zick, *J. Magn. Reson.*, 1992, **100**, 411.
128. E. W. Randall, A. A. Samoilenko and T. Nunes, *J. Magn. Reson.*, 1995, **A116**, 122.
129. S. L. Codd, M. J. D. Mallett, M. R. Halse, J. H. Strange, W. Vennart and T. Van Doorn, *J. Magn. Reson.*, 1996, **B113**, 214.
130. M. J. D. Mallett, S. L. Codd, M. R. Halse, T. A. P. Green and J. H. Strange, *J. Magn. Reson.*, 1996, **A119**, 105.
131. B. Blümich, J. Jansen, H. Nilgens, P. Blümler and G. L. Hoatson, *Magn. Reson. Biol. Med.*, 1993, **1**, 61.
132. B. Blümich, *Encyclopedia of Nuclear Magnetic Resonance* (ed. D. M. Grant and R. K. Harris), p. 4581, Wiley, New York, 1996.
133. J. Jansen and B. Blümich, *J. Magn. Reson.*, 1992, **99**, 525.
134. J. Stepisnik, *Prog. NMR Spectrosc.*, 1985, **17**, 187.
135. A. Caprihan and E. Fukushima, *Phys. Rep.*, 1990, **198**, 195.
136. Y. Xia and P. T. Callaghan, *Makromol. Chem., Macromol. Symp.*, 1990, **34**, 277.
137. R. Turner and P. Keller, *Prog. NMR Spectrosc.*, 1991, **23**, 93.
138. J. M. Pope and S. Yao, *Concepts Magn. Reson.*, 1993, **5**, 281.
139. D. Le Bihan, *Encyclopedia of Nuclear Magnetic Resonance* (ed. D. M. Grant and R. K. Harris), p. 1645, Wiley, New York, 1996.
140. H. Gudbjartsson and S. Patz, *Magn. Reson. Med.*, 1995, **34**, 567.
141. S. Patz, *Magn. Reson. Imaging*, 1988, **6**, 405.
142. M. Tyszka, R. C. Hawkes and L. D. Hall, *J. Magn. Reson.*, 1993, **B101**, 158.
143. T. J. Mosher and M. B. Smith, *Magn. Reson. Med.*, 1990, **15**, 334.
144. S. Chandra and Y. Yang, *J. Magn. Reson.*, 1996, **B111**, 285.
145. J. M. Pope and S. Yao, *Magn. Reson. Imaging*, 1993, **11**, 585.
146. J. L. Duerk and O. P. Simonetti, *Concepts Magn. Reson.*, 1993, **5**, 105.
147. E. O. Stejskal, *J. Chem. Phys.*, 1965, **43**, 3597.
148. J. E. Tanner and E. O. Stejskal, *J. Chem. Phys.*, 1968, **49**, 1768.
149. J. Kärger and W. Heink, *J. Magn. Reson.*, 1983, **51**, 1.
150. J. Crank, *The Mathematics of Diffusion*, Oxford University Press, Oxford, 1975.
151. D. A. McQuarrie, *Statistical Mechanics*, Harper & Row, New York, 1976.

152. P. T. Callaghan, D. MacGowan, K. J. Packer and F. O. Zelaya, *J. Magn. Reson.*, 1990, **90**, 177.
153. P. T. Callaghan, A. Coy, D. MacGowan, K. J. Packer and F. O. Zelaya, *Nature*, 1991, **351**, 467.
154. P. Mansfield and P. K. Grannel, *Phys. Rev.*, 1975, **B12**, 3618.
155. P. T. Callaghan, *Magn. Reson. Imaging*, 1996, **14**, 701.
156. P. T. Callaghan, C. D. Eccles and Y. Xia, *J. Phys.*, 1988, **E21**, 820.
157. P. T. Callaghan and Y. Xia, *J. Magn. Reson.*, 1991, **91**, 326.
158. P. T. Callaghan, K. R. Jeffrey and Y. Xia, *Magnetic Resonance Microscopy* (ed. B. Blümich and W. Kuhn), p. 328, VCH, Weinheim, 1992.
159. P. T. Callaghan, W. Köckenberger and J. M. Pope, *J. Magn. Reson.*, 1994, **B104**, 183.
160. P. J. Basser, J. Mattiello and D. Le Bihan, *Biophys. J.*, 1994, **66**, 259.
161. P. J. Basser and C. Pierpaoli, *J. Magn. Reson.*, 1996, **B111**, 209.
162. J. Mattiello, P. J. Basser and D. Le Bihan, *J. Magn. Reson.*, 1994, **A108**, 131.
163. P. J. Basser, J. Mattiello and D. Le Bihan, *J. Magn. Reson.*, 1994, **B103**, 247.
164. J. Mattiello, P. J. Basser and D. Le Bihan, *Magn. Reson. Med.*, 1997, **37**, 292.
165. E. Mischler, F. Humbert, B. Diter and D. Canet, *J. Magn. Reson.*, 1995, **B106**, 32.
166. P. T. Callaghan and J. Stepisnik, *Phys. Rev. Lett.*, 1995, **75**, 4532.
167. E. W. Randall, A. A. Samoilenko and T. Nunes, *J. Magn. Reson.*, 1995, **A116**, 259.
168. Y. Xia, K. R. Jeffrey and P. T. Callaghan, *Magn. Reson. Imaging*, 1992, **10**, 411.
169. J. S. Schoeniger and S. J. Blackband, *J. Magn. Reson.*, 1994, **B104**, 127.
170. W. A. Edelstein, *Encyclopedia of Nuclear Magnetic Resonance* (ed. D. M. Grant and R. K. Harris), p. 3950, Wiley, New York, 1996.
171. E. W. McFarland and A. Mortara, *Magn. Reson. Imaging*, 1992, **10**, 279.
172. Q. X. Yang, S. Li and M. B. Smith, *J. Magn. Reson.*, 1994, **A108**, 1.
173. C. Mahony, L. K. Forbes, S. Crozier and D. M. Doddrell, *J. Magn. Reson.*, 1995, **B107**, 145.
174. T. L. Peck, R. L. Magin and P. C. Lauterbur, *J. Magn. Reson.*, 1995, **B108**, 114.
175. C. E. Hayes, *Encyclopedia of Nuclear Magnetic Resonance* (ed. D. M. Grant and R. K. Harris), p. 968, Wiley, New York, 1996.
176. S. Crozier, K. Luescher, L. K. Forbes and D. M. Doddrell, *J. Magn. Reson.*, 1995, **B109**, 1.
177. S. Su and J. K. Saunders, *J. Magn. Reson.*, 1996, **B110**, 210.
178. W. U. Roffman, S. Crozier, K. Luescher and D. M. Doddrell, *J. Magn. Reson.*, 1996, **B111**, 174.
179. R. D. Black, T. A. Early, P. B. Roemer, O. M. Mueller, A. Mogro-Campero, L. G. Turner and G. A. Johnson, *Science*, 1993, **259**, 793.
180. Z. H. Cho and J. H. Yi, *Concepts Magn. Reson.*, 1995, **7**, 95.
181. R. Turner, *Encyclopedia of Nuclear Magnetic Resonance* (ed. D. M. Grant and R. K. Harris), p. 2223, Wiley, New York, 1996.
182. P. J. Back, P. T. Callaghan, B. Manz and C. J. Rofe, *Bruker Rep.*, 1996, **142**, 42.
183. R. Turner, *J. Phys. D*, 1986, **19**, L147.
184. S. Crozier and D. M. Doddrell, *J. Magn. Reson.*, 1993, **A103**, 354.
185. S. Crozier, L. K. Forbes and D. M. Doddrell, *J. Magn. Reson.*, 1994, **A107**, 126.
186. S. Kirkpatrick, C. D. J. Gelatt and M. P. Vecchi, *Science*, 1983, **220**, 671.
187. A. M. Peters and R. W. Bowtell, *MAGMA*, 1994, **2**, 387.
188. M. L. Buszko, M. F. Kempa, E. Szczesniak, D. C. Wang and E. R. Andrew, *J. Magn. Reson.*, 1996, **B112**, 207.
189. E. R. Andrew and E. Szczesniak, *Magn. Reson. Imaging*, 1995, **13**, 607.
190. Q. Liu, D. G. Hughes and P. S. Allen, *J. Magn. Reson.*, 1996, **B113**, 228.
191. Q. Liu, D. G. Hughes and P. S. Allen, *J. Magn. Reson.*, 1996, **B113**, 222.
192. C. F. Maier, K. C. Chu, B. A. Chronik and B. K. Rutt, *Magn. Reson. Med.*, 1995, **34**, 604.
193. M. Buszko and G. E. Maciel, *J. Magn. Reson.*, 1994, **A107**, 151.
194. R. Bowtell and A. Peters, *J. Magn. Reson.*, 1995, **A115**, 55.

195. D. Boudot, F. Montigny, K. Elbayed, P. Mutzenhardt, B. Diter, J. Brondeau and D. Canet, *J. Magn. Reson.*, 1991, **92**, 605.
196. D. Canet, B. Diter, A. Belmajdoub, J. Brondeau, J. C. Boubel and K. Elbayed, *J. Magn. Reson.*, 1989, **81**, 1.
197. F. Humbert, E. Mischler and D. Canet, *J. Chim. Phys.*, 1995, **92**, 1905.
198. F. Humbert, B. Diter and D. Canet, *J. Magn. Reson.*, 1996, **A123**, 242.
199. B. Simon, R. Kimmich and H. Köstler, *J. Magn. Reson.*, 1996, **A118**, 78.
200. K. Woelk, J. W. Rathke and R. J. Klinger, *J. Magn. Reson.*, 1993, **A105**, 113.
201. J. P. Boehmer, R. I. Prince and R. W. Briggs, *J. Magn. Reson.*, 1989, **83**, 152.
202. G. A. Barrall, Y. K. Lee and G. C. Chingas, *J. Magn. Reson.*, 1994, **A106**, 132.
203. J. M. Moore, P. Blümler, M. H. Sherwood, C. G. Wade, G. W. Collins and E. R. Mapoles, *J. Magn. Reson.*, 1994, **A110**, 248.
204. M. Neeman, J. P. Freyer and L. O. Sillerud, *J. Magn. Reson.*, 1990, **90**, 303.
205. P. C. M. Van Zijl, S. Sukumar, M. O. Johnson, P. Webb and R. E. Hurd, *J. Magn. Reson.*, 1994, **A111**, 203.
206. J. M. Pope, R. R. Walker and T. Kron, *Magn. Reson. Imaging*, 1992, **10**, 695.
207. J. M. Pope, D. Jonas and R. R. Walker, *Protoplasma*, 1993, **173**, 177.
208. P. T. Callaghan, *J. Magn. Reson.*, 1990, **87**, 304.
209. P. T. Callaghan, L. C. Forde and C. J. Rofe, *J. Magn. Reson.*, 1994, **B104**, 34.
210. R. Raulet, J.-M. Escanyé, F. Humbert and D. Canet, *J. Magn. Reson.*, 1996, **A119**, 111.
211. S. Posse and W. P. Aue, *J. Magn. Reson.*, 1990, **88**, 473.
212. P. T. Callaghan, A. Coy, A. L. C. Forde and C. J. Rofe, *J. Magn. Reson.*, 1993, **A101**, 347.
213. C. J. Rofe, J. Van Noort, P. J. Back and P. T. Callaghan, *J. Magn. Reson.*, 1995, **B108**, 125.
214. B. P. Hills, K. M. Wright and P. S. Belton, *Magn. Reson. Imaging*, 1990, **8**, 755.
215. W. B. Hyslop and P. C. Lauterbur, *J. Magn. Reson.*, 1991, **94**, 501.
216. D. Barsky, B. Puetz, K. Schulten, J. Schoeniger, E. W. Hsu and S. Blackband, *Chem. Phys. Lett.*, 1992, **200**, 88.
217. B. Pütz, D. Barsky and K. Schulten, *J. Magn. Reson.*, 1992, **97**, 27.
218. T. M. De Swiet, *J. Magn. Reson.*, 1995, **B109**, 12.
219. K. Kose, *J. Magn. Reson.*, 1992, **96**, 596.
220. G. J. Nesbitt, T. W. Fens, J. S. Van den Brink and N. Roberts, *Magnetic Resonance Microscopy* (ed. B. Blümich and W. Kuhn), p. 287, VCH, Weinheim, 1992.
221. J. M. Pope, D. Jonas and R. R. Walker, *Magn. Reson. Imaging*, 1995, **13**, 763.
222. P. T. Callaghan and C. D. Eccles, *J. Magn. Reson.*, 1987, **71**, 426.
223. Z. H. Cho, J. H. Yi and R. M. Friedenberg, *Rev. Magn. Reson. Med.*, 1992, **4**, 221.
224. E. W. McFarland, *Magn. Reson. Imaging*, 1992, **10**, 269.
225. R. Bowtell, P. Mansfield, J. C. Sharp, G. D. Brown, M. McJury and P. M. Glover, *Magnetic Resonance Microscopy* (ed. B. Blümich and W. Kuhn), p. 427, VCH, Weinheim, 1992.
226. V. Sarafis, J. Pope and Y. Sarig, *Magnetic Resonance Microscopy* (ed. B. Blümich and W. Kuhn), p. 459, VCH, Weinheim, 1992.
227. W. S. Price, H. Ide, Y. Arata, M. Ishikawa, *Australian Journal of Plant Physiology*, 1997, **24**, 599.
228. R. W. Bowtell, G. D. Brown, P. M. Glover, M. McJury and P. Mansfield, *Phil. Trans. R. Soc. Lond.* 1990, **A333**, 457.
229. R. W. Bowtell, A. Peters, J. C. Sharp, P. Mansfield, E. W. Hsu, N. Aiken, A. Horsman and S. J. Blackband, *Magn. Reson. Med.*, 1995, **33**, 790.
230. R. Jacobs and S. E. Fraser, *Science*, 1994, **263**, 681.
231. R. Kemp-Harper, P. Styles and S. Wimperis, *J. Magn. Reson.*, 1995, **B108**, 280.
232. J. M. Pope, H. Rumpel, W. Kuhn, R. Walker, D. Leach and V. Sarafis, *Magn. Reson. Imaging*, 1991, **9**, 357.
233. J. M. Pope, *Magnetic Resonance Microscopy* (ed. B. Blümich and W. Kuhn), p. 441, VCH, Weinheim, 1992.

234. H. Rumpel and J. M. Pope, *Magn. Reson. Imaging*, 1992, **10**, 187.
235. A. Metzler, W. Köckenberger, M. von Kienlin, E. Komor and A. Haase, *J. Magn. Reson.*, 1994, **B105**, 249.
236. U. Skibbe, J. T. Christeller, C. D. Eccles, W. A. Laing and P. T. Callaghan, *J. Magn. Reson.*, 1995, **B108**, 262.
237. P. J. Back, A. Coy, Y. Xia, P. T. Callaghan, L. M. Diamante and S. Umbach, *Int. J. Biol. Macromol.*, 1991, **13**, 181.
238. P. T. Callaghan, C. J. Clark and L. Forde, C. *Biophys. Chem.*, 1994, **50**, 225.
239. N. Ishida, H. Ogawa and H. Kano, *Magn. Reson. Imaging*, 1995, **13**, 745.
240. Y. Xia, V. Sarafis, E. O. Campbell and P. T. Callaghan, *Protoplasma*, 1993, **173**, 170.
241. W. Köckenberger, J. M. Pope, Y. Xia, K. R. Jeffrey, E. Komor and P. T. Callaghan, *Planta*, 1997, **201**, 53.
242. U. Görke, R. Kimmich and J. Weis, *J. Magn. Reson.*, 1996, **B111**, 236.
243. A. Zidansek, A. Blinc, G. Lahajnar, D. Keber and R. Blinc, *J. Mol. Struct.*, 1993, **294**, 283.
244. A. Zidansek, A. Blinc, G. Lahajnar, D. Keber and R. Blinc, *Biophys. J.*, 1995, **69**, 803.
245. H. Dai, K. Potter and E. W. McFarland, *J. Chem. Eng. Data*, 1996, **41**, 970.
246. K. Potter, R. S. Spencer and E. W. McFarland, *Biochim. Biophys. Acta*, 1997, **1334**, 129.
247. E. W. McFarland and D. Lee, *J. Magn. Reson.*, 1993, **A102**, 231.
248. A. R. Rajabi-Siahboomi, R. W. Bowtell, P. Mansfield, A. Henderson, M. C. Davies and C. D. Melia, *J. Controlled Release*, 1994, **31**, 121.
249. R. Bowtell, J. C. Sharp, A. Peters, P. Mansfield, A. R. Rajabi-Siahboomi, M. C. Davies and C. D. Melia, *Magn. Reson. Imaging*, 1994, **12**, 361.
250. W. A. Edelstein and E. M. Schulson, *J. Glaciology*, 1991, **37**, 177.
251. U. Tallarek, E. Baumeister, K. Albert, E. Bayer and G. Guiochon, *J. Chromatogr.*, 1995, **A696**, 1.
252. B. P. Hills, K. M. Wright, J. J. Wright, T. A. Carpenter and L. D. Hall, *Magn. Reson. Imaging*, 1994, **12**, 1053.
253. J. B. German and M. J. McCarthy, *J. Agric. Food Chem.*, 1989, **37**, 1321.
254. K. Kose, *J. Magn. Reson.*, 1996, **A118**, 195.
255. B. J. Balcom, T. A. Carpenter and L. D. Hall, *J. Chem. Soc., Chem. Commun.*, 1992, **4**, 312.
256. R. L. Armstrong, A. Tzalmona, M. Menzinger, A. Cross and C. Lemaire, *Magnetic Resonance Microscopy* (ed. B. Blümich and W. Kuhn), p. 309, VCH, Weinheim, 1992.
257. S. Su, M. Menzinger, R. L. Armstrong, A. Cross and C. Lemaire, *J. Phys. Chem.*, 1994, **98**, 2494.
258. A. R. Cross, R. L. Armstrong, A. Ried, S. Su and M. Menzinger, *J. Phys. Chem.*, 1995, **99**, 16616.
259. N. Nestle and R. Kimmich, *Appl. Biochem. Biotechnol.*, 1996, **56**, 9.
260. K. Potter and E. W. McFarland, *Solid State Nucl. Magn. Reson.*, 1996, **6**, 323.
261. J. J. Tessier, T. A. Carpenter and L. D. Hall, *J. Magn. Reson.*, 1995, **A113**, 232.
262. L. G. Butler, D. G. Cory, K. M. Dooley, J. B. Miller and A. N. Garroway, *J. Am. Chem. Soc.*, 1992, **114**, 125.
263. L. G. Butler, D. G. Cory, J. B. Miller, K. M. Dooley and A. N. Garroway, *ACS Symp. Ser.*, 1993, **517**, 260.
264. P. Barth, S. Hafner and W. Kuhn, *J. Magn. Reson.*, 1994, **110**, 198.
265. W. E. Maas, L. H. Merwin and D. G. Cory, *J. Magn. Res.*, 1997, **129**, 105.
266. S. L. Dieckman, P. Rizo, N. Gopalsami, J. P. Heeschen and R. E. Botto, *J. Am. Chem. Soc.*, 1992, **114**, 2717.
267. P. Blümler and B. Blümich, *Macromolecules*, 1991, **24**, 2183.
268. B. Blümich, P. Blümler, E. Günther, J. Jansen, G. Schauss and H. W. Spiess, *Magnetic Resonance Microscopy* (ed. B. Blümich and W. Kuhn), p. 167, VCH, Weinheim, 1992.

269. J. L. Koenig, *Magnetic Resonance Microscopy* (ed. B. Blümich and W. Kuhn), p. 187, VCH, Weinheim, 1992.
270. R. A. Komoroski and S. N. Sarkar, *Magnetic Resonance Microscopy* (ed. B. Blümich and W. Kuhn), p. 203, VCH, Weinheim, 1992.
271. W. Kuhn, E. Koeller and T. Isolde, *Magnetic Resonance Microscopy* (ed. B. Blümich and W. Kuhn), p. 217, VCH, Weinheim, 1992.
272. D. G. Cory and W. E. Maas, *Bull. Magn. Reson.*, 1993, **15**, 160.
273. C. G. Smith, P. B. Smith, A. J. J. Pasztor, M. L. McKelvy, D. M. Meunier and S. W. Froelicher, *Anal. Chem.*, 1995, **67**, 97R.
274. D. E. Axelson, A. Kantzas and A. Nauerth, *Solid State Nucl. Magn. Reson.*, 1996, **6**, 309.
275. A. N. Garroway, *Encyclopedia of Nuclear Magnetic Resonance* (ed. D. M. Grant and R. K. Harris), p. 3683, Wiley, New York, 1996.
276. W. Kuhn, P. Barth, P. Denner and R. Müller, *Solid State Nucl. Magn. Reson.*, 1996, **6**, 295.
277. S. Hafner and P. Barth, *Magn. Reson. Imaging*, 1995, **13**, 739.
278. O. Beuf, A. Briguet, M. Lissac and R. Davis, *J. Magn. Reson.*, 1996, **B112**, 111.
279. Z. Belahmer, P. Bernier and O. Davron, *Bruker Rep.*, 1994, **140**, 16.
280. M. Klinkenberg, P. Blümler and B. Blümich, *J. Magn. Reson.*, 1996, **A119**, 197.
281. H. Yasunaga, H. Kurosu and I. Ando, *Macromolecules*, 1992, **25**, 6505.
282. L. A. Weisenberger and J. L. Koenig, *Appl. Spectrosc.*, 1989, **43**, 1117.
283. L. A. Weisenberger and J. L. Koenig, *Macromolecules*, 1990, **23**, 2445.
284. L. A. Weisenberger and J. L. Koenig, *Macromolecules*, 1990, **23**, 2454.
285. M. Ilg, B. Pfleiderer, K. Albert, W. Rapp and E. Bayer, *Macromolecules*, 1994, **27**, 2778.
286. M. A. Rana and J. L. Koenig, *Macromolecules*, 1994, **27**, 3727.
287. R. A. Grinsted and J. L. Koenig, *Macromolecules*, 1992, **25**, 1229.
288. R. A. Grinsted, L. Clark and J. L. Koenig, *Macromolecules*, 1992, **25**, 1235.
289. P. Mansfield, R. Bowtell and S. Blackband, *J. Magn. Reson.*, 1992, **99**, 507.
290. S. Hafner and W. Kuhn, *Magn. Reson. Imaging*, 1994, **12**, 1075.
291. G. D. Cody and R. E. Botto, *Macromolecules*, 1994, **27**, 2607.
292. P. Maffei, L. Kiéné and D. Canet, *Macromolecules*, 1992, **25**, 7114.
293. M. Valtier, P. Tekely, L. Kiéné and D. Canet, *Macromolecules*, 1995, **28**, 4075.
294. A. S. Wallner and W. M. Ritchey, *J. Mater. Res.*, 1993, **8**, 655.
295. J. L. Ackerman, L. Garrido, J. R. Moore, B. Pfleiderer and Y. Wu, *Magnetic Resonance Microscopy* (ed. B. Blümich and W. Kuhn), p. 237, VCH, Weinheim, 1992.
296. D. G. Cory, *Encyclopedia of Nuclear Magnetic Resonance* (ed. D. M. Grant and R. K. Harris), p. 1226, Wiley, New York, 1996.
297. L. F. Gladden, *Chem. Eng. Res. Des.*, 1993, **71**, 657.
298. K. J. Packer, *Encyclopedia of Nuclear Magnetic Resonance* (ed. D. M. Grant and R. K. Harris), p. 3365, Wiley, New York, 1996.
299. P. D. Majors, J. L. Smith, F. S. Kovarik and E. Fukushima, *J. Magn. Reson.*, 1990, **89**, 470.
300. J. J. Attard, S. J. Doran, N. J. Herrod, T. A. Carpenter and L. D. Hall, *J. Magn. Reson.*, 1992, **96**, 514.
301. R. A. Waggoner and E. Fukushima, *Magn. Reson. Imaging*, 1996, **14**, 1095.
302. M. A. Horsfield, C. Hall and L. D. Hall, *J. Magn. Reson.*, 1990, **87**, 319.
303. R. L. Kleinberg, W. E. Kenyon and P. P. Mitra, *J. Magn. Reson.*, 1994, **A108**, 206.
304. L. L. Latour, R. L. Kleinberg and A. Sezinger, *J. Coll. Interfac. Sci.*, 1992, **150**, 535.
305. R. M. Cotts, M. J. R. Hoch, T. Sun and J. T. Markert, *J. Magn. Reson.*, 1989, **83**, 252.
306. V. Rajanayagam, S. G. Yao and J. M. Pope, *Magn. Reson. Imaging*, 1995, **13**, 729.
307. H.-P. Müller, J. Weis and R. Kimmich, *Phys. Rev.*, 1995, **E52**, 5195.
308. A. M. Peters, P. S. Robyr, R. W. Bowtell and P. Mansfield, *Magn. Reson. Imaging*, 1996, **14**, 875.
309. P. Mansfield and B. Issa, *J. Magn. Reson.*, 1996, **A122**, 137.
310. P. Mansfield and B. Issa, *J. Magn. Reson.*, 1996, **A122**, 149.

311. S. Chen, X. Yao, J. Qiao and A. T. Watson, *Magn. Reson. Imaging*, 1995, **13**, 599.
312. M. Bogdan, B. J. Balcom, T. W. Bremner and R. L. Armstrong, *J. Magn. Reson.*, 1995, **A116**, 266.
313. Z. Pearl, M. Magaritz and P. Bendel, *J. Magn. Reson.*, 1991, **95**, 597.
314. M. P. Hollewand and L. F. Gladden, *J. Catal.*, 1993, **144**, 254.
315. K. Y. Cheah, N. Chiaranussati, M. P. Hollewand and L. F. Gladden, *Appl. Catal.*, 1994, **115**, 147.
316. P. S. Belton, I. J. Colquhoun and B. P. Hills, *Annual Reports on NMR Spectroscopy*, Vol. 26 (ed. G. A. Webb), p. 1, Academic Press, New York, 1993.
317. M. J. McCarthy, *Magnetic Resonance Imaging in Foods*, Chapman & Hall, London, 1994.
318. B. P. Hills, *Dynamics of Solutions and Fluid Mixtures by NMR* (ed. J.-J. Delpuech), p. 549, Wiley, New York, 1995.
319. S. L. Duce and L. D. Hall, *Encyclopedia of Nuclear Magnetic Resonance* (ed. D. M. Grant and R. K. Harris), p. 2091, Wiley, New York, 1996.
320. A. M. Gil, P. S. Belton and B. P. Hills, *Annual Reports on NMR Spectroscopy*, Vol. 32 (ed. G. A. Webb), p. 1, Academic Press, New York, 1996.
321. Y. Xia, P. T. Callaghan and K. R. Jeffrey, *AIChE J.*, 1992, **38**, 1408.
322. S. J. Gibbs, T. A. Carpenter and L. D. Hall, *J. Magn. Reson.*, 1993, **A105**, 209.
323. J. Weis, R. Kimmich and H.-P. Müller, *Magn. Reson. Imaging*, 1996, **14**, 319
324. M. Nakagawa, S. A. Altobelli, A. Caprihan, E. Fukushima and E. K. Jeong, *Experiments in Fluids*, 1993, **16**, 54.
325. E.-K. Jeong, S. A. Altobelli and E. Fukushima, *Phys. Fluids*, 1994, **6**, 2901.
326. M. V. Icenogle, A. Caprihan and E. Fukushima, *J. Magn. Reson.*, 1992, **100**, 376.
327. K. Kose, *J. Magn. Reson.*, 1992, **98**, 599.
328. M. Tyszka, R. C. Hawkes and L. D. Hall, *J. Magn. Reson.*, 1992, **97**, 391.
329. S. A. Altobelli, R. C. Givler and E. Fukushima, *J. Rheol.*, 1991, **35**, 721.
330. J. R. Abbott, N. Tetlow, A. L. Graham, S. A. Altobelli, E. Fukushima, L. A. Mondy and T. S. Stephens, *J. Rheol.*, 1991, **35**, 773.
331. N. Phan-Thien, A. L. Graham, S. A. Altobelli, J. R. Abbott and L. A. Mondy, *Ind. Eng. Chem. Res.*, 1995, **34**, 3187.
332. Y. Xia and P. T. Callaghan, *Macromolecules*, 1991, **24**, 4777.
333. C. J. Rofe, R. K. Lambert and P. T. Callaghan, *J. Rheol.*, 1994, **38**, 875.
334. B. Manz, P. Stilbs, B. Jönsson, O. Söderman and P. T. Callaghan, *J. Phys. Chem.*, 1995, **99**, 11297.
335. P. T. Callaghan, M. E. Cates, C. J. Rofe and J. B. A. F. Smeulders, *J. Phys. II France*, 1996, **6**, 375.
336. S. Yao, M. Costello, A. G. Fane and J. M. Pope, *J. Membr. Sci.*, 1995, **99**, 207.
337. J. M. Pope, S. Yao and A. G. Fane, *J. Membr. Sci.*, 1996, **118**, 247.
338. J. C. Gatenby and J. C. Gore, *J. Magn. Reson.*, 1996, **A121**, 193.
339. K. Kose, *J. Phys. D.*, 1990, **23**, 981.
340. K. Kose, *J. Magn. Reson.*, 1991, **92**, 631.
341. K. Kose, *Phys. Rev. Lett.*, 1994, **72**, 1467.
342. E. S. Davies, T. P. L. Roberts, T. A. Carpenter, L. D. Hall and C. Hall, *J. Magn. Reson.*, 1992, **96**, 210.
343. J. Götz, H. Buggisch and W. Kreibich, *Bruker Biospec. Application Note*, 1993, **1/93**.
344. J. Götz, H. Buggisch, M. Peciar and W. Kreibich, *Bruker Biospec. Application Note*, 1994, **5/94**.

NMR Studies of Interfacial Phenomena

J. GRANDJEAN

University of Liège, Institute of Chemistry B6a, Sart-Tilman, B-4000 Liège, Belgium

Although conventional NMR methods such as relaxation rate or quadrupolar splitting measurements remain useful, multidimensional NMR and multiple-quantum filtering techniques have emerged as new tools to study interfacial phenomena in isotropic and anisotropic media. As this review deals with liquid–liquid, liquid–solid and solid–solid interfaces, solid high-resolution NMR techniques are sometimes required to obtain appropriate data. The results cited cover many domains of chemistry, including biochemical, polymer, surfactant, and colloid research.

1. INTRODUCTION

This article is an updating of an earlier contribution published in this series.[1] First, to delimit the scope of this review, one should recall that the interface may be defined as the space in which two phases perturb each other. Properties of interfacial species, different from those in the bulk phase, are used in many aspects of science and technology, and NMR studies of interfacial phenomena have been a growing area of research for several years. As a general rule for such NMR investigations, the two phases should be characterized by different mobilities. The less mobile phase (phase I) may be formed by dissolved

ANNUAL REPORTS ON NMR SPECTROSCOPY
VOLUME 35 ISBN 0-12-505335-5

Copyright © 1998 Academic Press Limited
All rights of reproduction in any form reserved

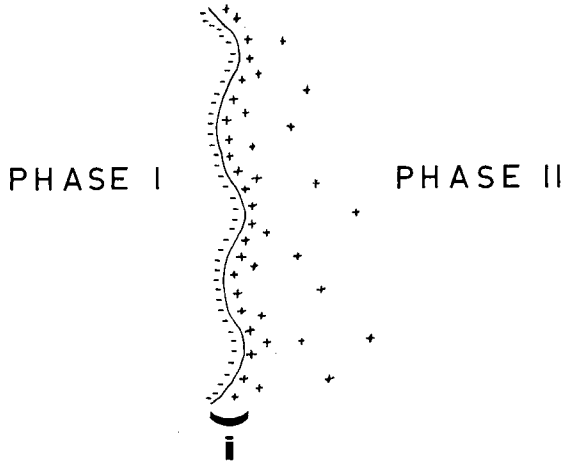

Fig. 1. Schematic representation of the interfacial region (**i**) for a negatively charged phase I.

macromolecules, dispersed aggregates or solid materials, and the second phase may consist of gaseous, liquid or solid components. A schematic representation of the interfacial region with a charged phase I is shown in Fig. 1.

The extent of the interfacial region depends on the experimental technique and, typically, the interfacial region observed by NMR covers a distance of a few (tens of) angstrøms from the surface of the less mobile component. Air–liquid interfaces have not been much studied by NMR methods. NMR studies of molecules and ions adsorbed onto a solid surface may require invasive techniques such as drying under high vacuum. These studies are usually not considered in this article, but the interested reader may find information on this topic in the literature.[2] Thus, observation of molecules or ions in the liquid phase or investigation of mobile groups at the surface of macromolecules, aggregates or solids has been envisaged.

For more than two decades, the state of water near the surface of biological and synthetic macromolecules has been a matter of debate. New techniques based upon the observation of nuclear Overhauser effects in the static or in the rotating frame have emerged more recently. The next section summarizes the main observations that are related to the residence time of water molecules on the surface of proteins and DNA. Different NMR relaxation techniques give access to the dynamics of these "bound" water molecules in biological and synthetic macromolecular systems.

When the water concentration is low, the NMR spectra are characteristic of anisotropic media, as revealed by quadrupolar splittings in water ^{2}H and ^{17}O spectra. In heterogeneous media, the quadrupolar splitting may remain

undetected, but local anisotropy may be detected with double-quantum filtering techniques.

Amphiphilic (surfactant) molecules consist of a polar group associated with an apolar chain. Their aggregation in solution gives rise to diverse structures such as micelles, microemulsions or lyotropic mesophases. Numerous industrial applications of these suspensions have boosted fundamental research of surfactant behaviour, and NMR reviews have been devoted to these molecules.[3–6] In contrast to these articles, which deal chiefly with the determination of phase diagrams, this paper focuses on interfacial phenomena that mainly concern dynamic processes. As shown with proteins, the water residence time near the aggregate surface can be estimated from measurements of nuclear Overhauser effects. Isotropic media as well as systems showing long-range ordering are considered, and the behaviour of interfacial water molecules is inferred from quadrupolar splitting, relaxation rate and self-diffusion coefficient measurements.

Minerals such as silica or clays suspended in water provide heterogeneous media with a liquid–solid interface. Applications of such suspensions can be found in drilling fluids, paints, cosmetics and water treatment. The mobility of polar and apolar molecules near the solid surface has been described within the framework of models deduced from NMR relaxation dispersion data. In clay suspensions, the NMR signal of quadrupolar nuclei of interfacial molecules is split as an effect of residual quadrupolar interaction. This splitting is a useful probe for studying the behaviour of interfacial molecules. Indeed, its value is influenced by different factors such as the type of clay, the nature of the counterions or the liquid composition. Macromolecules can also interact with minerals. Polymers adsorbed on inorganic substrates and swollen with solvents are useful in many applications such as coatings and adhesives. A review in this series has covered this subject[7] from the NMR point of view; only a few more recent articles are considered here.

When the phase I (Fig. 1) is charged, counterions are present in the liquid medium to preserve electroneutrality. These ions are mostly inorganic and their nuclei often have a spin quantum number greater than 1. NMR studies of these quadrupolar nuclei in different systems are summarized in Section 3. NMR techniques for the study of relaxation phenomena have been improved for both isotropic media and systems showing long-range ordering. Thus, multiple-quantum filtering methods have been applied here but they have been employed also to reveal local anisotropy or to show a loss of NMR visibility. The determination of counterion location and distribution near the surface of macromolecules or aggregates is discussed in several articles, but most papers deal with dynamic information of these ions in isotropic and anisotropic media. Relaxation data are usually explained in terms of a fast local motion and a slow lateral diffusion of ions near the surface of macromolecules or aggregates. In solid suspensions, loss of cation NMR visibility has been demonstrated from competition experiments and multiple-quantum filtering techniques. Alkali

NMR is also appropriate for studying polymer-based ionic conductors. Among organic ions, ionic surfactants are particularly important. NMR of these adsorbed charged molecules shows how their properties are affected by comparison with those in solution.

Species in phase II (Fig. 1), usually solvent or solute molecules, may perturb the structure and the dynamics of superficial groups in phase I, and nuclei at the surface of phase I are useful probes for investigating such perturbations. Obviously, these nuclei also intervene in nuclear Overhauser experiments cited above, but in Section 4 other NMR data, more specific to superficial groups, will be discussed. Polar head groups of amphiphilic molecules contain relevant nuclei for such studies. Polymers or alkyl chains may be grafted onto a solid surface. Changes in their conformation and dynamics compared to those in solution are seen by NMR methods. Alkyl-modified silica and alumina are used as stationary phases in reversed-phase liquid chromatography. A wealth of information on these systems has been obtained by NMR spectroscopy, as has been reviewed.[8] Results on other systems have been also described previously,[7] and only more recent contributions are presented in this article.

In solid mixtures, NMR techniques allow the study of the solid–solid interface when the components are characterized by different mobilities. These techniques have mostly been applied to polymer blends. Strictly speaking, such systems usually form an interphase since both phases interpenetrate each other. This subject has been summarized in a review in this series.[9] Solid–solid interfaces have been studied for other systems and a few recent works are reported at the end of this article.

This review, which mainly covers literature within the 1992–1996 period, emphasizes the applicability of NMR theories to the description of the structure and dynamics of interfacial species in quite different systems. Accordingly, updated NMR theories and techniques are also reported.

2. STUDY OF INTERFACIAL MOLECULES

Most of the work in this field deals with water molecules, as a result of the huge importance of hydration processes in (bio)chemistry. Thus, water molecules interacting with molecular surfaces give rise to perturbation either by ordering (nonpolar surfaces) or strain (polar surfaces). These water molecules adopt states of greater free enthalpy than that prevailing in the bulk. This stored energy helps to drive specific molecular events such as biological association. Indeed, when a substrate is complementary to the active site of an enzyme, it can displace these hydration water molecules easily to form a properly bonded complex.[10] Among different techniques, NMR has been used extensively to study hydration of macromolecular systems. The more traditional methods are based on the measure of self-diffusion coefficients or spin relaxation rates. Water molecules are rapidly exchanged between the interface and the bulk

regions. Compared to the bulk liquid, the self-diffusion coefficient decreases and the relaxation rates increase for interfacial water molecules. In systems with long-range anisotropy, the residual quadrupolar splitting of water ^{2}H or ^{17}O is another useful parameter for characterizing molecular properties at the interface. Such studies have been performed for many years,[1] and they are still useful. More recently, a further approach which uses the dipolar cross relaxation between water and macromolecular spins has emerged, and will be described first.

2.1. Hydration of macromolecules

2.1.1. Isotropic systems

Hydration of biological macromolecules. When two protons are close enough, their mutual dipolar interaction generates a nuclear Overhauser effect (NOE), which is currently observed from cross peaks in a two- (multi-) dimensional spectrum (NOESY). The short-range nature of NOE ensures that cross peaks occurring in the F2 dimension at the water chemical shift of the F1 dimension originate from magnetization transfer between protein and hydration water protons.[11] Hydration water molecules display the same chemical shift as bulk water, and fast chemical exchange occurs between these molecules. These observations can be translated into a lifetime for hydration water molecules lower than about 1 ms. To allow this magnetization transfer, a particular water molecule must reside long enough at the surface of the macromolecule. The amplitude and the sign of these cross peaks are sensitive to changes of the residence time in the nanosecond range. A positive NOE (negative cross peak) indicates an exchange rate faster than $\sim 10^{9}\,s^{-1}$ as observed typically for solvent-exposed protons. Internal water molecules show negative NOEs (positive cross peaks) owing to slower dynamical processes.[12,13] Cross peaks from proton exchange may also appear in the NOESY experiment; to discriminate between these two effects, NOE spectra in the rotating frame (ROESY) are also performed. The cross peaks at the water chemical shift in the F1 dimension may originate in different magnetization transfer processes (Fig. 2).

(1) Positive NOESY and negative ROESY peaks result from spin–spin cross relaxation between bound water (slow motion regime) and protons in proteins. Lifetimes with respect to exchange with the bulk water are greater than 10^{-9} s.[14]
(2) Both NOESY and ROESY peaks are negative when the reorientation of "bound" water molecules is fast ($\omega\tau_c < 1$), and the exchange lifetime is within the 10^{-11} to 10^{-10} s range.[11]
(3) Positive NOESY and ROESY cross peaks indicate proton exchange between water and macromolecules.

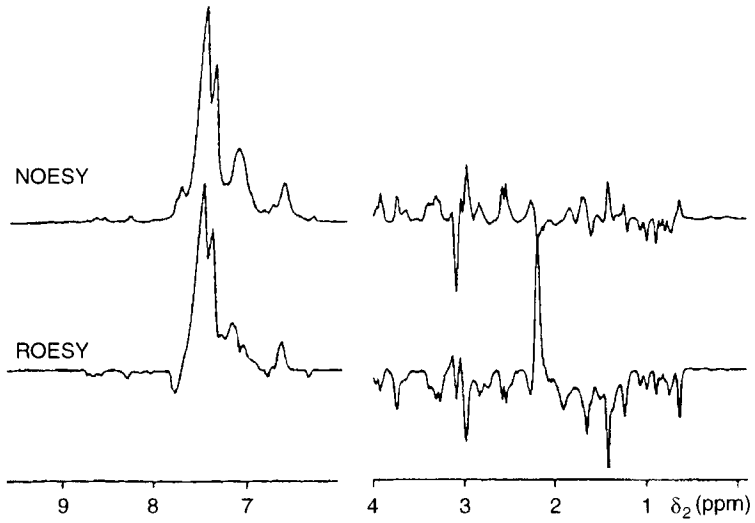

Fig. 2. Water–protein cross peaks in NOESY and ROESY (cross peaks between 6 and 9.5 ppm are scaled down and inverted). (Reprinted with permission from Ref. 12. Copyright 1995 American Chemical Society.)

(4) Cross peaks are also observed when protein proton signals are degenerate with the water resonance. Obviously, the latter cross peaks are not related to hydration processes.

Technical details on these methods are reported in the literature.[15] Continuous and discrete diffusion models have been proposed to provide better insight into the physical origin of cross relaxation data on surface hydration.[16,17] With the bovine pancreatic trypsin inhibitor (BPTI), all surface-bound water molecules exchange in the subnanosecond time range with the bulk water.[13] Four internal water molecules are characterized by residence times longer than ca. 10 ns. When they intervene in the structure of the protein, external water molecules may have lifetimes longer than 1 ns. For instance, in the immunoglobulin binding domain of streptococcal protein G, such water molecules form hydrogen bonds with specific amino acid residues and they contribute to the conformation of the protein in solution.[18] DNA–water interactions also give rise to NOEs. In the minor groove of adenine-thymine-rich regions, the residence time of water is longer (>1 ns) than that obtained in the major groove (<1 ns).[19–21] Water molecules are also present at the interface of protein–DNA complexes. NOEs with hydration water molecules are observed for specific protons of the protein and/or of the DNA.[22–24] A lifetime within the nanosecond to millisecond range is estimated for these water molecules.[22] The state of water molecules at the protein–inhibitor interface can also be approached by these NMR techniques.

Thus, in solution water molecules are present within the interface between the HIV-1 protease, a primary target of AIDS antiviral agents, and the potent inhibitors KNI-272[25] and DMP323.[26] The four interfacial molecules found in the first complex play a more significant structural role than that of the water molecule found in the second complex.

Suppression of the huge water signal is critical in these experiments. To improve it, these studies have increasingly used selective detection of protons bound to heteronuclei of ^{13}C- or ^{15}N-enriched proteins, and hetero-NOE(ROE)SY experiments (HOESY) have been performed.[12,27] These studies have also benefited from the use of pulsed field gradient (PFG) technique to determine water exchange rates.[27] Advances in gradient spectroscopy[28,29] allow the determination of exchange rates within the 10^9–$10^3\ s^{-1}$ range.[30] Pulse sequences using both selective water proton excitation and the PFG technique have been proposed for the study of protein hydration.[31–33] A technical limitation of this method based on NOE and ROE cross peaks stems from the overlap of water and protein resonances. Even in 2D and 3D experiments, the resolution may still be too low. In uniformly ^{15}N,^{13}C-isotope-enriched proteins, intramolecular NOEs can be suppressed using ^{15}N- and ^{13}C-filtering techniques, but to assign these peaks unambiguously a 100% enrichment is required. With selective excitation of the water signal in the first step of the pulse sequence, only water–macromolecule interactions are observed.[34,35]

Again, this approach works well as long as the solvent and macromolecule peaks are not superposed. Isolation of intermolecular solvent–protein NOEs has been achieved with diffusion filters that are based on the different diffusion properties of water molecules and macromolecules.[36] For investigation of proton exchange between water and protein molecules, a pulse sequence dedicated to detection of selectively exchangeable proton signals has been reported.[37]

As far as dynamic phenomena are concerned, water in the presence of macromolecules may be divided into three classes: free water, whose properties are similar to pure water; weakly bound (vicinal) water, with properties different from both the solid and the liquid states; and water bound to macromolecules.[15]

In contrast to many previous theories that focused on the role of bound water for analysis of water proton relaxation data, a new model has been proposed. This includes the effects of fast exchange between water and biopolymer (hydroxyl or amino) protons and dipolar cross relaxation between exchangeable and nonexchangeable biopolymer protons.[38,39] From transverse, longitudinal relaxation data in the static and in the rotating frames, it is argued that in dilute globular protein solutions the contribution of hydration (bound) water to the relaxation is relatively small.[38]

The dependence of the water proton longitudinal relaxation rate on the Larmor frequency (relaxation dispersion) (Fig. 3) has been explained from

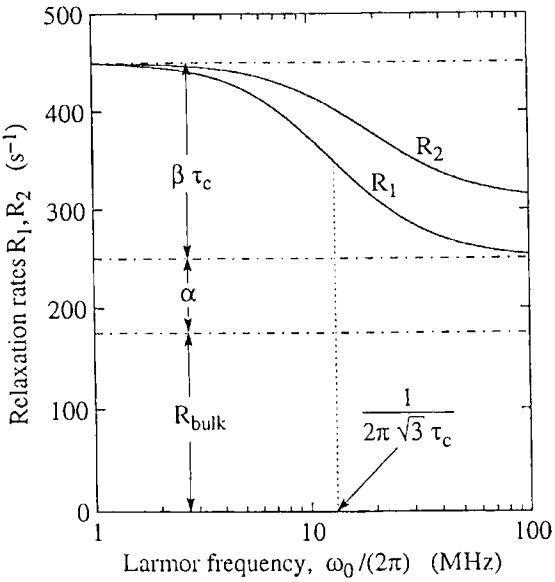

Fig. 3. Typical dependence of the water nuclei relaxation rates on the Larmor frequency in protein systems.

various theoretical models of water proton cross relaxation to gelatin or collagen protons.

On the high-frequency side, relaxation dispersion data are best explained by the fractal diffusion model with a 4/3 value for the fractal dimension. In the low-frequency range, a variation of the Rorschach–Hazlewood model is consistent with the results.[40] Thus, translational degrees of freedom with a reduced dimensionality appear for solvent molecules adsorbed onto the surface of macromolecules. Isolation of "bound" (nonfreezing) water can be achieved with frozen protein samples. The diffusion coefficient of adsorbed water molecules is one order of magnitude smaller than that of bulk water.[41] If the translational mobility of these water molecules (nonfreezing) remains high, as determined by PFG methods, their orientational correlation times obtained by proton or deuteron relaxation experiments are longer than those of bulk water by at least 6 orders of magnitude.[42] The authors interpret this as an effect of translational displacements on the orientational correlation of water molecules. In analogy with scattering theory, they introduce an orientational structure factor to separate structural information of the macromolecular surface from the dynamics of molecules diffusing on this confining system.[42] Among water nuclei, the ^{17}O nucleus ($I = 5/2$) is probably the best candidate to provide information on water reorientation near the protein surface. Indeed, its quadrupolar relaxation is not influenced by proton

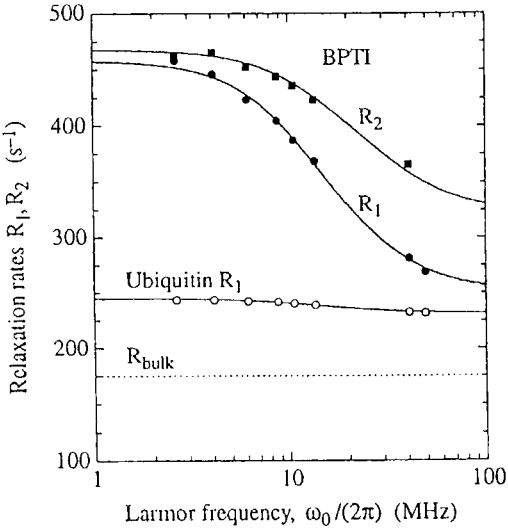

Fig. 4. Water ^{17}O NMR relaxation dispersion for a BPTI solution and for a ubiquitin solution.

(deuteron) exchange or by cross relaxation effects as observed with protons. Denisov and Halle have carried out a well-documented study of ^{17}O NMR relaxation dispersion data on BPTI and ubiquitin solutions.[43] Although it does not seem possible to determine both the number of perturbed water molecules and the degree of this perturbation, their results strongly suggest that the dispersion arises from internal water molecules. According to previous NMR studies, BPTI contains[11,14] such water molecules, and shows strong relaxation dispersion. Conversely, ubiquitin, which is devoid of internal water molecules, exhibits a reduced relaxation dispersion within the 2.6–49 MHz frequency range (Fig. 4).[43] An upper limit of 4 μs for the residence time of these trapped water molecules is 5000 times lower than (but consistent with)[43] the values obtained from paramagnetic shift experiment.[14] Deuteron (proton) exchange effects on the relaxation dispersion have been evaluated from comparison between the ^{17}O and ^{2}H NMR curves.[44]

Fast chemical exchange implies that water ^{17}O NMR relaxation rates are weighted averages on the different water sites. For a two-state model, which is often applied, fast exchange between bulk and "bound" (in slow motion) water molecules is usually assumed. Theoretically, the relaxation process is multiexponential, but, owing to the small amount of "bound" water, deviation from a monoexponential behaviour is difficult to observe by conventional methods, and multiple-quantum filtering techniques have emerged as an alternative for studying quadrupolar nuclei in the slow motion regime. In my previous review in this series[1] I reported the possibility of exciting multiple-

quantum coherence of 3/2 spin nuclei.[45] This theory has been extended to nuclei with a spin quantum number of 5/2 such as the ^{17}O nucleus.[46] Such an approach allows direct visualization of the motionally hindered water fraction in biological tissues.[47] This experiment has been quantified in protein and erythrocyte solutions from transverse and longitudinal relaxation of triple-quantum coherences, and the fraction of water in slow motion and its correlation time have been determined. The population of "bound" water molecules varies from 0.062 to 0.096 within a concentration of bovine serum albumin (BSA) between 50 and 150 g/l. The behaviour of bulk water was different from pure water and was interpreted as due to weak or transient interactions with macromolecules. The correlation time of "bound" water molecules evolves from 5.7 to 9.0 ns within the same concentration range.[48]

Hydration of synthetic macromolecules. The hydration process has been also studied for polymers. Poly(oxyethylene) is water-soluble to any extent and recent molecular dynamics studies have shown that the water residence time near a monomer unit is ~25 ps[49] compared to values ranging from tens to a few hundreds of picoseconds for hydration water molecules on the BPTI surface.[50,51] A value of 25 ps is near the lowest limit of the water residence time range for application of the NOE NMR techniques. Thus, these techniques are probably not well suited to study the behaviour of water molecules near this polymer surface.

The number of water molecules per monomer unit has been a controversial matter in literature. Recently, water proton and deuterium relaxation rates in aqueous solutions of poly(ethylene glycol) have been determined in a broad range (3–90 wt%) of water concentration. Assuming fast exchange of water between a bound state and the bulk, the number of water molecules per repeat unit is estimated to be unity.[52] At water contents lower than one molecule per monomer unit, both the water and the polymer mobilities are reduced. Water molecules form bridges between two chains of poly(ethylene glycol) and the resulting anisotropic motion gives rise to a residual quadrupolar splitting in the water deuteron spectrum.[52]

To study hydration of poly(ethylene oxide) solutions, a Dutch group has measured the quadrupolar relaxation of water ^{2}H and ^{17}O nuclei and the ^{1}H–^{17}O dipolar relaxation of ^{17}O-enriched water. As the intramolecular part of the latter relaxation process is proportional to the inverse of the sixth power of the O–H bond length, the authors conclude an increase of this distance compared to the pure water value, and they postulate increased hydrogen-bonding at both the hydrophilic and the hydrophobic interface.[53]

Polymer hydrogels are also good candidates for study of the hydration phenomenon. Here again, relaxation rates of water nuclei may be used to infer dynamic information. For instance, the introduction of hydrophilic side-chains in methacrylate hydrogels leads to an increase of water molecule mobility.[54] More interestingly, dipolar cross relaxation between water and polymer

protons are observable. 2D-NOESY experiments on hydrolysed starch-g-polyacrylonitrile ("g" indicates grafted) have shown water–polymer positive cross peaks. Using previous data from ^{13}C NMR NOE measurements on the same system,[55] this study lends support to the importance of cross relaxation between starch and water protons rather than proton chemical exchange.[56] In such gel systems, magic angle spinning (MAS) improves spectral resolution. In polyacrylamide hydrogel, NOESY and ROESY experiments under MAS have revealed positive cross peaks between water and the polymer network.[57] Thus, the dominant mechanism for magnetization transfer is chemical exchange between water and polymer protons. Water-selective ^{13}C-{^1H}HOESY[58] and MAS have also been combined for studying hydration in polyacrylamide–water systems. Selective inversion of the water proton signal allows study of the cross relaxation between water protons and carbonyl carbons of the polymer.[58] Using a correlation time value of 0.58×10^{-10} s determined from ^{17}O longitudinal relaxation time measurements, a mean distance of 3.45 Å is estimated between water protons and amide carbonyls.[59]

2.1.2. Anisotropic systems

In long-range-ordered media, the quadrupolar (dipolar) interaction is not averaged out by fast molecular motions, and line splitting occurs. Macromolecules with low water contents provide such systems. Quadrupolar splittings of water deuterons allow identification of different types of water molecules. In this way, three kinds of water bound to the cellulose matrix have been detected: nonfreezable, strongly bound water molecules remaining rigid but amorphous at low temperatures; highly mobile water molecules exhibiting isotropic motion even below 270 K; and water molecules that undergo 180° flips around their bisector axis with a rate greater than 10^5 s^{-1}.[60] This last component cannot be removed from the polymer matrix by high-temperature drying. In oriented cellulose fibres, water deuteron NMR spectra indicate that the molecular motion of adsorbed D_2O is only slightly anisotropic, and its average residence time on a fibril is estimated at ~1.5 ms.[61]

Deuterium NMR studies of water in oriented nylon-6 fibres have shown three types of water molecules: isotropic water and two classes of water with different amounts of residual orientational order. The water molecules that exhibit the largest anisotropy are associated with intrafibrillar channels, the less anisotropic water molecules reside in the intralamellar regions, and the isotropic water is probably located at the surface or in macroscopic fibre defects.[62] Similar studies have been performed on polyimide (Kapton) films of varying thickness. Two distinct water sites have been found, neither of which is strongly bound to the polymer or isotropically free. One site is uniformly distributed throughout the volume of the film while the second appears to be small molecular clusters.[63] Water diffusion in wood pulp cellulose fibres has been investigated by diffusion measurements. The reduction of the water

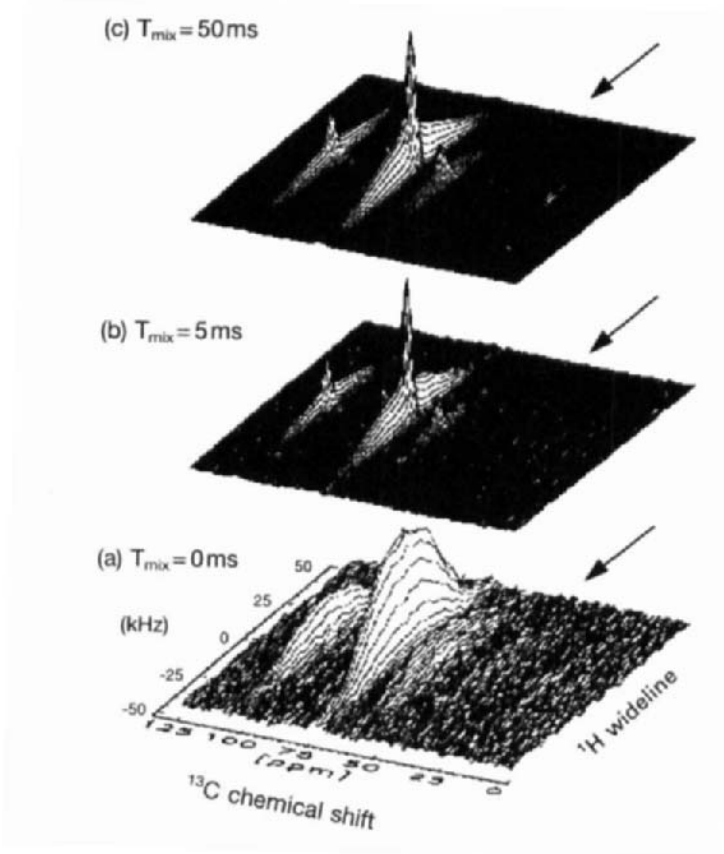

Fig. 5. 2D-WISE spectra of pure cellulose: (a) spectrum without mixing time before cross polarization; (b) spectrum after allowing a 5 ms mixing time (the mobile component due to mobile water is seen at the cellulose signals); (c) spectrum after allowing a 50 ms mixing time (the arrows mark the position where the PVA CHOH signal is observed for the blends). (Reprinted with permission from Ref. 60. Copyright 1996 American Chemical Society.)

self-diffusion between the fibres is caused by the obstruction effect of the cellulose fibres, whereas the hydration of macromolecules is of minor importance.[64]

In cellulose–poly(vinyl alcohol) blends, water distribution throughout the polymer matrix can be determined. 2D wide-line separation (WISE) experiments emphazise spin diffusion due to dipolar couplings between water and polymer protons. These proton signals are resolved in the second dimension along ^{13}C chemical shifts. Since narrow water signals occur only at the ^{13}C chemical shifts of cellulose signals (Fig. 5), this gives evidence that water molecules are predominantly associated with the cellulose polymer.[60]

Anisotropy in macroscopically disordered systems may be difficult to detect in the single-quantum ^2H NMR spectrum since the quadrupolar splitting may not be resolved. As the double-quantum-filtered (DQF) signal originates exclusively in the anisotropic motion, such a peak reveals the presence of anisotropy.[65] Analysis of water deuteron DQF spectra of suspensions of collagen and cartilage leads to a wide distribution of quadrupole splittings (110 ± 73 Hz). The water deuteron quadrupole constant (~220 kHz) is reduced as a result of fast exchange between free and bound water molecules, anisotropic motion of bound water molecules, and diffusion of water molecules on the surface of the macromolecules.[65]

2.2. Hydration of aggregates

Amphiphilic molecules in solution are known to form self-assemblies. Solutions of micelles or vesicles (discrete units) are isotropic. Conversely, long-range ordering is found with surfactant aggregates that extend over macroscopic distances in one, two, or three dimensions. The behaviour of water near the aggregate surface can be studied by several NMR techniques. In the previous section, we have seen that the dipolar interaction between hydration water and protein protons generates NOEs. To study the behaviour of water molecules in suspensions of 1-palmitoyl-2-oleyl-*sn*-glycero-3-phosphocholine (POPC), a similar NMR approach, combined with the MAS technique, has been used.[66] The 2D-NOESY spectrum combined with proton magic angle spinning shows negative cross peaks between water and protons near the aggregate surface, i.e. those of the polar headgroup, the glycerol backbone, and the hydrocarbon chain close to the carbonyl group of POPC. This indicates a residence time shorter than ~500 ps[11], which is consonant with a value of 100 ps determined independently from relaxation time measurements on progressively hydrated POPC.[66] Nonionic surfactants are used for membrane protein crystallization and reconstitution, and their effect on lipid hydration is of interest. In the presence of a nonionic surfactant (tetraethyleneglycol dodecyl ether: $C_{12}EO_4$), the above negative cross peaks disappear, presumably owing to the lipid dehydration. Positive cross peaks are observed between water and ethylene oxide protons, corresponding to residence times of water molecules longer than ~10 ns.[66] Similar studies have been undertaken to examine surface hydration in suspensions of monomethyldioleophosphatidylethanolamine (MeDOPE). In the lamellar phase at room temperature, two water signals are observed at 4.75 and 4.88 ppm for bulk water outside the multilamellar vesicles and interlamellar water, respectively.[67] Positive NOESY cross peaks are observed between the low-field water signal and both NCH_3 and CH_2N- segments of the phospholipid headgroup. Again, a water residence time longer than ~10 ns may be inferred from this observation. It should be remembered that positive NOESY cross peaks may also occur from

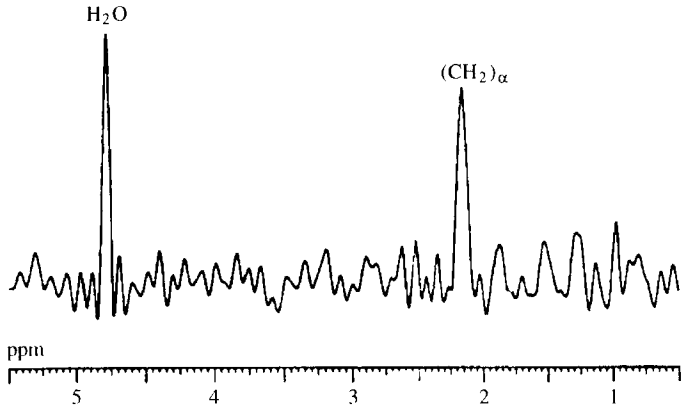

Fig. 6. Cross peaks at the carboxylate chemical shift with water and α-methylene proton signals. (Reprinted with permission from Ref. 58. Copyright 1992 American Chemical Society.)

exchange between labile protons of the aggregate surface and bulk water.[12] This alternative process, when suspected, may be tested by ROESY experiments. Dipolar interactions also occur between protons and nearby hereronuclei. A previously mentioned HOESY experiment[58] has been applied to sodium octanoate micelles. Cross peaks at the carboxylate carbon chemical shift for water and α-methylene protons are detected (Fig. 6).

Upon selective excitation of water protons, the intensity of the carboxylate ^{13}C NMR resonance increases and levels off with the length of excitation. From the well-known Solomon equations, a mean distance of ~2.8 Å is obtained between water proton and the carboxyl carbon nucleus.[58] Further studies on similar systems have confirmed that this distance varies within the 3–4 Å range, depending on the surfactant concentration. An increase of this distance is observed in the course of micelle build-up.[68] Magnetization transfer from solvent protons to superficial nuclei of surfactant molecules is relatively easy to observe when the relevant nucleus–proton interaction is not overwhelmed by stronger interactions due to protons directly bound to the nucleus under consideration. The ^{13}C nuclei of carboxylate[58,68] or ^{31}P nuclei of phosphate[69] groups are good candidates for such studies. Cross-relaxation peaks are expected to be more easily detected in ^{1}H-^{19}F HOESY experiments than in other heteronuclear cross relaxation studies, owing to their large gyromagnetic ratio. Furthermore, the sign of the cross peaks can be obtained as the Larmor frequencies of these two nuclei are of the same order, in contrast with the ^{1}H–^{13}C experiment. In a micellar solution of caesium pentadecafluoro-octanoate, a small positive cross relaxation rate for fluorine on the carbon atom next to the carboxylate group indicates a short residence time for interfacial

water. The mean distance between water and fluorine nuclei deduced from these data is about 3 Å.[70]

Interaction between the quadrupolar moment of a nucleus with $I \geqslant 1$ and the electric field gradient formed by the nucleus environment gives rise to a line splitting in the presence of long-range ordering. Lyotropic liquid crystals are probably the best examples of such systems. Water deuteron splittings have been used to study heterogeneous systems for many years, but this review deals only with a few recent results. The dynamic properties of water in POPC, 1,2-dioleyl-*sn*-glycero-3-phosphatidylcholine (DOPC), and egg yolk phosphatidylcholine (EYL) aqueous dispersions have been described by analysing water deuteron splittings, longitudinal relaxation times, and water proton self-diffusion coefficients versus the water/lipid ratio.[71] Only a small fraction of water molecules is significantly affected by the bilayer surface and, for water/lipid ratios greater than 5, water molecules share essentially isotropic, free-water characteristics in terms of correlation times and molecular order. Hydration properties of POPC and EYL are similar but differ from those of DOPC. At very low water contents, water molecules are strongly coupled to the lipid lattice, and their behaviour depends on the head group conformation. A somewhat smaller number of water molecules are more strongly immobilized and ordered with this last lipid.[71] In the lamellar phase L_α of these lipidic systems, the quadrupolar splitting of heavy water varies linearly with the water activity up to ~98%. Using a simple interaction potential containing an orientation-independent and an orientation-dependent term, a good fit of the data is obtained. The energy for hydration (dehydration) of lipids is mainly stored in the orientation-dependent term.[72]

Water dynamics in oriented 1,2-dipalmitoyl-*sn*-glycero-3-phosphocholine (DPPC) have been studied by ^2H NMR relaxation. At low water content, longitudinal relaxation rates depend on fast water motions and transverse relaxation rates are related to slower water mobility. These data are explained in terms of two correlation times. A uniaxial rotation of water molecules tightly bound to DPPC headgroups is characterized by a correlation time of ~62 ps, whereas the slower reorientation of the rotational axis occurs in the nanosecond time scale.[73] ^2H NMR relaxation rates of heavy water have been used to determine the free energy of hydration of two phospholipids. Using a simple two-state binding model, energy values of 36 and 28 kJ/mol have been determined for DOPC and POPC lipids, respectively.[74] These data are in good agreement with those obtained from sorption measurements.

A similar approach is used to calculate hydration free energies of homologous nonionic alkyl oligo(ethylene oxide) surfactants forming lamellar phases. A linear relationship between this energy and the number of oxyethylene units is found and the energy grows by 7 kJ/mol per additional group (n = 2–8).[75]

The cesium perfluorooctanoate–water mixture forms a nematic phase. Recent NMR studies of this system deal with the measurement of water

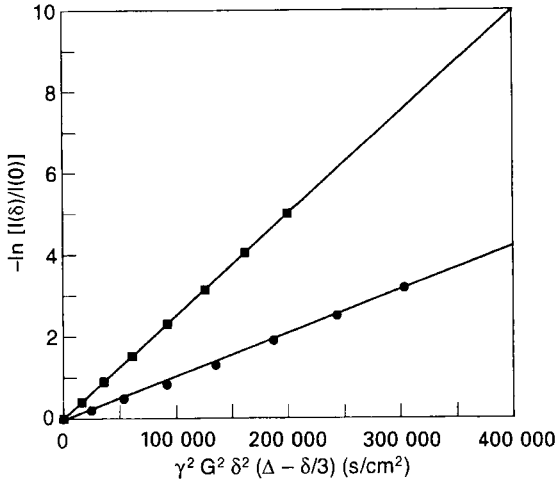

Fig. 7. Typical decay of the water proton signal intensity as a function of the gradient amplitude in caesium perfluorooctanoate–water nematic system (upper and lower curves for gradients perpendicular and parallel to the field direction, respectively). (Reprinted with permission from Ref. 76. Copyright 1993 American Chemical Society.)

self-diffusion by the pulsed field gradient spin echo (PFGSE) technique.[76–78] Experiments with field gradients parallel and perpendicular to the magnetic induction field show anisotropic water diffusion in a few liquid crystals (Fig. 7).[76]

Water diffusion in these systems proceeds from two basic effects, leading to a reduction of the diffusion coefficient compared to that of bulk water: interaction of water molecules with polar headgroups (hydration or "bound" water) and obstruction of water diffusion by the apolar part of the aggregate. Data obtained in the long-time and short-time diffusion regimes are related to the population of water bound to the lamellar surface and to the obstruction factor, respectively.[79] Meaningful physical information requires accurate self-diffusion coefficients, and data with errors smaller than 0.5% have been reported.[77] Using a theoretical description of obstruction and hydration effects, water deuteron diffusion coefficients support a discrete-micelle model for the microstructure of the nematic phase of the above fluorinated surfactant.[78]

Water self-diffusion has been also determined in aqueous solutions of hydrophobically end-capped poly(ethylene oxide) (associative polymer).[80] This parameter decreases smoothly when the polymer concentration increases, independently of the polymer molecular mass and of the terminal alkyl chains. This decrease is due to the combined effect of obstruction and hydration. A cell-diffusion model that assumes two spherical diffusion zones des-

cribes reasonably well the water diffusion, but at the highest polymer concentrations.[80] The degree of obstruction due to the presence of particles depends on the particle size and geometry. Therefore, such diffusion experiments can be used to give information on the shape and size of colloidal particles, after correction for hydration (solvation) effects. These applications are beyond the present scope, but interested readers may find more details in two recent reviews.[5,81]

Measurement of self-diffusion coefficients is a well-established method and a few pulse sequences can be used for it. However, it has been pointed out recently that proton cross relaxation perturbs the value of self-diffusion coefficients determined by stimulated-echo methods, and that effect must be taken into account.[82]

The most popular NMR parameter is obviously the chemical shift. Examples of its use to describe properties of interfacial species are rather scarce. Nevertheless, the structure of water at interfaces of microemulsions or aqueous micelles has been approached by this way. The deuterium solvent isotope effect on the water proton chemical shifts of micelles in H_2O–^2H_2O mixtures indicates an increase of interfacial water structure compared to the bulk water.[83–85]

2.3. Molecules adsorbed at a solid surface

Silica. Proton relaxation of water adsorbed on silica gel shows a multi-exponential behaviour. A model introduced to explain quantitatively this observation assumes three phases: the OH groups at the mineral surface, the protons of "bound" water molecules, and the protons of the other water molecules ("free" water). This model accounts for cross relaxation between superficial OHs and "bound" water protons and exchange between "bound" and "free" water.[86]

At temperatures lower than 273 K, "bound" water molecules do not freeze,[87] and special relaxation mechanisms for water protons can act in such confined systems. Disordered structures define some local preferential orientations, whereas some translational motions with reduced dimensionality are allowed.[42] Thus, the dipolar correlation function of diffusing molecules reflects not only the molecular dynamics but also the structural properties of the confining system.

A reorientational model of water molecules mediated by translational displacements (RMTD) has been considered to explain the longitudinal relaxation dispersion curves of water protons in some silica samples. The low-frequency plateau (α process) indicates a long correlation time of $\sim 10^{-4}$ s, eight orders of magnitude longer than that of bulk water.[88] The high-frequency plateau implies a correlation time of the order of 10^{-9} s (β process). The interaction of water molecules with the solid surface apparently leads to a very

fast but restricted rotation along an axis normal to the solid surface (γ process). This process may contribute to longitudinal relaxation at high frequency. Direct evidence of this third process has been obtained with ceramics of controlled porosity whose relaxation dispersion curve shows a third plateau at the highest frequencies.[88] The analysis of experimental data is based on a correlation function with three components accounting for exchange between "free" and "bound" water: reorientation by the γ process, and the α and β processes which are successfully interpreted as RMTD mechanism. Using diffusion coefficient data, the β process is consonent with a small reorientation, typically of the order of a silica fine particle. In contrast, the α dispersion must refer to longer length scales determined by the network of particles or by the pore size.[88] In later studies on porous glasses, similar deuteron and proton dispersion curves have been obtained.[89] The fluid polarity plays an important role in liquid behaviour. As the RMTD mechanism becomes effective with polar molecules, it is expected that the relaxation dispersion curves will show only a strong frequency dependence with these molecules, as experimentally observed.[89,90] To explain the high water diffusivity at the solid (or macromolecular) surface, mediation by the bulk medium has been proposed.[91] This model accounts for data on porous glass. Indeed, when "free" water is frozen, leaving liquid about two superficial water layers, the longitudinal relaxation dispersion curve changes drastically and the frequency dependence is much lower, similar to that of nonpolar liquids in porous glasses.[89] As with water adsorbed on proteins, the diffusivity inside the nonfreezing layer is only reduced by one order of magnitude as compared with that of bulk water.[89]

The water–pyrogenic silica interaction has been also investigated by NMR techniques for solids. Combining magic angle spinning and multiple-pulse averaging of proton–proton dipolar interactions, the proton NMR spectrum shows three peaks corresponding to hydrogen-bonded silanol groups, physisorbed water, and non-hydrogen-bonded silanol protons, respectively. Upon dehydration, the freezing point depression is ~40 K.[92] More recently, combining broad-line and MAS ^{1}H NMR at 4 K with ^{29}Si data, the superficial composition of two silicas has been assigned to geminal silanols, single silanols, water molecules relatively strongly hydrogen-bonded to silanols, and water not interacting with OH groups.[93] Water adsorption on pyrogenic silica surfaces modified by phosphorous compounds has also been investigated by ^{1}H NMR. The amount of water increases hydrolysis of the Si–O–P groups, and this perturbs the overall location of water.[94]

Polymers adsorbed on solid surfaces in contact with a liquid are important for different purposes such as structural coatings, stabilizers, or adhesives. The ways in which the polymer interaction affects the conformation and dynamics of the macromolecule at the interface are the main questions addressed by NMR. If the solvent is able to penetrate the polymer layer, NMR solution techniques are adequate to characterize the material. If the polymer is tightly bound to the solid with little solvent penetration, this part of the system is

solid-like. As this subject has been discussed extensively in a review in this series,[7] only one article which introduces a new NMR technique for studying the adsorption selectivity for polymers with a high polydispersity will be mentioned. As the self-diffusion coefficient is related to the molecular mass of the investigated species, pulsed-gradient spin-echo NMR has been applied to the polyoxyethylene–silica system to study the process known as "adsorption fractionation".[95] The self-diffusion coefficient distributions resulting from the inverse Laplace transform of the echo attenuation function have been examined before and after exposure to the solid surface. The results indicate that the adsorption process favours the larger molecules, as predicted by the theory and confirmed by other experimental techniques.[95]

Clays. Smectite clays belong to the 2:1 phyllosilicate family, and they are formed by an octahedral layer sandwiched between two tetrahedral layers. Silicon(IV) is at the centre of the tetrahedra. In a trioctahedral clay such as saponite or hectorite, the three octahedral sites are occupied by Mg(II). Two out of three sites are occupied with Al(III) in a dioctahedral phyllosilicate (montmorillonite). The clay platelets are negatively charged as a result of cation isomorphous substitution, either in the octahedral layer (Li(I) for Mg(II) in trioctahedral clays, or Mg(II) for Al(III) in dioctahedral clays), or in the tetrahedral layer (Al(III) for Si(IV)). These negative charges are counterbalanced by exchangeable cations (sodium, for instance) present in the interlamellar space. The location of the defects affects both cation and water interactions with the solid surface.

Nuclear magnetic relaxation dispersion studies on suspensions of bentonite (a montmorillonite-rich mineral) demonstrate that the water proton longitudinal relaxation rates are dominated by magnetic interaction with paramagnetic centres present in the solid matrix.[96] To avoid this effect, hectorite clay, which does not contain paramagnetic species, was used to investigate the water proton relaxation in solid suspensions. Transverse R_2 and longitudinal R_1 relaxation data as a function of temperature and angular frequency indicate that the dominant relaxation mechanism of water molecules in the presence of clay is not the intramolecular proton–proton dipolar coupling modulated by molecular rotation but the interparticular dipolar Hamiltonian affected by the diffusion of adsorbed water at the clay surface.[97] This diffusion process accounts for the logarithmic decrease of R_1 in the static and the rotating frames, respectively, and for a large difference between R_1 and R_2, as found experimentally. A strong liquid–solid interaction is responsible for the 2D diffusion of the adsorbed liquid, even at large distance from the pore walls. At times larger than the residence times, longer than 10^{-6} s, water molecules start to desorb and diffuse in a 3D space.[97] These conclusions are consistent with the above studies on silica.[88–90]

The quadrupolar splittings of solvent nuclei in solid suspensions provide information on the structure and dynamics of molecules at the interface since

the bulk liquid exhibits a single line. Thus, molecules near the solid surface are preferentially oriented with respect to a director (which may be the normal to the solid surface). Variation of molecular orientation with respect to the director modulates the value of the splitting, and this problem was solved mathematically for water molecules several years ago.[98] Fast water exchange between the clay interface and the bulk drastically reduces this splitting. Typically, NMR spectra of aqueous clay suspensions show water ^{2}H and ^{17}O splittings of a few tens and hundreds of hertz, respectively.[99–101]

In smectite clays, the location of cation isomorphous substitution, in either the octahedral or the tetrahedral layer, influences the mean orientation of interfacial molecules. Data obtained with montmorillonites, one hectorite, and one saponite, or with their 1:1 mixtures, indicate water deuteron splittings of opposite signs for tetrahedrally (saponite) or octahedrally (montmorillonites and hectorite) substituted clays.[102,103] With montmorillonite from Wyoming (Mon-WY), in which cation replacement occurs in both layers, a sign reversal of the splitting is observed when increasing the calcium content of exchangeable cations.[100,104] No sign inversion was detected for clays with isomorphous cation substitution either in the octahedral or in the tetrahedral layer.[105,106] Two average water orientations at the clay interface may account for the sign reversal of water deuteron splittings: a cationic director prevails with tetrahedral cation replacement,[103] or for Mon-WY when the calcium content is larger than ~10%[104] (Fig. 8).

From similar studies on suspensions in aqueous binary mixtures, similar conclusions are deduced for cosolvent molecules such as acetonitrile, acetone, dimethylsulfoxide or methanol. Accordingly, deuteron splittings of the deuterated cosolvent have opposite signs for tetrahedrally or octahedrally

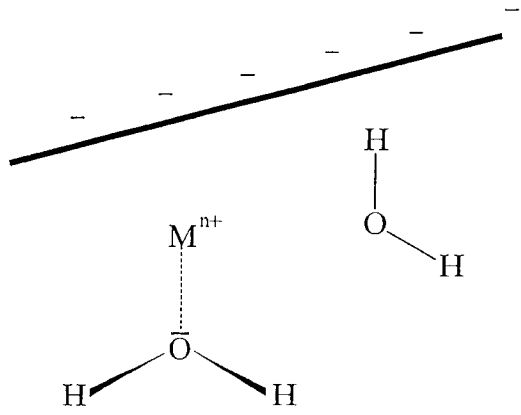

Fig. 8. Mean water orientations of opposite anisotropies (sign reversal of the splitting) at a clay interface.

substituted clays[103] or for Mon-WY suspensions when the content of calcium counterions increases.[104] Again, two plausible orientations of interfacial molecules can be inferred from these data.[104]

Conversely, water ^2H and ^{17}O splittings are not significantly affected by the molar fraction of acetonitrile in water–acetonitrile suspensions of a lithiated saponite. Thus, water orientation remains basically unchanged within the 0–50% (v/v) concentration range of the organic solvent.[107] Deuteron and ^{14}N splittings of acetonitrile-d_3 decrease, disappear, and reappear with the opposite sign when the concentration of the organic cosolvent increases. As a single interfacial site was deduced for saponite,[102,105] variation of the acetonitrile splittings is due to the change of the $(3\cos^2\theta_{DM} - 1)$ factor, where θ is the azimuthal angle between the Z axes of the referents associated with the director and the molecule. Interfacial organic molecules remain bound directly to lithium counterions, but, as the acetonitrile concentration increases, their orientation varies relative to the saponite surface.[107] A similar behaviour is observed for acetone molecules when the same saponite is suspended in water–acetone mixtures.[108] By contrast, water and methanol splittings vary similarly in suspensions of this lithiated saponite in water–methanol mixtures. Splitting data and self-diffusion coefficient measurements of both liquids attest to the increased liquid structuring at the clay surface as compared to that of the solution in the absence of clay.[108]

The layer charge is expected to influence the behaviour of interfacial species. To verify this, similar studies have been performed with synthetic saponites differently charged. The mean water orientation at the synthetic clay interface differs from that observed with the previously investigated natural saponite. The relative population of water molecules near the solid surface decreases as the charge increases. Indeed, a larger number of layers per clay aggregate (tactoid) is formed when the layer charge increases, resulting in smaller external surface areas.[109] The importance of the charge effect is also displayed with suspensions in water–acetonitrile mixtures. As observed with the natural saponite, water orientation at the surface of more highly charged clays (0.5, 0.6 and 0.75 charge per formula unit) is not perturbed by the molar fraction of acetonitrile, within the 0–50% (v/v) range. With a less charged clay (0.3 unit charge), water molecules do not interact strongly enough with the solid surface, and a sign reversal of the water deuteron splitting is observed as the cosolvent content increases.[109]

Other solids. Aluminophosphate molecular sieves form structures with relatively wide unidimensional channels. Water deuteron NMR spectra of two members of this family ($AlPO_4$-5 and VPI-5) are explained in terms of a two-site jump between free and bound water ($AlPO_4$-5) and a three-site exchange with an additional 3-site jump (VIP-5).[110] This latter model has been improved subsequently to account for data in the temperature range from 225 to 348 K.[111]

NMR studies of porous media are devoted to other aspects than interfacial phenomena, and the interested reader may find such information elsewhere.[112]

Deuteron longitudinal relaxation times have been used to monitor solvent association with stationary phases used in reversed-phase liquid chromatography. Suspensions of these alkyl-modified silicas in D_2O–CD_3OD and D_2O–CD_3CN binary mixtures have been studied by such ^2H NMR data. Results have been analysed in terms of interactions between solvent molecules, interactions of each solvent with the solid support, on conformational changes of the alkyl chain.[113,114]

3. STUDY OF INTERFACIAL IONIC SPECIES

3.1. Advances in NMR study of quadrupolar nuclei

Isotropic medium. This section first summarizes the main features of the relaxation theory for quadrupolar nuclei ($I \geq 1$). More detail can be found in a previous review[1] or in the original papers cited in the following sections. When the electric quadrupole moment of the nucleus is high enough, as observed for most quadrupolar nuclei, the dominant relaxation mechanism stems from the interaction of this moment with the electric field gradient generated by the surroundings of the nucleus. In an isotropic solution, fast molecular motion cancels (or averages to zero) the value of the electric field gradient, and a single line is observed. In the extreme narrowing limit ($\omega\tau_c \ll 1$), the longitudinal (R_1) and transverse (R_2) relaxation rates are governed by the same exponential function. Above this limit, these relaxation rates are different and they show a multiexponential behaviour ($=I+\frac{1}{2}$) if $I > 1$, and the NMR lineshape is super-Lorentzian. Generally, the relaxation rates R are expressed as

$$R = K \sum_m J(m\omega) \tag{1}$$

where K depends on the magnetic interaction (quadrupolar, here) responsible for the relaxation process. The spectral density $J(m\omega)$ has usually the form

$$J(m\omega) = \frac{\tau_c}{1 + (m\omega)^2 \tau_c^2}$$

with τ_c being the correlation time characteristic of the fluctuation of the quadrupolar interaction. The sum ($m = 0$, 1 or 2) of the spectral densities $\Sigma_m J(m\omega)$ differs for the longitudinal and transverse relaxation rates. Approxi-

mate expressions for relaxation rates have been reported previously for half-integer spin nuclei[115,116] (or equations (21) and (22) of Ref. 1). They are valid only for small differences between $J(0)$, $J(\omega)$ and $J(2\omega)$, i.e. when R_1^{tot} and R_2^{tot} are nearly equal. More recently, a set of approximations for isotropic media has been used to account for situations where $R_1{}^{tot}$ differs significantly from $R_2{}^{tot}$.[117] In addition to single-quantum transitions, the understanding of the spin dynamics of quadrupolar nuclei has improved by consideration of multiple-quantum transitions, and their spin dynamics have been described for nuclei with spin quantum number of 3/2,[45] 5/2,[46] and 7/2.[118]

Anisotropic medium. When counterion mobility is not fast enough, a residual quadrupolar interaction persists and the NMR spectrum shows $2I$ lines. In these anisotropic media, the splitting is a population-weighted average between a free (bulk, no splitting) and "bound" sites in the simplest case of a two-site model.

The growing use of quadrupolar nuclei in quite diverse applications requires more sophisticated theoretical exchange models. Thus, contrary to previous studies that mainly describe the single-quantum lineshape of 3/2-spin nuclei, spin dynamics of quadrupolar nuclei have been extended to arbitrary spin I and to other density matrix elements, i.e. zero- and multiple-quantum coherences. This broader approach involves four parameters: the Larmor frequency ω, the residual quadrupolar frequency ω_Q, the mean residence time τ_A in an anisotropic site, and the molar fraction of studied nuclei in all anisotropic sites. Direct exchange is allowed only between sites of two classes, i.e. anisotropic and isotropic (bulk medium) environments, and all the sites in a given class are characterized by their equilibrium population P and their mean residence time τ. Typical curves are simulated for different situations, and particularly the dilute regime ($P_A \ll 1$), a quite common case, where the longitudinal relaxation is effectively exponential for all values of $\omega\tau_A$ and $\omega_Q\tau_A$. It should be pointed out that the relaxation curve at different values of ω (relaxation dispersion curve) is uncorrelated with molecular dynamics when $\Omega_Q\tau_A \gg 1$ (the quadrupolar coupling constant $\Omega_Q = \frac{3}{4}\omega_Q$).[119]

NMR theory of counterions has been also developed for macroscopically aligned anisotropic fluids such as liquid crystals, and the relaxation rates differ from those in isotropic media.[1] As an extension of the previous theory, the contribution of the director fluctuation to the relaxation behaviour of quadrupolar nuclei has been considered. Such a situation occurs near the nematic–isotropic phase transition.[120] In a previous review in this series,[1] the development of a new 2D quadrupolar echo sequence for relaxation studies of $I > 1$ nuclei was mentioned.[121] This experiment allowed homogeneous line widths to be obtained, a prerequisite for determining accurate spectral densities. The applicability of this method has been further extended.[122,123] Besides single-quantum coherences, multiple-quantum coherences can also provide independent information on the motional spectral densities or useful

redundancy. The highest coherence ($=2I$) of a quadrupolar nucleus is unaffected by quadrupolar inhomogeneity, and its line width can be determined by a spin-echo experiment. The other satellites from lower multiple-quantum transitions suffer from quadrupolar inhomogeneous broadening (e.g. imperfect alignment), and quadrupolar echo techniques are required to obtain homogeneous line widths.[124] Appropriate pulse sequences have been designed to achieve this.[124] A derived 1D NMR experiment with selection of even-rank coherences makes possible the determination of homogeneous widths of satellite transitions in heterogeneous systems and has been applied to reveal static quadrupolar effects in tissues.[125] In heterogeneous systems, the central line contains an isotropic component that may hide the observation of the quadrupolar splitting. This contribution can be suppressed by multiple-quantum filtering techniques as described later. To obtain relaxation data for $I = 1$ and $I = 3/2$ nuclei, the highest rank quantum-filtered method is most appropriate.[126] A 2D version of the Jeener–Broekaert experiment has also been proposed for obtaining homogeneous line widths for a 3/2-spin nucleus.[127]

When the quadrupolar splitting is small, the satellite peaks may be unresolved and a single super-Lorentzian line occurs. To distinguish between isotropic and anisotropic situations, experiments based upon double-quantum coherences have been proposed for a 3/2-spin nucleus. The first two 90° pulses (usually with a refocusing 180° pulse between them) are used to generate a double-quantum coherence. A third 90° pulse is applied to detect the NMR signal. Although the central peak is suppressed, there is not necessarily clear evidence for quadrupolar splitting. Obviously, the first 90° pulse excites in-phase quantum coherence, represented by a combination of the first-rank, single-quantum tensor operators $T_{1,+1}$ and $T_{1,-1}$. Under biexponential quadrupolar relaxation, characteristic of 3/2-spin nuclei outside the extreme narrowing limit in isotropic solutions, this coherence evolves into doubly antiphase single-quantum coherence described by the third-rank tensors $T_{3,+1}$ and $T_{3,-1}$ (odd ranks from l to $2I$). In contrast, under quadrupolar splitting, the above in-phase coherence evolves into both singly ($T_{2,\pm 1}$, even ranks from 2 to $2I - 1$) and doubly antiphase single-quantum coherence. Thus, a filtration experiment that selects second- (even)-rank tensor operators ($T_{2,p}$) identifies the cause of the non-Lorentzian behaviour observed in the single-pulse NMR spectrum. With the basic sequence, filtration through a state of double-quantum coherence ($T_{2,\pm 2}$ and $T_{3,\pm 2}$) results in the formation of single-quantum coherences with l = 2 and l = 3. A flip angle of 54.7° for one of the last two pulses cancels the contribution of the third-rank tensor operator and phase cycling eliminates triple-quantum coherences formed after the second pulse.[128] An ordered structure (local anisotropy) is shown by an asymmetric doublet with suppression of the central band (Fig. 9).

In the Jeener–Broekaert experiment with the last two pulses of 45°, the unwanted signal components are deleted as a result of the orthogonality of the

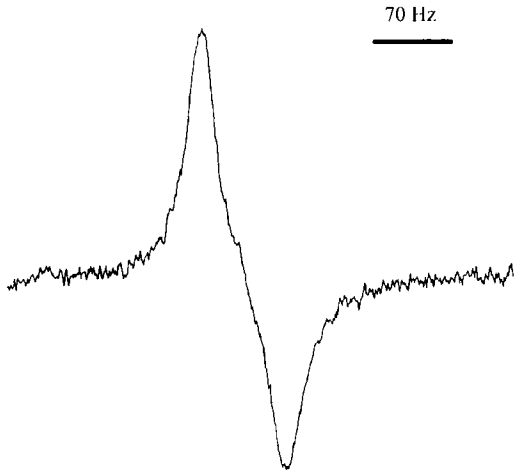

Fig. 9. Typical ^{23}Na NMR asymmetric doublet obtained with double-quantum filtering techniques in the presence of anisotropy (aqueous suspension of natural saponite).

phase of the first 45° pulse compared to that of the initial 90° pulse, and not from a flip angle effect. This sequence is claimed to be more robust.[129] Recently, the equations describing both the second- and the third-rank double-quantum signals have been reformulated. This makes easier the analysis of the double-quantum signal derived from a double-quantum filtering scheme, and new pulse sequences have been suggested. If some improvements are obtained in acquiring the third-order double-quantum signal or in maximizing the total double-quantum signal with nonvanishing quadrupolar coupling, it appears that the above conventional double-quantum filtering (or zero-quantum filtering) should be employed to select the second-rank double- (multiple-) quantum signal.[130]

Broadening of the fast relaxation component(s) in the isotropic case or of the satellite signals may lead to a loss of NMR visibility. Extensive broadening may arise from inhomogeneous effects due to spatial variation of the splitting or from homogeneous effects due to large adiabatic spectral density. A third cause may be insufficient radiofrequency pulse power to excite the satellite transitions if the quadrupolar coupling is large. To understand the physical basis of NMR invisibility, it is important to establish whether one is dealing with a static or a dynamic quadrupolar effect. The above sequences based on multiple-quantum transitions (not affected by the spectrometer dead time) can be useful in this respect.

Chemical exchange of nuclei with spin $I > 1$ between a rotationally immobilized and an isotropic environment has been also considered.[131] When the quadrupolar coupling constant is large, the contribution of the central $(\frac{1}{2} \rightarrow -\frac{1}{2})$

transition may be observed only in the NMR spectrum. This central line is anisotropically broadened to second and higher orders, and the anisotropy of the lineshape may contain information about local dynamic averaging. When ion exchange is too low to sample different orientations of the bound sites, a powder pattern results. The lineshape becomes distorted with an intermediate exchange rate. Fast exchange gives rise to a single super-Lorentzian line.[131]

3.2. Counterions of macromolecules

The electric field gradient at the counterion nucleus originates in surrounding species. Different models have been proposed to account for the observed quadrupolar relaxation rates. One of the more recent has used sodium dimethyl phosphate as a model for DNA to investigate the influence of counteranion and solvent on the electric field gradient at the sodium nucleus. These molecular dynamics simulations conclude that the contributions from counteranions and solvent molecules largely cancel each other. It is also expected that both contact and solvent-separated ion pairs make potentially important contributions to the NMR observations in DNA solutions.[132]

Magnesium–DNA interactions have been investigated by ^{25}Mg ($I = 5/2$) NMR. Both longitudinal relaxation rate and lineshape have been analysed using the isotropic two-site discrete exchange model reported above. Although the variation of the experimental lineshape with temperature has been rather well fitted with a set of theoretical parameters, it was not possible to fit simultaneously both the lineshape and the longitudinal relaxation rate with the same parameters.[133] Furthermore, this model was not able to reproduce the field dependence of the lineshape.[134] More than two sites being in the exchange process, multiple correlation times involved in relaxation at the bound site, residual anisotropy at the bound site, and loss of ^{25}Mg NMR visibility may explain the failure of this model to fit experimental data.[134] The last two causes could be evaluated with multiple-quantum filtering techniques adapted to 5/2-spin nuclei. The distribution of counterions near the macromolecular surface has been estimated with various theoretical models, the most popular being based on the Poisson–Boltzmann equation. ^{23}Na NMR data of highly concentrated DNA solutions with different salt contents have been analysed using such models. For low and moderate salt concentrations, ions accumulate into the grooves, and then onto phosphate groups. The residence times of counterions near the phosphate oxygens and the carbonyl-oxygen of guanine in the major groove are of the order of a few picoseconds and do not depend on DNA concentration. With counterions at distances greater than 11 Å, the residence time decreases with increasing DNA concentration.[135]

Motions of ions parallel and perpendicular to the helix axis are restricted, and their anisotropy increases with a decrease of the DNA concentration. ^{23}Na NMR quadrupolar splittings have opposite signs for cations located either near

the base atoms in the grooves or around phosphate oxygens. The dependence of the ^{23}Na NMR quadrupolar splittings as a function of DNA concentration and temperature is explained by changes of the relative populations of these two cation sites.[135] The effect of temperature on the coupling constants and correlation times has also been reported for salt-free DNA solutions under different magnetic fields.[136] Using a 2D quadrupolar echo sequence, the authors conclude that the quadrupolar splitting is homogeneous throughout the sample. This indicates that the director is uniformly oriented perpendicular to the magnetic field. The relaxation behaviour of sodium counterions in isotropic and anisotropic solutions is caused by at least two processes on different time scales. The fast process is probably associated with fast water dynamics in solution. The second process occurs on the nanosecond time scale and is presumably caused by counterion diffusion near the macromolecule. No additional slow motions in the frequency range between 200 and 9000 Hz are observed,[136] but counterion relaxation rates are not greatly influenced by the macroscopic organization. Thus, a similar decrease of the relaxation rates with increasing temperatures is found for isotropic and anisotropic solutions. Studies at different fields show that this observation stems from a decrease of the coupling constant in the isotropic phase and from a decrease of the correlation time in the anisotropic phase. This emphasizes the importance of field-dependent measurements in data analysis.[136] Another group has also monitored field-dependent ^{23}Na NMR relaxation studies of sodium counterions in ordered DNA. Again, these results indicate that the main contribution to the field-dependent spectral densities occurs from slow and fast local ion motions near the macromolecule.[137]

Quadrupolar NMR splittings of macroscopically oriented samples also allow the study of the hydration of counterions. When ion exchange between different sites is fast relative to the inverse of the quadrupolar interaction, the observed splitting is a weighted average of the values for each anisotropic site (no splitting occurs in isotropic medium). In oriented DNA fibres, ^{7}Li, ^{23}Na and ^{133}Cs NMR splitting changes with water content and temperature are explained in terms of a three-site model: free ions, specifically (site-) bound ions and nonspecifically bound (condensed) ions.[138]

The location and dynamics of Na^+ in frozen proteins, relevant in the context of food storage, has been addressed by NMR.[139] With BSA, the alkali ions are concentrated within the nonfrozen water layer. Multiexponential relaxation is due to separate relaxation rates for the central and outer transitions of the ^{23}Na NMR signal, and no residual quadrupolar interaction can be displayed by multiple-quantum filtering techniques. The apparent correlation times at different temperatures have been deduced from transverse relaxation rates at two different fields. Their values are similar to those of liquids in contact with proteins.[139] In collagen, proteins form fibres, an organized structure. Using ^{23}Na NMR double-quantum-filtered spectra, local anisotropy has been evidenced. Collagen is mainly responsible for the Na^+ local anisotropy found in

suspensions of cartilage.[140] This is in agreement with results obtained with water deuteron spectra.[65]

The behaviour of counterions has also been studied by ^{23}Na, ^{35}Cl and ^{39}K NMR in poly[methacrylic acid-*co*-(*N*,*N*-dimethylamino)ethyl methacrylate] hydrogel (MMA-*co*-DMAMA). Within the low water content range, decreasing the water content of the sodium salt hydrogel (MMA Na-*co*-DMAMA) gives rise to an increase of the line width and an upfield shift of the ^{23}Na NMR signal. This upfield shift supports the formation of contact ion pairs with the polyions, whereas the line broadening results mainly from the variation of the electric field gradient at the nucleus.[141] At water concentrations greater than 6 molecules per sodium cation, contact ion pairs are progressively disrupted and hydrogen bonds between hydrated cations and COO^- groups of methacrylic acid are formed. Addition of KCl broadens the ^{23}Na NMR signals, indicating that the competitive binding of potassium ions to COO^- groups is not very effective. Chain contraction and/or water mobility restriction due to K^+ account for this observation. Within the concentration range investigated, the potassium form of the hydrogel as studied by ^{39}K NMR exhibits a similar behaviour.[141] Protonation of the amino group by hydrochloric acid allows study of this system by ^{35}Cl NMR. As expected, hydrated chloride ions interact with protonated amino groups.[141]

Gel electrolytes formed by solutions of lithium or sodium salts in organic solvents such as propylene carbonate or ethylene carbonate can be immobilized in a polymer matrix based on polyacrylonitrile (PAN) or poly(methyl methacrylate) (PMMA). These composite materials have conducting properties. Alkali NMR relaxation rates have evidenced ion–polymer interactions. Indeed, above the glass transition temperature, the polymer network determines fluctuations of the electric field gradient generated at the alkali nuclei, even for the shortest time scale of observation by NMR.[142,143]

In polyelectrolyte solutions, the alkali NMR relaxation is often biexponential. From the resulting super-Lorentzian line, the apparent correlation time and the $p_B\chi$ product can be extracted. The determination of the quadrupolar coupling constant χ requires the knowledge of the population p_B of cations interacting with the macromolecules. As noted above, the counterion distribution can be estimated from theoretical models. The Poisson–Boltzmann cell model has been used for poly(2-hydroxyethyl methacrylate-*co*-methacrylic acid). ^{23}Na NMR quadrupolar coupling constants of ~200 kHz and a correlation time for electric field gradient fluctuation within the nanosecond range have been obtained.[144] This model has also been used in polysaccharide solutions. The applicability of this model for poly(galacturonic acid) has been studied as a function of polymer concentration and neutralization. Agreement with the Poisson–Boltzmann model is not obtained over the full concentration range, and this is explained by an effect of polymer conformational change.[145] To describe the field dependence of the longitudinal and transverse ^{23}Na NMR relaxation rates in aqueous solutions of xanthan, at least two correlation times

are needed, and the largest value is typically a few nanoseconds.[146] ^{23}Na NMR has been also used to show whether heparin, a polysaccharide with anticoagulant properties, behaves like a polyelectrolyte. Analysis of relaxation rates at different pD values according to the Manning's model indicates that both Na^+ and Mg^{2+} are mainly condensed (polyelectrolyte behaviour) to carboxylate groups of heparin, whereas Ca^{2+}, Zn^{2+} and La^{3+} form site-specific interactions with the carboxylate and sulfamino groups.[147] Addition of electrolytes into a polyelectrolyte solution results in a decrease of ^{23}Na NMR relaxation rate owing to the displacement of Na^+ from the polyion environment by the added cation. Using Bull's formalism based on a two-site exchange model,[115] the binding order $Ca^{2+} > Mg^{2+} > K^+ \approx Na^+$ has been found for poly(sodium acrylate) and poly(sodium-3-acrylamido-3-methylbutanoate). Conversely, the sequence $Ca^{2+} \approx Mg^{2+} > K^+ > Na^+$ has been obtained with poly(sodium 2-acrylamido-2-methylpropanesulfonate).[148] Copolymers of 2-(1-naphthylacetamido)ethylacrylamide (NAEAM) and acrylic acid (AA) contain hydrophobic components (NAEAM) which induce a stronger binding of Na^+ to carboxylates, consistent with the decrease of the dielectric constant in the hydrophobic domains.[149]

Although most studies of polyelectrolyte counterions concern cation nuclei, a few examples of anion studies have also been reported. For instance, interaction of anions with the helix of low-charge carragenans has been investigated by ^{14}N NMR relaxation of SCN^- ion. NMR results have been rationalized within the Poisson–Boltzmann cell model by assuming a single class of anion binding. Intrinsic binding constants have been determined for different anions, and the sequence $Cl^- < NO_3^- < Br^- < SCN^- < I^-$ has been obtained.[150]

3.3. Counterions of aggregates

This section is mainly concerned with dynamic information from counterions, but it should be pointed out that these data may give access to the microstructure of aggregates. The most popular counterion nucleus is certainly sodium-23, and relaxation data may be analysed in terms of Bull's equations.[115] For instance, sodium dodecyl sulfate (NADS) in aqueous and nonaqueous systems has been investigated by this way.[151] More recently, a similar study has been carried on aqueous solutions of sodium dodecylbenzenesulfonate (NaDBS). This commercial product has a composite nature as reflected by the non-linearity of the plot of ^{23}Na NMR relaxation rates versus the reciprocal of the surfactant concentration (above the critical micellar concentration (CMC)).[152] Modelling of the surfactant as a binary mixture leads to a consistent description of the experimental results. The characteristic parameters of the spectral density function for this system[152] are quite similar to those obtained with NADS.[151] Thus, the correlation time associated with the modulation of the

electric field gradient generated at the sodium nucleus near micelles is a little less than 1 ns. The relaxation is caused by local motions and not by dynamics on a length or time scale associated with the size of micelles. A similar ^{23}Na NMR relaxation study has been performed with NaDBS–PMMA latex mixtures.[117] In contrast to the observed behaviour with the surfactant, the transverse relaxation decay curves are clearly biexponential. The faster relaxation components are determined almost completely by the fraction of surfactant adsorbed onto the particle surface. Here, a much longer correlation time of 28.5 ns is found but the quadrupolar coupling constants are similar for sodium cations near surfactant molecules in micelles or adsorbed at the surface of latex particles. Clearly, the relaxation is caused by similar processes in both environments. Water movement does not seem to be the principal cause of relaxation associated with the correlation time of 28.5 ns. The discrete charges at the micelle or particle surface can also cause a fluctuating electric field gradient at the sodium nucleus upon cation diffusion parallel to the surface. A distance of 11 Å between the charges at the latex surface compared to a distance of 6 Å in the micellar system accounts for the observations.[117]

The interpretation of spin relaxation data from isotropic media such as micelles or microemulsions is always difficult since, in contrast to anisotropic fluids, only a single spectral density function is probed (Eq. (1)). To alleviate this problem partially, dynamic shifts that are related to the imaginary part of the complex-valued density function are also measured. ^{23}Na NMR longitudinal and transverse (slow and fast) relaxation rates, together with the dynamic shift, have been measured in microemulsion droplets formed from appropriate mixtures of sodium bis(2-ethylhexyl)sulfosuccinate (AOT), water, and isooctane. The model assumes that fluctuation of the magnitude and orientation of the electric field gradient at the sodium nucleus is due to fast local and slow motions. Dynamics within the Na^+ hydration layer or local diffusive motions of ionic species within the interfacial region and lateral diffusion of the counterion at the interface account for fast local motions and slow motions, respectively. Thus, ^{23}Na NMR data are described in terms of the Na^+ lateral diffusion coefficient, a spectral density contribution to fast local motion, and the residual quadrupolar coupling obtained from the dynamic shift.[153] The close agreement between the present data and those obtained for the same system in the reversed hexagonal phase indicates that the local structure and dynamics at the interface are highly similar in both systems.[153]

An isotropic phase formed by NADS–decanol–water mixtures has been also studied through its ^{23}Na NMR relaxation at different magnetic fields. The data were analysed in terms of fast local motion, counterion diffusion, and micelle reorientation.[154] Polymers with ionic groups at one chain-end are studied as models of ionomers. Inverse micelles of a narrow size distribution are formed by these simple models. ^{6}Li and ^{7}Li NMR have been used to describe ion behaviour within the micelle cores. Lineshape analysis or double-quantum filtering techniques indicate a homogeneous biexponential relaxation process

for all the investigated lithium sulfonated polystyrenes in toluene. Fluctuations of the electric field gradient, in the nanosecond range, are due to lithium ion exchange between different coordination sites within the ionic core.[155]

Within the motional narrowing regime (no quadrupolar splitting), the spin relaxation rates are completely determined by the three laboratory-frame spectral densities $J_m(m\omega)$ with $m = 0, 1, 2$ (Eq. (1)). In macroscopically ordered samples, quadrupolar splittings occur. Thus, the spectral density functions are influenced by the sample orientation, and they are described in terms of director-frame spectral density functions. For uniaxial systems there are three such functions for each m value. To determine the resulting nine spectral densities, at least three linearly independent relaxation rates must be measured for three different orientations. Such a study has been performed for the macroscopically oriented hexagonal phase of the system NADS–decanol–water.[156] A model assuming fast, weakly anisotropic local motions and a slower counterion diffusion around the cylindrical aggregates accounts for the six high-frequency spectral densities ($m = 1, 2$). The three zero-frequency functions ($m = 0$) also contain large contributions from the slow director fluctuations.[156]

With nematic liquid crystals, the magnetic field used to polarize the nuclear spin system also aligns the nematic phase. Lyotropic nematic phases are composed of amphiphilic micellar aggregates having a long-range orientational order and no translational order. In such systems, spin relaxation of counterions is expected to reflect the diffusion of ions over the curved micelle surface and thereby to contain information about the size and shape of the micelle. Spectral densities have been calculated for such motions, and a set of appropriate relaxation experiments allow their determination.[157] From the values obtained, uniaxial micelles with an axis ratio of 3–4 have been proposed for the NADS–decanol–water system.[157] More recent experiments, using angularly dependent longitudinal ^{23}Na NMR relaxation in the same nematic phase, have shown that these micelles are biaxial, with approximate axial ratios of 3:8. Comparison with previous results indicates that the interfacial curvature of the micelles changes with the composition of this nematic phase.[158] The ternary mixture also shows a discotic nematic phase and ^{23}Na NMR relaxation dispersion data have been described in terms of fast and slow motions, as previously noted.[154]

Alkali NMR is also an appropiate probe for detection of small structural differences. Thus, ^{133}Cs NMR reveals that Cs^+ is more tightly bound to the carboxylate group of pentadecafluorooctanoate in heavy than in light water.[159]

In heterogeneous systems, the quadrupolar splitting may be unresolved. Local anisotropy around sodium ions can be revealed by multiple-quantum experiments (Section 3.1). As an example, double-quantum quadrupolar-echo measurements on red blood cells and resealed ghosts have shown such behaviour. Line fitting of the observed curves allows the values of the residual

quadrupolar interaction to be obtained. Changes in the structure of the sodium anisotropic binding sites are correlated with known conformational changes of the membrane cytoskeleton.[160]

3.4. Counterions of solids

Inorganic ions. As clays are negatively charged solids (Section 2.3), cations — alkali ions for instance — are present to counterbalance these charges. The Poisson–Boltzmann theory fails to reproduce the cation behaviour near the solid surface. More sophisticated Monte Carlo simulations indicate that the location of isomorphous cation substitution, either in the octahedral layer or in the tetrahedral layer, leads to cation inner-sphere complexes (i.e. site-bound) in the last case or to cation outer-sphere complexes (i.e. atmospherically bound) in the former.[161] The ^{7}Li NMR spectrum of lithium-exchanged clays suspended in aqueous solutions shows either a super-Lorentzian signal[109,162,163] or a triplet structure when the quadrupolar interaction is not averaged to zero, as found with a natural saponite.[107] In this latter case, the double-quantum-filtered spectrum exhibits the expected asymmetric doublet for long-range anisotropic systems (Fig. 9), whereas in the former case the spectrum is characteristic of the homogeneous biexponential type (Section 3.1). Rather surprisingly, the ^{23}Na NMR spectrum obtained with clay suspensions of sodium-exchanged clays exhibits a Lorentzian lineshape.[99,104,109,162] Competition experiments between sodium and tetrapropylammonium cations lead to a 60% increase of NMR visibility with suspensions of laponite, a synthetic trioctahedral clay with cation isomorphous substitution in the octahedral layer (see Section 2.3) (Table 1). Removal of sodium cations from the clay surface by the organic ions is responsible for the increase of the ^{23}Na NMR signal intensity.[163] Conversely, the ^{7}Li NMR spectrum of lithiated laponite suspensions is totally visible, although organic cations progressively replace alkali ions at the clay interface.[162,163]

Thus, for sodium-exchanged clays only the signal associated with the $(m = \frac{1}{2} \rightarrow m = -\frac{1}{2})$ transition is detected. Double-quantum filtering techniques indicate a broad distribution of Na^+ sites near the clay surface.[163] With synthetic saponites, NMR visibility upon addition of tetrapropylammonium

Table 1. ^{23}Na NMR visibility as a function of the tetrapropylammonium cation $(Q^+)/Na^+$ molar ratio.

Q^+/Na^+ (mol/mol)	0	17	34	50	57	67	84	100	118	134	151
NMR visibility (%)	40	40	40	42	43	81	99	106	97	97	107

cations depends on the layer charge. At similar layer charges, cation interaction is expected to be stronger for trioctahedral clays with cation replacement in the tetrahedral layer than for laponite clay.[161] Increase of NMR visibility with addition of the organic cation is observed only for the less charged solids.[109]

The ^{133}Cs NMR spectrum of caesium-exchanged bentonite suspended in water shows only the NMR visibility of the central transition and the signal intensity increases with the addition of polycations.[164] The weak electric quadrupole moment of the ^{113}Cs nucleus implies a rather narrow NMR signal, as indeed observed. Spectra of hectorite slurries in CsCl solutions exhibit two peaks due to the hydrated cations in solution and to cations near the clay surface. Cation exchange between these two types of site is slower than 120 s^{-1} at 50°C.[165] At low water concentrations, the spectrum pattern is solid-like and the MAS technique is used. Typical values of the electric field gradient result in a quadrupolar interaction that remains small compared to the Zeeman interaction. Thus, the chemical shift of the central signal is not expected to be influenced by second-order effects, and its value is the isotropic one (Section 3.1). Hydration studies on different clay samples reveal two sites for caesium ions at the solid surface. The low-field and high-field signals are assigned to relatively tightly bound (site-binding, Stern layer) and loosely bound (atmospheric binding, Gouy layer) cations, respectively.[165,166] Motional averaging between these two cationic environments occurs with an increase of water content or of temperature, and a narrow peak is observed for frequencies larger than 100 kHz.[165,166] The ^{23}Na NMR line width of montmorillonite dispersed in aqueous poly(ethylene gycol) monooctyl ethers broadens with the concentration of the nonionic surfactant.[167] This broadening results from the interaction between sodium cations and the oxygen atoms of the polyether. Similarly, intercalation of polyoxyethylene between the platelets of lithiated clays displaces cation hydration molecules. In the solid state, these materials behave like ionic conductors and provide an alternative to traditional solid polymer electrolytes.[168]

Organic ions. Interaction of organic cations, in particular ionic surfactants, with solid surfaces has been studied by NMR spectroscopy. Surfactant adsorption at a solid–liquid interface modifies its surface properties such as charge, wettability, or biocompatibility. Selective deuteration of the choline methyl groups of hexadecylphosphocholine (HDPC-d_6) has been used to investigate the binding of this lipid to polystyrene particles. The ^{2}H NMR spectrum of bound lipids consists of an axially symmetric powder pattern, indicating that bound surfactant molecules experience fast anisotropic motional averaging, and that there is a narrow distribution of motional environments. This is in agreement with the formation of a monolayer of surfactant molecules at the particle surface.[169] Addition of ionic surfactants reveals that the choline group undergoes a conformational change due to surface charge similar to that of phosphatidylcholine in bilayer membranes.[170] Upon binding,

an effective correlation time of 5.84×10^{-11} s, longer than that in micelles, has been calculated from ^{2}H NMR longitudinal relaxation times of choline groups.[171] The effect of sodium polystyrenesulfonate and cetyltrimethylammonium bromide on this system shows that the dynamics of the HDPC polar head group is only affected for high contents of both added compounds.[172] Interaction of silica particles with dipalmitoylphosphatidylcholine (DPPC) liposomes occurs through the formation of hydrogen bonds between Si—OH and O—P groups, but the conformation of the choline group is not significantly affected.[173]

Adsorption of dodecyltrimethylammonium bromide from aqueous solution onto silica particles has been followed by ^{2}H NMR spectroscopy. Surfactant molecules selectively deuterated at the methyl or at the α-methylene positions have been synthesized for this purpose. Data analysis indicates that two slowly exchanging molecular domains exist on the solid surface, and accordingly a bilayer adsorbate structure is suggested.[174] The mobility of the head group is strongly hindered as compared to that in the dissolved state. The relaxation rates are described in terms of a model assuming fast anisotropic local and slow isotropic collective motions. The spectral densities $J(\omega)$ (Eq. (1)) are changed according to[98]

$$J(\omega) = \left(\frac{1 + \eta^2}{3 - S_b^2}\right) J_f(0) + S_b^2 J_s(\omega) \tag{2}$$

where the frequency-independent spectral density $J_f(0)$ characterizes the fast motion and $J_s(\omega)$ is associated with the slow motion, η is the asymmetry parameter of the electric field gradient (EFG) tensor, and S_b is the order parameter.

Fast motions are slower than those obtained in micelles and slow motions are similar to those observed for aggregates with a radius similar to the particle radius.[174] More attention has been paid to slow motions in a subsequent study with didodecyldideuteromethylammonium chloride. Using the well-known Carr–Purcell–Meiboom–Gill (CPMG) pulse sequence with variable pulse spacings, motions with correlation times in the microsecond time scale have been observed.[175] With spherical supported vesicles of POPC, ^{31}P NMR has revealed that slow motions, in addition to the diffusion of the lipid molecules along the solid surface, can be due to an area mismatch between the bilayer and the surface of its solid support.[176] Similarly, ^{2}H NMR spectra reveal the interaction of sodium 4-(1′-heptylnonyl)deuterobenzenesulfonate with alumina in aqueous suspensions. Again, these results support the formation of a surfactant bilayer made of two slowly exchanging domains. The inner layer next to the solid surface gives rise to a quadrupolar splitting, whereas the outer layer gives rise to a broad unsplit signal indicative of a more isotropic environment.[177] Using sodium dodecyl sulfate deuterated at the α-position, ^{2}H NMR methods are appropriate for investigating the local ordering and

dynamics of this surfactant at the alumina–water interface. Fast, slightly anisotropic motions (Eq. (2)) are probably dominated by the alkyl chain *trans–gauche* isomerization.[178] On another hand, the quadrupolar splitting is sensitive to the curvature of the surfactant aggregate interface. Among the possible structures of the adsorbed surfactant, residual quadrupolar couplings are consistent with long, ribbon-like aggregates, oblate micelles, or a porous bilayer.[179] From a chain conformational point of view, ^{13}C chemical shifts of several surfactants adsorbed on to silica or alumina indicate that the state of surfactants is similar to that in the micellized state.[180]

4. STUDY OF SUPERFICIAL GROUPS OF THE LESS MOBILE PHASE

Hydration studies based on NOE experiments and reported in Section 2 involve cross peaks with superficial groups of macromolecules or aggregates, but here we are dealing with selective observation of groups at the surface of the phase I (Fig. 1). In macromolecular systems, it has been shown recently that C=O···HOH protein–solvent hydrogen-bonding has a marked influence on the value of the coupling constants $^1J_{NC}$ of amide groups. Conversely, this constant is weakly affected by the formation of N–H···HOH hydrogen bonds. Thus, this parameter can also provide useful information in the study of protein hydration.[181]

Properties of the polar head groups of amphiphiles are affected by the composition of the mobile phase II. Among possible nuclei, ^2H and ^{14}N isotopes have been studied, and relaxation measurements give rise to quantitative information on the dynamics of the interface. These data have been analysed with a reorientational model,[98] assuming a fast motion associated with the internal motion of surfactant molecules within the aggregate and a slow motion due to the lateral diffusion of surfactant molecules and/or the aggregate tumbling (Eq. (2)). This model is strictly valid for micelles,[182] but it has been successfully applied to describe dynamics in other systems. For nonspherical particles, simulated curves have been used to evaluate how these spectral densities are influenced by oblate and prolate particles.[183,184] These calculations also serve to estimate the particle size. In most mesophases, however, fluctuation of the EFG over three time scales must be considered.[185]

^{14}N NMR relaxation experiments have been carried out on the micellar and cubic phases formed by the cetylpyridynium chloride–sodium salicylate–water system.[186] The longitudinal relaxation rate R_1 is rather insensitive to the surfactant concentration; it is affected by fast local motions that do not depend on the aggregate concentration and microstructure. Conversely, the transverse relaxation rate R_2 is governed by slow motions. No discontinuity in the

relaxation rates (and in the self-diffusion coefficient) is found at the phase boundary, indicating a similar microstructure in the micellar and cubic phases. The effective correlation time calculated from both relaxation rates decreases from ~300 ns to ~40 ns with an increase of the surfactant concentration, a peculiar observation that has been rationalized within the frame of a bicontinuous structure.[186] The two-step model (Eq. (2)) should remain appropriate for describing the dynamics of surfactant molecules in the lamellar phase, as exemplified by the didodecyldimethylammonium bromide–water system.[187]

The general orientation dependence of longitudinal relaxation rate of spin-1 nuclei has been described from a theoretical point of view,[188] but to the best of our knowledge this approach has not been used to describe dynamics of polar head groups on amphiphiles. The mean orientation of polar head groups with respect to the aggregate surface can be estimated from NMR studies of selectively deuterated amphiphiles. Deuterium quadrupolar splittings and longitudinal relaxation rates were recorded for three selectively deuterated head group segments of DPOC over a range of water:lipid ratios from 4 to 100. Increasing the water concentration provokes a concerted change in the head group conformation together with an enhancement in its motion rate. These molecular changes result in an increase of the accessibility of the polar headgroups.[189] A quantitative correlation has been found between the ^2H NMR parameters and the thermodynamics of hydration.[190] With phosphatidylcholines, deuterated on the α- and β-carbons of the choline group, the dependence of the splitting on the hydrostatic pressure suggests a tipping of the head group away from the surface, as found for an effect of the membrane surface charge.[191]

Dipolar nuclei are other useful probes for defining motions of the polar head groups. In oriented phases, dipolar coupling constants and anisotropy of the chemical shift lead to structural information on molecular fragments at the aggregate surface. Several glycolipid analogues, labelled with ^{13}C on the sugar ring, have been incorporated into bilayers of oriented dimyristoylphosphatidylcholine.[192] Comparison of dipolar ^{13}C couplings for the natural sugar rings and some of their deoxy analogues reveals some subtle changes in the orientation of the polar head groups of interfacial glycosides. This suggests the presence of hydrophobic interactions at the membrane surface, in addition to the more often cited hydrogen-bonding interactions.[192]

^{31}P NMR anisotropic relaxation times of POPC membranes have been measured to define slow motions of lipid molecules. Lateral diffusion and collective slow motions of phospholipids such as surface undulations and/or collective director fluctuations can account for these data.[176] Longitudinal relaxation times also give insight on the interfacial structure. This can be exemplified with reverse micelle systems formed by AOT in liquid hydrocarbon. The effect of solubilized H_2O and D_2O on the ^{13}C spin–lattice relaxation time of the two AOT carboxylates indicates that the carbonyl group of the

α-chain is more tightly bound to water molecules than that of the β-chain.[193]

Silica and modified silica are versatile materials. Their numerous applications rely on their surface properties, which in turn are determined by the silanol groups on the surface. Cross polarization (CP) ($^1H \rightarrow {}^{29}Si$) can give a rough estimate of heteronuclear dipolar interaction strengths. Thus, ^{29}Si CP-MAS NMR experiments allow hydrogen-bonded silanols to be distinguished from nonbonded silanols, and their ratio to be quantified under different conditions.[194] With two untreated silicas, all the surface silanols are hydrogen-bonded, either to adjacent silanols or to water molecules.[195]

The alkyl chain mobility of modified silicas has been investigated by solid-state and solution-state ^{13}C and ^2H NMR. These results have been summarized,[7] particularly in the context of reversed-phase liquid chromatography,[8] and are not considered further here.

5. STUDY OF SOLID–SOLID INTERFACES

These studies mainly concern polymer and composite systems. Strictly speaking, an interface is present between two incompatible polymers, whereas the region between two more or less compatible polymers is called interphase. This zone is of major importance in determining many of the physical and mechanical properties in advanced materials that are increasingly used as compatibilizers, surfactants or adhesives. Some NMR results have been reported in earlier reviews,[7,9] and more recent works are reported here.

Various solid-state NMR methods have been designed for the characterization of solid–solid interfaces. Recent approaches use the r^{-6} dependence of polarization transfer to excite selectively nuclei of the interfacial region. Conventional NMR methods based on proton or ^{13}C relaxation time measurements have been used to characterize the interphase of dimethylsiloxane–styrene block copolymers,[196] polybutadiene–poly(methyl methacrylate),[197] and poly(divinylbenzene) poly(*n*-butyl acrylate) core–shell latexes.[198] More recent techniques are based on polarization transfer, from protons to nuclei of lower gyromagnetic ratios such as ^{13}C or ^{29}Si under MAS (CP-MAS).[199] When one of the immiscible polymers is deuterated, ^1H-^2H cross polarization magic angle spinning spectroscopy has been proposed to elucidate the composition of the interphase.[200] This method requires an appropriate deuteron spin counting procedure, which has been described in the literature.[201] In symmetric diblock copolymers of perdeuterated polystyrene and poly(methyl methacrylate), an interphase width of ~40 Å has been determined.[200] Polarization transfer between nuclei and unpaired electrons using dynamic nuclear polarization has been also described. At the interface of polycarbonate

and doped polystyrene heterogeneous blends, the dominant mechanism of polarization transfer occurs between electrons in the polystyrene phase and protons in the polycarbonate phase. The chain mobility of interfacial polycarbonate is lower than that in the bulk polymer.[202,203] The interface of immiscible polymer blends has been also investigated by rotational-echo double resonance (REDOR).[204] This method, which requires a stable isotope labelling for each component of the blend, has been applied to a heterogeneous blend of [^{13}C]polycarbonate and poly(*p*-fluorostyrene-*co*-styrene). By this means, the spectrum of interfacial polycarbonate is selectively isolated and can be used to examine the structure and dynamics of the chains at the interface.[203,204] The shorter ^{13}C–^{19}F distances are estimated between 4 and 7 Å.[204] Selective deuteration of one polymer component has also been used to describe mobility within the interfacial region. With poly(styrene-*b*-isoprene), ^{2}H NMR indicates that the portion of polystyrene close to the junction with polyisoprene remains flexible even below its nominal glass transition temperature. On the other hand, polyisoprene molecules near the interface are less mobile than those far from the interface.[205] Similarly in poly(dimethylsiloxane) (PDMS)–nylon-6 block copolymers, an extra narrow peak is observed in the ^{2}H NMR spectrum of the copolymer. This signal arises from a shell of softened nylon in the vicinity of PDMS domains.[206] Thus, a gradient of mobility, i.e. partial immobilization of the soft component and mobilization of the rigid component, occurs across the interface between the two polymers. This has been used to show differences in the interfacial structure of core–shell polymers. A 2D WISE (wide-line separation) experiment provides both structural and dynamic information from the isotropic ^{13}C chemical shift in one dimension and the proton lineshape in the other dimension, respectively. Again, this experiment reveals that the dynamics in the interfacial region is different from the respective dynamical behaviour in the pure phases.[207] Confirmation of this is obtained from dipolar filtered ^{13}C NMR, which is able to select regions with different mobilities. For many years, ^{1}H spin-diffusion experiments have been used to determine the interface thickness up to ~150 nm.[9] Here, advantage has been taken of dipolar filter and ^{1}H-^{13}C CP-MAS to detect selectively ^{13}C NMR spectra of interfacial molecules. Increasing the mixing time of the pulse sequence results in a remagnetization of the less mobile component by spin diffusion. The interface thickness of poly(butyl acrylate)–poly(methyl methacrylate) core–shell latexes is typically 10 nm. Analysis of these data gives also rise to information on the morphology: the low-temperature latexes consist of a core–shell structure, the high-temperature latexes form an interface with microdomains. Poly(butyl acrylate)–polystyrene latexes are characterized by a confetti-like structure (Fig. 10).[207]

These NMR techniques have been applied to poly(styrene-*b*-methylphenylsiloxane) diblock copolymers. As expected from the partial compatibility of these systems, a rather broad interphase of 4.2–5 nm thickness has been determined.[208]

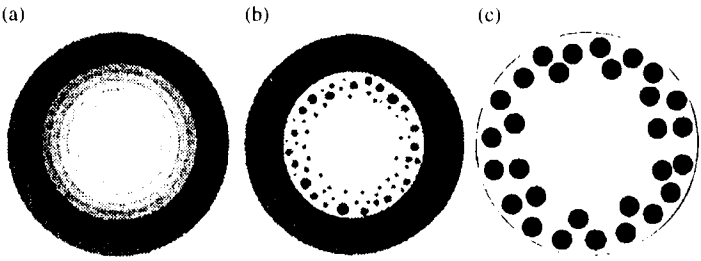

Fig. 10. Morphologies of investigated latexes: a core-shell structure with an interface formed by two components mixed on a molecular level with a continuous concentration gradient (a) or built up of microdomains (b) and a non-core-shell structure but particles with a confetti-like structure (c). (Reprinted with permission from Ref. 207. Copyright 1996 American Chemical Society.)

6. CONCLUSIONS

The past few years have seen the emergence of multidimensional NMR techniques for characterizing interfacial molecules. These studies are based on nuclear Overhauser effects between water protons and superficial nuclei of macromolecules or aggregates. The results are interpreted in terms of water location or residence time at the interface.

The relaxation behaviour at an interface has been considered in isotropic and anisotropic media. These data have generally been analysed by assuming fast and slow motions of the interfacial species, and appropriate forms of spectral density functions have been developed. In heterogeneous systems, long-range ordering can be difficult to see. Multiple-quantum filtering techniques can reveal local anisotropy. These methods also reveal the cause of NMR invisibility of quadrupolar nuclei with $I \geq 3/2$.

Quadrupolar splittings have been used to define the number and characteristics of molecular (water) sites at different interfaces.

For characterization of some solid–solid interfaces, NMR methods are useful in describing the size of this region. They also indicate the presence of a mobility gradient across the interface.

ACKNOWLEDGEMENTS

I thank D. Canet (Nancy), R. Kimmich (Ulm) and P. Stilbs (Stockholm) for providing me with reprints and preprints of their results. I am also grateful to L. Delaude (Liège) for reading the manuscript. FNRS (Brussels) is acknowledged for support in our NMR studies.

REFERENCES

1. J. Grandjean, in *Annual Reports on NMR Spectroscopy* (ed. G. A. Webb), Vol. 24, p. 181, Academic Press, London, 1992.
2. H. Pfeifer and H. Ernst, in *Annual Reports on NMR Spectroscopy* (ed. G. A. Webb), Vol. 28, p. 91, Academic Press, London, 1994.
3. B. Lindman, O. Söderman and P. Stilbs, in *Surfactants in Solution* (ed. K. L. Mittal), Vol. 7, p. 1, Plenum Press, New York, 1989.
4. A. Khan, in *Nuclear Magnetic Resonance* (ed. G. A. Webb), Vol. 20, p. 497, The Royal Chemical Society, London, 1991.
5. O. Söderman, P. Stilbs, *Prog. NMR Spectrosc.*, 1994, **26**, 445.
6. G. Lindblom, *Curr. Opin. Colloid Interface Sci.*, 1996, **1**, 287.
7. F. D. Blum, in *Annual Reports on NMR Spectroscopy* (ed. G. A. Webb), Vol. 28, p. 277. Academic Press, London, 1994.
8. K. B. Sentell, *J. Chromatogr.*, 1993, **A656**, 231.
9. K. Takegoshi, in *Annual Reports on NMR Spectroscopy* (ed. G. A. Webb), Vol. 30, p. 97, Academic Press, London, 1995.
10. R. U. Lemieux, *Acc. Chem. Res.*, 1996, **29**, 373.
11. G. Otting, E. Liepinsh and K. Wüthrich, *Science*, 1991, **254**, 974.
12. G. Otting and E. Liepinsh, *Acc. Chem. Res.*, 1995, **28**, 171.
13. K. Wüthrich, G. Otting and E. Liepinsh, *Faraday Discuss.*, 1992, **93**, 35.
14. G. Otting, E. Liepinsh and K. Wüthrich, *J. Am. Chem. Soc.*, 1991, **113**, 4363.
15. I. P. Gerothanassis, *Prog. NMR Spectrosc.*, 1994, **26**, 171.
16. R. Brüschweiler and P. E. Wright, *Chem. Phys. Lett.*, 1994, **229**, 75.
17. S. Grzesiek and A. Bax, *J. Biomol. NMR*, 1993, **3**, 627.
18. G. M. Clore and A. M. Gronenborn, *J. Mol. Biol.*, 1992, **223**, 853.
19. E. Liepinsh, G. Otting and K. Wüthrich, *Nucleic Acids Res.*, 1992, **20**, 6549.
20. M. G. Kubinec and D. E. Demmer, *J. Am. Chem. Soc.*, 1992, **114**, 8739.
21. S. A. Fawthrop, J.-C. Yang and J. Fisher, *Nucleic Acids Res.*, 1993, **21**, 4860.
22. Y. Q. Qian, G. Otting and K. Wüthrich, *J. Am. Chem. Soc.*, 1993, **115**, 1189.
23. V. A. Chuprina, J. A. C. Rullmann, R. M. J. N. Lamerichs, J. H. van Boom, R. Boelens and R. Kaptein, *J. Mol. Biol.*, 1993, **234**, 446.
24. G. M. Clore, A. Bax, J. G. Omichinski and A. M. Gronenborn, *Structure*, 1994, **2**, 89.
25. Y.-X. Wang, D. I. Freedberg, P. T. Wingfield, S. J. Stahl, J. D. Kaufman, Y. Kiso, T. N. Bhat, J. W. Erickson and D. A. Torchia, *J. Am. Chem. Soc.*, 1996, **118**, 12287.
26. Y.-X. Wang, D. I. Freedberg, S. Grzesiek, D. E. Torchia, P. T. Wingfield, J. D. Kaufman, S. J. Stahl, C.-H. Chang and C. N. Hodge, *Biochemistry*, 1996, **35**, 12694.
27. R. W. Kriwacki, R. B. Hill, J. M. Flanagan, J. P. Caradonna and J. H. Prestegard, *J. Am. Chem. Soc.*, 1993, **115**, 8907.
28. G. Wider, V. Dötsch and K. Wüthrich, *J. Magn. Reson. A*, 1994, **108**, 255.
29. V. Dötsch, G. Wider and K. Wüthrich, *J. Magn. Reson. A*, 1994, **109**, 263.
30. V. Dötsch and G. Wider, *J. Am. Chem. Soc.*, 1995, **117**, 6064.
31. C. Dalvit, *J. Magn. Reson. A*, 1995, **113**, 120.
32. C. Dalvit and U. Hommel, *J. Magn. Reson. B.*, 1995, **109**, 334.
33. C. Dalvit, *J. Magn. Reson. B*, 1996, **112**, 282.
34. G. Otting and E. Liepinsh, *J. Biomol. NMR*, 1995, **5**, 420.
35. S. Mori, M. O. Johnson, J. M. Berg and P. C. M. Van Zijl, *J. Am. Chem. Soc.*, 1994, **116**, 11982.
36. G. Wider, R. Riek and K. Wüthrich, *J. Am. Chem. Soc.*, 1996, **118**, 11629.
37. S. Mori, M. O'Neil Johnson, J. M. Berg and P. C. M. van Zijl, *J. Am. Chem. Soc.*, 1994, **116**, 11982.
38. B. P. Hills, *Mol. Phys.*, 1992, **76**, 489.

39. B. P. Hills, *Mol. Phys.*, 1992, **76**, 509.
40. R. Blinc, V. Rutar, I. Zupancic, A. Zidansek, G. Lahajnar and J. Slak, *Appl. Magn. Reson.*, 1995, **9**, 193.
41. R. Kimmich, F. Klammer, V. D. Skirda, I. A. Serebrennikova, A. I. Maklakov and N. Fatkullin, *Appl. Magn. Reson.*, 1993, **4**, 425.
42. R. Kimmich and H. W. Weber, *Phys. Rev. B*, 1993, **47**, 11788.
43. V. P. Denisov and B. Halle, *J. Mol. Biol.*, 1995, **245**, 682.
44. V. P. Denisov and B. Halle, *J. Mol. Biol.*, 1995, **245**, 698.
45. G. Jaccard, S. Wimperis and G. Bodenhausen, *J. Chem. Phys.*, 1986, **85**, 6286.
46. C. W. Chung and S. Wimperis, *Mol. Phys.*, 1992, **76**, 47.
47. C. W. Flesche, M. L. H. Gruwet, A. Deussen and J. Schrader, *Biochim. Biophys. Acta*, 1995, **1244**, 253.
48. E. Baguet, B. E. Chapman, A. M. Torres and P. H. Kuchel, *J. Magn. Reson. B*, 1996, **111**, 1.
49. K. Tasaki, *J. Am. Chem. Soc.*, 1996, **118**, 8459.
50. R. M. Brunne, E. Liepinsh, G. Otting, K. Wüthrich and W. F. van Gunsteren, *J. Mol. Biol.*, 1993, **231**, 1040.
51. E. W. Knapp and I. Muegge, *J. Phys. Chem.*, 1993, **97**, 11339.
52. S. Lüsse and K. Arnold, *Macromolecules*, 1996, **29**, 4251.
53. T. W. N. Bieze, J. R. C. van der Maarel and J. C. Leyte, *Chem. Phys. Lett.*, 1993, **216**, 56.
54. A. Yamada-Nosaka and H. Tanzawa, *J. Appl. Polym. Sci.*, 1991, **43**, 1165.
55. G. Ganapathy, M. V. Badiger, P. R. Rajamohanan and R. A. Mashelkar, *Macromolecules*, 1992, **25**, 4255.
56. S. Ganapathy, P. R. Rajamohanan, P. M. Ramanujulu, A. B. Mandhare and R. A. Mashelkar, *Polymer*, 1994, **35**, 888.
57. P. R. Rajamohanan, S. Ganapathy, S. S. Ray, M. V. Badiger and R. A. Mashelkar, *Macromolecules*, 1995, **28**, 2533.
58. D. Canet, N. Mahieu and P. Tekely, *J. Am. Chem. Soc.*, 1992, **114**, 6190.
59. S. Ganapathy, S. S. Ray, P. R. Rajamohanan and R. A. Mashelkar, *J. Chem. Phys.*, 1995, **103**, 6783.
60. D. Radloff, C. Boeffel and H. W. Spiess, *Macromolecules*, 1996, **29**, 1528.
61. T.-Q. Li, *Appl. Spectrosc.*, 1996, **50**, 1512.
62. J. L. Hutchison, N. S. Murthy and E. T. Samulski, *Macromolecules*, 1996, **29**, 5551.
63. S. Z. Li, S. Pak, K. Adamic, S. G. Greenbaum, B. S. Lim, G. Xu and A. S. Nowick, *J. Electrochem. Soc.*, 1992, **139**, 662.
64. T.-Q. Li, U. Henriksson, T. Klason and L. Ödberg, *J. Colloid Interface Sci.*, 1992, **154**, 305.
65. Y. Sharf, U. Eliav, H. Shinar and G. Navon, *J. Magn. Reson. B*, 1995, **107**, 60.
66. F. Volke and A. Pampel, *Biophys. J.*, 1995, **68**, 1960.
67. Z. Chen, L. C. M. Van Gorkom, R. M. Epand and R. E. Stark, *Biophys. J.*, 1996, **70**, 1412.
68. N. Mahieu, P. Tekely and D. Canet, *J. Phys. Chem.*, 1993, **97**, 2764.
69. M. P. Milburn and K. R. Jeffrey, *Biophys. J.*, 1990, **58**, 187.
70. R. Raulet, I. Furó, J. Brondeau, B. Diter and D. Canet, to be published.
71. F. Volke, S. Eisenblätter, J. Galle and G. Klose, *Chem. Phys. Lipids*, 1994, **70**, 121.
72. F. Volke, S. Eisenblätter and G. Klose, *Biophys. J.*, 1994, **67**, 1882.
73. S. König, E. Sackmann, D. Richter, R. Zorn, C. Carlile and T. M. Bayerl, *J. Chem. Phys.*, 1994, **100**, 3307.
74. St. Eisenblätter, J. Galle and F. Volke, *Chem. Phys. Lett.*, 1994, **228**, 89.
75. G. Klose, St. Eisenblätter, J. Galle, A. Islamov and U. Dietrich, *Langmuir*, 1995, **11**, 2889.
76. J. Chung and J. H. Prestegard, *J. Phys. Chem.*, 1993, **97**, 9837.
77. I. Furo and H. Johannesson, *J. Magn. Reson. A*, 1996, **119**, 15.
78. H. Johannesson, I. Furo and B. Halle, *Phys. Rev. E*, 1996, **53**, 4904.
79. L. Coppola, C. La Mesa, G. A. Ranieri and M. Terenzi, *J. Chem. Phys.*, 1993, **98**, 5087.

80. S. Abrahmsen-Alami, P. Stilbs and E. Alami, *J. Phys. Chem.*, 1996, **100**, 6691.
81. B. Lindman and U. Olsson, *Ber. Bunsenges. Phys. Chem.*, 1996, **100**, 344.
82. L. J. C. Peschier, J. A. Bouwstra, J. A. de Bleyser, H. E. Junginger and J. C. Leyte, *J. Magn. Reson. B*, 1996, **110**, 150.
83. O. A. El Seoud, A. Blaskó and C. A. Clifford, *Langmuir*, 1994, **10**, 653.
84. O. A. El Seoud, A. Blaskó and C. A. Clifford, *Ber. Bunsenges. Phys. Chem.*, 1995, **99**, 1214.
85. O. A. El Seoud, L. T. Okano, L. P. Novaki and G. K. Barlow, *Ber. Bunsenges. Phys. Chem.*, 1996, **100**, 1147.
86. K. Overloop and L. Van Gerven, *J. Magn. Reson. A*, 1993, **101**, 147.
87. K. Overloop and L. Van Gerven, *J. Magn. Reson. A*, 1993, **101**, 179.
88. S. Stapf, R. Kimmich and J. Niess, *J. Appl. Phys.*, 1994, **75**, 529.
89. S. Stapf, R. Kimmich, R.-O. Seitter, A. I. Maklakov and V. D. Skirda, *Colloids Surfaces A*, 1996, **115**, 107.
90. R. Kimmich, T. Zavada and S. Stapf, *Mater. Res. Soc. Symp. Proc.*, 1997, **464**, 313.
91. O. V. Bychuk and B. O'Shaughnessy, *J. Chem. Phys.*, 1994, **101**, 772.
92. D. R. Kinney, I.-S. Chuang and G. E. Maciel, *J. Am. Chem. Soc.*, 1993, **115**, 6786.
93. C. Dorémieux-Morin, L. Heeribout, C. Dumousseaux, J. Fraissard, H. Hommel and A. P. Legrand, *J. Am. Chem. Soc.*, 1996, **118**, 13040.
94. V. V. Turo, V. M. Gun'ko, V. I. Zarko, V. M. Bogatyr'ov, V. V. Dundik and A. A. Chuiko, *Langmuir*, 1996, **12**, 3503.
95. P. C. Griffiths and P. Stilbs, *Langmuir*, 1995, **11**, 898.
96. S. K. Sur, J. F. Heinsbergen and R. G. Bryant, *J. Magn. Reson. A*, 1993, **103**, 8.
97. A. Delville and M. Letellier, *Langmuir*, 1995, **11**, 1361.
98. B. Halle and H. Wennertröm, *J. Chem. Phys.*, 1981, **75**, 1928.
99. J. Grandjean and P. Laszlo, *J. Magn. Reson.*, 1989, **83**, 128.
100. J. Grandjean and P. Laszlo, *Clays Clay Miner.*, 1989, **37**, 403.
101. J. A. Ripmeester, L. S. Kotlyar and B. D. Sparks, *Colloids Surfaces*, 1993, **78**, 57.
102. J. Grandjean and P. Laszlo, *Clays Clay Miner.*, 1994, **42**, 652.
103. J. Grandjean, *J. Colloid Interface Sci.*, 1997, **185**, 554.
104. A. Delville, J. Grandjean and P. Laszlo, *J. Phys. Chem.*, 1991, **95**, 1383.
105. J. Grandjean and P. Laszlo, *Magn. Reson. Imaging*, 1994, **12**, 375.
106. C. A. Weiss, Jr and W. V. Gerasimowicz, *Geochim. Cosmochim. Acta*, 1996, **60**, 265.
107. J. Grandjean and P. Laszlo, *J. Am. Chem. Soc.*, 1994, **116**, 3480.
108. J. Grandjean and P. Laszlo, *J. Colloid Interface Sci.*, 1995, **175**, 207.
109. J. Grandjean and J.-L. Robert, *J. Colloid Interface Sci.*, 1997, **187**, 267.
110. D. Goldfarb, H.-X. Li and M. Davis, *J. Am. Chem. Soc.*, 1992, **114**, 3690.
111. M. Duer, H. He, W. Kolodziewski and J. Klinowski, *J. Phys. Chem.*, 1994, **98**, 1198.
112. Proceedings of the Third International Meeting on Recent Advances In Magnetic Resonance Applications to Porous Media, Louvain-La-Neuve, Belgium, 3–6 September 1995, *Magn. Reson. Imaging*, 1996, **14**.
113. D. M. Bliesner and K. B. Sentell, *Anal. Chem.*, 1993, **65**, 1819.
114. D. M. Bliesner and K. B. Sentell, *J. Chromatogr.*, 1993, **631**, 23.
115. T. E. Bull, *J. Magn. Reson.*, 1972, **8**, 344.
116. B. Halle and H. Wennerstrøm, *J. Magn. Reson.*, 1981, **44**, 89.
117. J. P. H. Zwetsloot and J. C. Leyte, *J. Colloid Interface Sci.*, 1996, **181**, 351.
118. L. Tsoref, U. Eliav and G. Navon, *J. Chem. Phys.*, 1996, **104**, 3463.
119. B. Halle, *Progr. NMR Spetrosc.*, 1996, **28**, 137.
120. B. Halle, P.-O. Quist and I. Furó, *Phys. Rev. A*, 1992, **45**, 3763.
121. I. Furó, B. Halle and T. C. Wong, *J. Chem. Phys.*, 1988, **89**, 5382.
122. I. Furó and B. Halle, *J. Magn. Reson.*, 1992, **98**, 388.
123. I. Furó, *Chem. Phys. Lett.*, 1992, **194**, 435.

124. I. Furó and B. Halle, *Mol. Phys.*, 1992, **76**, 1169.
125. I. Furó, B. Halle and P-O. Quist, *J. Magn. Reson. B*, 1993, **102**, 84.
126. U. Eliav and G. Navon, *J. Magn. Reson. A*, 1995, **115**, 241.
127. S. P. Brown and S. Wimperis, *J. Magn. Reson. B*, 1995, **109**, 291.
128. U. Eliav, H. Shinar and G. Navon, *J. Magn. Reson.*, 1992, **98**, 223.
129. R. Kemp-Harper and S. Wimperis, *J. Magn. Reson. B*, 1993, **102**, 326.
130. K. J. Jung, J. S. Tauskela and J. Katz, *J. Magn. Reson. B*, 1996, **112**, 103.
131. H. Zhang and R. G. Bryant, *Biophys. J.*, 1995, **68**, 2556.
132. A. S. W. Chen and P. J. Rossky, *J. Phys. Chem.*, 1993, **97**, 10803.
133. E. Berggren, L. Nordenskiöld and W. H. Braunlin, *Biopolymers*, 1992, **32**, 1339.
134. L. A. Wright and L. E. Lerner, *Biopolymers*, 1994, **34**, 691.
135. T. E. Strzelecka and R. L. Rill, *J. Phys. Chem.*, 1992, **96**, 7796.
136. L. C. A. Groot, J. R. C. Van der Maarel and J. C. Leyte, *J. Phys. Chem.*, 1994, **98**, 2699.
137. J. Schultz, B. Andreasson, L. Nordenskiöld and A. Rupprecht, *J. Phys. Chem.*, 1994, **98**, 8507.
138. J. Schultz, L. Nordenskiöld and A. Rupprecht, *Biopolymers*, 1992, **32**, 1631.
139. P. S. Belton and S. J. Kitchen, *J. Chem. Soc., Faraday Trans.*, 1995, **91**, 1459.
140. U. Eliav and G. Navon, *J. Magn. Reson. B*, 1994, **103**, 19.
141. S. K. Kang and M. S. Jhon, *Macromolecules*, 1993, **26**, 171.
142. P. E. Stallworth, J. Li, S. G. Greengaum, F. Croce, S. Slane and M. Salomon, *Solid State Ionics*, 1994, **73**, 119.
143. P. E. Stallworth, S. G. Greengaum, F. Croce, S. Slane and M. Salomon, *Electrochim. Acta*, 1995, **40**, 2137.
144. J. D. Song and M. S. Jhon, *J. Polym. Sci., Polymer Chem.*, 1993, **31**, 1687.
145. S. Ghagare, G. B. Savitsky and H. G. Spencer, *Polymer*, 1992, **33**, 4725.
146. A. Gamini, J. de Bleijser and J. C. Leyte, *Carbohydr. Res.*, 1991, **220**, 33.
147. D. L. Rabenstein, J. M. Robert and J. Peng, *Carbohydr. Res.*, 1995, **278**, 239.
148. J. K. Newman and C. L. McCormick, *Macromolecules*, 1994, **27**, 5114.
149. J. K. Newman and C. L. McCormick, *Macromolecules*, 1994, **27**, 5123.
150. W. Zhang, L. Picullel and S. Nilsson, *Macromolecules*, 1992, **25**, 6165.
151. A. Ceglie, G. Colafemmina, M. Della, M. L. Burlamacchi and M. Monduzzi, *J. Colloid Interface Sci.*, 1991, **146**, 363.
152. J. P. H. Zwetsloot, J. G. Hollander and J. C. Leyte, *J. Colloid Interface Sci.*, 1996, **178**, 233.
153. P. Huang Kenéz, G. Carlström, I. Furó and B. Halle, *J. Phys. Chem.*, 1992, **96**, 9524.
154. I. Furó and B. Halle, *Phys. Rev. E*, 1995, **51**, 466.
155. P. Vanhoorne, J. Grandjean and R. Jérôme, *Macromolecules*, 1995, **28**, 3553.
156. P.-O. Quist, I. Blom and B. Halle, *J. Magn. Reson.*, 1992, **100**, 267.
157. P.-O. Quist, B. Halle and I. Furó, *J. Chem. Phys.*, 1992, **96**, 3875.
158. P.-O. Quist, *J. Phys. Chem.*, 1996, **100**, 4976.
159. N. Boden, K. W. Jolley and M. H. Smith, *J. Phys. Chem.*, 1993, **97**, 7678.
160. T. Knubovets, H. Shinar, U. Eliav and G. Navon, *J. Magn. Reson. B*, 1996, **110**, 16.
161. E. S. Boek, P. V. Coveney and N. T. Skipper, *J. Am. Chem. Soc.*, 1995, **117**, 12608.
162. J. Grandjean and P. Laszlo, *J. Magn. Reson.*, 1991, **92**, 404.
163. J. Grandjean and P. Laszlo, *J. Magn. Reson. A*, 1996, **118**, 103.
164. C. Breen, J. O. Rawson and B. E. Mann, *J. Mater. Chem.*, 1996, **6**, 253.
165. C. A. Weiss Jr, R. J. Kirkpatrick and S. P. Altamer, *Geochim. Cosmochim. Acta*, 1990, **54**, 1655.
166. Y. Kim, R. J. Kirkpatrick and R. T. Cygan, *Geochim. Cosmochim. Acta*, 1996, **60**, 4059.
167. J. Grandjean and P. Laszlo, *Magn. Reson. Imaging*, 1996, **14**, 983.
168. S. Wong, S. Vaudevan, R. A. Vaia, E. P. Giannelis and D. B. Zax, *J. Am. Chem. Soc.*, 1995, **117**, 7568.
169. P. M. Macdonald, Y. Yue and J. R. Rydall, *Langmuir*, 1992, **8**, 164.

170. Y. Yue, J. R. Rydall and P. M. Macdonald, *Langmuir*, 1992, **8**, 390.
171. S. C. Kuebler and P. M. Macdonald, *Langmuir*, 1992, **8**, 397.
172. Y. Yue and P. M. Macdonald, *Langmuir*, 1993, **9**, 1206.
173. Y. Chunbo, Z. Daqing, L. Aizhuo and N. Jiazuan, *J. Colloid Interface Sci.*, 1995, **172**, 536.
174. E. Söderlind and P. Stilbs, *Langmuir*, 1993, **9**, 2024.
175. E. Söderlind, M. Björling and P. Stilbs, *Langmuir*, 1994, **10**, 890.
176. C Dolainsky, A. Möps and T. M. Bayerl, *J. Chem. Phys.*, 1993, **98**, 1712.
177. E. Söderlind and F. D. Blum, *J. Colloid Interface Sci.*, 1993, **157**, 172.
178. E. Söderlind, *Langmuir*, 1994, **10**, 1122.
179. P.-O. Quist and E. Söderlind, *J. Colloid Interface Sci.*, 1995, **172**, 510.
180. E. Söderlind and P. Stilbs, *Langmuir*, 1993, **9**, 1678.
181. N. Juranic, V. A. Likic, F. G. Prendergast and S. Macura, *J. Am. Chem. Soc.*, 1996, **118**, 7859.
182. H. Wennerstrøm, B. Lindman, O. Söderman, T. Drakenberg and J. B. Rosenholm, *J. Am. Chem. Soc.*, 1984, **101**, 6860.
183. B. Halle and H. Wennerström, *J. Chem. Phys.*, 1991, **94**, 3150.
184. R. Skurtveit and U. Olsson, *J. Phys. Chem.*, 1992, **96**, 8640.
185. B. Halle, P.-O. Quist and I. Furó, *Liquid Cryst.*, 1993, **14**, 227.
186. M. Monduzzi, U. Olsson and O. Söderman, *Langmuir*, 1993, **9**, 2914.
187. F. Caboi and M. Monduzzi, *Langmuir*, 1996, **12**, 3548.
188. C. Morrisson and M. Bloom, *J. Magn. Reson. A*, 1993, **103**, 1.
189. A. S. Ulrich and A. Watts, *Biophys. J.*, 1994, **66**, 1441.
190. A. S. Ulrich and A. Watts, *Biophys. Chem.*, 1994, **49**, 39.
191. B. B. Bonev and M. R. Morrow, *Biophys. J.*, 1995, **69**, 518.
192. C. R. Sanders and J. H. Prestegard, *J. Am. Chem. Soc.*, 1992, **114**, 7096.
193. A. Yoshino, H. Okabayashi and T. Yoshida, *J. Phys. Chem.*, 1994, **98**, 7036.
194. I.-S. Chuang, D. R. Kinney and G. E. Maciel, *J. Am. Chem. Soc.*, 1993, **115**, 8695.
195. I.-S. Chuang and G. E. Maciel, *J. Am. Chem. Soc.*, 1996, **118**, 401.
196. R. Soltani, F. Lauprêtre, L. Monnerie and S. Krause, *Polymer*, 1995, **36**, 275.
197. D. Tembou Nzudie, L. Delmotte and G. Riess, *Makromol. Chem. Phys.*, 1994, **195**, 2723.
198. V. Nelliappan, M. S. El-Aasser, A. Klein, E. S. Daniels and J. E. Roberts, *J. Appl. Polym. Sci.*, 1995, **58**, 323.
199. N. Zumbulyadis and J. M. O'Reilly, *Macromolecules*, 1991, **24**, 5294.
200. N. Zumbulyadis, M. R. Landry and T. P. Russell, *Macromolecules*, 1996, **29**, 2201.
201. N. Zumbulyadis, *Solid State Nucl. Magn. Reson.*, 1995, **5**, 3.
202. M. Afeworki, J. Schaefer, *Macromolecules*, 1992, **25**, 4097.
203. M. Afeworki, R. A. McKay and J. Schaefer, *Macromolecules*, 1992, **25**, 4084.
204. G. Tong, Y. Pan, M. Afeworki, M. D. Poliks and J. Schaefer, *Macromolecules*, 1995, **28**, 1719.
205. D. D. Smith, I. Noda, C. Marcott, A. E. Dowrey, P. T. Russel, A. Mayes, J. A. Kornfield, C. C. Chung and E. T. Samulski, *Polym. Propr. (Am. Chem. Soc., Div. Polym. Chem.)*, 1994, **35**, 596.
206. U. Mukai, K. K. Gleason, A. S. Argon and R. E. Cohen, *Macromolecules*, 1995, **28**, 4899.
207. K. Landfester, C. Boeffel, M. Lambla and H. W. Spiess, *Macromolecules*, 1996, **29**, 5972.
208. B. Gerharz, A. Du Chesne, G. Lieser and E. W. Fischer, *J. Mater. Sci.*, 1996, **31**, 1053.

Index

This Page Intentionally Left Blank